Role of Heterogeneous Ecosystems in Modulating Surface-Atmosphere Transport

By

Sreenath Paleri

A dissertation submitted in partial fulfillment of

the requirements for the degree of

Doctor of Philosophy

(Atmospheric and Oceanic Sciences)

at the

UNIVERSITY OF WISCONSIN-MADISON

2023

Date of final oral examination: 05/11/2023

The dissertation is approved by the following members of the Final Oral Committee:

Ankur R. Desai, Professor, Atmospheric and Oceanic Sciences
Gregory Tripoli, Emeritus Professor, Atmospheric and Oceanic Sciences
Grant Petty, Professor, Atmospheric and Oceanic Sciences
Tristan L'Ecuyer, Affiliate Professor, Nelson Institute for Environmental Studies
Stefan Metzger, Adjunct Assistant Professor, Atmospheric and Oceanic Sciences

Abstract

Role of Heterogeneous Ecosystems in Modulating Surface-Atmosphere Transport

by Sreenath Paleri

Accurate and reliable knowledge of the surface-atmospheric transport of mass and energy is essential to inform our theories and models of Earth system processes. However, the Earth's surface is heterogeneous at multiple scales owing to spatial variability in various properties. Hence, the atmospheric responses to these heterogeneities through fluxes of energy, water, carbon and other scalars are also scale-dependent and non-linear. Although these exchanges can be directly measured using the conventional, tower-mounted eddy covariance technique, such single-point measurement approaches suffer from spectral losses in lower frequencies when using typical averaging times. The Chequamegon Heterogeneous Ecosystem Energy-balance Study Enabled by a High-density Extensive Array of Detectors 2019 (CHEESEHEAD19) was a field campaign designed to intensively sample and scale the land surface properties, surface energy balance and the atmospheric boundary layer (ABL) responses to those within a 10 $\times$ 10 km heterogeneous forested domain (that would fit within a 'grid cell' of a weather/climate model) in northern Wisconsin, USA. In this dissertation, I studied the relevance of landscape scale, low-frequency (meso-β, meso-γ), secondary circulations in the ABL transport of surface heat fluxes during the Intensive Observation Periods (IOP) of CHEESEHEAD19. Specifically, I was interested in the effects of boundary layer static stability and surface heterogeneity on modulating ABL organisation and examined the same using a combination of high resolution measurements and numerical simulations.

Applying wavelet analysis to the airborne turbulence measurements during the IOP days allowed us to evaluate and spectrally resolve the flux contributions at 100 m above ground over the heterogeneous landscape. Diurnal cycles for two days in the August IOP and two days in the September IOP over a 27×30 km^2 extended CHEESEHEAD19 domain were simulated using the PArallelized Large Eddy Simulation Model (PALM). The simulated and measured horizontal wind profiles and near surface time series agree well with each other. The mean simulated values have a dependence on the imposed non-periodic boundary conditions derived from the NCEP HRRRv4 data product. Finally, the coupled LES of the CHEESEHEAD19 field experiment days were diagnosed to identify secondary circulations induced by the heterogeneous land surface through time and ensemble averaging. The coupled simulations reveal quasi-stationary and persistent heterogeneity induced secondary circulations in the daytime ABL over the CHEESEHEAD19 study domain that span the entire mixed layer height. In the convective boundary layer, wavelengths that scale as the effective surface heterogeneity length scales at $\sim 3z_i$ contribute the most to the heterogeneity induced transport.

This study underscores the role of ABL static stability, the ABL height and surface heterogeneity length scales in modulating the contributions from secondary circulations. Our study supports ongoing parameterisation efforts for the contributions from secondary circulations to tower measured surface energy imbalance using non-local scaling factors: z_i, $u_* \,/\, w_*$ and effective surface heterogeneity length scales. Our findings about the atmospheric coupling to surface heterogeneity scales can help to inform consistent assumptions for sub-grid heterogeneity in land surface schemes and ABL /convection schemes while representing the sub-grid coupling between land surface and atmospheric heterogeneities in weather and general circulation models.

Acknowledgements

This thesis would not have been possible without the support, love and guidance from a multitude of colleagues, collaborators, friends and relatives ; the family that I was born with and the one that I picked up during my journeys around the sun. I am deeply indebted to my advisor, mentor and good friend Ankur Desai, for being the light house of fortitude, clarity and humanity that has steered this dissertation and my PhD life ashore. Throughout my professional and personal life, I have been fortunate enough to have had more than one instance of serendipitous happenstance and I consider the opportunity to work with him among one of those. I express my most sincere gratitude to Ankur for demonstrating through his personal and professional life that a great scientist would also be a great human being, with integrity and kindness.

I am profoundly thankful for the patience, constant encouragement and understanding of my family. My sister, Anagha, who's my oldest friend for her incessant outpouring of positivitea and grace. My parents for their understanding and kindness while I was trying to figure out my scientific path. Achan (Dad) for his curiosity about my research and untiring enthusiasm to understand surface-atmosphere interactions, which helped me understand my own research more clearly. Amma (Mom) for her warmth and words of wisdom from her own thesis writing days. Both of them for instilling in me a sense of curiosity and groundedness that I carry within as my piece of our home. My best buddy and partner in life Akshaya, and her effervescent optimism while dealing with all the uncertainties and difficult situations that come about while co-navigating two PhD lives. For reminding me to always be non-judgemental and respectful in our everyday lives. I am grateful to have the support of my loving inlaws, Hari, Aai, Papa, Didi, Jijju, Bhaiyu and my two joyous nephews for the happiness they have added on to my life during these five years.

I was extremely fortunate to work with the my colleagues on the CHEESEHEAD project who have gone on to become some of my dear friends. I'd like to thank Stefan Metzger at NEON, who's also in my PhD committee for his kind and very thoughtful mentoring and a generosity of deep insights throughout my PhD journey. A lot of what I've understood about my work was by listening in to the conversations between Ankur, Stefan and Matthias Mauder. Luise Wanner for being the best colleague and co-PhD one could ask for, with her impeccable work ethic, genuine

friendship and clarity of thought. Matthias Sühring, without whose guidance, mentorship and technical support we would not have been able to setup and finish our LES production runs in the two years it took us to. Matthias was instrumental in helping me understand the physics of surface-atmosphere coupling through secondary circulations and their LES solutions. I'd like to thank Matthias Mauder for hosting me at TU Dresden, for his guidance and spirit of enquiry throughout our collaboration on the airborne and LES analysis. I'd also like to thank Brian Butterworth and David Durden, for al their support in helping me process and work with the tower and aircraft data respectievly and the good cheer and company they always bring about.

Throughout my stay at UW Madison and AOSS, I've always felt at home at the Desai Lab, where I always felt like I belong here, from my first day. This would not have been possible without my lab mates being who they are and I'd like to thank all of them. Bailey, who's essentially a sister from another mother, for always being there and willing to share the chaos and excitement of my research and personal life. Ammara for being the best office mate one could ever imagine. Thank you for sharing your tea, excitement about hydrology and heartfelt enthusiasm to keep learning as much as one can. I am grateful to have shared my office space with you. Andi, for his graceful, kind and wise soul and always making time for any of my queries and showing me that one will always have time for things should one choose so. I'd like to thank Susi, Jonathan, Jess, James, Nikaan and Emily for their friendship and camaraderie. I'd like to thank Vijit for all his time, support and companionship for the last five years that we have been housemates in Madison. Thank you for suggesting me to apply to UW for graduate school and pointing me towards Ankur, for helping me settle in an unknown country and for always being there no matter the time or your own personal constraints. This PhD would not have been possible without having you around as well! I'd like to acknowledge and thank Abhilash for the generous soul that he is, with his time, advice, and support as a genuine friend. I'd like to acknowledge the support from the other candidates in my PhD cohort, James and Kari who, once again, welcomed me wholeheartedly into a new country and new system and was always open and understanding.

I'd also like to acknowledge my friends in India without whose love and support it would have been impossible for me to muster up the courage and prepare to apply for graduate school internationally. Most of whom have in-turn found their own personal lives dock at the shores

of the US. Neeraj Surendran, for being the loving, grounded and pragmatic brotherly soul that he is. TS for always reminding me what I am capable of. Bs, 7f and Kaushik who have always been around for the last 10 years of my long winding journey since Insti. I am deeply grateful for their wise counsel, good home cooked food, loving company and the chai. Psych and Poorva and their little bundle of joy, Dhriti for the happiness and warmth they have always graciously showered on me. I'd like to thank Ali for being the wonderful friend and brother in arms that he has been. Always looking out for me and Akshaya and restoring my faith in the integrity of a scientist who can also be political without being obtuse or snobby. Sahithya and Beth and their Azhagi for always treating me as their own family and for always being there for me and Akshaya during these last five years. For never hesitating to help us and for never hesitating to offer me space and time. It's once again serendipitous that they would come to live close by across an entire ocean. I'd like to thank Nandu Gopan from the bottom of my heart for all he has been and done for me from multiple time zones, countries and institutions. For all the illuminating long walks and discussions. I still strongly believe that it was him who convinced me to resign my corporate job and give my passion for academic research a shot in the sciences. I will forever be grateful for your kind counsel, for generously offering me a home whenever I've needed one, for always being yourself and for introducing me to so much of film, music amd for being my comrade in words.

I would like to extend my deepest appreciation for the mentoring and support from Prof. G. S. Bhat at the Centre for Atmospheric and Oceanic Sciences, Indian Institute of Sciences, Bangalore. For offering me a position tending to flux towers and processing EC tower data, which was my first foray into Boundary Layer Meteorology. His kind, humane, but unwaveringly objective way to approach science and life has left a deep impression on me that I hope to carry forward for the rest of my time here. I'd like to thank the rest of the members of my PhD committe, Grant Petty, Greg Tripoli and Tristan L'Ecuyer for their guidance and always enthusiastic reviews and discussions of this work. It was always personally very educational and insightful for me to discuss my research proposals and work with them. I'd like to thank the wonderful staff at AOSS, Pete, Dee, Christi and Carolyn for being generous with their time, always lending a helping hand and support. I could not have finished this dissertation without Pete's dedicated support and maintenance of our lab servers. I've enjoyed being able to discuss

aspects of my work with Khalid Ghannam at GFDL, whose suggestions and questions have helped me dig deeper into questions of organisation in the atmospheric boundary layers.

This doctoral research was supported by the National Science Foundation through the CHEESEHEAD19 project (grant no. AGS-1822420) and the NEON Program (grant no. DBI-0752017). The National Ecological Observatory Network is a program sponsored by the National Science Foundation and operated under cooperative agreement by Battelle. I'd like to thank the developers of PALM at the Institute of Meteorology and Climatology of Leibniz Universität Hannover, Germany for the open source model and their prompt technical support. I would also like to acknowledge high-performance computing support from Cheyenne (doi:10.5065/D6RX99HX) provided by NCAR's Computational and Information Systems Laboratory, sponsored by the National Science Foundation.

Finally I also recognise that our field research occurs on the traditional territories of the Ojibwe people, which have been unjustly ceded and whose ancestors were the original scientists and naturalists who stewarded the land, air, and waters we are fortunate to observe, reflect, and hopefully help continue to flourish.

Contents

List of Figures

List of Tables

Chapter 1

Background and Motivation

"All that you touch you Change.

All that you Change Changes you.

The only lasting truth is Change."

Octavia Butler, Parable of the Sower

Surface atmospheric fluxes of energy, momentum, water, carbon and other scalars are integral components of earth system processes. Terrestrial ecosystems act as important intermediaries for these exchange processes, influencing earth's weather and climate systems (Pielke et al., 1998). These surface-atmospheric fluxes can be directly measured using the eddy-covariance (EC) technique (Aubinet et al., 2012; Foken, 2017). The EC technique uses Reynolds decomposition of the Navier-Stokes equation for momentum and scalar transport, with the assumptions of stationarity and horizontal homogeneity, to calculate turbulent fluxes in the atmospheric boundary layer (ABL). Tower based EC measurements are widely used to study ecosystem level biosphere-atmosphere interactions and quantify surface-atmospheric fluxes (Aubinet et al., 1999; Baldocchi et al., 2001).

Using Reynolds decomposition on the conservation equation of a scalar χ, assuming incompressibility, and writing the turbulent advection terms in their flux forms, we can get (Aubinet et al., 2012; Stull, 1988) :

$$\overline{\rho_d}\frac{\overline{\partial\chi}}{\partial t} + \overline{\rho_d u}\frac{\overline{\partial\chi}}{\partial x} + \overline{\rho_d v}\frac{\overline{\partial\chi}}{\partial y} + \overline{\rho_d w}\frac{\overline{\partial\chi}}{\partial z} + \frac{\partial\overline{\rho_d}\overline{u'\chi'}}{\partial x} + \frac{\partial\overline{\rho_d}\overline{v'\chi'}}{\partial y} + \frac{\partial\overline{\rho_d}\overline{w'\chi'}}{\partial z} = \overline{S} \tag{1.1}$$

Integrating Equation1.1 over a Cartesian control volume as shown in Fig. 1.1, gives us

$$\frac{1}{4L^2}\int_{-L}^{L}\int_{-L}^{L}\int_{0}^{h_m}\left[\underbrace{\overline{\rho_d}\frac{\overline{\partial\chi}}{\partial t}}_{I} + \underbrace{\overline{\rho_d u}\frac{\overline{\partial\chi}}{\partial x} + \overline{\rho_d v}\frac{\overline{\partial\chi}}{\partial y} + \overline{\rho_d w}\frac{\overline{\partial\chi}}{\partial z}}_{II} + \underbrace{\frac{\partial\overline{\rho_d}\overline{u'\chi'}}{\partial x} + \frac{\partial\overline{\rho_d}\overline{v'\chi'}}{\partial y}}_{III} + \underbrace{\frac{\partial\overline{\rho_d}\overline{w'\chi'}}{\partial z}}_{IV}\right] dzdxdy = \frac{1}{4L^2}\int_{-L}^{L}\int_{-L}^{L}\int_{0}^{h_m}\underbrace{\overline{S}dzdxdy}_{V} \tag{1.2}$$

The complete budget of χ within the control volume (CV) states that the scalar could be stored in the CV (term I) or transported by advection (terms in II) or turbulence (terms in III and IV) because of a source or sink (term V). The most common simplification of this budget which aids the generalised Eddy Covariance approach gives the following expression for the vertical turbulent flux measured at the top of the CV:

$$\int_{0}^{h_m}\underbrace{\overline{\rho_d}\frac{\overline{\partial\chi}}{\partial t}}_{I}dz + \underbrace{\overline{\rho_d}\overline{w'\chi'}|_{h_m}}_{IV} = \underbrace{F_s}_{V} \tag{1.3}$$

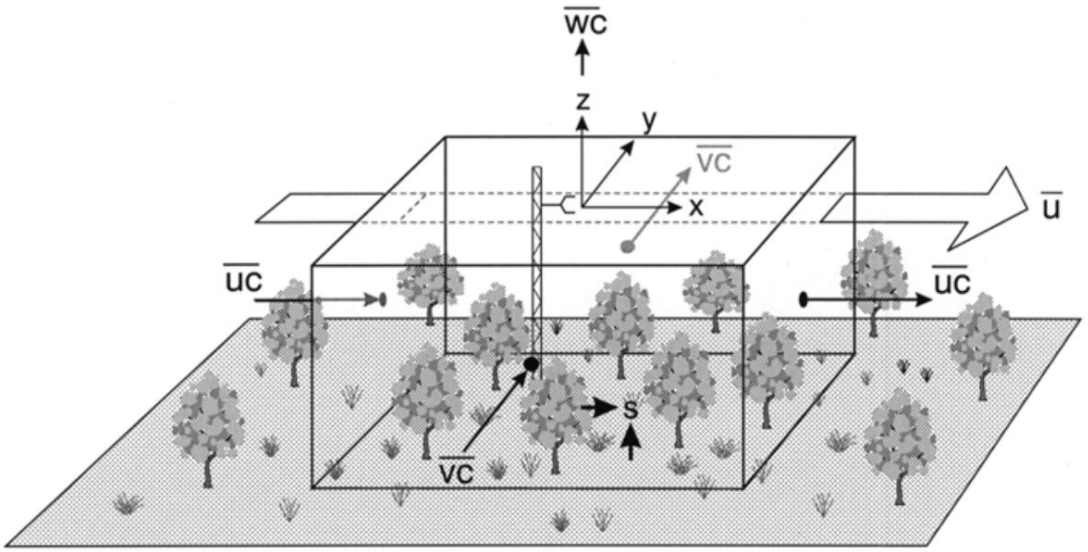

FIGURE 1.1: Cartesian control volume over a homogeneous surface (reproduced from Finnigan et al. (2003) Figure 1.a), over which the vertical flux $\overline{WC}$ is to be measured

This 1D simplification presupposes that the measurements are performed in a horizontally homogeneous equilibrium layer where all horizontal gradients are negligible (Finnigan et al., 2003). The vertical fluxes of the scalar at the surface and subsidence or convection are assumed to be negligible as well, cancelling out the w' term at the surface and the $\overline{w}$ term. Simplifying this further and assuming steady state for the CV, term I can also be neglected. Term I can be considered to be small only over the full diurnal cycle, but can be significant over shorter time intervals. The assumption that the measurements are made in the surface layer of the ABL is also made, because within the surface layer the vertical turbulent flux divergence is small (within 10%, Foken (2017)). Which gives us the vertical turbulent flux over the CV as the turbulent covariance with the vertical wind:

$$F_s = \overline{w'\chi'}|_{h_m} \tag{1.4}$$

With such strict assumptions and idealisations, over realistic surfaces EC measurements run into issues. Hence, routine quality check criteria are included in EC flux calculations and experiment design to check and ensure that turbulence is stationary and well mixed during the averaging intervals and over the domain. Tower measurements are also made in the surface layer, well above the roughness sub-layer of the ABL where the effects of surface roughness elements are considered to be blended (Mahrt, 2000). It should be noted that, despite requirements for idealised experimental conditions and strict assumptions, the EC method provides a direct measure of surface atmospheric transport.

However, even with such experimental design and quality control, single point tower measurements are limited by their footprints (part of the upstream surface contributing to the measured flux). Moreover, requirements for stationarity can complicate sampling flux contributions from lower frequencies (Desjardins et al., 1997; Mahrt, 2010) as well.

Here, I investigate how variations in land surface properties can influence the ABL response and thereby affect single-point tower measured surface energy budgets and fluxes. I hope to further advance our understanding of the diurnal and seasonal ABL evolution and circulation characteristics using observations and numerical simulations over a heterogeneous mid-latitude forested landscape.

1.1 Surface Energy Balance Closure Problem

A good first order sanity check on tower measured turbulent fluxes would be to check for the closure of the measured surface energy budget (SEB); Whether available energy within the

control volume sampled by the tower is balanced by the measured turbulent fluxes. Such a check would also be important to validate land surface and biological model parameters such as surface flux parameterizations in weather/climate models, water vapour surface conductances in ecosystem/land surface models or validating model predictions of Net Ecosystem Exchange.

A simple 1D energy balance can be written as:

$$Rn = H + LE + G \tag{1.5}$$

Where, Rn is the net radiation at the surface, H is the sensible heat flux, LE is the latent heat flux and G stands for the storage term associated with soil heat fluxes and canopy storage.

However, a non- closed energy balance was observed starting with some of the earliest field experiments with EC measurements in Australia (Leuning et al., 1982) and Germany (Koitzsch et al., 1988). These studies pointed out possible issues with the fundamental assumptions of the EC method. Subsequent field experiments in the late 80's and early 90's observed persistent SEB residuals of the order of 10-20%.

Some of the early approaches to deal with the non-closure was to 'correct' the measured fluxes by preserving the Bowen ratio, adjusting both the sensible and the latent heat fluxes by the same percentage, based on the 30-minute energy balance residual (Twine et al., 2000).

To systematically go over the instrumentation and fundamental issues with measuring the energy budget a European Geophysical Society Workshop was held in Grenoble, France in 1994

Experiment	Reference	Residual (%)	Duration (days)	Surface
FIFE-89	Verma et al. (1992)	0-10	40	grass
Vancouver Island-90	Lee and Black (1993)	17	9	16 m deciduous forest
TARTEX-90	Foekn et al. (1993)	33	24	barley/bare soil
KUREX-91	Panin et al. (1998)	38	27	agricultural
LINEX-96/2	Foken et al. (1997)	21	3	medium grass
LINEX-97/1	Foken (1998)	32	9	short grass
LITFASS-98	Beyrich et al. (2002)	14	21	bare soil

FIFE is the First International Satelite Land Surface Climatology Project (ISLSCP) Field Experiment, TARTEX is the Tartu Experiment, LINEX is the Lindenberg Experiment, and LITFASS is the Lindenberg Inhomogeneous Terrain - Fluxes between Atmosphere and Surface : a long term study

TABLE 1.1: Table 1 from Oncley et al. 2007, listing the energy balance residuals reported by field measurements

(Foken and Oncley, 1995). Following this workshop, an international field experiment, EBEX (Energy Balance Experiment) was designed over a flood irrigated cotton field in San Juan Valley, Southern California. The idea of the experiment was to choose a field site that satisfies the assumptions of the generalised eddy covariance approach and quantify any errors and uncertainties involved with the instrumentation and data processing pipelines.

Oncley et al. (2007) gives an overview and some of the early results from EBEX. Using a distributed tower network, the experiment was able to inter-compare the EC instrumentation being employed and quantify the roles of processes not accounted for in conventional measurements such as advection, canopy storage, soil heat flux etc. Their measurements indicated that the measured residuals remain greater than the error ranges, uncertainty estimates and minor losses. They also noted that the measured radiation values are always higher than the measured fluxes and point out that this would not be so had the issue been solely one of random measurement error.

Later, Stoy et al. (2013) did a comprehensive analysis of EC flux measurements from 173 sites across multiple ecosystems. The synthesis study found consistent energy balance non-closures

across the sites and more importantly, noted that non-closure is linked to the degree of landscape heterogeneity, quantified using MODIS products and GLOBEstat elevation data. They found the best average closures in evergreen forests and savannas and the worst over crops, deciduous broadleaf forests, mixed forests and wetlands. It is interesting to note that prior investigations and subsequent studies have marked these same ecosystems to be particularly effected by heterogeneity effects. Based on their study, they suggested that mesoscale circulations linked to landscape-scale heterogeneity might be playing an important role in surface-atmospheric exchanges, as proposed in earlier synthesis studies (Foken, 2008; Foken et al., 2010) with fewer sites.

These secondary circulations generated in relation to surface heterogeneities are a leading hypothesis to be the cause for the observed persistent non-closure of surface energy balance at EC tower sites (Foken et al., 2011; Charuchittipan et al., 2014; Mauder et al., 2020).

1.2 Landscape Scale Low Frequency Transport Due to Quasi-Stationary Sub-Mesoscale Processes

Based on their analysis of tower measured EC data, Blanford et al. (1991) and Bernhofer (1992a) had attributed the residuals to large scale non-turbulent transport driven by surface gradients. Finnigan et al. (2003) also pointed out that the conventionally used averaging windows of 30 minutes, along with rotating the coordinates so that the x-axis is aligned with the mean horizontal wind would act as a high pass filter for the data. This would remove contributions from motions with periods longer than the averaging times to the covariance being measured. They used data from 3 forested sites, compared short-term and long-term averaged fluxes and showed underestimations in the range of 10-15% when the longer-term fluxes are not considered.

During periods when the longer duration covariances differed substantially from the short-time averaged values they also noted how the flux cospectra show higher power in the lower frequencies, unlike what is expected from classical theories, that assume non-significant powers in the lower frequencies (Kaimal and Finnigan, 1994a).

Such circulations can be captured by turbulence resolving numerical experiments using Large Eddy Simulations (LES). The LES study of ABL over homogeneously heated surface by Kanda et al. (2004) showed that local advection by Turbulent Organised Structures (TOS) would lead to a systematic underestimation of turbulent fluxes at point measurements. Inagaki et al. (2006) extended this study by including a 1D sinusoidally varying surface heterogeneity. They decompose the total flux to a turbulent and mesoscale component by phase averaging the turbulent signals and identified thermally induced mesoscale circulations driven by differential heating of the surface as a potential cause for the observed SEB residuals. They also note that measuring the transport due to TOS over an experimental study domain is not a trivial problem as they are randomly generated within the domain, even over homogeneous surfaces.

Using data from the LITFASS-2003 field experiment in Germany Foken (2008); Foken et al. (2010) showed that area averaged flux measurements reduce the SEB residuals. This, combined with the observations that the residuals are worse for sites with more heterogeneous surfaces, lead to his hypothesis that what has remained unaccounted for in the budgets could be transport due to secondary circulations tied to landscape heterogeneity. These would only be sampled by tower mounted stationary instruments if they drift with the mean wind or if they spin up within those tower footprints. This poses the energy balance closure problem as a scale problem, of resolving the important scales of transport, instead of a measurement or instrumentation problem.

The Stoy et al. (2013) study followed Foken's analysis and since then a growing body of research has suggested that quasi-stationary low-frequency eddies in the ABL tied to land surface heterogeneity can play an important role in surface-atmospheric transport (Mauder et al., 2020). These circulations can get attached to land surface features or drift slowly with the mean wind (Mahrt, 2010). Longitudinal roll-like vortices, aligned with the mean wind can be generated in atmospheric boundary layers (Lemone, 1973; Etling and Brown, 1993; Weckwerth et al., 1999). Over heterogeneous surfaces, they can become localised over gradients of land surface temperature (Blanford et al., 1991; Maronga and Raasch, 2013a) or roughness (Desjardins et al., 1997; Sun et al., 1997; Gryschka et al., 2008; Kröniger et al., 2018).

Maronga and Raasch (2013a) conducted a LES study using tower-measured sensible and latent heat fluxes as imposed surface boundary conditions over the LITFASS-2003 field experiment domain. Previous LES studies investigating the effects of surface heterogeneities had only included idealised heterogeneities, like stripes, checker-board or sinusoidal variations. They also came up with a combined time and ensemble averaging method to filter out signals of secondary circulations from the primary convective turbulence signal over the more realistic surface fluxes. They note that the secondary circulations become more roll like and less cellular with increasing wind speed.

Identification and measurement of such structures from field observations call for spatially resolving measurement techniques, such as aircraft measurements, scintillometers, a distributed tower network etc. Spectral analysis of tower measured turbulence data can also give some insight into the nature of flux contributions from the lower frequencies. Using turbulence measurements from different heights during the EBEX-2000 field campaign Zhang et al. (2010) identified the influences of large eddies on convective and stable boundary layer. They observed

large variations in the LE data manifested as saw tooth patterns. Gao et al. (2017) observed a similar saw tooth pattern in daytime LE values and a phase shift between large-scale vertical wind and water vapour density. Eder et al. (2015) measured the contributions from mesoscale turbulent organised structures by combining three Doppler wind LiDARs. These low frequency contributions would be missed by single-point tower measurements unless they are either swept across the tower measuring points by the mean wind or the point measurements happen to be in their vicinity (Mahrt, 2010; Charuchittipan et al., 2014).

1.3 Integrated Approaches to Resolve Eddy Covariance Challenges

Quantifying and diagnosing the 3 dimensional transport and horizontal variability of surface atmospheric fluxes associated with stationary or slow moving eddies over heterogeneous domains experimentally calls for deployment of intensive instrumentation that can sample the surface atmospheric exchanges at multiple, overlapping scales (Wulfmeyer et al., 2018). Previous studies have looked at how ABL stability regimes affect the spectral responses using tower measurements (Gao et al., 2017, 2020) and LES studies have looked at the role of coherent structures in modulating domain-mean flux transport as was pointed out earlier. However, the relationships between the mesoscale transport, the surface heterogeneity scales and flux imbalances remain to be investigated in a systematic field study in more detail (Steinfeld et al., 2007; Mahrt, 2010; Zhou et al., 2019)

The Chequamegon Heterogeneous Ecosystem Energy-balance Study Enabled by a High-density Extensive Array of Detectors 2019 (CHEESEHEAD19) was a field campaign designed to intensively sample and scale the ABL response, surface energy balance and land surface properties

within a 10 × 10 km heterogeneous forested domain (that would fit within a 'grid cell' of a weather/climate model) in northern Wisconsin, USA (Butterworth et al., 2021). The field campaign collected measurements of ground based and airborne fluxes, atmospheric profiles and surface environment at varying scales. A network of 20 towers were deployed above the forest canopy, including one 400 m tall tower, to sample the surface fluxes across the domain from June to October of 2019. Profile measurements were done using a suite of LiDAR soundings and radiosonde releases. LiDAR measurements of the forest canopy and hyperspectral imagery of the land surface were performed. During three 7-day intensive observation periods (IOPs), the University of Wyoming King Air (UWKA) measured EC fluxes, ABL depth and profiles over an extended 30 × 30 km domain. Butterworth et al. (2021) provides a detailed review of the field campaign setup. Two main motivations for the campaign were

1. How does spatial heterogeneity of the surface impact the energy balance and local atmosphere circulations?

2. How does the presence or absence of these circulations influence the representativeness of single-point surface fluxes compared to the grid average?

1.4 Research questions and hypothesis

Combining the comprehensive CHEESEHEAD19 observational dataset with high resolution numerical modelling can help explore questions about the relationships between ABL secondary circulations (low frequency responses) and heterogeneous landscapes. For my doctoral dissertation, I use the CHEESEHEAD19 airborne observations and a 'realistic' LES informed by the

field campaign measurements to that effect. The specific research questions and hypothesis investigated are:

Research Question 1

How do spatial scales of surface-atmosphere fluxes vary over heterogeneous surfaces across the day and across seasons? What is the role of ABL stability and land surface variability in modulating these surface atmospheric exchanges?

- **Hypothesis 1**: Persistent contributions of larger scale (in the range of meso-β to meso-γ) fluxes to the daytime sensible and latent heat fluxes exist with diurnal and seasonal variations.

Research Question 2

Can LES be used to evaluate mechanisms that generate surface-heterogeneity induced mesoscale circulations in the diel ABL ?

- **Hypothesis 2**: Large eddy simulations, initialised with real-world surface heterogeneity, develop similar mesoscale structures and patterns as observations.

Research Question 3

Can diagnosing and quantifying these circulations and scale-separated transport help observe the "true" transport and how do their effects scale with the length scales of surface heterogeneity and the convective boundary layer height?

- **Hypothesis 3**: Surface flux heterogeneity modulates the atmospheric boundary layer response to it by inducing quasi-stationary coherent structures that transition from roll vortices to cellular structures as the boundary layer becomes more convectively unstable.

The following conceptual framework is proposed to tie these research questions and their implications together:

Quasi–stationary, mesoscale eddies tied to landscape scale heterogeneity can be superimposed over ABL turbulence. Since they would contribute to fluxes in these 'landscape-scales', as the amplitudes of these surface heterogeneity scales become more important, there would be more transport in these larger scales. Their effects would be stronger in convective boundary layers, with weaker mean winds so that they are not smeared by the mean flow. Signals of this landscape related transport would be reflected in the single-point, Reynolds averaged, tower measured surface energy balance residuals.

Chapter 2

Space-scale resolved surface fluxes across a heterogeneous, mid-latitude forested landscape

Paleri, S., Desai, A.R., Metzger, S., Durden, D., Butterworth, B.J., Mauder, M., Kohnert, K. and Serafimovich, A. [1]

2.1 Introduction

Surface-atmospheric fluxes of energy, momentum, water, carbon and other scalars are integral components of Earth system processes. Terrestrial ecosystems act as important intermediaries for these exchange processes, influencing Earth's weather and climate systems (Pielke et al., 1998). However, the land–surface is heterogeneous at multiple scales owing to spatial variability in multiple properties and the atmospheric responses to these heterogeneous surface forcings through the fluxes of energy, water, carbon and other scalars are also scale dependent and non-linear (Avissar and Schmidt, 1998). Since the scales of transport vary from Kolmogrov

[1]Reprinted from Space-scale resolved surface fluxes across a heterogeneous, mid-latitude forested landscape. Journal of Geophysical Research: Atmospheres, p.e2022JD037138. Copyright (2022), with permission from Wiley.

microscale in the turbulent regime to the mesoscale it is not easy to resolve the contributions from all of the relevant scales directly using observations or simulations (Bou-Zeid et al., 2020)

The primary transport process in the atmospheric boundary layer (ABL) is turbulence and the surface-atmospheric turbulent fluxes can be directly measured using the eddy-covariance (EC) technique (Aubinet et al., 2012; Foken, 2017). The EC technique uses Reynolds decomposition of the Navier-Stokes equation for momentum and scalar transport, with the assumptions of stationarity and horizontal homogeneity, to calculate turbulent fluxes in the ABL. Tower based EC measurements are widely used to study ecosystem level biosphere-atmosphere interactions and quantify surface-atmospheric fluxes (Aubinet et al., 1999; Baldocchi et al., 2001). Even with careful experimental design and quality control, they are however limited by their surface flux footprints (i.e., part of the upstream surface contributing to the measured flux). Moreover, requirements for stationarity can complicate sampling flux contributions from lower frequencies as well (Desjardins et al., 1997; Mahrt, 2010)

So, a good first order sanity check on tower measured turbulent fluxes would be to check for the closure of the measured surface energy budget, evaluating whether available energy (the difference between measured net radiation and ground heat flux) within the control volume sampled by the tower is balanced by the measured sum of turbulent sensible and latent heat fluxes (Oncley et al., 2007; Foken, 2008; Foken et al., 2010; Mauder et al., 2020). Such a check would also be important to validate land–surface and biological model parameters such as surface flux parameterisations in weather and climate models, water vapor surface conductances in ecosystem and land–surface models or validating model predictions of net ecosystem exchanges (NEE). However, a persistent surface energy balance residual has been reported in prior investigations across multiple sites in multiple ecosystems (Oncley et al., 2007; Foken et al., 2010;

Mauder et al., 2020)

Simulations and observational studies have shown that there can be larger scale transport linked to landscape variability. Based on their analysis of tower measured EC data Bernhofer (1992b) had attributed the residuals to large scale non-turbulent transport driven by surface gradients. Finnigan et al. (2003) pointed out that the conventionally-used averaging windows of 30 minutes could act as a high pass filter for the data. They also noted that pre-treating tower measured turbulent data by rotating the measurement coordinates so that x-axis of measurement is aligned with the mean horizontal wind could also contribute to the same. Such data processing would remove contributions of motions with periods longer than the averaging times to the covariance being measured. Early Large Eddy Simulation (LES) studies (Kanda et al., 2004; Inagaki et al., 2006; Steinfeld et al., 2007) with idealized surface forcings indicated that transport due to turbulent organized structures and thermally-induced mesoscale structures can cause systematic underestimation of fixed point tower flux measurements. Maronga and Raasch (2013a) conducted a LES study using measured sensible and latent heat fluxes as imposed surface boundary conditions over the LITFASS-2003 field experiment domain and diagnosed signals of heterogeneity-induced vertical velocities linked to landscape heterogeneities. Using a wavelet analysis of airborne turbulent data during the BOREAS field experiment, Mauder et al. (2008a) quantified the mesoscale transport across a temperate heterogeneous landscape to be 10% of surface measured available energy and of the same order of magnitude as tower measured residuals over the domain. The LES study by Xu et al. (2020) employed simulated towers over idealized heterogeneities. Following a spatio-temporal eddy covariance approach for simulated towers they could account for 95% of the available energy with one tower per 40 km^2. Such a spatial approach seems to account for the landscape-scale low frequency transport. The

recent LES study by Margairaz et al. (2020) over idealized heterogeneities also shows that fluxes by secondary circulations can account for 5-10% of near surface sensible heat fluxes.

These investigations indicate that when surface heterogeneity starts influencing the surface-atmospheric transport, there can be quasi-stationary circulations modulated by the heterogeneity amplitudes and background wind. Such structures could lead to increased advective transport and flux divergences, thereby altering the net transport associated with the turbulent covariance term, measured through the eddy covariance method (Mahrt, 2010; Mauder et al., 2020). Quantifying and diagnosing such a 3 dimensional transport and horizontal variability of surface atmospheric fluxes over heterogeneous domains in the field calls for the deployment of intensive instrumentation that can sample the surface atmospheric exchanges at multiple, overlapping scales (Wulfmeyer et al., 2018). Identification and measurement of such structures and their contributions from field observations call for spatially resolving measurement techniques, such as a distributed tower network (Oncley et al., 2007; Mauder et al., 2008b; Engelmann and Bernhofer, 2016; Morrison et al., 2021), airborne measurements (Mahrt, 1998; Strunin and Hiyama, 2004; Bange et al., 2002, 2006; Mauder et al., 2007b), scintillometers (Foken et al., 2010; Xu et al., 2017; Meijninger et al., 2006) and LiDAR measurements (Drobinski et al., 1998a; Higgins et al., 2013; Eder et al., 2015) etc. Spectral analysis of tower measured turbulence data can also give some insight into the nature of flux contributions from the lower frequencies (Zhang et al., 2010, 2014; Zhou et al., 2019; Gao et al., 2020).

Among these measurements, airborne EC measurements are one of the few that can directly measure the spatial distribution of 3D turbulence across a study domain (Mahrt, 1998, 2010). Moreover, with spatial transects, airborne measurements can directly sample contributions from larger (of the order of meso-β 20-200 km, meso-γ 2-20 km, from Orlanski (1975)) scale persistent

structures excited by surface heterogeneities. In contrast, for ground-based measurements these larger scale structures would have to drift by their field-of-view. Airborne transects through a study domain can also pass through multiple quasi-stationary eddies, giving robust statistics for the measured fluxes.

Here, we use airborne turbulence data collected over a heterogeneous mid-latitude forested landscape interspersed with creeks and lakes in the Chequamagon-Nicolet National forest near Park Falls, Wisconsin USA. Through this analysis we aim to address the following research questions:

1. Can spatially-resolved airborne eddy covariance identify spatial scales of surface-atmosphere fluxes over heterogeneous surfaces?

2. How do spatial scales of surface-atmospheric fluxes vary across the day and across seasons? What is the role of ABL stability and land–surface variability in modulating these exchanges?

3. What are the ensuing implications for improving the surface energy balance closure or understanding scales of turbulent transport?

The airborne measurements were collected as part of the Chequamegon Heterogeneous Ecosystem Energy-balance Study Enabled by a High-density Extensive Array of Detectors (CHEESEHEAD19) field experiment (Butterworth et al., 2021), conducted from July to October 2019. The experimental study design aimed to sample the landscape transition from late summer to early fall and the associated ABL responses. The CHEESEHEAD19 airborne dataset presents

a unique opportunity to analyse long periods of airborne EC over long legs (30 km) in a heterogeneous region over multiple times a year with differing patterns of surface sensible and latent heat fluxes. The dataset provides an extensive set of scenarios to investigate our research questions and derive principles from. To quantify and spatially localise contributions from all the relevant scales of transport we calculate the surface atmospheric fluxes through the wavelet cross-scalograms of the turbulent data (Strunin and Hiyama, 2004, 2005; Mauder et al., 2007a; Metzger et al., 2013). A wavelet based analysis can distinguish surface-atmosphere fluxes at multiple scales and quantify the contributions from larger scales, allowing us to resolve scale transport across space.

To those ends, we pose the following null and alternative hypotheses:

- H0: Mesoscale transport is an invariant, small fixed fraction of the total flux.
- HA: Persistent contributions of larger scale (in the range of meso-β to meso-γ) fluxes to the daytime sensible and latent heat fluxes exist with diurnal and seasonal variations.

2.2 Data and Methods

2.2.1 Experiment description

The Chequamegon Heterogeneous Ecosystem Energy-balance Study Enabled by a High-density Extensive Array of Detectors (CHEESEHEAD19) was a field campaign conducted from June to October 2019, in Chequamegon-Nicolet National Forest, Wisconsin, USA. The experiment was designed to intensively sample and scale land–surface properties and the ABL responses to it across a heterogeneous mid-latitude forested landscape interspersed with creeks and lakes. The two main motivations for the field experiments were to determine how spatial heterogeneity

of the surface impacts the local energy balance and atmospheric circulations and to evaluate how the presence or absence of these circulations influence the representativeness of single-point surface fluxes compared to the grid average.

Measurements were made using a suite of observing platforms over a core 10×10 km domain (that would fit within a 'grid cell' of a weather/climate model) and a 30×30 km extended domain centred on the Department Of Energy Ameriflux regional tall tower (US PFa 45.9459° N, −90.2723° W). EC fluxes have been measured nearly continuously at the US PFa tall tower since 1996 (Berger et al., 2001) and the study domain is well documented in previous studies that used flux data from the tall tower (Davis et al., 2003; Desai, 2014; Desai et al., 2015). The field campaign collected measurements of ground based and airborne fluxes, atmospheric profiles and surface environment at varying scales. Butterworth et al. (2021) gives a detailed overview of the field experiment design and all of the deployed instrumentation.

Figure 2.1 shows the land cover classes across the extended domain from the State of Wisconsin Department of Natural Resources Landcover Data (Wiscland 2.0) accessed from `https://dnr.wisconsin.gov/maps/WISCLAND`. The vegetation and land cover within the study domain is characteristic of a mid-latitude temperate forest, dominated by conifers, broadleaf deciduous trees and wetlands. The study domain is also interspersed with open water bodies, the largest being the Flambeau Lake to the North-Eastern sector of the domain. The presence of such a vertically and horizontally heterogeneous surface, with maximum canopy heights ranging from a couple of metres to 35 metres, gives a unique opportunity to study surface atmospheric exchanges over unstructured land–surface heterogeneity where multiple surface properties and roughness elements vary at multiple scales, addressing a crucial gap in our current understanding Bou-Zeid et al. (2020). Site descriptions of 17 flux tower sites, set up as part of the National Center

for Atmospheric Research (NCAR)-Integrated Surface Flux Station (ISFS) network, within the core 10×10 km domain can be found at http://cheesehead19.org. This gives an idea about the variation in surface and vegetation properties across the domain. The extended 3-month duration of the field experiment also allows us to sample the shift in the surface energy budget partitioning as the study domain shifts from a latent heat-dominated late summer landscape to a more sensible heat flux-dominated early autumn landscape.

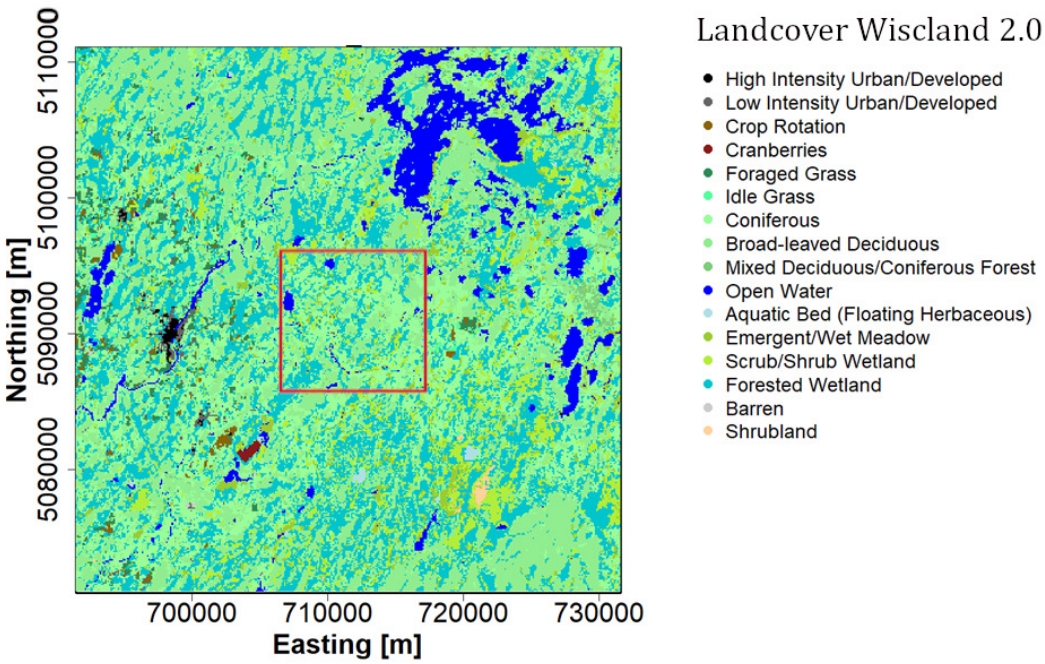

FIGURE 2.1: Land Cover classes for a 40×40 km area bounding the study domain from the Wiscland 2.0 landcover classification dataset. The 10×10 km core CHEESEHEAD19 domain is shown in the red box.

2.2.2 Airborne intensive observations

Airborne turbulence data were collected over the extended domain with the University of Wyoming King Air (UWKA) research aircraft. The UWKA is a Beechcraft King Air 200T model, a part of the National Science Foundation's Lower Atmosphere Observation Facility that has been in use for insitu airborne measurements of cloud and boundary layer properties

since 1977 (Rodi, 2011; Wang et al., 2012). Three seven-day Intensive Observation Periods (referred to as IOPs henceforth) were conducted during the experiment during each month from July to September when all the available field instrumentation were deployed simultaneously. During these IOPs the UWKA Research Aircraft flew linear transects across the domain on four days sampling turbulent measurements of wind velocities, temperature, water vapor, and CO2, at a frequency of 25 Hz (Table 2.1). The airborne experiment was designed with the help of numerical experiments to maximise spatial coverage over the domain, ensure adequate sampling of larger scale eddies and ensure crew safety. Metzger et al. (2021) provides details about the numerical simulations, analysis framework and design strategy used to come up with the final flight patterns for the airborne measurements. Figure 2.2 shows these different patterns and their respective waypoints. Each research flight pattern was composed of flight transects connecting consecutive waypoints. We refer to these individual transects as flight legs. The flight legs were designed to be 30 km so that they extend about 10 km outside of the core 10×10 km domain to ensure that enough mesoscale contributions to the core 10×10 km domain could be sampled.

On each day there was a morning (14:00 - 17:00 Universal Time Coordinated) flight and an afternoon (19:00 - 22:00 Universal Time Coordinated) research flight. Each Research Flight (RF) performed 30 km down-and-back transects at 100 m and 400 m above ground between two consecutive waypoints, alternating between straight and diagonal passes. The first leg of all transects was at 400 m and the return legs at 100 m. For example, from Table 2.1, on 2019 July 11th, the morning research flight was RF03 with the WE1 (west-east 1) flight pattern. For RF03, from Figure 2.2, the first leg was from waypoint 1 to waypoint 2 at 400 m and the second leg was back to 1 from 2 at 100 m. Then the third leg would be from 1 to 4, diagonally at 400

TABLE 2.1: Dates, times, flight patterns of the flights analysed for all 3 IOPs

Date	Domain start time (UTC)	Domain end time (UTC)	Flight Number	Flight Pattern	Wind Dir (deg)	Wind Speed (m/s)	Short Wave Incoming (W/m^2)
2019-07-09	14:00	16:00	RF01	West-East 2	180	6	643
2019-07-09	19:00	21:00	RF02	West-East 2	210	5	701
2019-07-11	14:00	16:00	RF03	West-East 1	345	3	852
2019-07-11	19:00	21:00	RF04	West-East 1	45	5	829
2019-07-12	14:00	16:00	RF05	West-East 2	225	6	686
2019-07-12	18:00	21:00	RF06	West-East 2	225	5	642
2019-07-13	14:00	16:00	RF07	South-East 2	330	3	833
2019-07-13	19:00	21:00	RF08	South-West 1	330	3	869
2019-08-20	14:00	16:00	RF09	South-East 1	215	3	244
2019-08-20	19:30	22:00	RF10	South-East 1	180	1	648
2019-08-21	14:00	16:30	RF11	South-West 1	0	5	663
2019-08-21	19:00	21:30	RF12	South-West 1	315	6	639
2019-08-23	14:00	16:30	RF15	West-East 2	80	0.5	681
2019-08-23	19:30	21:30	RF16	West-East 2	120	3	703
2019-09-24	14:00	16:30	RF17	South-East 1	230	4	503
2019-09-24	19:00	21:30	RF18	South-East 1	180	5	342
2019-09-25	14:40	17:00	RF19	South-West 1	270	5	573
2019-09-25	19:30	22:00	RF20	South-West 1	310	5	326
2019-09-26	14:00	16:30	RF21	South-East 1	270	3	518
2019-09-26	18:45	21:15	RF22	South-East 1	265	5	422
2019-09-28	14:30	17:00	RF23	West-East 1	353	3	674
2019-09-28	19:00	21:30	RF24	West-East 1	15	3	500

m and so on.

The primary scientific purpose of the higher 400 m legs was to observe the temperature and moisture profiles using a downward pointing Compact Raman Lidar. The low-altitude legs were flown at 100 m since this was the lowest altitude deemed safe to fly for the maximum forest canopy height of 35 m. This also ensures that the measurements taken were in the surface layer and above the roughness sublayer of the forested domain. Wavelet cross scalograms of the atmospheric turbulence data from the 100 m legs were used to calculate the surface atmospheric fluxes during the IOPs.

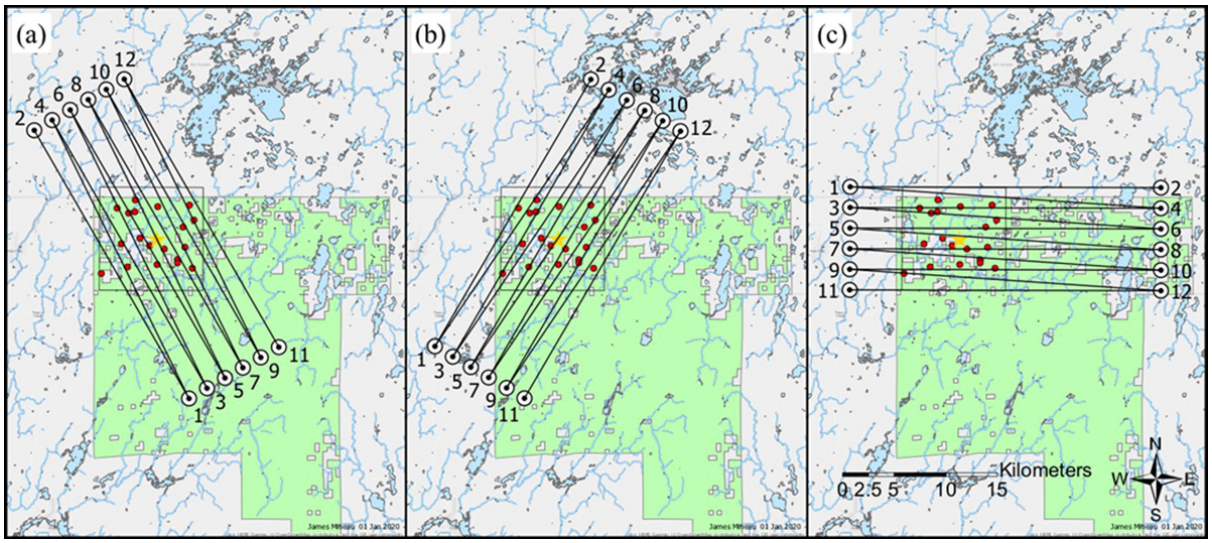

FIGURE 2.2: Three sets of waypoints define three distinct flight patterns, named after the starting location and direction of their first waypoint: (a) south-east (SE), (b) south-west (SW) , and (c) west-east (WE). Flying the numbered waypoints either in ascending order (SE1, SW1, WE1) or descending order (SE2, SW2, WE2) results in six distinct flight sequences that maximize data coverage under different wind conditions. Map credit: James Mineau, University of Wisconsin – Madison. [Metzger et al. (2021): Figure 14, published by Atmospheric Measurement Techniques, reproduced with permissions under https://creativecommons.org/licenses/by/4.0/]

2.2.3 Wavelet Analysis

Wavelet transforms can reveal information localised in both space and frequency domains (Farge, 1992; Mahrt et al., 1994) for a given input signal. This distinct property makes wavelet based time-frequency analysis suited for the analysis of in-homogeneous or non-stationary geophysics data, unlike other conventional methods such as a Fourier transform or its windowed version (Kumar and Foufoula-Georgiou, 1994) that require periodicity. Airborne measurements over the CHEESEHEAD19 study domain sampled a spatially and temporally varying surface flux field, including measurements over varying surface roughness heights, canopy heights and soil properties. In this regard, a wavelet decomposition of the airborne turbulence measurements over the heterogeneous domain can extract scale-resolved information and quantify contributions from larger scale quasi-stationary modes induced by landscape scale heterogeneities. A wavelet

analysis also yields a space-scale mapping of the measured fluxes, throughout the day and across seasons.

The wavelet functions and analysis methods were developed for time-frequency analysis (Farge, 1992; Thomas and Foken, 2005), but since we are working with spatial data, we've expanded upon the existing methodology to facilitate space-scale analysis. In wavelet analysis, one starts with choosing a wavelet function or mother wavelet, Ψ, which is localised in both space and frequency domains and has zero mean (Torrence and Compo, 1998; Farge, 1992). The mother wavelet of choice for this study is the complex Morlet wavelet, $\Psi(\eta) = \pi^{-1/4} e^{i\omega_0 \eta} e^{-\eta^2/2}$, with the frequency parameter $\omega_0 = 6$ as suggested by Torrence and Compo (1998). The Morlet wavelet is a complex sine wave modulated by a Gaussian envelope and has been in use for the analysis of atmospheric turbulence data because the resulting wavelet transform offers good localisation in the scale domain (Strunin et al., 2004; Thomas and Foken, 2005; Mauder et al., 2007a). The mother wavelet Ψ can be stretched and squeezed or translated across the spatial domain to construct 'daughter wavelets' $\Psi_{p,a,b}$ where a is the dilation parameter and b is the translation parameter.

$$\Psi_{p,a,b}(x) = \frac{1}{a^p} \Psi\left(\frac{x-b}{a}\right) = \Psi_p(\eta) \tag{2.1}$$

Here, p is a normalisation parameter and is set as $1/2$ for this study, and η is a non-dimensional coordinate in the space-scale domain. The wavelet transform is a convolution, $\int f(x) \Psi^*_{p,a,b}\, dx$, of a given signal $f(x)$ with the daughter wavelets to yield a series of wavelet coefficients $T(a,b)$ that are functions of the dilation and translation parameters. $\Psi^*_{p,a,b}$ is the complex conjugate of $\Psi_{p,a,b}$. Since both the scale and the location of the mother wavelet filter kernels can be adjusted,

such an analysis can yield localised details matched to their scale (subject to the fundamental Heisenberg uncertainties, (Addison, 2017)). In the discrete limit, for a spatial series $f(n)$ with N data points the wavelet coefficients become,

$$T_f(a,b) = \sum_{n=0}^{N} f(n)\Psi^*_{p,a,b} \tag{2.2}$$

Different localisations or 'daughter wavelets' of the same mother wavelets are scaled and translated across the input data to extract information about the amplitudes and locations of matching details corresponding to equivalent amplitudes at corresponding locations present in the input signal. This allows us to calculate the wavelet spectral energy density (E_f) for a chosen dilation and locations from the coefficients as $E_f(a,b) = |T_f(a,b)|^2$, referred to as the wavelet scalogram matrix. Consequently, the variance (σ_f) of the chosen signal, $f(x)$ can be calculated by averaging the matrix and summing across the scales,

$$\sigma_f = \frac{\delta j \delta t}{C_\delta N} \sum_{j=0}^{J} \sum_{n=0}^{N-1} \frac{|T_f(a_j, b_n)|^2}{a_j} \tag{2.3}$$

Here, $\delta t = 0.04$ for the 25 Hz data and δj, the discrete intervals in scale, is set as 0.125, setting up 8 octaves, following Torrence and Compo (1998). C_δ is an admissibility constant defined for each mother wavelet of choice, to reconstruct the original series from its wavelet transform. For the complex Morlet wavelet $C_\delta = 0.776$ (Torrence and Compo, 1998). Similarly, given two signals, $f(n)$ and $g(n)$, a cross-scalogram matrix can be calculated as $T_f(a,b) \times T^*_g(a,b)$, where $*$ denotes a complex conjugate. Their co-variance can be estimated by integrating their co-spectral energy spanning the constituent scales across their cross-scalograms as:

$$cov_{ab} = \frac{\delta j \delta t}{C_\delta N} \sum_{j=0}^{J} \sum_{n=0}^{N-1} \frac{T_f(a_j, b_n) T_g^*(a_j, b_n)}{a_j} \tag{2.4}$$

A sample wavelet cross-scalogram of vertical wind and water vapour mole fraction space series is shown in Figure 2.3 b. Integrating the cross-scalogram in scale and converting the variance magnitudes to energy units lets us calculate the associated scale-integrated flux space series, shown in Figure 2.3 a. The shading in the cross-scalograms denote the amplitude of the wavelet coefficients. The peaks in the calculated latent heat flux space series can be seen coinciding with segments of strong amplitudes, which vary throughout the length of the series reflecting the variability of surface atmospheric transport across the transect.

The summation operation in Equation 2.4 can be performed over any desired subset of scales to calculate the wavelet covariance between two chosen signals (Torrence and Compo, 1998; Mauder et al., 2007a). Doing so gives the contribution from those ranges of scales to the total covariance. This presents the opportunity to quantify the contributions from different scales over choice of spatial segments by integrating across subsets of scales without neglecting contributions from scales larger than the choice of spatial segment. For this study we chose a flux partitioning scale of 2 km to distinguish between small-scale boundary layer turbulence and larger mesoscale contributions following Mauder et al. (2007a) and Strunin et al. (2004). The 2 km cutoff serves as proxy for the maximum boundary layer height, which would be the largest scale for the turbulent energy producing eddies in the ABL. ABL height shifts are observed in response to temporal factors such as seasonal and diurnal cycles (Figure 2.7) as well as

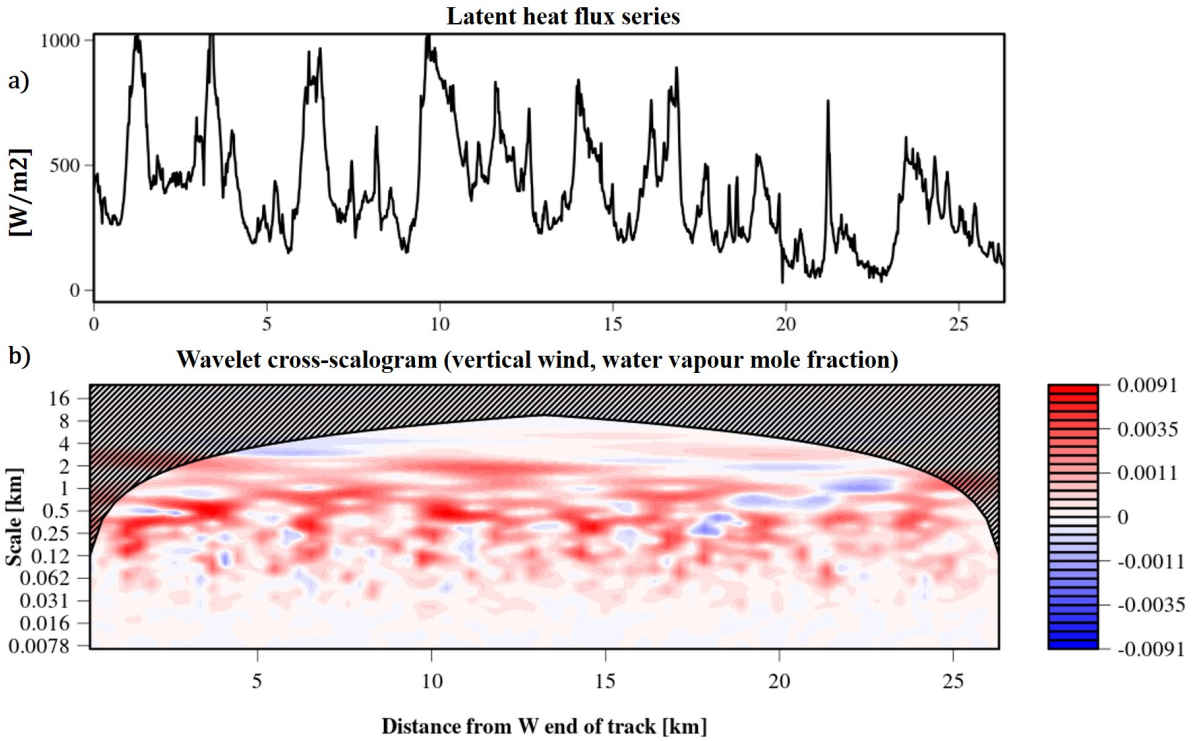

FIGURE 2.3: A sample wavelet cross-scalogram (b) between vertical velocity and water vapour mole fraction illustrating the scale-resolved spatial contributions along RF02 flight leg 04. This cross-scalogram is calculated by integrating across spatial scales along the y-axis giving the latent heat flux space series shown in (a). The shading in (b) denotes amplitudes with red shaded regions denoting positive contributions, while blue shades denote negative and white neutral. Hashed portions represent the cone of influence for edge effects.

spatial variations in land-cover heterogeneity. However, the 2 km threshold seems to be a good indicator for the the relative variation in the magnitude of mesoscale fluxes (Section 2.3.1).

2.2.4 Flux measurement and data processing

Wavelet based flux processing of the campaign data was done using the eddy4R family of open source packages Metzger et al. (2017). The 25 Hz airborne data product used in this study was preprocessed by the UWKA research crew to include routine UWKA corrections and is hosted at the NCAR-Earth Observing Laboratory (EOL) repository as part of the public CHEESEHEAD19 project data repository French et al. (2021). Table 2.2 gives details of the UWKA instrumentation used for measuring aircraft and atmospheric state variables. Each

research aircraft deployment had a resulting 25 Hz netcdf data file. The data from these files with all the necessary atmospheric and aircraft state variables were read in to the eddy4R processing environment. The air temperature, pressure and water vapour mole fraction data were lag corrected by maximising the cross-correlation with vertical velocity data (Hartmann et al., 2018). Flight leg start and end times were used to slice the research flight data into flight leg specific data. This ensured that only data collected during the linear transects across the study domain are used for the study and data collected during the over turnings at the way-point edges are excluded. Convective boundary layer (CBL) height was measured during the IOP days by two 915-MHz Wind Profiler Radars (WPRs) deployed roughly 45 km west and south to the WLEF tall tower (locations in Figure 1.a Duncan Jr et al. (2022) and data available from Bianco and Duncan (2020)) at the Lakeland and Prentice airports in Wisconsin. CBL heights from the hourly averaged data product were also added to the flight leg level data.

Flux calculations were performed individually for each flight leg. The missing data threshold was set to 90%. Each flight leg covered spatial transects of 25 to 30 km, depending on whether they were horizontal or diagonal along the cardinal wind directions (Section 2.2.2). With 25 Hz frequency and an averaged airspeed of 86 m/s, the mean spatial resolution of the data was 3.5 metres. Hence, the average number of data points for the flight leg level datasets analysed for each flight was 8200, with datasets ranging from 6500 to 9000 data points. The minimum daughter wavelet frequency was set at the Nyquist frequency of 12.5 Hz and the maximum depended on the duration of the dataset (averaging to 30 km). The wavelet frequencies were converted to scale space using the Fourier wavelength for the Morlet wavelet (Torrence and Compo, 1998). Adaptive, high frequency corrections were applied to the wavelet scalograms following (Nordbo and Katul, 2013). A spatial series of wavelet covariance fluxes was calculated

TABLE 2.2: Univerity of Wyoming King Air instrumentation details

Measurement	Instrument	Description
	Aircraft State	
3D position, ground velocity, orientation, Body-axis longitudinal/lateral/vertical acceleration	Applanix AV 410 GPS/Inertial Measurement Unit	Applanix Position Orientation System for Airborne Vehicles; combined solid-state/GPS system with real-time differential corrections; higher accuracy post processed data available Haimov and Rodi (2013)
Altitude	Stewart Warner APN159 radar altimeter	Altitude above ground level Range:0 - 60000 ft(18288 m); accuracy 1%; resolution: 0.24 ft (0.07 m)
Airspeed	Honeywell Laseref SM Inertial Reference System (IRS)	Range:0-4095 kts; accuracy: 13.5 ft/s ; resoluton: 0.0039 kts
flow angles	Rosemount 858AJ five-hole gust probe	Range:+-15; accuracy:0.2; resolution:0.00015
	Atmospheric State	
Air temperature	Reverse-flow housing with Minco platinum-resistive element Rodi and Spyers-Duran (1972)	Range: -50 to +50 C; accuracy: 0.5 C ; resolution: 0.006 °C
Wind Components	Applanix AV 410 GPS/Inertial Measurement Unit	Earth relative 3D wind
Atmospheric Pressure	Rosemount 1501 HADS	High Accuracy Digital Sensing module static pressure, corrected for dynamic effects Rodi and Leon (2012) ; Range: 0-1034 mb; accuracy : 0.5 mb, resolution: 0.006 mb
Water vapor	LICOR Li-7500A	LI-COR LI-7500 open-path CO2/H2O Gas Analyzer

from the wavelet cross-scalograms using Equation 2.4, for overlapping subintervals of 1000 m (Metzger et al., 2013). The 1000 m subintervals were centred above each cell of the 100 m resolution Wiscland 2.0 landcover classification dataset for the study domain (Figure 2.1, Section 2.2.5), giving window averaged flux measurements every 100 m. Random and systematic flux errors were calculated following (Lenschow and Stankov, 1986) and (Lenschow et al., 1994). The turbulent scale flux space series was calculated by setting the maximum wavelet scale for scalograms at 2 km. The mesoscale flux contributions were then calculated as the difference between fluxes from all scales and the turbulent scale fluxes. While creating summary statistics and figures an absolute threshold of 10 Wm^{-2} was applied for sensible and latent heat fluxes to ensure that the fluxes are well resolved. A hard threshold of (-400, 1000) Wm^{-2} was set for the LE space series and (-50,400) Wm^{-2} for the H series to remove spurious measurements.

2.2.5 Footprint modelling and flux topographies

Footprint of a flux measurement refers to the effective finite measurement area upwind of the sensors from where the eddies are being sampled from (Foken et al., 2006). Kljun et al. (2004) is a 1D parameterisation of a backward Lagrangian model (Kljun et al., 2002) in the stable to strongly convective ABL. Since this is not crosswind-integrated, Metzger et al. (2013) combined it with a Gaussian crosswind dispersion function. This is implemented in the analysis currently. The model requirements measurements of friction velocity ($u*$), measurement height (z), standard deviation of the vertical wind (σ_w) and the aerodynamic roughness length (z_0). With the exception of z_0 all the other variables are directly measured by the UWKA. z_0 is inferred from a logarithmic wind profile with the integrated universal function for momentum exchange after Businger et al. (1971) in the form of Högström (1988) (Metzger et al., 2013). For each of the 1000 m subintervals geolocated above the centres of the landcover classification dataset an individual footprint weight matrix was calculated as the subintervals were moved forward in space along the flight leg. This generated a footprint weight matrix for every flight leg analysed (Figure 2.4 a). This matrix is used to weigh and cumulatively sum the landcover contributions along the flight leg to give the space series of land–surface contribution to the flux series (Figures 2.4 b, c). The latent heat flux space series presented in Figure 2.4.c is the same series whose cross-scalogram was presented in Figure 2.3 b.

To investigate how the flux contributions vary over the course of a research flight and spatially over the domain, the measured fluxes are back-projected to their surface source as gridded two-dimensional data following the flux topography method of Mauder et al. (2008a). Flux topographies are the footprint-weighted flux contributions measured across the domain from the

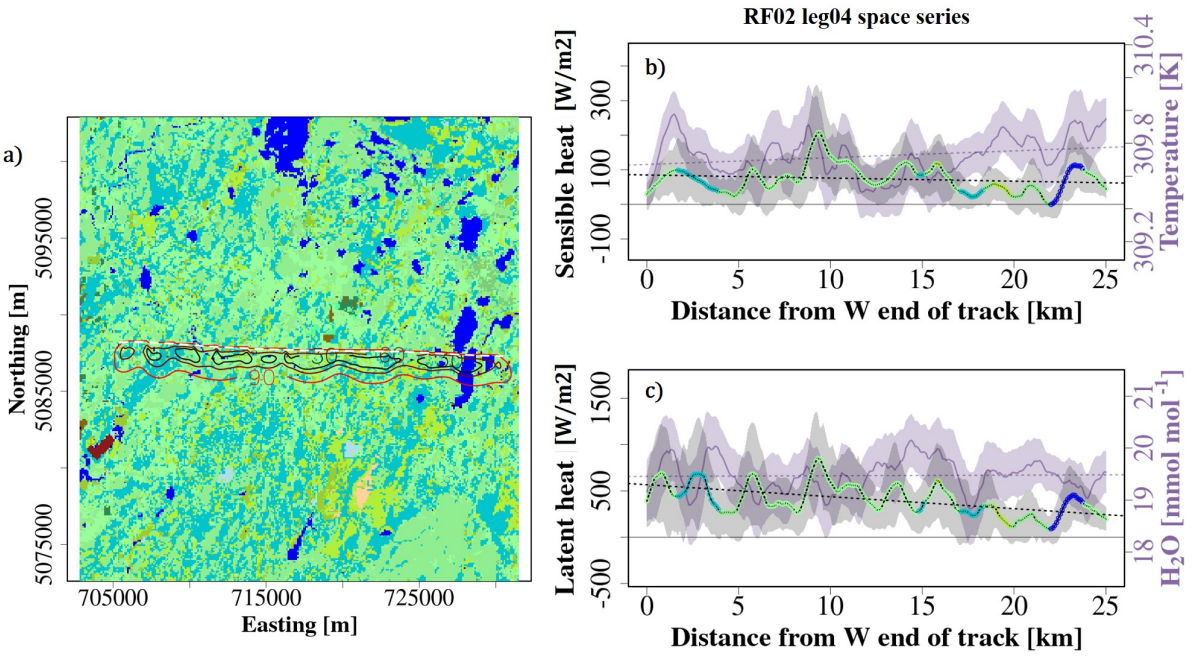

FIGURE 2.4: Footprint weights and window averaged flux space series calculated for RF02 flight leg 04. a) Cumulative flux footprint along the flight leg (shown in white dashed lines). Contour lines show 30, 60 and 90% source area contributions to the fluxes measured. b) Space series of measured air temperature (purple line) and calculated sensible heat flux (black line with coloured dots). Shading around each line indicate the random sampling errors. colour of the circles in the flux series indicate the dominating land cover type. Legend in Figure 2.1. c) Space series of measured water vapour mole fraction (purple line) and calculated latent heat flux (black line with coloured dots). Coloured and shaded the same as *b*. 251 flux estimates were calculated at each 100 m grid cells located below the flight leg as seen in *a*. Giving a 1000 m window averaged version of Figure 2.3.a.

airborne data (Amiro, 1998). The flux topographies are calculated over a 10×10 km CHEESEHEAD19 domain sub-set at the 100 m resolution of the flux space series. The calculated fluxes are projected back to the surface grid, weighted at each grid cell by the cumulative flux footprint from all the sub intervals in a processed flight leg.

For each flight leg from a RF, a flux topography was calculated, then the cumulative footprint weighted contribution (F_{ij}) for a RF was calculated at each grid cell in space (Kohnert et al., 2017) according to Equation 2.5.

$$F_{ij} = \frac{\sum_j^N (\sum_i^M f_{i,j} * g_{i,j})}{\sum_j^N (\sum_i^M g_{i,j})} \tag{2.5}$$

In Equation 2.5, f denotes the flux magnitudes measured, g the footprint weights, with the number of flight legs going from j to N and indices i to M denoting the number of footprint weights. For example, for RF02 leg 04, the calculated flux space series (Figures 2.4.b and 2.4.c) were projected on to the flux footprint source area shown in Figure 2.4.a, weighed in space by the footprint weights. Source areas with low footprint values ($< 0.05\%$) are excluded from the analysis. This procedure was repeated for all the flight legs of RF02 using Equation 2.5 to calculate the cumulative, footprint weighted spatial distribution of the measured fluxes.

2.3 Results

We start by looking into the scale composition of the fluxes measured across the domain in Section 2.3.1. To illustrate the seasonal variation and evolution of measured turbulent and mesoscale fluxes we present the seasonally averaged and scale-separated contributions across the IOPs in Section 2.3.2. Following this, we present the domain-averaged and scale-separated diel data of the fluxes for each of the IOPs. Then the flight averages for all of the research flights analysed here are also presented. In Section 2.3.3 we discuss the observed relationship between mesoscale transport and local ABL stability. Then, we investigate the composition of land cover contributions within the footprint of flight legs and how those might relate to the observed mesoscale transport in Section 2.3.4.

2.3.1 Scale-resolved fluxes

Wavelet cospectra for the sensible and latent heat fluxes were calculated for all research flights analysed (Figures 2.5, 2.6) to investigate the scale-resolved contributions to surface fluxes across the domain. The wavelet cross-scalograms from each flight leg were averaged across the space domain. These were then ensemble averaged across all flight legs that make up a research flight. The cospectra are not normalised to retain the relative magnitudes of the sensible and latent heat fluxes as well as to illustrate the flux magnitudes measured during the different flight campaign days. The flux cospectra follow a 2/3 rd power law scaling in the small scales, indicating the inertial subrange of atmospheric turbulence (Kaimal and Finnigan, 1994b). The cospectral power drops suddenly after about 7m, which is reasonable considering the spatial resolution of the UWKA high frequency data is 3 to 4 metres, with the average flight speed of 86 m/s and data resolution of 25 Hz. Both semi-log and log-log depictions are included to illustrate the spatial scales spanning the intertial subrange and turbulence production ranges as well as cospectral magnitudes and spectral power variability in the larger scales.

The latent heat flux cospectra calculated for research flights in the July IOP (Figures 2.5.a and 2.5.c) reveal a clustering of secondary maxima between 1 and 2 kilometres. The inertial subrange for most of the flights ends around 200 m, which would allow these peaks to be in the production scales for turbulence or signals of larger scale non-turbulent structures. The secondary maxima are less prominent in RF02 and RF03 LE cospectra, both with larger magnitude for the measured turbulent fluxes. Their peak is around a spatial scale of 800 m. The peak flux magnitude for the IOP is also from these two flights and is of the order of 1000 Wm^{-2}. However, the sensible heat flux cospectra for the July IOP do not reveal any such clustering. The cospectra in their log-log representation flatten out into the production scales of turbulence around 200 m for most of

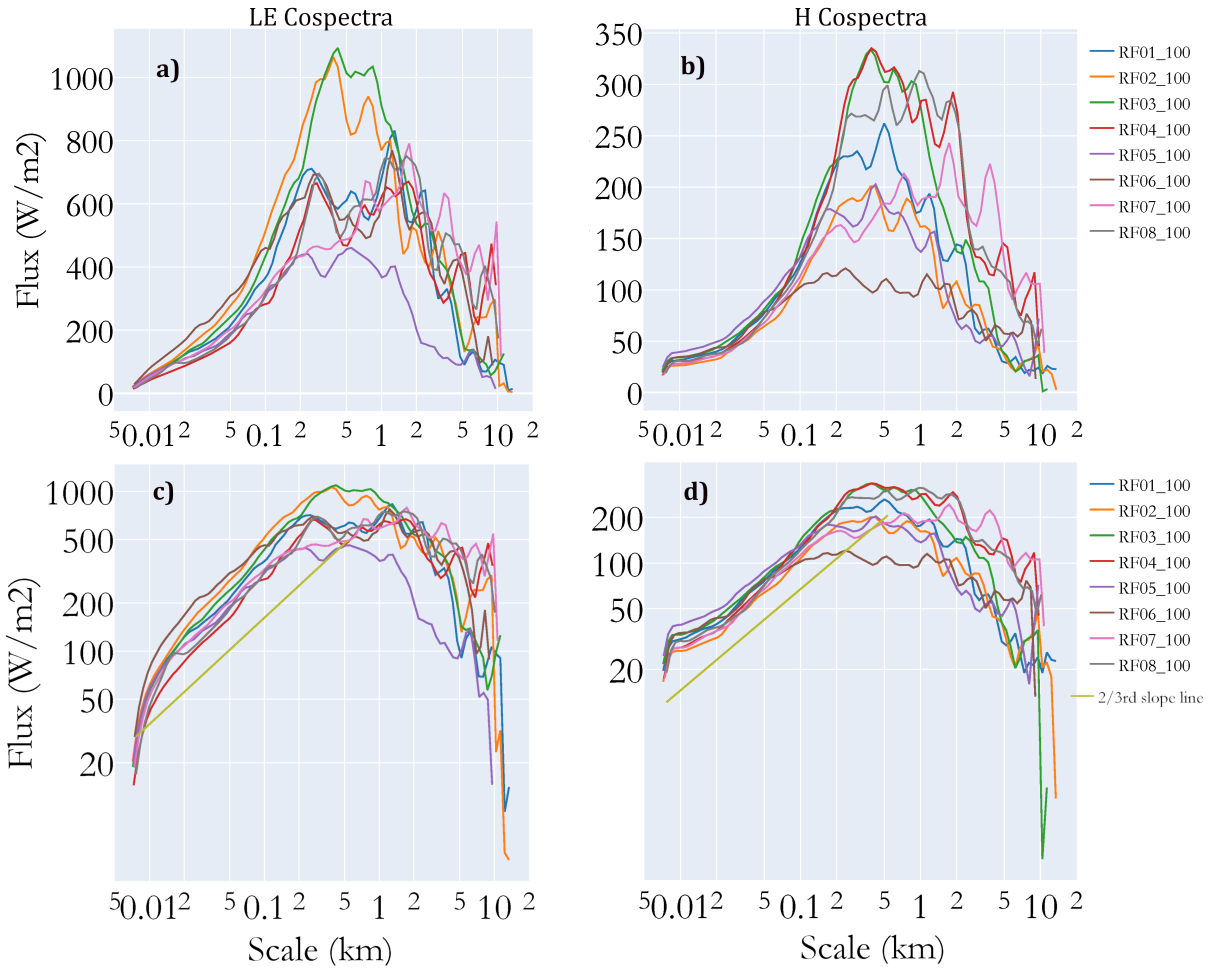

FIGURE 2.5: Wavelet cospectra for latent (a,c) and sensible heat(b,d) fluxes measured during each research flight at 100m above ground during the July IOP. Cospectra were calculated for each flight leg during the research flights and then ensemble averaged over all the flight legs used in the analysis. The first row, shows a semi-log depiction and the second row shows a log-log representation. Different colours indicate different Research Flights and the 2/3 slope line. Please note that even though both the subplots in a row (a,b and c,d) share the y axis labels, their ordinate ranges are kept different to better illustrate the variations in sensible heat flux spectra.

the flights (Figure 2.5.d). The magnitudes are also more variable between different flight days, with the peaks in the turbulence production scales reaching out to 300 Wm^{-2}. H cospectral power reduces for the spatial scales larger than 2 km while the LE cospectra still has power in the larger scales.

The prominent clustering of secondary peaks is no longer present in the latent heat flux cospectra

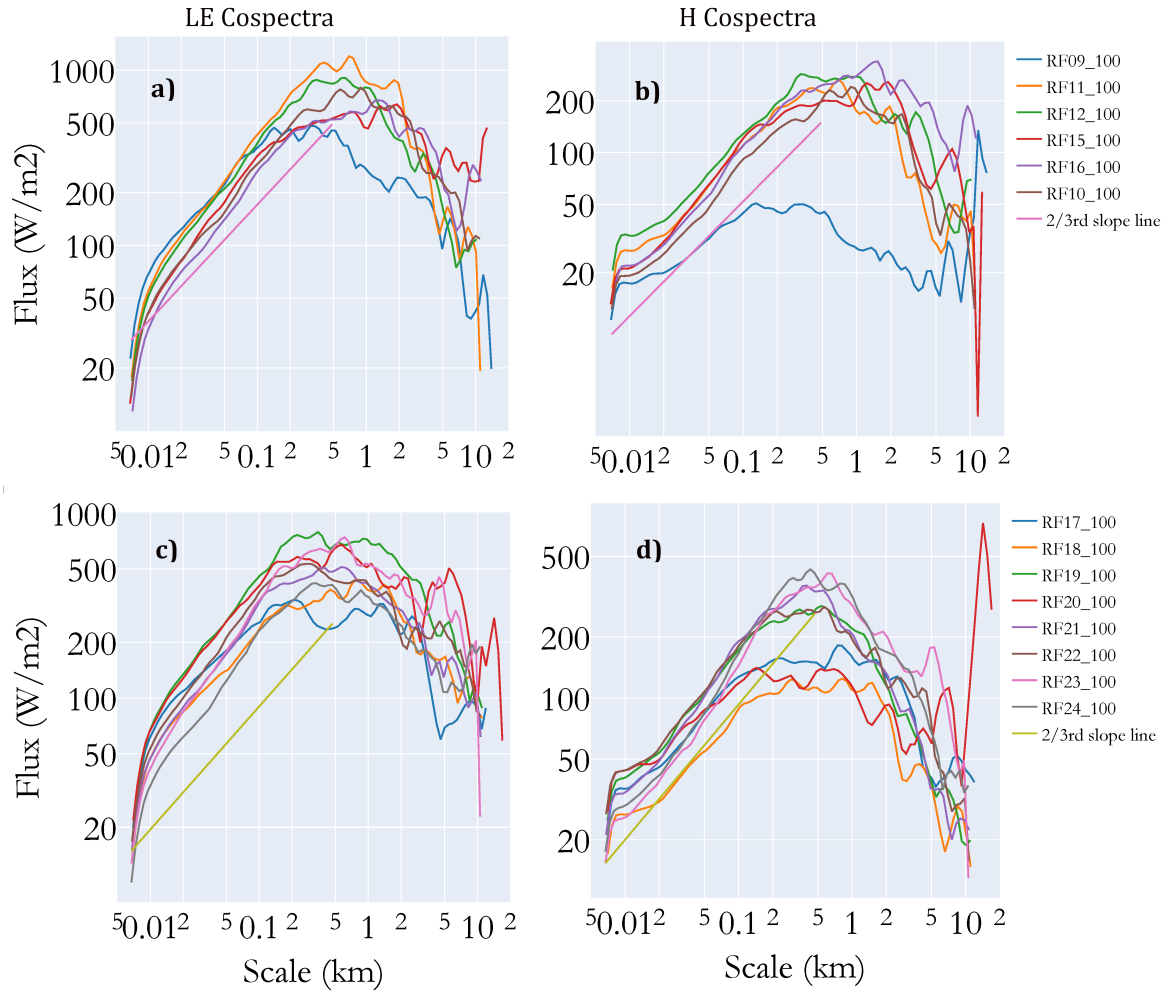

FIGURE 2.6: Wavelet cospectra for latent (a,c) and sensible heat(b,d) fluxes measured during each research flight at 100 m above ground during the August(a,b) and September(c,d) IOP. The first row show cospectra for the August IOP flights and the second row show cospectra for the September IOP flights. Cospectra were calculated for each flight leg during the research flights and then ensemble averaged over all the flight legs used in the analysis. Different colours indicate different Research Flights and the 2/3 slope line. Please note that even though both the subplots in a row (a,b and c,d) share the y axis labels, their ordinate ranges are kept different to better illustrate the variations in sensible heat flux spectra.

for the August IOP research flights (Figure 2.6.a). Cospectra for RF 15 and RF 16 show maximum flux magnitudes around spatial scales of 2000 m and 1200 m respectively (Figures 2.6.a and 2.6.b). Research flights 10, 11 and 12 have LE local maxima around spatial scale of 500 m to 1 km. These three flights measured peak latent heat flux magnitudes of the order of 1000 Wm^{-2} while the other flights have their maxima around 600 Wm^{-2}. For the LE cospectra,

spectral power in the large scales are similar order of magnitude as the July IOP measured values. The sensible heat flux cospectra for August IOP (Figure 2.6.b) are similar to the July IOP cospectra. They are broader in the turbulence production scales than the latent heat flux cospectra (Figure 2.6.a), with spatial scales ranging from 300 m to 2 km. RF09 has stands out with a low measured H cospectral power due to a rain event during early morning. Apart from this research flight, the other flights measured peak fluxes in the 200 to 300 Wm^{-2} range.

Most of the sensible heat flux cospectra for research flights in the September IOP show a shorter range of spatial scales in the turbulence production scales (Figure 2.6.d). Research flights 17 and 18 stand out with a broader range of spatial scales in the turbulence production range. The peak copsectral power for sensible heat fluxes are also higher in the September IOP, with values reaching around 400 Wm^{-2}. Compared to the July and August sensible heat flux cospectra, the September cospectral data show lesser power in the larger scales. The latent heat flux cospectral peaks are smaller than the values in the other two IOPs and more variable between different flight days. LE cospectra for RF 19 has a maximum around 800 Wm^{-2} while RF 17 has a double maxima, both around 300 Wm^{-2}. Such a prominent double peak nature is only seen in the RF17 LE cospetcra, with the first maxima around 200 m spatial scale and the second one at 1200 m. A more diffused double peak structure is seen in the cospectra for RF 19, where the peaks are of the same order of magnitude, at around 400 m and 1 km.

The heat flux cospectra do not show a distinct separation of the energy producing turbulent scales and mesoscales of atmospheric motion. The ABL height provides a theoretical maximum for the largest scales of atmospheric turbulence. ABL height was measured during the IOP days by two Wind Profiler Radars deployed roughly 45 km west and south to the Ameriflux tall tower (locations in Figure 1.a Duncan Jr et al. (2022) and data available from Bianco and

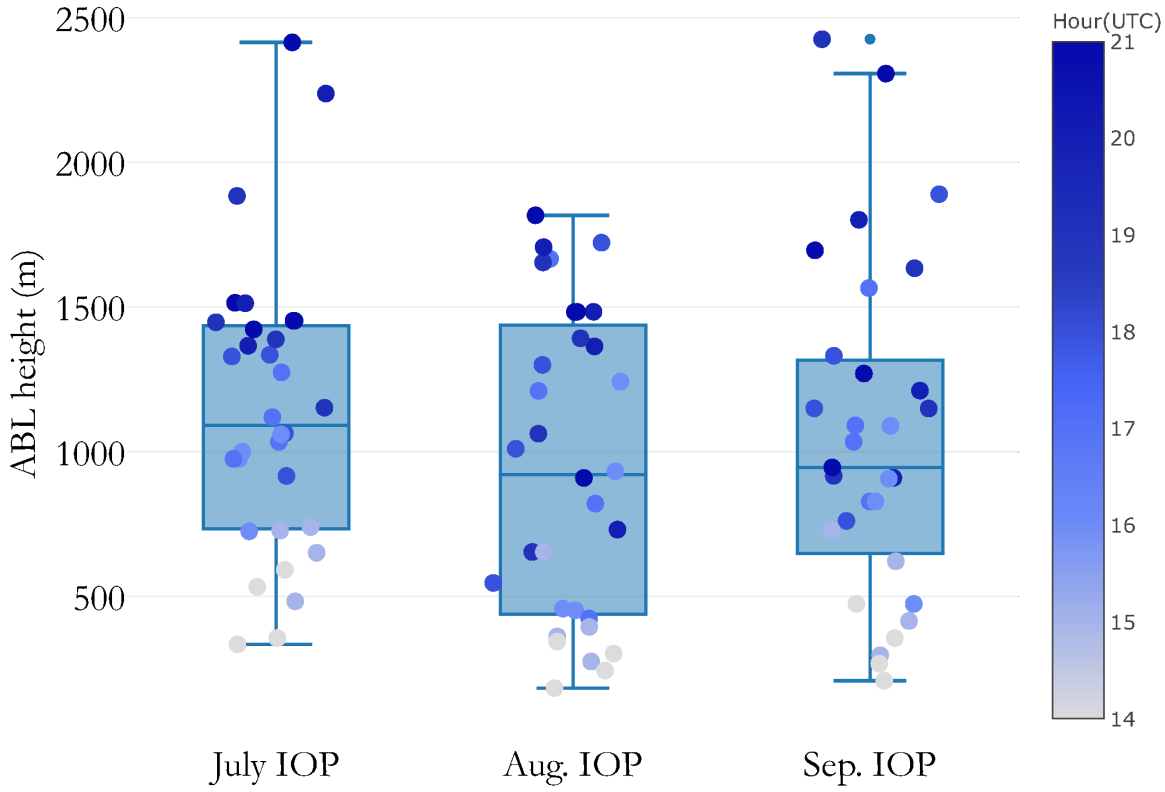

FIGURE 2.7: Distribution of hourly Wind Profiler Radar measured ABL height during the IOPs, coloured by the time of day.

Duncan (2020)) at the Lakeland and Prentice airports in Wisconsin. Duncan Jr et al. (2022) gives an overview of the instruments and presents a validation of the ABL height data with radiosonde measurements during the field experiment. Figure 2.7 presents the distribution of the hourly averaged boundary layer height measurements, averaged over both the instruments and coloured by the time of day. Little change is observed in the median ABL height measured across the IOPs. The boundary layer height increase with the development of the convective boundary layer can also be seen. During the July IOP, save for three data points, most values are bound between 300 m and 1500 m. The range of values broaden for the next two IOPs. For the August IOP, the boundary layer height measurements range from 200 m to 1800 m and for the September IOP they range from 200 m to 2000 m. These measurements indicate that 2

km is a reasonable order of magnitude threshold for the large scale structure/transport across the IOPs and can help partition the contributions from the largest scales of boundary layer turbulence and mesoscale structures.

2.3.2 Seasonal and diurnal variations

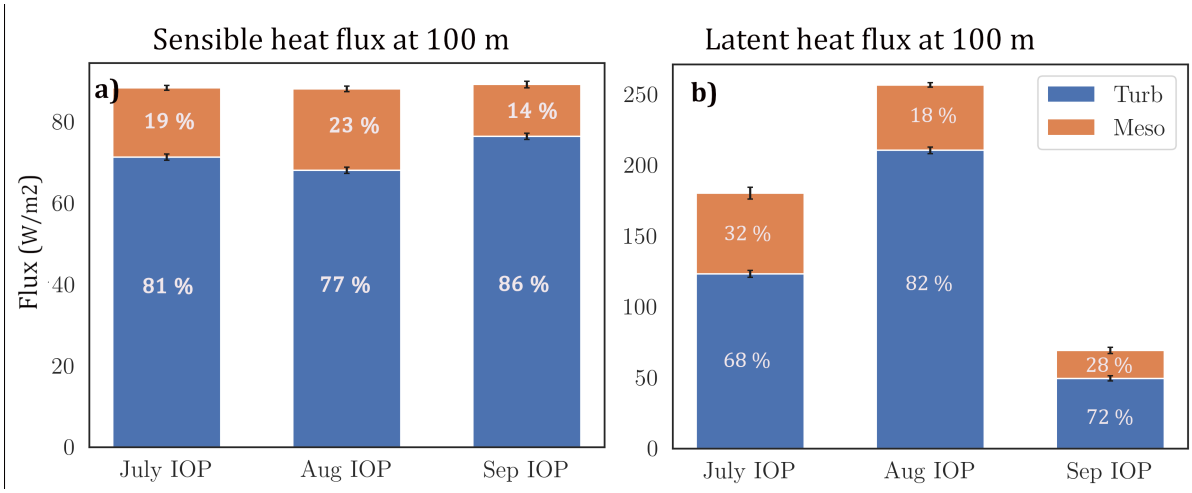

FIGURE 2.8: Mean turbulent (blue) and mesoscale (orange) (a) H and (b) LE fluxes for the three IOPs showing seasonal flux transitions. The flux percentages of the total are shown in white within the bars. Please note that even though both the subplots share the y axis label, their ordinate ranges are kept different to better illustrate the variations in sensible heat flux magnitudes.

IOP averaged flux magnitudes reflect the seasonal shift in the landscape (Figure 2.8). IOPs were conducted from late summer in the start of July to early autumn at the end of September 2019. In July the study domain is latent heat flux-dominated and towards the end of September as senescence starts to set in, it transitions to a sensible heat flux-dominated landscape. The mean sensible heat flux magnitude for all scales does not change substantially between the three IOPs and remains around 89 Wm^{-2}. However, there is a substantial variation in the magnitudes of the latent heat fluxes measured across the months. The measured total LE is higher than the total H in the July and August IOPs, increasing from 179 $\pm$ 5 Wm^{-2} to 256 $\pm$ 3 Wm^{-2} and then reduces to 69 $\pm$ 3 Wm^{-2} in the September IOP (Figure 2.8 and Table 2.3) ,

falling below the total sensible heat flux measured (89 ± 1 Wm^{-2}). The percentage mesoscale and turbulent contributions to the total measured fluxes also show a seasonal variation for the sensible and latent heat fluxes. For the sensible heat flux, the percentage turbulent contribution for the July IOP is 81%, which reduces to a further 77% in August and then increases to 86% in September. Similarly, for latent heat fluxes, the percentage turbulent contribution for the July IOP is the least, at 68%, increasing to 82% in August and then decreasing to 72% for September. When a particular heat flux dominated the surface atmospheric exchange it also had the lowest percentage mesoscale contribution among the IOPs. In August when the total(turbulent + mesoscale) latent heat flux magnitude is at its maximum at 256 ± 3 Wm^{-2}, the mesoscale fraction of the same is at its minimum, at 18%. Similarly, when the evaporative fraction is at its minimum September at 0.76, the sensible heat mesoscale fraction is also at a minimum at 14%.

The sensible heat flux data averaged across the domain and all flight days shows a diurnal cycle for all of the IOPs (Figure 2.9 column 1, black lines). The calculated turbulent scale fluxes follow the same patterns closely, but mesoscale fluxes do not. For the July IOP data, the total sensible heat flux peaks at 128.8 ± 1.31 Wm^{-2} around 16:20 UTC. In August the sensible heat flux maximum is of the same order, at 121.1 ± 1.3 Wm^{-2} but shifted to later in the afternoon around 20:20 UTC (Figure 2.9.c). The measured fluxes in the August IOP also show sustained values of the order of 100 Wm^{-2} from late morning to after noon (15:50-20:30 UTC) until later in the day towards the end of the afternoon. The September IOP sensible heat flux data has a more pronounced peak at 148.7 ± 1.5 Wm^{-2}. Our scale analysis reveals that this clear diurnal signal is present only for the turbulent scale fluxes which follow the total fluxes diel pattern closely for most of the flight day. In the July IOP the calculated mesoscale sensible heat fluxes

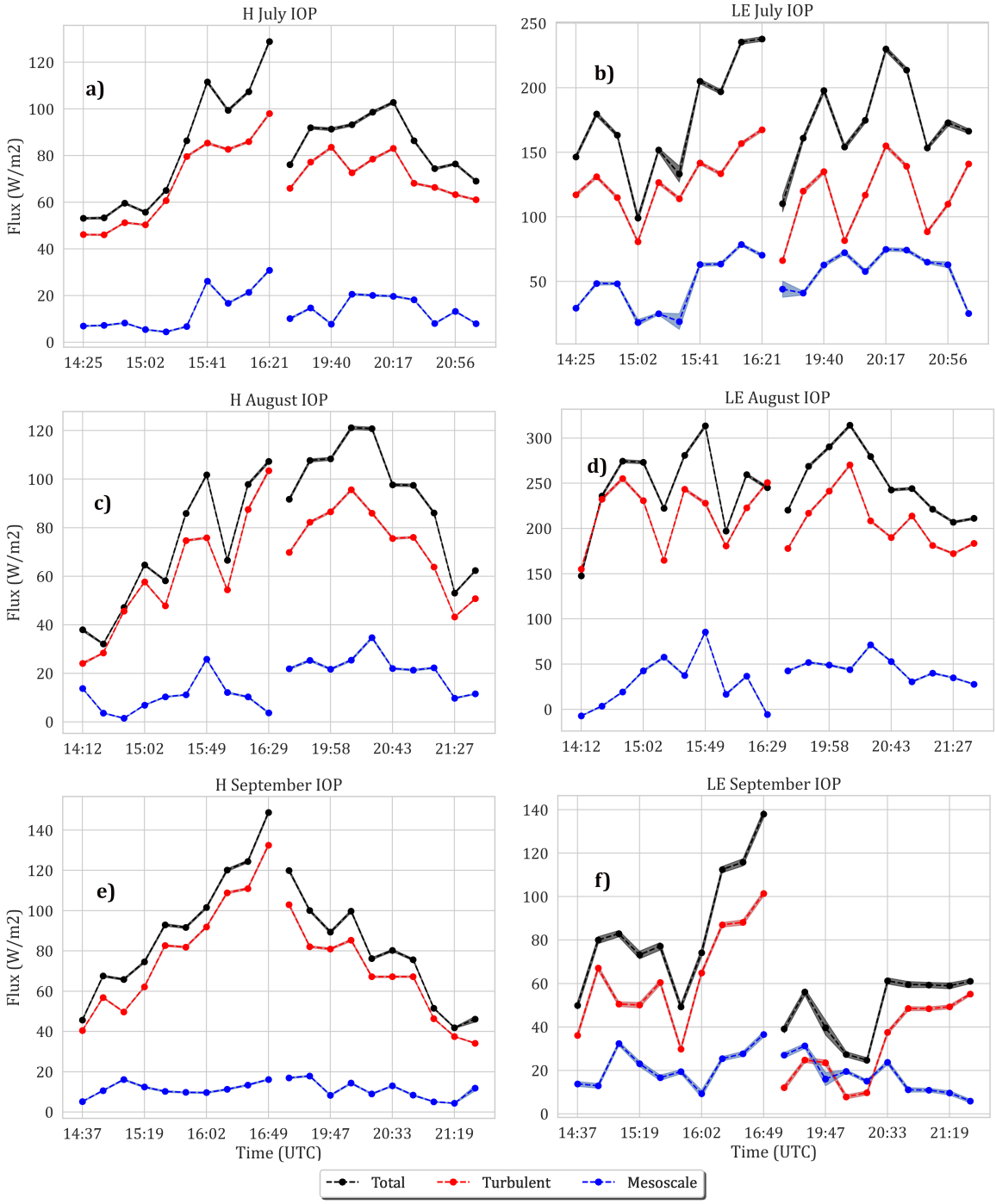

FIGURE 2.9: H and LE fluxes averaged for flight legs at the same time across all analysed days for the three IOPs. Every day had 2 RFs, a morning and afternoon flight. Every flight had 20 flight legs, numbered 1 to 20. Each data point is the mean value of fluxes measured from all flight legs at the same time of day in an IOP. The scale-resolved diel time series is shown. x axis shows the mean time of those flight legs in UTC. Since the x axis is ordered according to the flight leg timings, the 2.5 hours break between the end of the morning leg and the start of the afternoon leg is included as discontinuities in the plots. The first column shows the sensible heat flux values (subplots a, c and e) and the second column shows the latent heat flux values (subplots b, d and f). Each row shows data for an IOP (a,b July IOP; c,d August IOP; e, f September IOP).

peak around 30.8 ± 0.8 Wm^{-2} before noon and in the afternoon there are sustained values around 20 Wm^{-2} till later in the evening towards the end of the research flights. This can also be seen reflected in the difference between the total and turbulent flux diel plots in Figure 2.9.a. Similarly for the August IOP, mesoscale fluxes show sustained values in the afternoon around 25 Wm^{-2}, peaking at 34.8 ± 1 Wm^{-2}. Sensible heat mesoscale values are the lowest in the September IOP as observed earlier in the IOP averaged data. The median value for the IOP data is 11 Wm^{-2}, and the maximum value observed was 18 ± 0.7 Wm^{-2} around 19:30 UTC. The latent heat fluxes do not show such a clear diurnal variation for the domain averaged data. The domain averaged flux magnitudes are of the same order of magnitudes as the IOP averaged values presented earlier.

The total fluxes measured for all research flights analysed is presented in Figure 2.10. This picture at a research flight level reflects the seasonal variation detailed in Figure 2.8. Flux measurements from RF 2 (July 9th afternoon) and RF 3 (July 11th morning) stand out in the July IOP data (July 09 - 13) with total fluxes measured at 430.2 Wm^{-2} and 436.5 Wm^{-2}. This is due to increased contributions from turbulent latent heat fluxes for the two flights. The mesoscale contributions measured were of the same order of magnitude as other days of the IOP. Similarly, RF 23 (Sep. 28th morning) stands out in the September IOP (Sep. 24 - 28) with measured turbulent fluxes the same order of magnitude as the late summer IOPs. This was due to an increase in the measured turbulent latent heat fluxes due to a rain event earlier that day.

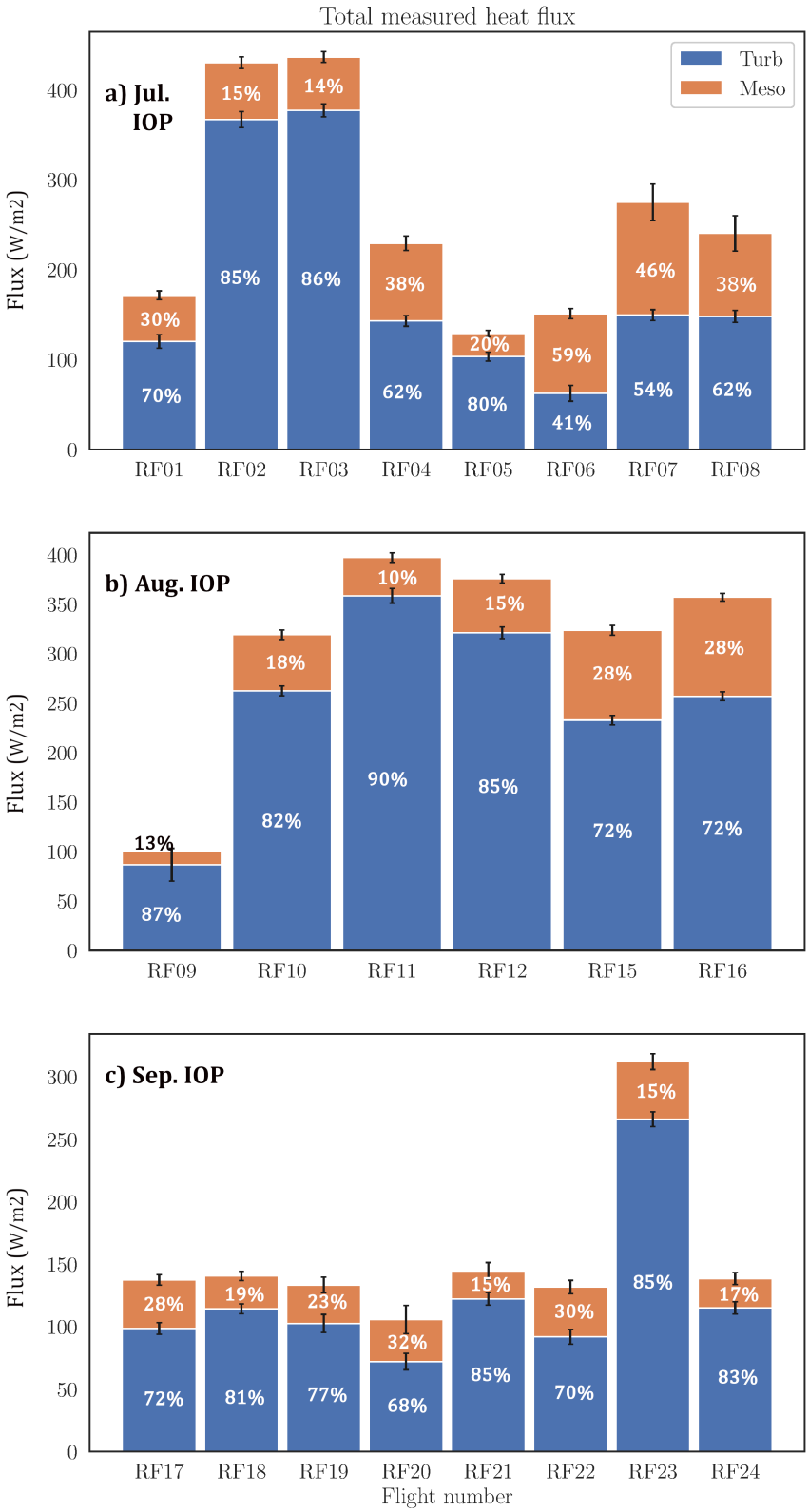

FIGURE 2.10: Total (H + LE) fluxes measured on each research flight for all the processed research flight data. The first (a) panel shows flights for the July IOP, the second (b) panel for the August IOP and the third (c) for the September IOP. Each bar graph represents the mean, scale-resolved flux for a research flight. The x axis shows the research flights and y axis flux magnitudes. Turbulent fluxes in blue and mesoscale fluxes in orange. Percentage contributions in white numbers.

2.3.3 ABL and land–surface drivers of transport

2.3.3.1 ABL dynamics

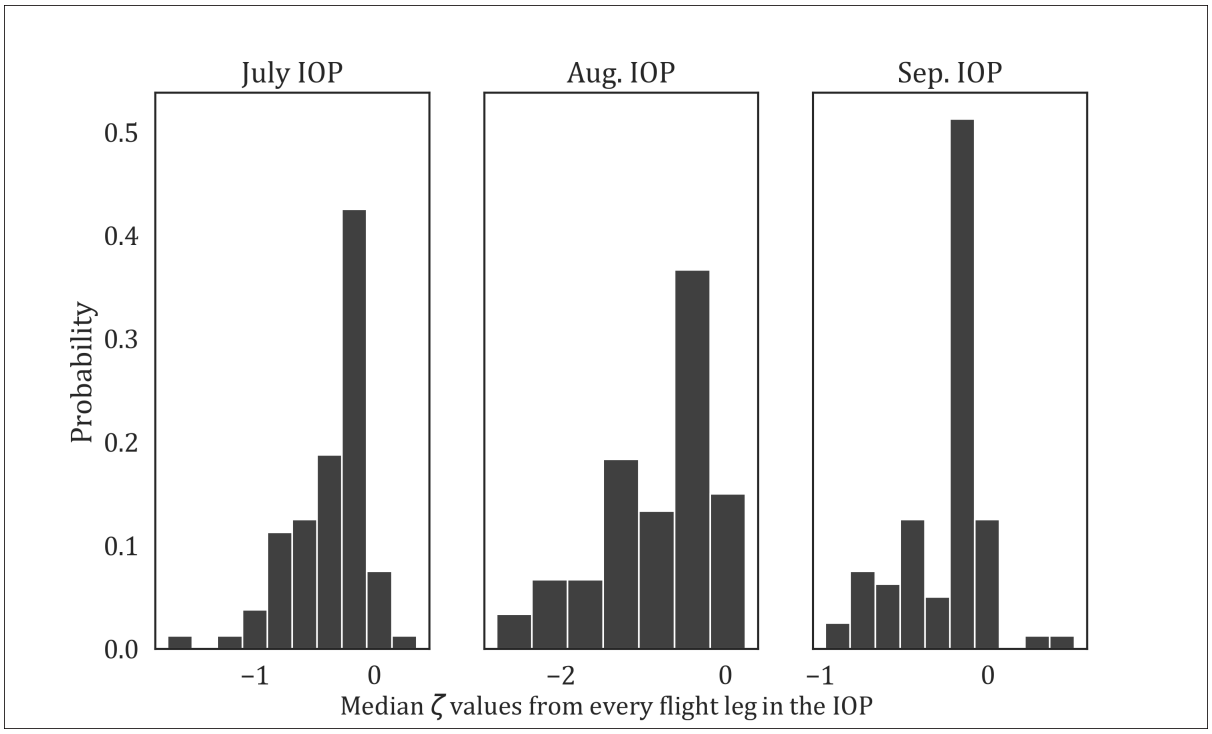

FIGURE 2.11: Probability distributions for the atmospheric boundary layer stability parameter, ζ for the three IOPs. ζ values were calculated over 1000 m subintervals along a flight leg. The median values calculated per flight leg are presented here.

The Obukhov length (Obukhov, 1946; Monin and Obukhov, 1954) was calculated for each of the 1000 m flux calculation windows (Section 2.2.4) as $L = -u^{*3}\overline{\theta_{v0}}/kgQ_{v0}$. Here, u^* is the measured surface friction velocity (turbulent velocity scale representative of surface shear stress); $g/\overline{\theta_{v0}}$, a buoyancy parameter where g is the gravitational acceleration and $\overline{\theta_{v0}}$ the average surface virtual potential temperature; k is the von Kármán constant set as 0.4 and Q_{v0} the calculated surface kinematic vertical heat flux ($\overline{w'\theta'_v}$) of the virtual potential temperature θ_v. The values used for $u^*, \overline{\theta_{v0}}$ and Q_{v0} were the local averages calculated over the 1000 m spatial subintervals. Since L has units of length, a non-dimensional turbulent surface layer stability parameter $\zeta = \frac{z}{L}$,

where z is the measurement height, can be defined (Stull, 1988). Negative values of ζ close to 0 indicate a statically neutral surface layer and as the value decreases, the surface layer becomes more statically unstable.

ζ values were calculated like so for all the flight legs analysed giving 250 to 300 values per space series for every leg. The median values were calculated for every flight leg as representative of the spatial transect over the heterogeneous domain. Normalised histograms of median ζ values show that the August IOP is more convective than the other two IOPs with more data points within the $\zeta <$ -1 range (Figure 2.11). On the other hand the September IOP looks strongly shear driven, with most of the data falling within $\zeta \in$ [-1 , 0). In this regard, the July and September IOPs seem to be dynamically similar.

To understand how scale-separated contributions vary with ABL dynamics, we compare the probability density functions (PDFs) of mesoscale flux fractions between shear driven ($\zeta \in (-1, 1]$) and convectively driven ($\zeta \in (-20, 1]$) ABLs. The mesoscale fractions of the total flux contributions are calculated for each of the 1000 m subintervals for sensible and latent heat flux space series. Based on the calculated ζ values of their subinterval, the mesoscale flux fraction data were grouped into neutral and unstable categories for all three IOPs. For all six subsets, outlier removal was done for the mesoscale percentage values based on median absolute deviations (Iglewicz and Hoaglin, 1993). Using data from all the subintervals gives us a good number of data points for robust statistical analysis. For N_s denoting the number of data points for neutral,shear driven ABL and N_c denoting the number of data points for unstable, free convectively driven ABL, the July IOP data had $N_s = 15428$ and $N_c = 2203$. Likewise, for the August IOP $N_s = 9298$ and $N_c = 5158$, and for the September IOP $N_s = 17041$ and $N_c = 1308$.

Kernel density estimations (KDEs) are used to calculate PDFs from the airborne spatial data. KDEs are a way to estimate the continuous, non-parametric PDF of a given distribution of random variable using smoothing window functions or kernels (Scott, 1979, 2015). A histogram of the data can provide a non-parametric estimate of the underlying probability density when the bin counts are normalised by the total sample size and multiplied by the bin width. This conventional discrete PDF representation of the data in a histogram uses stacked rectangular bars. In KDEs, a window function (such as a Gaussian kernel with a chosen bandwidth) is employed instead of rectangular bars to estimate a continuous PDF of the data.

In this study we use Gaussian kernels with a sample size depended band width, given by a rule-of-thumb bandwidth estimate $h = N^{-1/(1+d)}$, where N is the number of data points and d the number of dimensions (1 for the univariate distributions here) following Scott (2015). PDFs were calculated using KDEs for the mesoscale flux fraction distributions in the neutral and unstable regimes. For the sensible heat flux distributions, the two distributions were found to be significantly different from each other for all 3 IOPs using the Mann-Whitney U rank test with 95% confidence. The PDFs show statistically significant higher fraction of mesoscale transport observed in convectively driven ABLs across all the three IOPs (Figure 2.12).

For latent heat fluxes, the kernel density estimates of mesoscale fraction distributions for the July and August IOPs show higher mesoscale fluxes for convective cases (Figure 2.13). Performing a Mann-Whitney U rank test again showed that the distributions are significantly different for the two stability regimes at 95% confidence. However, for September IOP the mesoscale transport does not have a preference between a shear or convectively driven ABL. Even though July and September IOPs have similar ABL stability distributions their latent heat mesoscale transport

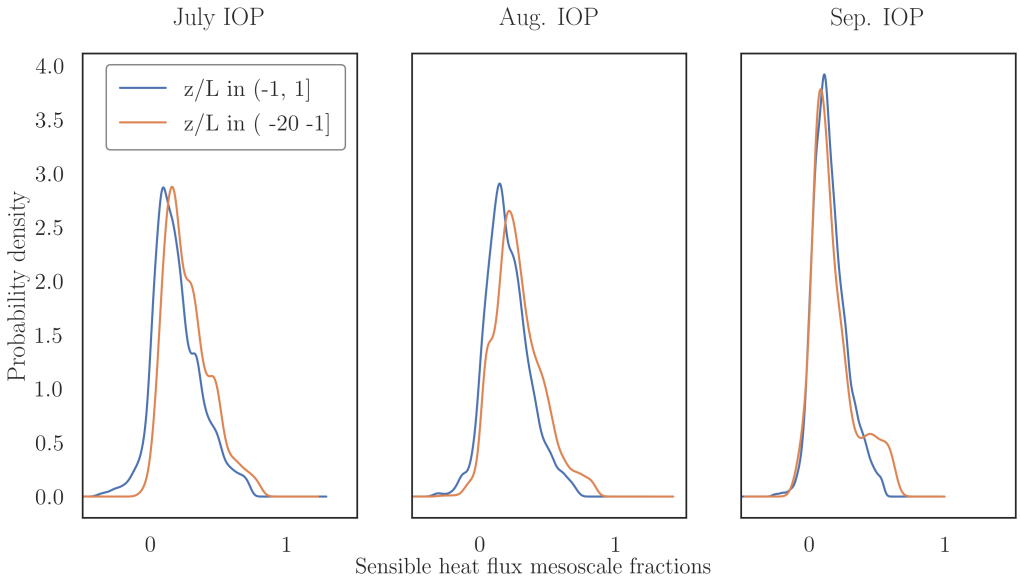

FIGURE 2.12: Probability density functions for sensible heat flux mesoscale fractions calculated from kernel density estimates. Mesoscale flux fractions of the total fluxes were calculated over 1000 m subintervals for the flux space series from every flight leg.

does not show the same behaviour, hinting at the role of seasonality through changing surface characteristics and insolation.

The PDFs of sensible and latent heat mesoscale fractions show values when the flux fractions are > 1 and < 0 (albeit near-zero for the sensible heat distributions when mesoscale fractions are > 1). These occur when the measured mesoscale and turbulent fluxes are out of phase with each other. For both sensible and latent heat fluxes, the histograms of turbulent and mesoscale fluxes when the mesoscale fraction is greater than 1 show higher, positive values of mesoscale fluxes and lower negative values of turbulent scale fluxes (Fig. 2.22). Indicating that the mesoscale fluxes dominate such instances, driving the fraction to be over 1. Similarly for mesoscale fractions < 0, the sensible heat flux histograms for scale-resolved fluxes show higher, positive values for turbulent fluxes and lower negative values for mesoscale fluxes causing the mesoscale fraction of the total flux to be negative (Fig. 2.21). The same phase difference

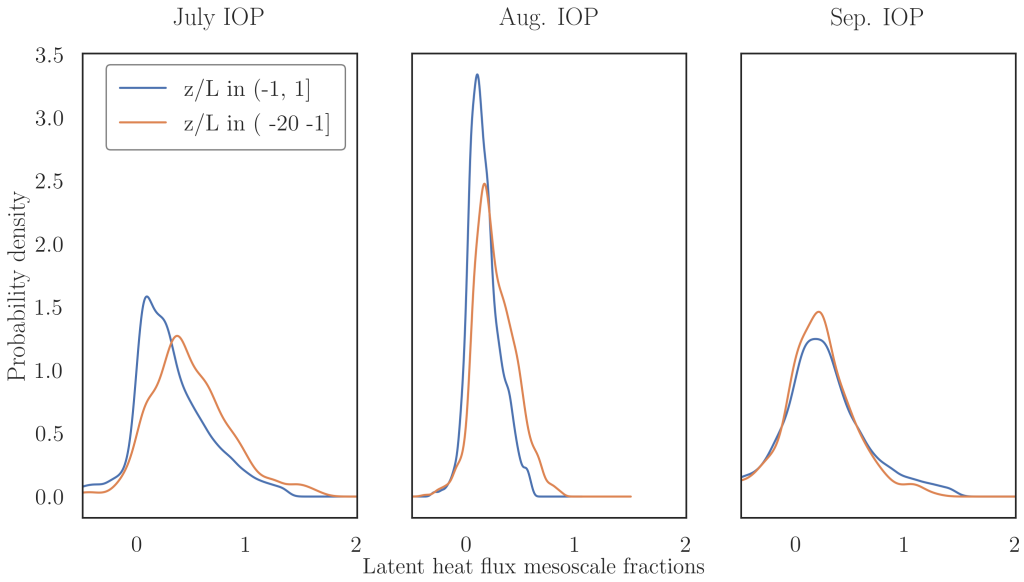

FIGURE 2.13: Probability density functions for latent heat flux mesoscale fractions calculated from kernel density estimates. Mesoscale flux fractions of the total fluxes are calculated over 1000 m subintervals for the flux space series from every flight leg.

between turbulent and mesoscale fluxes can be seen in the latent heat fluxes too, although they behave more uniformly.

The surface layer friction velocity, u^* can capture the magnitude of surface Reynolds' stress as a velocity scale. For the 1000 m spatial subintervals it is calculated from the vertical momentum fluxes as $u^* = (\overline{u'w'}^2 + \overline{v'w'}^2)^{1/4}$. Similarly, the convective velocity scale $w^* = (\frac{g}{\theta_v} z_i \overline{w'\theta_v})^{1/3}$ captures the importance of free convection as a velocity scale. It follows that, u^*/w^* is a non-dimensional parameter that can succinctly capture the competing effects of free and forced convection in the ABL. If the ABL is strongly shear driven, one would expect higher u^* values and lower w^* values, leading to higher values for u^*/w^* and vice versa for a free convectively driven ABL. Kernel density estimates of u^*/w^* calculated reflect the ζ distribution characteristics for the 3 IOPs seen earlier in Figure 2.11. September IOP has a median u^*/w^* value of 0.55, higher than the July (0.45) and August (0.43) IOPs, indicating more shear driven surface

atmospheric transport. Similarly, the distributions for July and August IOPs were also similar, with the august IOP having a slightly lower median value indicating more convectively driven transport.

A binned scatter plot can help to succinctly visualise non-parametric relationship between two random variables. It has been a popular tool in applied microeconomics to visualise the conditional expectations in large datasets (Chetty and Szeidl, 2005; Chetty et al., 2009; Starr and Goldfarb, 2020). We use the *binsreg* in Python (`https://nppackages.github.io/binsreg/`) as introduced in Cattaneo et al. (2019). The number of bins for the independent variable of interest is calculated such that it minimises the integrated mean squared error of the binned scatter (much like a piece wise linear regression). The distribution of the predictor variable is then divided into equal quantiles corresponding to the chosen number of bins and the conditional means of the second variable is calculated.

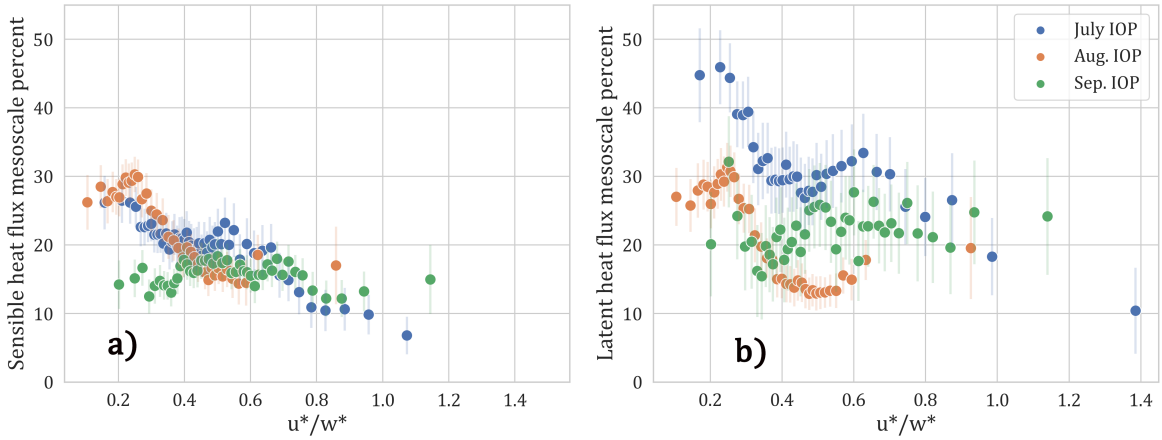

FIGURE 2.14: Binned scatter plots of mesoscale flux percentages vs u^*/w^* for all three IOPs. Bin values of the flux fractions plotted are calculated as conditional means for the u^*/w^* bins. 95% confidence limits of the mean values are shown as vertical lines at each bin estimate.

The mesoscale H percentages show a decreasing trend with increasing u^*/w^* values in July and August IOPs indicating higher mesoscale transport during more convective scenarios (Figure

2.14.a). This is especially clear in the almost flat scatter for the shear driven September IOP data which also has lower magnitudes, with the same order of magnitude throughout the range of u^*/w^* values. The highest values in July and August IOPs are of the same order of magnitude. July IOP shows the lowest percentage values for $u^*/w^* >= 0.7$. The latent heat mesoscale flux percentages do not behave similarly to the sensible heat flux mesoscale fractions (Figure 2.14.b). Mesoscale fractions measured during the July and August IOPs are higher at lower u^*/w^* values but they are not of the same magnitude. This separation between the magnitudes of the July and August IOP values persists across the range of u^*/w^* values although both the scatters have similar shapes. The August IOP has lower mesoscale LE percentages at lower u^*/w^* values than the July IOP unlike the H mesoscale percentages. The August IOP data also shows the lowest values for mesoscale LE percentages for $u^*/w^* > 0.4$ while July IOP values are consistently the highest across the u^*/w^* range. The same behaviour is seen in the IOP averaged mesoscale percentages in Figure 2.8.b where the mesoscale LE percentage for August IOP is the lowest at 18%. Meanwhile, the LE mesoscale percentages during the more shear driven September IOP for $u^*/w^* > 0.4$ show values higher than August IOP. Figure 2.8.b also shows high (29%) mesoscale fluxes for LE in the September IOP. There is also more variation in the September IOP LE values when compared with the H mesoscale percentages for the same time.

2.3.3.2 Flux contributions by land cover

The land cover class data from wiscland 2.0 database as shown in Figure 2.1 for the 40×40 km domain was grouped into open water (9% domain area composition), wetlands (34%), deciduous broadleaf forests (30%), shrubs/grass/open land (3.5%), coniferous (22%) and mixed forests

(1.3%). Fractional footprint contributions from each of the land cover classes were calculated for each research flight (Figure 2.15). Wetlands dominate the footprint contributions to the measured fluxes across IOPs as they do for the study domain surface area. They were most prominently sampled during the September IOP research flights of September 24th and 26th, when the UWKA flew a South-East flight pattern with moderate to strong Southerly and South-Westerly winds (Table 2.1). Further breaking down the wetland class, we find that most of the contributions come from the forested wetlands that account for 27% of the domain area. The deciduous broadleaf forests and confiers were sampled fairly equally across the IOPs. Although open water bodies showed strong local contributions to the flux space series (For example the blue dots highlighted in the space series shown in Figure 2.4.b and 2.4.c) the averaged contribution during a research flight reflect their lower percentage area composition.

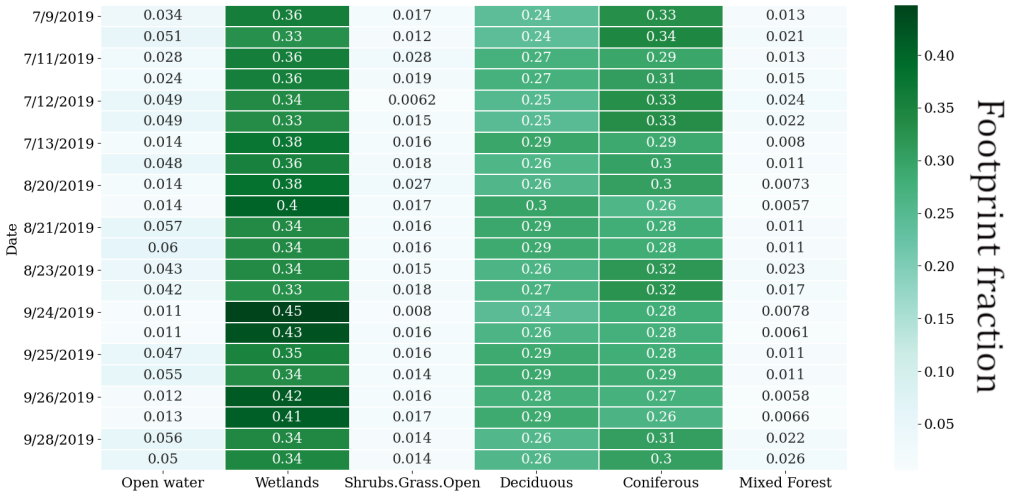

FIGURE 2.15: Heat map of fractional footprint contributions from the major land cover classes within the study domain for each research flight. The land cover classes are presented in columns and the airborne campaign dates are presented along rows. The first row for every date corresponds to the morning flight and the second row the afternoon flight. The numbers inside the boxes show fractional footprint contributions and they are coloured according to the colour bar

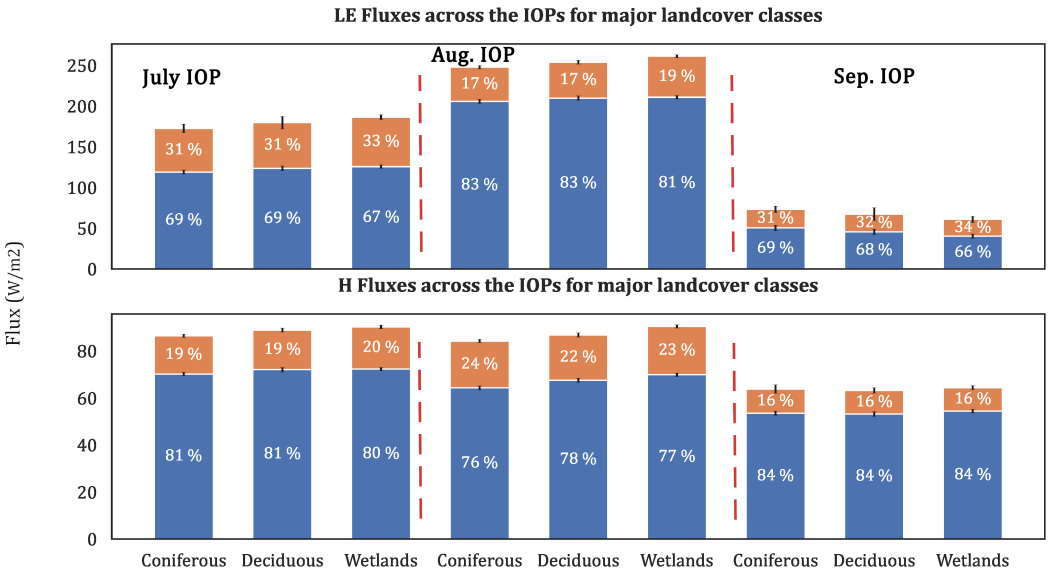

FIGURE 2.16: Turbulent and mesoscale sensible and latent heat fluxes measured for the major land cover classes across the IOPs. Turbulent fluxes in blue and mesoscale fluxes in orange. Panel on top shows the LE and panel at the bottom shows H. Bar graphs for each of the three IOPs are separated by vertical dashed red lines and ordered as contributions from coniferous, deciduous forests and wetlands within each IOP group.

For a more detailed investigation of flux footprint contributions with time, IOP averaged, scale-separated footprint contributions were calculated (Figure 2.16). For all research flights analysed, the land cover class with the maximum footprint contribution to the measured fluxes at each 1000 m subinterval was picked. This was then grouped by their respective IOP to calculate the scale-separated fluxes for each IOP from all the land cover classes. The same overall pattern across the IOPs seen in Figure 2.8 is repeated in Figure 2.16 as well, with regards to the magnitudes of the fluxes across IOPs and the scale-resolved percentages. The sensible heat flux magnitudes measured are fairly consistent across the IOPs while the latent heat fluxes show strong seasonality between the IOPs. Although wetlands contribute the most to flux footprints, the scale-composition of the fluxes do not change substantially between the land cover classes. The highest mesoscale LE percentage was measured in the September IOP with

all the major landcover classes averaging around 32% and the most H mesoscale percentage values were measured in the July IOP, averaging at 23% between all 3 land cover classes. The kernel density estimates for mesoscale fractions did not show significant differences between the three major land cover classes.

2.3.4 Space scale resolved fluxes

We present a case study for one good flight, with a sample flux topography for a summertime morning flight, RF03, conducted on July 11th, 2019 from 09:20 to 11:30 CDT (Central Day Time, 5 hours behind UTC). The flight did east-west transects across the domain, starting from the northern edge and moving to the south. Aircraft logs for the day mention observing shallow cumulus clouds indicating local convection and weak winds for this day. This ensured that the flight transects had a good footprint coverage over the domain for this research flight.

Spatially resolved sensible and latent heat flux topography maps (Figure 2.17.a) show similar order of magnitude values as the IOP averaged behaviour in Figure 2.8. The spatial distribution patterns of both the fluxes do not look similar with latent heat flux showing more spatial variability than the sensible heat flux and dominating over the latter. The percentage mesoscale contributions for the two fluxes are qualitatively similar over the western part of the domain but show differing spatial patterns towards the eastern sections (Figure 2.17.b). These flux topographies illustrate the fact that the CHEESEHEAD19 tower sites inside the study domain sample differing Bowen ratios within the same 10×10 km domain and there are spatially varying, concomitant mesoscale surface-atmospheric transport. This would imply that not all of the towers are sampling the same flux transport and the mesoscale transport associated with their locations would also be different. The flux topographies indicate stronger mesoscale contributions

towards the southern edge of the domain in the sensible heat flux plots (Figure 2.17.b). This is due to the inherent time dependency in calculating the topographies from the flight transects. Each research flight duration is about 2 hours. This particular flight started measurements at the north end of the domain in early morning and by the time it reached the southern edge it was close to noon and by then a fully developed CBL would have formed. Sensible heat mesoscale fluxes develop more later in the day as well (Figure 2.9.a, 2.9.c). The scale-resolved fluxes for latent heat for this flight indicate that the turbulent and meso peaks do not align in space (Figure 2.18.a). Flux topographies for research flights in the August and September IOPs are presented in the supplement along with the standard error percentages for the footprint weighted fluxes (Gatz and Smith, 1995) following Kohnert et al. (2017).

The inherent time dependency of the topographies leads to source strength non-stationarity, since the surface heat flux magnitudes change over the course of the measurement. This makes the flux topographies harder to interpret. A fusion Land Surface Temperature (LST) product over the domain (Desai et al., 2021) for the measurement time shows a high amplitude west-east band in the centre (Figure 2.18.b). Mesoscale gradients can be observed close to this band in the latent heat flux plots of Figures 2.18.b and 2.18.c. However, since the large scale transport would be from quasi stationary structures we can't directly link the same to land cover or LST gradients in our current analysis framework.

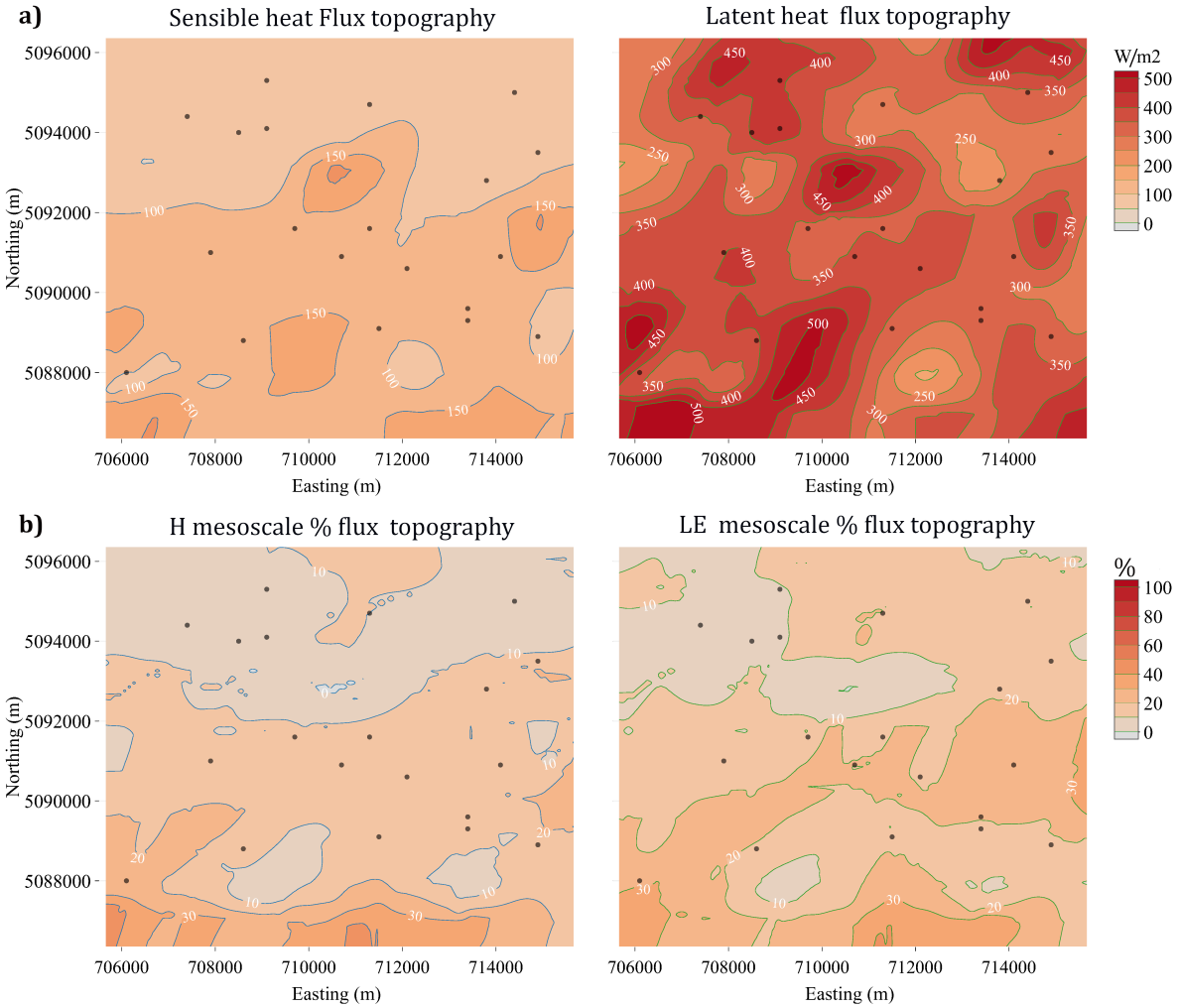

FIGURE 2.17: Flux topographies for RF 03 in the July IOP, 11 July 09:20 to 11:20 CDT over the 10×10 km CHEESEHEAD19 core domain. The brown dots are the NCAR-ISFS tower locations. The top row (a) shows the sensible (left) and latent (right) heat flux topographies. The percentage mesoscale contributions to the fluxes are shown in the bottom row (b) below their flux topographies.

2.4 Discussion

Implications for Surface-Atmospheric Transport and Surface Energy Budget closure

Airborne measurements sampled across the heterogeneous study domain could resolve the constituent surface-atmospheric transport scales. The aircraft campaign experiment design allowed us to measure the diel and seasonal shifts in surface energy balance and investigate its impact

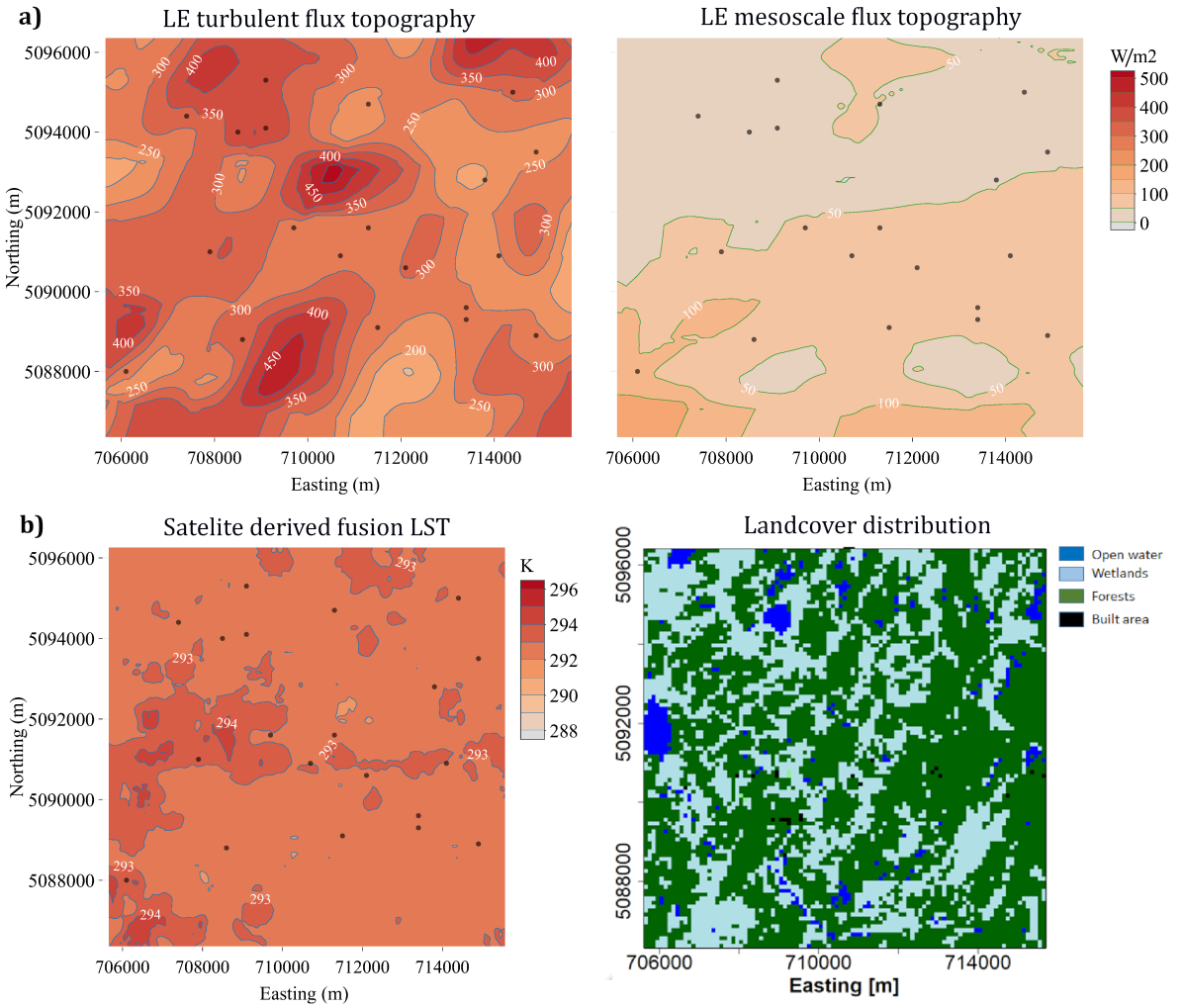

FIGURE 2.18: (a) scale-resolved, turbulent (left) and mesoscale (right) topographies for the latent heat flux and (b) distribution of land–surface properties LST (left, from Desai et al. (2021)) and land–surface classes (right, from Wiscland 2.0) across the domain.

on the scales of surface atmospheric transport. We observed higher fractions of mesoscale transport for sensible and latent heat fluxes in convectively driven ABLs as shown in the KDE plots (Figure 2.12 and Figure 2.13) in Section 2.3.3. Previous observational studies have noted the inverse relationship between tower measured surface energy balance imbalance and u^* (Stoy et al., 2013; Eder et al., 2015), indicating that strong mechanical mixing in shear driven ABL leads to larger turbulent transport. Our findings also indicate the same, that lower frequency transport seems to have a preference for convectively driven boundary layers. The dependency

of latent heat fluxes is more complicated than the sensible heat flux transport.

Using data from the LITFASS-2003 field experiment in Germany Foken (2008) and Foken et al. (2010) showed that area averaged surface flux measurements reduce the surface energy budget residuals. This, combined with the observations that the residuals are worse for sites with more heterogeneous surfaces, leads to his hypothesis that what has remained unaccounted for in the budgets could be the transport due to quasi-stationary secondary circulations tied to landscape heterogeneity. The synthesis study by Stoy et al. (2013) found consistent energy balance non closures across the sites and more importantly, noted that non-closure is linked to the degree of landscape heterogeneity, quantified using MODIS products and GLOBEstat elevation data. Since then a growing body of research has suggested that quasi-stationary low-frequency eddies in the ABL tied to land–surface heterogeneity can play an important role in surface-atmospheric transport.

LES studies with homogeneous (Salesky et al., 2017; Li and Bou-Zeid, 2011) and heterogeneous (Margairaz et al. (2020), idealised heterogeneities) surface forcings have observed secondary circulations in the ABL transition from convective rolls to a cellular structure as the ABL becomes more convectively unstable. Margairaz et al. (2020) notes that for their simulations, with imposed surface temperature heterogeneities in irregular rectangular patches, the convective-cell structure adjusts to the imposed surface temperature variations. The surface atmospheric transport associated with these circulations would be missed by tower based measurements unless they are either swept across the spatially-stationary measuring points by the mean wind or only if the point measurements happen to be in their vicinity (Mahrt, 2010; Charuchittipan et al., 2014). These studies along with observations of better closure with longer averaging times and

spatial measurements have led to a leading hypothesis that the surface energy balance closure problem is in fact a problem of scale (Foken, 2008; Foken et al., 2010; Mauder et al., 2020)

Large scale organisations in the form of longitudinal roll vortices, aligned with the mean wind can be generated in daytime convective boundary layers (Lemone, 1973; Etling and Brown, 1993) while stationary circulations can also be induced by horizontal variations in surface roughness and heat flux (Desjardins et al., 1997; Sun et al., 1998). LES studies have shown that over homogeneous surfaces, strongly unstable conditions can lead to the formation of standing convective cells akin to those that form in Rayleigh-Benard convection (Kanda et al., 2004; De Roo and Mauder, 2018a). Over heterogeneous surfaces these free convective cells tend to become quasi-stationary secondary circulations, tied to the surface temperature, roughness or vegetation gradients (Inagaki et al., 2006; Maronga and Raasch, 2013a). Such secondary circulation cells can lead to a persistent local-mean advective transport, leading to an underestimation of surface energy exchange (Morrison et al., 2021).

Desai et al. (2021) presents a 50 m resolution fusion LST product for the same study domain, derived using a fusion of land–surface model and satellite products. They note that the spatial standard deviation of the fusion product increases towards autumn and is also high for summer afternoons, with higher LST spatial gradients. This could be playing a role in the higher sensible heat mesoscale fluxes observed in the late morning and afternoon for the July and August IOPs (Figures 2.9.a and 2.9.b)

In this regard, using wavelet methods on high-frequency airborne data has allowed us to retain the larger scale surface-atmosphere transport across the heterogeneous study domain and account for relevant transport scales. Figure 2.19 shows an IOP averaged representation of the

scale resolved fluxes presented in Figures 2.5 and 2.6. We do not see a prominent separation of scales between the turbulent and mesoscale regimes as was reported in the similar study of Mauder et al. (2007a). There is a secondary peak in the LE cospectra for the July IOP around 1200m, which persisted across multiple research flights throughout the day (Figures 2.5.a and 2.5.c). Nonetheless, the flux cospectra show consistent and substantial contributions from the mesoscales $>$ 2 km. Cospectra calculated for the July and August IOPs show higher values in the larger scales compared to the September IOP cospectrum for both H and LE. The H copsectra for July and August IOPs also show a flattening for scales greater than 5 km. An increase in the magnitude and range of turbulent scales is also seen between the August and September H copsctra. For the LE July and August IOP cospectra, the mesoscale contributions are around the same magnitude. The IOP averaged cospectra for LE also suggest that even with 30 km flight legs we might still be missing contributions from larger scales, with the cospectra tails ending around 150 to 200 Wm^{-2}.

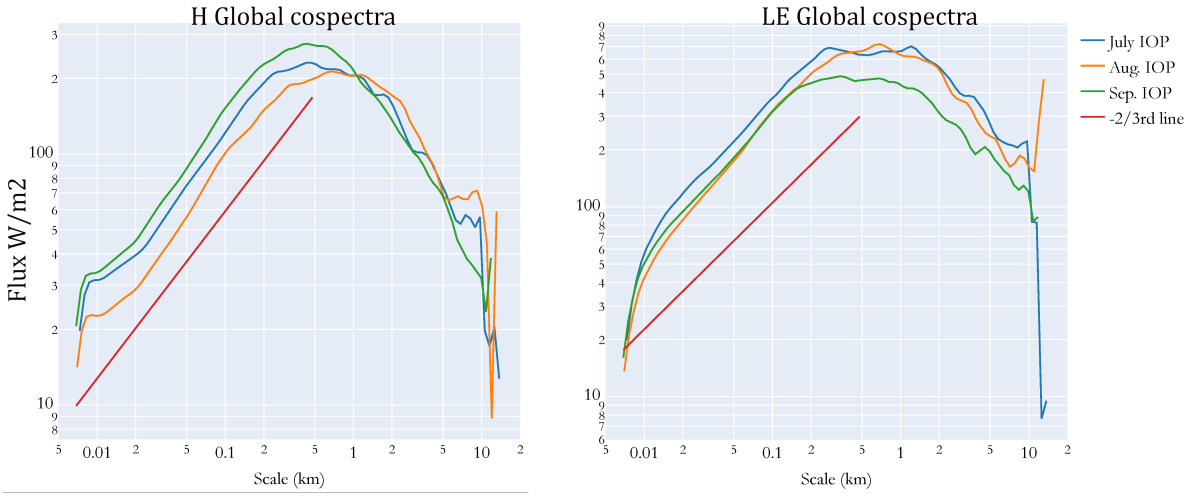

FIGURE 2.19: Global cospectra for H and LE for the 3 IOPs. Presented here are the ensemble averages of the wavelet cospectra presented in Figures 2.5 and 2.6.

Looking at the scale-averaged picture, we see that the mesoscale contributions are not a fixed fraction of the total or turbulent fluxes but vary throughout the day and as the landscape

undergoes seasonal transitions (Figure 2.8 and Figure 2.9). The scale-separated sensible and latent heat fluxes do not behave similarly either. During the August IOP, (08/20 to 08/23), the measured Bowen ratio is the lowest at 0.3 and this IOP has the lowest mesoscale fraction for latent heat fluxes. Similarly, during the September IOP in early autumn (09/24 to 09/28) , the Bowen ratio is the highest at 1.3 and mesoscale sensible heat flux fraction was the lowest during this IOP. The total mesoscale flux percentages for July IOP = 29%, August IOP = 20% and September IOP = 21%. The total percentages are closer in magnitude because of the seasonal sensible and latent heat flux balance. It is interesting to note that the August and September IOPs with very different Bowen ratios have the same mesoscale flux percentages.

The scale analysis of surface-atmospheric transport can provide valuable input for process based parametric correction methods for the tower-measured surface energy imbalance. Wanner et al. (2022) presents a parametric non-local correction factor for surface energy imbalance over heterogeneous surfaces by extending the parametric surface energy balance correction over homogeneous surfaces by De Roo et al. (2018). Wanner et al. (2022) incorporated the effects of idealised heterogeneities using data from the LES work by Margairaz et al. (2020). Mauder et al. (2021) tested the De Roo and Mauder (2018a) method for three midlatitude flux tower sites and found satisfactory results. Currently work is underway to extend the Wanner et al. (2022) method for the CHEESEHEAD19 flux towers and our results on the magnitudes and diel and seasonal variations of mesoscale fluxes can provide valuable order of magnitude benchmarks while correcting for the bias in eddy-covariance measurements due to the presence of large-scale dispersive fluxes.

We did a comparative study of the aircraft fluxes with flux measurements at 122 m height from the Ameriflux tall tower at the centre of the study domain (US PFa). The tall tower did not have

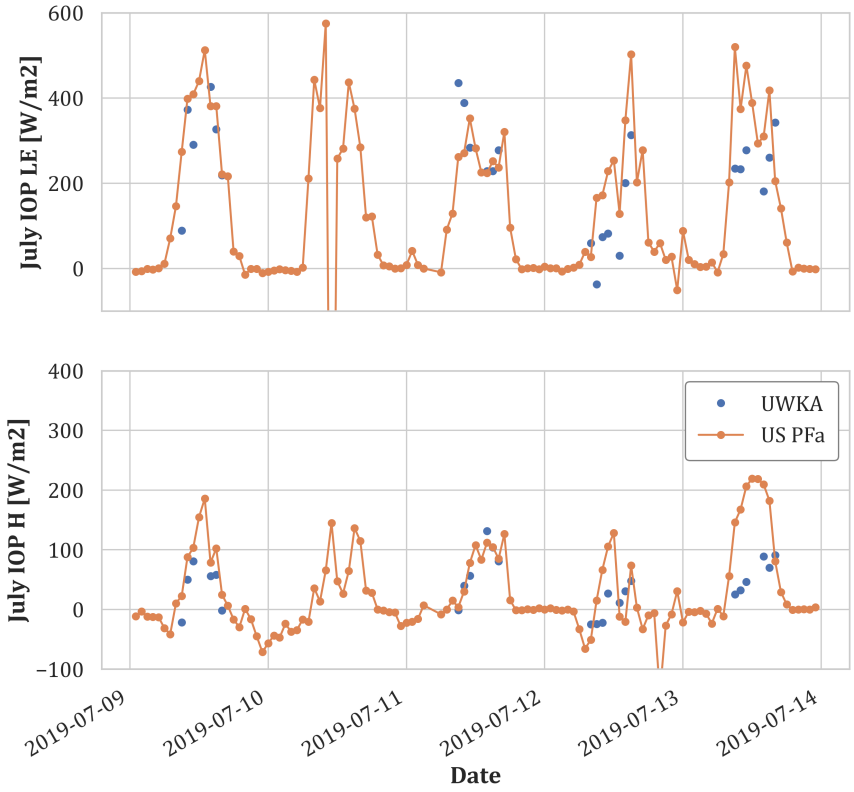

FIGURE 2.20: Hourly flux measurements from the UWKA flights and the 122 m tower measurements from the Ameriflux regional tall tower, US Pfa, at the center of the study domain. Data shown for the July IOP. The UWKA flux space series was averaged to hourly data points to match the hourly time resolution of the tower measurements.

reliable flux data at 122 m height during the August and September IOPs but the comparisons for the July IOP is presented in Figure 2.20. US PFa makes hourly flux measurements and at 122 m measurement height has a much broader flux footprint than the CHEESEHEAD19 flux towers, with maximum measurement height at 32 m. Here, the wavelet analysis based airborne fluxes compare reasonably well with the tall tower flux measurements made over a 1 hour averaging window that could include landscape level fluxes.

We tried to extend this approach by comparing total (H+LE) footprint weighted flux measurements from the flux topographies to the total flux measured by the NCAR-ISFS towers in the domain. The flux topographies calculated present a direct and physics-based flux map over the domain for the research flights analysed, providing a scale-resolved spatial distribution of sensible and latent heat fluxes. They show persistent areas of large scale flux contributions within the study domain which could be linked to variations of land–surface properties. However, they are also inherently limited by the foot prints of airborne transects and can only be extrapolated within those flight transect footprints. Flux measurement in space from the topography was matched with the flux measurement from the tower located in the same 100×100 grid point in space and corresponding to the same time as the UWKA data sample. However, for all case studies conducted with six research flights over three days in the three IOPs (July 11, August 21 and September 24) the scatter plots between fluxes values from the topography grid and the tower measured values did not show any clear relationships. This could be because of the vertical flux divergences between the tower measurement heights and the 100m aircraft measurement height, random errors of tower and flux measurements compounding each other etc.

One should be careful while interpreting footprint weighted flux maps to study surface-atmospheric transport. The experimental design introduces a temporal element to the topographies calculated in this study. Even though spatially adjacent flight transects during a single flight are only about 6-8 minutes apart , a research flight across the domain takes about 2.5 hours, imprinting the diel pattern to a calculated flux topography. Kohnert et al. (2017) and Rey-Sanchez et al. (2022) present flux map based approaches to detecting methane hotspots from aircraft and tower measurements, respectively. Unlike methane fluxes, surface heat fluxes have a strong diurnal

cycle. Hence, attributing sources for the fluxes solely based on aircraft measured flux topography maps and linking the horizontal flux gradients and surface gradients can be complicated. This presents impactful opportunities to parsimoniously combine aircraft and tower data, when available as is the case for the CHEESEHEAD19 experiment, to arrive at a space-time aligned view of surface fluxes. The airborne campaign numerical experiment design involved calculating space and time resolved flux maps across the domain from simulated tower and aircraft data (from candidate flight patterns) using a machine learning approach with the land–surface properties as drivers (Figure 12 in Metzger et al. (2021)).

2.5 Conclusions

We present a systematic regional-scale observational analysis over a heterogeneous domain that quantifies the multi-scale nature of sub-grid scaling and patterning. The CHEESEHEAD19 field experiment provided a unique dataset to diagnose and quantify the diel and seasonal contributions from large scale transport over the study domain as its surface energy balance shifts from a more latent heat flux-dominated late summer landscape to a more sensible heat flux-dominated early autumn landscape.

Using airborne measurements from this comprehensive field experiment dataset we sought to answer whether spatially resolved airborne eddy covariance can identify spatial scales of surface-atmosphere fluxes over heterogeneous surfaces? Applying wavelet analysis to the airborne flux measurements from the field experiment data allowed us to evaluate and spatially resolve the mesoscale contributions at 100 metres above ground over the heterogeneous landscape. The measured heat fluxes were partitioned into turbulent and mesoscale contributions based on a 2000 m fixed threshold, serving as a proxy for the ABL height, the largest possible length scales

for turbulent eddies in the ABL. Although this is supported by the measured observations of ABL heights (Figure 2.7) and previous studies (Strunin and Hiyama, 2004; Mauder et al., 2007a), the average flux distribution by scale showed no clear evidence of a particular pattern changing around that scale, especially in the August and September IOPs (Figure 2.5). We looked at the diel and seasonal variability of the scale-resolved fluxes. The measured latent heat flux magnitudes had more pronounced seasonal changes than the sensible heat fluxes. Meanwhile, the measured domain-averaged sensible heat flux values had a more pronounced diurnal cycle. We observed larger mesoscale transport for sensible heat fluxes in convectively driven ABLs across the three IOP scenarios, while for latent heat fluxes only the July and August IOPs showed more fractional mesoscale transport in convectively driven ABLs. For the September IOP, which had mostly shear driven ABL cases, we did not find any significant change between the fractional mesoscale transport in convectively and shear driven ABLs. We hypothesise that the larger scale transport measured in our study could be linked to organised structures in the ABL as has been reported in previous numerical (Kanda et al., 2004; Inagaki et al., 2006; Salesky and Anderson, 2020; Margairaz et al., 2020) and observational (Lemone, 1973; Eder et al., 2015; Morrison et al., 2021) studies. The flux topography case studies indicate that the mesoscale transport spatial variability would be missed by tower measurements in the domain. Areas of persistent contributions in the domain could be linked to the presence of co-located forested wetlands, creating roughness and thermal surface heterogeneities.

From our observations and analyses we reject our null hypothesis that the mesoscale transport is an invariant, small fixed fraction of total flux. We conclude that our alternate hypothesis, persistent contributions of larger scale (meso-β to meso-γ) fluxes to the daytime sensible and latent

heat fluxes exist with diurnal and seasonal variations, holds. We report substantial dissimilarities between the sensible and latent heat flux transport suggesting different physical mechanisms under play, warranting further investigations. The analysis helps further our understanding of the interactions between surface spatial heterogeneity and lower atmosphere feed-backs. Measurements of flux contributions over heterogeneous landscapes have not been studied well. In particular the shifts associated with seasonal, landscape level transitions as is covered in this study. We believe that this study, by highlighting the importance of larger-scale sub-grid transport, adds a critical piece of information in assimilating and integrating observations and model outputs at multiple scales.

2.6 Open Research

All of the CHEESEHEAD19 observations including UWKA airborne measurements are archived at the NCAR EOL repository at https://www.eol.ucar.edu/field_projects/cheesehead

The eddy4R v.0.2.0 software framework used to generate eddy-covariance flux estimates can be freely accessed at https://github.com/NEONScience/eddy4R. The eddy4R turbulence v0.0.16 and Environmental Response Functions v0.0.5 software modules for advanced airborne data processing were accessed under Terms of Use for this study (https://www.eol.ucar.edu/content/cheesehead-code-policy-appendix) and are available upon request. The current version of the production code is hosted following a development and systems operation (DevOps) framework for collaborative software development. The DevOps framework allows for a portable, reproducible and extensible EC processing software capabilities that are modular and version controlled using GitHub. The code base is maintained as Docker images to preserve the same dependencies and ensure reproducibility and portability across platforms.

Pre-processed input data for the Eddy4R flux processing routines and the calculated scale-resolved fluxes are available at the Ecometeorology lab UW server at http://co2.aos.wisc.edu/data/CHEESEHEAD-incoming/uwka_waveletfluxes/. The python code used to create figures for the manuscript is available at https://github.com/sreenathpaleri/CHEESEHEAD/blob/analysis/scripts/UWKA/manuscript/plot_MS.py

Acknowledgments

This material is based in part upon work supported by the National Science Foundation through the CHEESEHEAD19 project (grant no. AGS-1822420) and the NEON Program (grant no. DBI-0752017). The National Ecological Observatory Network is a program sponsored by the National Science Foundation and operated under cooperative agreement by Battelle. Brian Butterworth was additionally supported by the NOAA Physical Sciences Laboratory. Katrin Kohnert and Andrei Serafimovich were supported by the Helmholtz Association of German Research Centres through a Helmholtz Young Investigators Group grant (grant VH-NG-821) and by the European Union's Horizon 2020 research and innovation program under grant agreement No 72789. We also recognize that our field research occurs on the traditional territories of the Ojibwe people, which have been unjustly ceded and whose ancestors were the original scientists and naturalists who stewarded the land, air, and waters we are fortunate to observe, reflect, and hopefully help continue to flourish.

Supplementary Information

TABLE 2.3: IOP averaged scale-resolved heat fluxes. RMS error values scaled by $\sqrt{N_{samples}}$

IOP	Total LE	Total H	Turb. LE	Meso. LE	Turb. H	Meso. H
July	179.98 ± 4.78	88.31 ± 0.94	123.07 ± 2.40	56.92 ± 4.14	71.25 ± 0.74	17.05 ± 0.58
Aug.	256.44 ±2.92	88.04 ± 1.02	210.28 ± 2.38	46.16 ± 1.69	68.02 ± 0.78	20.01 ± 0.66
Sep.	69.01 ± 2.86	89.13 ± 1.13	49.36 ± 1.87	19.65 ± 2.17	76.36 ± 0.78	12.77 ± 0.81

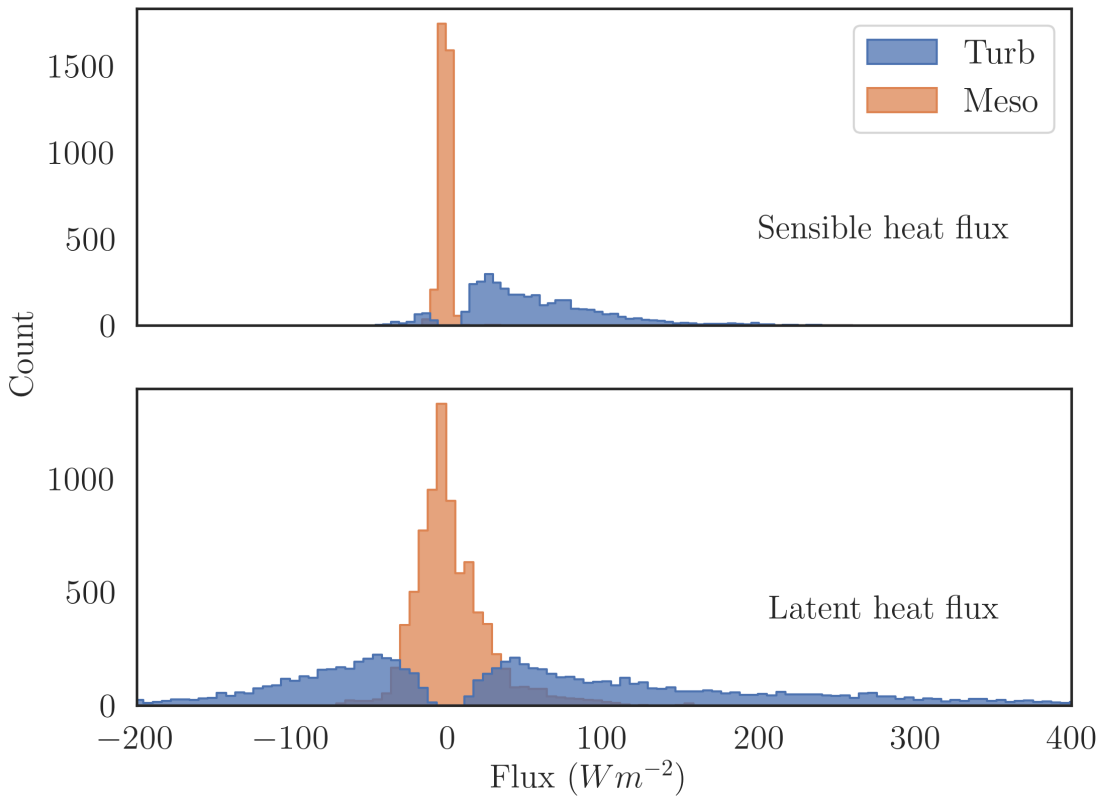

FIGURE 2.21: Histograms of turbulent and mesoscale fluxes for cases when the measured mesoscale fractions are lesser than 0

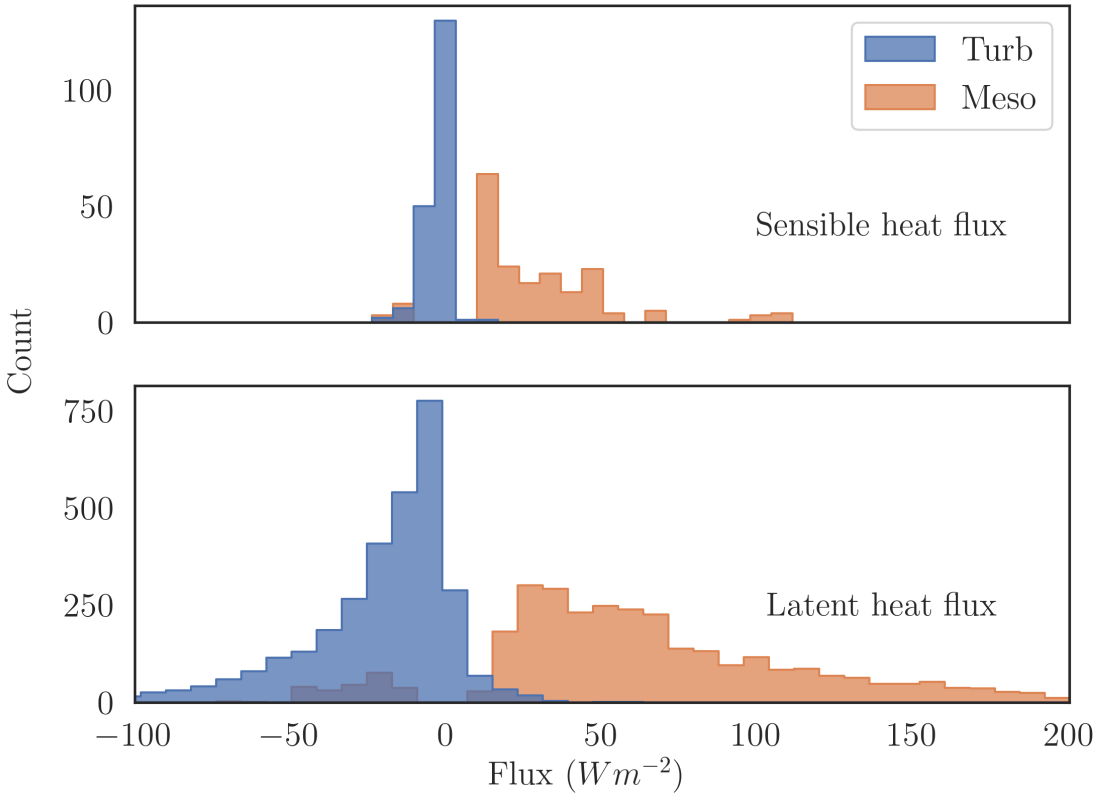

FIGURE 2.22: Histograms of turbulent and mesoscale fluxes for cases when the measured mesoscale fractions are greater than 1

Chapter 3

Simulating surface heterogeneity effects and diurnal evolution of late summer and early autumn atmospheric boundary layers during the CHEESEHEAD19 field campaign

S. Paleri, L. Wanner, M. Sühring, A. Desai, M. Mauder[1]

[1]This chapter is a draft of an article, Surface heterogeneity induced effects on the diurnally evolving convective boundary layer from coupled large eddy simulations of the CHEESEHEAD19 field campaign - Part I, to be submitted to *Boundary Layer Meteorology*

3.1 Introduction

Heterogeneity is pervasive over land surfaces. Land surface properties can vary at multiple scales, with simultaneous variations of multiple properties at multiple scales (Paleri et al., 2022; Desai et al., 2022b; Paleri et al., 2023). This phenomenon means that atmospheric boundary layer (ABL) flow can be perturbed not just at one specific length or time scale but at multiple scales, which excites physical processes such as advection, secondary circulations, and non-equilibrium turbulence (Bou-Zeid et al., 2020). Further, the issue of land surface heterogeneity is fundamentally an issue of scale as well (Mahrt, 2000; Bou-Zeid et al., 2020) that is coupled to local biogeophysical processes as well as larger scale synoptic circulations. As pointed out in Chapter 2, Section 2.1, observing and quantifying these interactions and their role in ABL development, cloud processes etc calls for space and scale intensive deployments seldom seen in micrometeorological field experiments. Observational studies and large eddy simulations to understand the interactions between landscape heterogeneities and secondary circulations in the ABL have been limited in their ability to capture these events and robustly test hypotheses.

There have not been a lot of modelling studies exploring the surface-atmospheric coupling in a diurnally evolving boundary layer over realistic, irregular heterogeneities. Huang and Margulis (2010) performed a 12 hour daytime LES of the Convective Boundary Layer (CBL) for the Soil Moisture–Atmosphere Coupling Experiment 2002 and evaluated the simulations against experimental measurements. Their results showed up to 18% errors in surface sensible heat fluxes when surface-atmospheric coupling is ignored. In their LES investigation of the diurnal ABL for the Horizontal Array Turbulence Study (HATS) field experiment using prescribed and homogeneous surface fluxes Kumar et al. (2006) found that local scaling approaches were

appropriate to describe the free convective and transitioning ABL. LeMone et al. (2010a,b) performed simulations of CBL conditions from the 2002 International H2O Project (IHOP 2002) using the advanced research version of the Weather Research and Forecasting model (WRF-ARW) coupled to the Noah land surface model. Their simulations were able to capture mesoscale circulations during clear sky days ($\sim$ 1 - 10 km) consistent with aircraft measurements. Maronga and Raasch (2013b) (hereafter referred to as MR13) investigated the role of irregular and multi scale surface heterogeneities on the ABL using LESs of the Lindenberg Inhomogeneous Terrain Fluxes between Atmosphere and Surface - 2003 field experiment days using the PArallelized LES Model (PALM). They used prescribed surface fluxes, prepared from eddy covariance tower measurements and land surface class distributions within their 20 km $\times$ 20 km study area with cyclic boundary conditions and a range of imposed geostrophic winds (2, 3, 4, 6 m s^{-1}). Using time-ensemble averaging of their 3D LES data, they diagnose signals of surface heterogeneity induced secondary circulations, that were roll-like and aligned along the mean wind for strong mean winds and localised for CBL with weaker horizontal winds.

The PALM model system (Maronga et al., 2020a) has since been widely used to study the relationship between land surface heterogeneities and secondary circulations in the ABL (Kanani-Sühring and Raasch, 2017; Gronemeier et al., 2017; Kröniger et al., 2018; De Roo and Mauder, 2018b; Xu et al., 2020; Akinlabi et al., 2022).

As a first step towards understanding the diurnal evolution of surface heterogeneity induced coherent structures in the ABL, we present and evaluate the CHEESEHEAD19 LES framework. We use information about real world surface heterogeneity over the predominantly forested study domain, with multiple scales of variability in surface properties, and mesoscale forcings during the field experiment, to simulate diurnal cycles of two days during the IOPs of the field

campaign. The days chosen are two days in late summer and two days in autumn. This design helps us to capture the shift in the surface energy budget partitioning of the study domain as it shifts from a latent heat flux dominated, free convective boundary layer in the summer to a forced convective boundary layer in autumn with lower Bowen ratios (as reported from aircraft measurements in Paleri et al. (2022) and tower measurements in Butterworth et al. (2021)).

We hypothesise that large eddy simulations, initialised with realistic surface heterogeneity, develop similar mesoscale structures and patterns as observed in reality. Following through, we ask, can such a LES be used to evaluate mechanisms that generate surface-heterogeneity induced mesoscale circulations in the diel ABL ? This Chapter is organised as follows: Section 3.2 briefly describes the field measurements used to inform the LES setup, then goes into the description of the LES modules setup. The simulation results are discussed in Section 3.3 and a summary and outlook for future studies and the Chapter 4 are presented in Section 3.4.

3.2 Methods

3.2.1 Field Experiment Data

3.2.1.1 Radiosonde Measurements

During the IOPs, atmospheric profiling was performed by the National Center for Atmospheric Research (NCAR) Earth Observing Laboratory (EOL) Integrated Sounding System (ISS) and the University of Wisconsin – Madison Space Science and Engineering Center Portable Atmospheric Research Center (SPARC) using the Vaisala RS41-SGP radiosondes. The data was processed by the Vaisala MW41 sounding system and the quality controlled data is hosted at the NCAR EOL CHEESEHEAD19 repository (Facility and , SSEC) During the IOP days there

were 4 radisonde launches per day. On 23 August these were at 0610, 0915, 1300 and 1645 CDT. On 24 September the launches were at 0615, 0913, 1300 and 1645 CDT. The radiosonde profile data were linearly interpolated to the Child01 model vertical grid for inter-comparisons.

3.2.1.2 Tower and Plot-Level Measurements

The EC tower data used in this study was collected from 17 flux tower sites, set up as part of the National Center for Atmospheric Research (NCAR)-Integrated Surface Flux Station (ISFS) network, and the AmeriFlux US-PFa site within the core 10 km $\times$ 10 km CHEESEHEAD19 study domain (Fig. 3b and Table ES2 in Butterworth et al. 2021). Ground based measurements of forest canopy leaf phenology were done at 51 plots within the domain (Schwartz, M.D et al. 2019). The tower network collected measurements of 3D-wind, temperature, moisture and CO_2 at 20 Hz using the Campbell Scientific CSAT3AW sonic anemometer and the open path Campbell Scientific EC150 infra-red gas analyser. The processed and quality controlled 30-minute flux data are hosted in the AmeriFlux repository. Drone-based LiDAR measurements were performed at 9 select forested flux tower sites to characterise the three-dimensional forest structure (Table 1 in Murphy et al. 2022). The measurements were made from 25-29 June 2019, at 60 m above ground using a Routescene discrete-return LiDAR onboard a UAS hexacopter DJI M600 Pro to collect high-density 3D scans ($\sim$ 600 points m^{-2}).

3.2.2 Large Eddy Simulations Model Setup

We used the PArallelized LES Model (PALM) V 6.0 (Maronga et al., 2020b) revision number 21.10-rc.2 for the numerical simulations. PALM solves the non-hydrostatic, filtered, incompressible Navier-Stokes equations in Boussinesq-approximated form on an Arakawa staggered

C-grid (Harlow and Welch, 1965; Arakawa and Lamb, 1977). Prognostic equations are solved for the velocity components u, v, w, the potential temperature θ, water vapour mixing ratio q, a passive scalar s and the subgrid-scale turbulent kinetic energy (SGS-TKE) e . The sub-grid scale terms are parameterised using the 1.5 order turbulent kinetic energy scheme of Deardorff (1980) modified by Moeng and Wyngaard (1988) and Saiki et al. (2000). The advection terms were discretised using a fifth-order scheme (Wicker and Skamarock, 2002), and a third-order Runge–Kutta scheme by Williamson (1980) was used for the time integration.

The dynamical core of the model system and additional modules that enable modelling capabilities for diel surface-atmospheric exchanges over realistic surface have been extensively validated (Heinze et al., 2017; Resler et al., 2020; Gronemeier et al., 2021). Resler et al. (2020) presents a validation of PALM simulations, constrained by field measurements and boundary conditions driven by WRF outputs of the diel boundary layer over Prague, Czech Republic. Wanner et al. (2021) did a comparative simulation study using PALM, with varying surface boundary conditions that included prescribed surface fluxes, a coupled LSM and a coupled LSM combined with a Plant Canopy Model. Based on their idealised simulation results, they recommend the used of a LSM combined with a PCM as the surface boundary condition to better represent the near-surface dispersive fluxes associated with secondary circulations.

Simulations of the diurnal cycle for two consecutive CHEESEHEAD19 IOP days during the summer and autumn IOPs were performed. August 22 and 23 were chosen for the August IOP and September 24 and 25 for the September IOP. During the August IOP, towards the end of summer, the CHEESEHEAD19 experimental conditions were more free convective than during the September IOP, when they were more forced convective (Paleri et al., 2022). So choosing

these two test cases lets us compare and contrast the secondary circulations between two different dynamic stability regimes. Eight ensemble member runs were performed for each of the IOP test cases. At the start of each ensemble member model run, the imposed perturbations by the synthetic turbulence generator (Sect. 3.2.2.1) are randomly generated and thus different, which in turns produces a unique turbulence realisation for each ensemble member. The maximum model timestep was kept fixed at 0.6 s. The simulations were performed in the NCAR Cheyenne supercomputer (Computational and Laboratory, 2017) and the Casper data analysis and visualisation cluster was used for 3D visualisations and exploratory data analysis. A total of 6,500,000 core hours were used for the production runs.

3.2.2.1 Large Scale Forcing, Boundary Conditions:

In order to simulate the diurnal variations during the field experiment, with evolving synoptic conditions over a heterogeneous study domain, non-stationary lateral and top boundary Dirichlet conditions were prescribed for the simulations using an offline-nesting approach (Kadasch et al., 2021). The large scale forcing data for the boundary conditions were prepared using the National Centers for Environmental Prediction - High Resolution Rapid Refresh (NCEP-HRRRv4) version of the Weather Research and Forecasting - Advanced Research WRF (WRF-ARW) model (Benjamin et al., 2016) with a native resolution of 3 $\times$ 3 km. 2D surface and 3D isobaric data were extracted from the University of Utah HRRR archive (Blaylock et al., 2017). The HRRR data was extracted over the 49 $\times$ 50 km Parent simulation domain (Sect. 3.2.2.2) and averaged horizontally to 1D profile data. The isobaric HRRR data were interpolated to the PALM model grid by adapting the open-source WRF4PALM v1.0 code (Lin et al., 2021). These profiles are prescribed at the model lateral and top boundaries as non-cyclic conditions,

refreshed every hour. The forcing-profiles are read and mapped onto the boundaries during the simulation as well as interpolated linearly in time. A Synthetic Turbulence Generator (STG) module was used to impose turbulent fluctuations at the model boundaries in conjunction with the mesoscale forcings since the imposed boundary conditions do not have information about boundary layer turbulence. Kadasch et al. (2020) give a detailed description of PALM's internal routines which read and process the initial and boundary conditions as well as the STG. Turbulence is triggered at the model lateral boundaries by imposing spatial and time varying perturbations to the velocity components with characteristic amplitude depending on the Reynolds stress tensor following Xie and Castro (2008), as modified by Kim et al. (2013) and the Reynolds stress parameterisation of Rotach et al. (1996).

With regard to surface forcings, the initial surface soil temperature and moisture values were extracted from the HRRR data and regridded to match the Parent domain horizontal grid. The Parent domain mean surface incoming shortwave and longwave radiation values were also prescribed using the same data. The incoming radiative fluxes are passed to PALM's Radiative Transfer Model to model the influences of the heterogeneous plant canopy and high clouds on surface radiative fluxes (Krč et al., 2021). PALM can support nested LES domains that are recursively nested within and run parallel to each other with continuous communication at run time through its self-nesting capabilities (Hellsten et al., 2020). Self-nesting was applied in combination with the offline-nesting, with the outermost Parent model receiving input from the larger-scale model and two children (Child01 and Child02, 3.1, Sect. 3.2.2.2) recursively nested within the outermost Parent model (Fig. 3.1). In this setup, only the outermost Parent model requires the initialisation and boundary data from the larger-scale model. One-way nesting was employed between the three models, where only the parent communicates with its immediate

child at the model lateral and top boundaries at every time step and child model solutions do not affect flow in its Parent model. Employing both the offline-nesting and self-nesting modules lets us include the synoptic-scale effects over the simulation domain and model the influence of a heterogeneous land surface and plant canopy over a wide range of scales.

3.2.2.2 Domain Resolutions And Nesting Setup

A rather coarse Parent domain covering a 48.6×52 km^2 region, centred around the Department Of Energy Ameriflux regional tall tower (US-PFa 45.9459° N, −90.2723° W, Desai et al. (2022a)) was set up with a horizontal resolution of 90 m to guarantee that turbulence is fully developed in the area of interest. Since the large-scale forcing data does not have resolved turbulence, adjustment zones are needed to allow for turbulence development at the inflow boundary so that realistic turbulence is simulated within the domain of interest. Initial test simulations were done for just the Parent domain and the e horizontal profiles from these simulations show that turbulent flow is well developed after about 10 km downstream of the inflow boundary (Fig. 3.12). At 1100 hours simulation time the boundary layer is still in a transition phase from stable to convective conditions so that the horizontal e profile shows variations, but at 1300 hours and 1500 hours it clearly shows an equilibrium value. Hence, the Child01 domain was set up covering a 27×32 km^2 region inside the parent domain, ensuring that the domain is sufficiently far away from the inflow boundaries. This Child01 domain also covers the greater-CHEESEHEAD19 study domain where airborne turbulence measurements were conducted during the IOPs. Inside the Child01 domain, a fine resolution Child02 model was set up, with 12×12 km ^{2} horizontal extent, covering the core CHEESEHEAD19 experiment study area (Fig. 3.1).

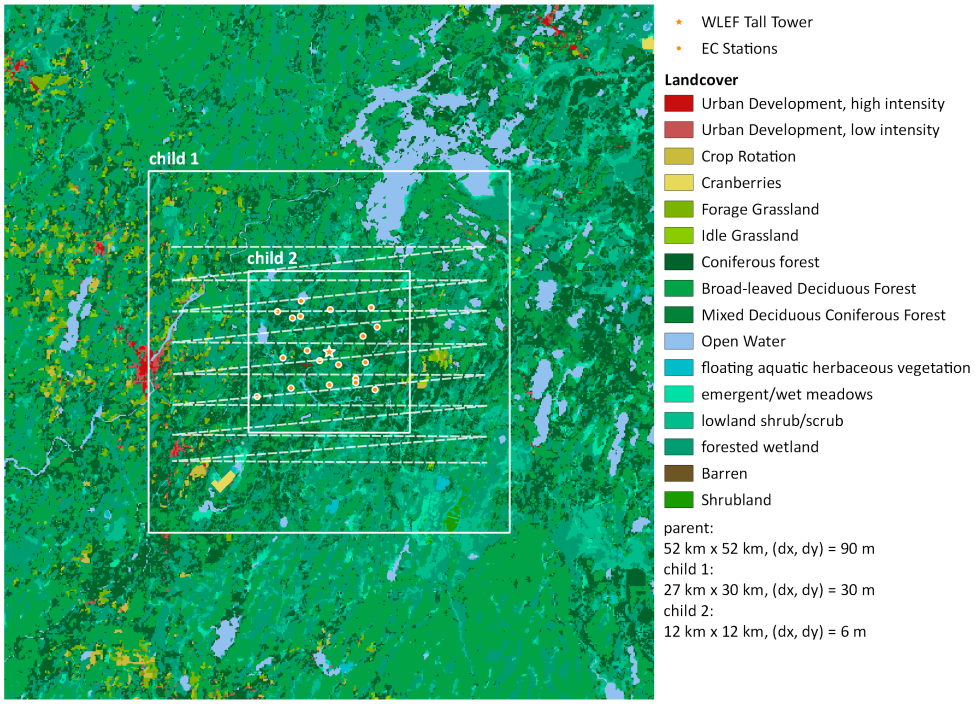

FIGURE 3.1: Land surface class distribution within the Parent model. Child01 model is shown as a 27 × 30 km^2 box outlined in white. Child02 model domain is shown as a white outlined 12 × 12 km^2 box within Child01. The orange dots within Child02 denote the CHEESEHEAD19 tower locations. The orange star indicates the location of the US-PFa tall tower. The dotted white line over Child02 is a representative virtual flight pattern which was set up in Child01. Map credit Luise Wanner

Simulations for the August IOP days start at 0000 Central Daylight Time (CDT = UTC - 6h, abbreviated as CDT from now) 22 August 2019 and go on for 44 hours till 2000 CDT on 23 August 2019. Likewise, simulations for the September IOP days start at 0000 23 September 2019 CDT and go on for 44 hours till 2000 CDT on 24 September 2019. Table 3.1 gives an overview of the model resolutions used for the August and September IOP simulations. The horizontal extents were kept the same for both the IOP test cases and all 3 nested models. Parent model vertical extents were changed between the two IOP cases reflecting the change in the maximum boundary layer heights between the summer and autumn IOP while optimising

the available computational resources and ensuring that all of the ABL was included in the simulations. For the August IOP runs, the Parent model vertical extent was fixed at 5000 m, with vertical grid stretching starting at 3000 m to optimise computational resources, with the maximum vertical grid spacing set to 60 m. The Parent model domain for the September IOP runs had a vertical domain extent of 3050 m, with grid stretching starting at 1800 m and the maximum vertical grid spacing set again to 60 m. In the Child01 model domain, the vertical model extent was set to ensure that at least one of the IOP days simulated would have a fully resolved CBL. In this manuscript we focus on 3D data from the Child01 model, for August 23 and September 24 when the model domain encompassed the whole of CBL (Sect. 3.3.1). The Child02 model domain has a vertical extent of 240 m for both the IOP test cases. Its horizontal resolution of 6 m and a vertical resolution of 4 m allows us to have a resolved plant canopy in this finer resolution domain.

TABLE 3.1: Grid resolution and domain extents for both August and September IOP test cases

Simulation time (CDT)		Domain	Horizontal extent (km)	Vertical extent (km)	Grid spacing (m)	Grid points
Start	End					
08.22|00:00	08.23|20:00	parent	lx = 48.6, ly = 51.84	lz = 5.0	dx = dy = 90, dz = 12	nx = 540, ny = 576, nz = 296
		child1	lx = 27, ly = 30.240	lz =2.49	dx = dy = 30, dz = 12	nx = 900, ny = 1008, nz = 248
		child2	lx = ly =12	lz = 0.24	dx = dy = 6, dy = 4	nx = ny = 2000, nz = 60
09.24|00:00	09.25|20:00	parent	lx = 48.6, ly = 51.84	lz = 3.05	dx = dy = 90, dz = 12	nx = 540, ny = 576, nz = 180
		child1	lx = 27, ly = 30.240	lz =1.8	dx = dy = 30, dz = 12	nx = 900, ny = 1008, nz = 148
		child2	lx = ly =12	lz = 0.24	dx = dy = 6, dy = 4	nx = ny = 2000, nz = 60

3.2.2.3 Land Surface and Plant Canopy Model

TABLE 3.2: Wiscland land surface classes and their assigned PALM LSM classes

Wiscland Land surface type	PALM Surface Type
Open Water	lake
Floating Aquatic Herbaceous Vegetation	lake
Developed, High intensity	concrete
Developed, Low intensity	asphalt/concrete mix
Barren	bare soil
Crop Rotation	crops, mixed farming
Cranberries	irrigated crops
Grassland	tall grass
Emergent/Wet Meadow	tall grass
Shrubland	deciduous shrubs
Lowland Scrub/Shrub	deciduous shrubs
Coniferous Forest	short grass†
Coniferous Forested Wetland	short grass†
Broad-leaved Deciduous Forest	short grass†
Forested Wetland - Deciduous Forest	short grass†
Mixed Deciduous/Coniferous Forest	short grass†
Mixed Deciduous/Coniferous Forested Wetland	short grass†

†To avoid double-accounting for surface radiative effects of the canopy, the forested domains are assigned 'short-grass' classes in the LSM setup

To accurately simulate the physical processes as observed during the IOPs as realistic as possible, we apply a Land Surface Model (LSM) with coupled soil, radiative transfer and a Plant Canopy Model (PCM). The use of the LSM and PCM runs instead of prescribed surface fluxes enables the investigation of surface atmospheric feedback such as self-reinforcement of mesoscale circulations over the heterogeneous study domain (Wanner et al., 2021). This offers a direct interaction with the synoptic and radiative forcing.

The inbuilt LSM implementation is based on the European Centre for Medium-Range Weather Forecasts-Integrated Forecast System (ECMWF-IFS) land surface parameterisation (H-TESSEL) and its adaptation in the Dutch Atmospheric LES model (Heus et al., 2010). Gehrke et al. (2020) presents a detailed description of the LSM implementation in PALM (Their Table 1, 2 and 3 give a detailed description of PALM's land surface classes) and presents evaluations against in-situ measurements. The same soil type was used for the entire domain. We used a 'medium fine' texture following the ECMWF-IFS classification that is based on the parameterisation after Van Genuchten (1980). The soil model was configured as an eight layer model. Having a thin

soil layer can lead to unrealistic high-frequency feedback effects with near surface atmospheric temperature and moisture (Liu and Shao, 2013). Each layer thickness in metres starting from top was set as: 0.01, 0.02, 0.04, 0.06, 0.14, 0.26, 0.54 and 1.86. The 2D initial and deep soil temperatures and initial soil moisture was taken from the HRRR data (Sect. 3.2.2.1). The distribution of different land cover types within the domain is based on the Wiscland 2.0 digital database (Wisconsin Department of Natural Resources, Fig. 3.1) which is a land cover map of the entire state of Wisconsin with a resolution of 30 m and providing multiple levels of detail. The data was collected from 2014 to 2016. Wiscland2 landcover types were grouped into 18 categories (Table 3.2)

Before the simulations start we used a 44 hour spin up for the LSM where only the surface-soil model is updated (based on the HRRR data), while the wind speed is held constant at its initial time and temperature experiences the daily cycle. This allows for the near surface soil moisture and temperature values and atmospheric values to come to an equilibrium, which would be important over the heterogeneous domain as shown by Maronga et al. (2020b).

The plant canopy is modelled as a porous viscous medium that removes momentum from the flow (Shaw and Schumann, 1992; Watanabe, 2004), and acts as source/sink for heat, humidity, or passive scalar. We use the land-surface model at the surface of the entire domain and stack the plant canopy model on top in areas covered by trees. †To avoid double-accounting for surface radiative effects of the canopy, the forested domains are assigned 'short-grass' classes in the LSM setup. The forested areas are vertically resolved by up to 12 grid layers in the Child02 domain and up to 5 grid layers in the Parent and Child01 domains. The leaf-area density (LAD) profiles are based on field observations at 9 forested sites within the CHEESEHEAD19 study area (Sect. 3.2.1.2). We grouped these observations into broadleaf, needle leaf and mixed

forests. Within each group, the LAD profiles were averaged and extrapolated toward the ground since no measurements were available near the surface. These profiles are shown in Fig. 3.2 a, b, c. The profiles were then scaled in height so that they correspond to the mean canopy heights that were found near the eddy covariance stations within the individual forest types and finally resampled to the PALM grid spacing. The resulting lad profiles are shown in Fig. 3.3.

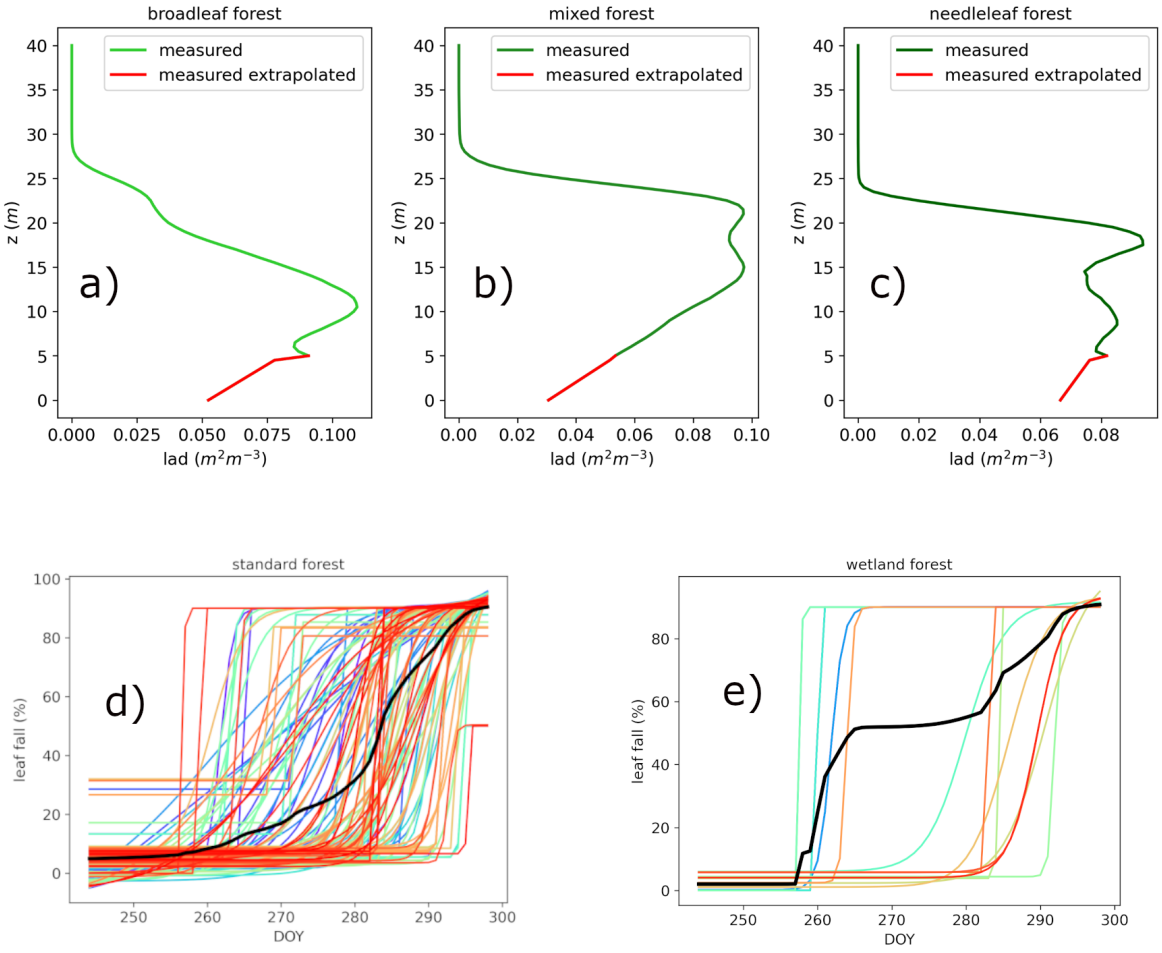

FIGURE 3.2: Drone measured LAD profiles classified as a) broadleaf, b) needle leaf, and c) mixed forests. Profiles were linearly extrapolated from the lowest measurement value towards the surface. Measured leaf fall percentage for a standard (e) and wetland (e) forest in the study domain. Different colours indicate individual measurements and the black line indicates the mean across trees

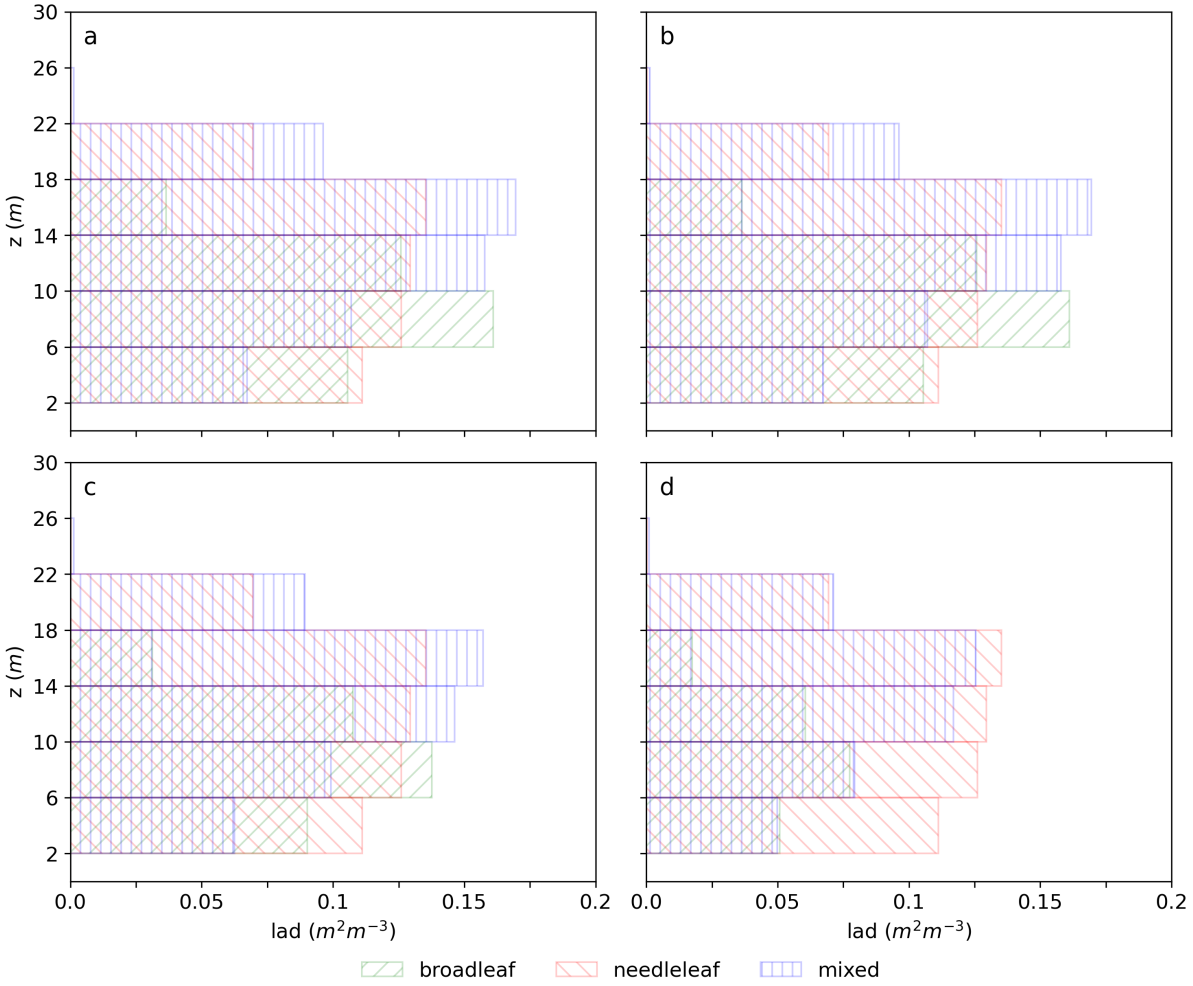

FIGURE 3.3: Scaled and resampled profiles used in the Child02 domain. Panels a and b show lad profiles for the August IOP and panels c and d show profiles for the September IOP. Panels a and c show profiles for normal forests and panels b and d show panels for wetland forests

To adapt the LAD profiles to seasonal changes in leaf-area index (LAI), we used phenological observations of leaf fall that were also carried out at different plots within the CHEESEHEAD19 field sites to scale the LAD profiles. A sigmoid curve was fitted to the leaf fall observations of each single tree. Afterwards, we grouped the plots into wetland and non-wetland plots and averaged the fitted sigmoid curves of all trees within each group as shown in Fig. 3.2 d, e. The resulting curves provide the percentage of fallen leaves. We then multiplied the LAD profiles in

deciduous forest areas with the percentage of remaining leaves. For the mixed forest areas, we assumed that the reduction in LAI would be half that of the deciduous forest. This approach resulted in three different LAD profiles for the August IOP simulations before the beginning of leaf fall (broadleaf, needle leaf, mixed) as shown in Fig. 3.3 a, b, and five LAD profiles for the September IOP simulations after the beginning of leaf fall (broadleaf, wetland broadleaf, mixed, wetland mixed, needle leaf) that are shown in Fig. 3.3 c,d. The LAD profiles were then assigned to different WISCLAND 2.0 land cover types (Table 3.2).

Virtual tower measurements are conducted in the Child02 domain to be compared to actual field measurements at the EC stations. To create model conditions that are as similar as possible, the high-resolution profiles at these locations were not adjusted to the mean value for the forest type, but were adjusted to the actual height of the vegetation at the respective station on a 100 $\times$ 100 m^2 area surrounding the virtual tower location.

3.2.2.4 Virtual observational Infrastructure

Virtual tower sites were set up in the Child02 model at the same location as the 17 CHEESEHEAD19 tower sites. The volume averaged turbulent time series data of u,v,w,θ,q were extracted at the model time step resolution at these locations. The data were extracted at vertical grid points corresponding to the field experiment tower measurement heights and also at one grid point offsets by north-south and east-west. The virtual tower data were switched on after 0500 CDT of the first simulation day to account for simulation spin up.

Virtual flight tracks emulating the IOP airborne campaign flight tracks were simulated in the Child01 model for both August and September test cases. Virtual flights are performed according to the methods described in Schröter et al. (2000) and Sühring and Raasch (2013). Virtual flights are effectively passive sensors that move along prescribed tracks, at prescribed heights with specific velocities. Flight heights were prescribed at 100 and 400 m a.g.l, and speed was kept fixed at 82.31 m s^{-1} reflecting the field experiment transects. Virtual flights start at a waypoint, matching the field experiment location in space, move to their ending waypoint and then start back once they reach the end point. All flight legs start simultaneously, at 0900 CDT of the first simulation day.

3.3 Comparisons of Simulations With Field Measurements

TABLE 3.3: Comparisons between simulated and measured profiles of θ, q and time series of θ,q, H and LE. Intensity of the red highlight denotes higher differences.

			θ (K)				q (g kg^{-1})				Daytime H (W m^{-2})	Daytime LE (W m^{-2})
Aug IOP	Time (CDT)		600	900	1300	1700	600	900	1300	1700		
	Profiles	Median of Absolute Difference	1.66	1.21	0.61	0.46	0.62	0.48	0.43	1.23		
		Mean Absolute Difference	1.47	1.3	1.04	1.27	0.96	0.87	0.76	1.05		
		RMSE	2.71	2.06	1.4	2.62	1.16	0.92	0.72	1.23		
	Time series	Correlation Coefficient	0.94				0.49				0.87	0.91
		RMSE	2.74 K				5.39 g kg^{-1}				48	60
Sep. IOP	Time (CDT)		0645	0915	1300	1645	0645	0915	1300	1645		
	Profiles	Median of Absolute Difference	1.45	1.66	1.58	0.38	1.29	1.19	0.55	1.52		
		Mean Absolute Difference	1.74	1.8	1.31	0.51	1.27	1.51	1.02	1.55		
		RMSE	2.08	2.13	1.45	0.63	1.48	1.82	1.59	1.64		
	Time series	Correlation Coefficient	0.88				0.96				0.87	0.86
		RMSE	2.8 K				7.19 g kg^{-1}				49	59

As a first order fidelity check of our simulations of the field experiment days, we compare LES profiles and near-surface fixed-point time series with the field measurements. For profile comparisons, we present results for 23 August 2019 and 24 September 2019, when all of the

CBL was fully resolved in the Child01 model in Sect. 3.3.1. For the August IOP simulation, instantaneous data were output at every 30 minutes and for the September IOP they were written out at every 15 minutes. For the profile comparisons, the LES data output closest in time with the radiosonde measurements were used. Some of the differences between the profiles can be attributed to this offset in time ($\sim$ couple of minutes). We compare the time series of *theta*, q, H and LE between the Child02 model and the CHEESEHEAD19 tower data. Table 3.3 presents summary statistics for the comparisons between simulated and measured profiles and time series data.. For the profile data mean, median and Root Mean Squared Error (RMSE) of the deviations are reported. For the time series comparisons, their Pearson's correlation coefficient (r) and RMSE are reported. Only the daytime values of the heat fluxes were used for the calculation of summary statistics. All time mentions that follow refer to the corresponding simulation time.

3.3.1 Temperature and Moisture Profiles

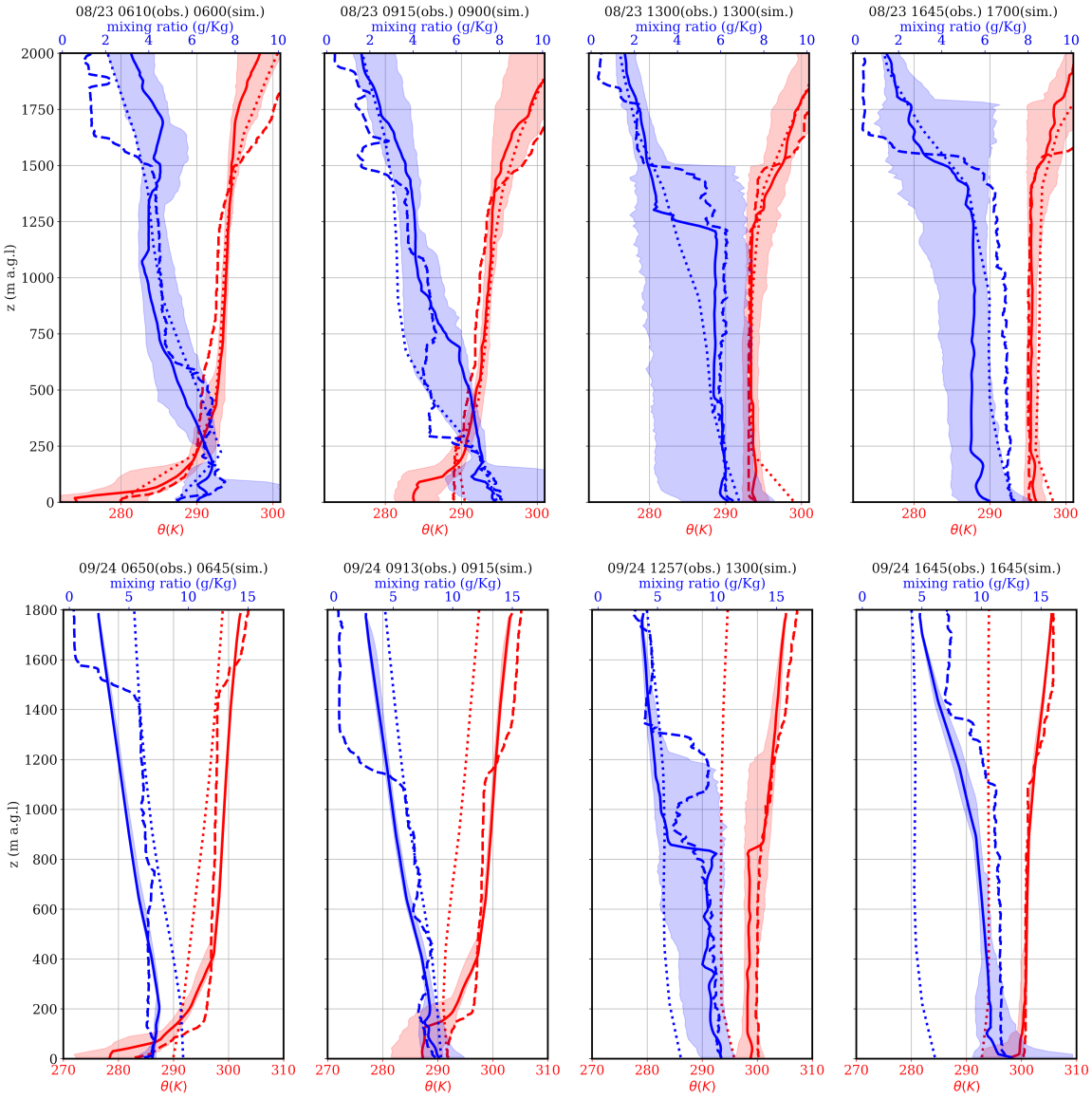

FIGURE 3.4: Comparisons between PALM simulated (solid lines) radiosonde measured (dashed lines) and HRRR (dotted lines) profiles of theta (red) and water vapour mixing ratio (blue) for August and September IOPs. The shading around each simulated profile indicates the minimum-maximum range at each vertical level in the LES.

Radiosondes were released during the field experiment close to the US-PFa tall tower. Instantaneous LES profiles were extracted from the Child01 domain, at the location of the US-PFa tall

tower. For both the August and September IOP simulations, PALM simulated early morning θ profiles show lower near surface temperatures than the radiosonde profiles (Fig. 3.4). In their diurnal simulations using PALM Resler et al. (2020) and Gehrke et al. (2020) reported lower than observed near surface night-time temperatures and a more stable ABL than observations. Gehrke et al. (2020) discusses this issue, suggesting the role of the SGS model and radiation scheme in combination with the grid resolution as well as the role of the LSM's surface energy balance parameterisation in combination with Monin-Obukhov Similarity Theory based computation of atmospheric fluxes at the first model grid point.

For the August IOP, the mean difference for the 1st 200 m between simulated and observed θ profiles at 0600 CDT simulation time is 2 K, with a peak of $\approx$ 6 K near the surface. At 0900 CDT, the mean difference for the 1st 200 m becomes 3 K and near the surface $\approx$ 5 K. Later during the day, the mean differences reduce substantially to 0.7 K at 1300 CDT and 0.6 K at 1700 CDT. Once the CBL is well mixed and fully developed in the afternoon, the simulations are able to capture the CBL height well. At 1300 CDT, $z_{i\,simulated} \approx$ 1300 m, while $z_{i\,observed} \approx$ 1500 m. The differences between $\theta_{simulated}$ and $\theta_{observed}$ profiles at 1300 and 1700 CDT of the simulations arise mainly from their differences above the CBL, where the LES profiles are closer to the HRRR forcing data (Fig. 3.4). At 1300, the mean absolute difference between the two below 1500 m is 0.5 K and at 1700 CDT the mean absolute difference between the two below 1500 m is 0.3 K. Amongst all the four times comparisons were made, the mean absolute difference and the RMSE are the lowest at 1300 CDT at 1.04 K and 1.4 K respectively (Table 3.3).

The $q_{simulated}$ profiles for the fully developed CBL at 1300 CDT on August 23 and the evening ABL at 1700 CDT follow radiosonde measured profiles of $q_{observed}$. For the 1300 CDT profiles,

the RMSE between the two is 0.72 g kg^{-1}, most of which occurs above the simulated CBL between 1250 and 1500 m where the simulated values are lower. At these heights, the radiosonde values are within the range of horizontal variability in $q_{simulated}$. The maximum horizontal variability in $q_{simulated}$ within the simulated CBL is also seen at 1300 CDT, with a mean range of 4 g kg^{-1}. At 1700 CDT the simulations are drier, with an RMSE of 1.23 g kg^{-1}.

The September IOP simulations show the same patterns as the August IOP simulations for $\theta_{simulated}$ and $q_{simulated}$ profiles while comparing them with the radiosonde measured profiles. The early morning near surface $\theta_{simulated}$ values are smaller, while the fully developed mixed layer values later agree well. The mean absolute difference for the 1st 200m between $\theta_{simulated}$ and $\theta_{observed}$ profiles at 0645 CDT is 4.2 K with a peak of 7.6 K at 30 m. At 0915 CDT the mean absolute difference for the 1st 200m between $\theta_{simulated}$ and $\theta_{observed}$ profiles is 4.25 K. At 1300 CDT $\theta_{simulated}$ and $\theta_{observed}$ have mean absolute difference and RMSE of 1.31 K and 1.45 K. At 1645 CDT they reduce to their lowest at 0.51 K and 0.63 K and remain nearly constant throughout the model vertical extent. The spatial variation of θ profiles inside Child01 model is lower for the September IOP simulations than the August IOP simulations. Most of the variation occurs in the 1st 100 m at 0645 CDT and 1645 CDT and within the 1st 200 m for 0915 CDT. The maximum spread is seen at 1300 CDT which $\approx$ 4 K.

The $q_{simulated}$ values for September IOP, correspond well with $q_{observed}$ during the morning hours at 0645 CDT and 0915 CDT. They diverge as higher up from the surface, above around 600 m. They follow the shape of the input HRRR forcing q profiles then. $q_{simulated}$ and $q_{observed}$ profiles at 1300 are very close to each other within the simulated CBL ($\approx 800m$) with a mean absolute difference of 0.39 g kg^{-1}. The radiosonde data shows an advection event centred around 1180 m which is not seen in the simulated profiles. However this spike falls within the spatial variability

seen in the $q_{simulated}$ profiles. Similar to the August IOP, the 1645 CDT values are very similar in shape but $q_{simulated}$ values are lower with a RMSE of 1.64 g kg^{-1}. At 1300 CDT and 1645 CDT the simulated values are higher than the HRRR forcing profiles for the spatially local profiles shown in Fig 3.4 but the domain averaged values are closer to each other (Fig. 3.5)

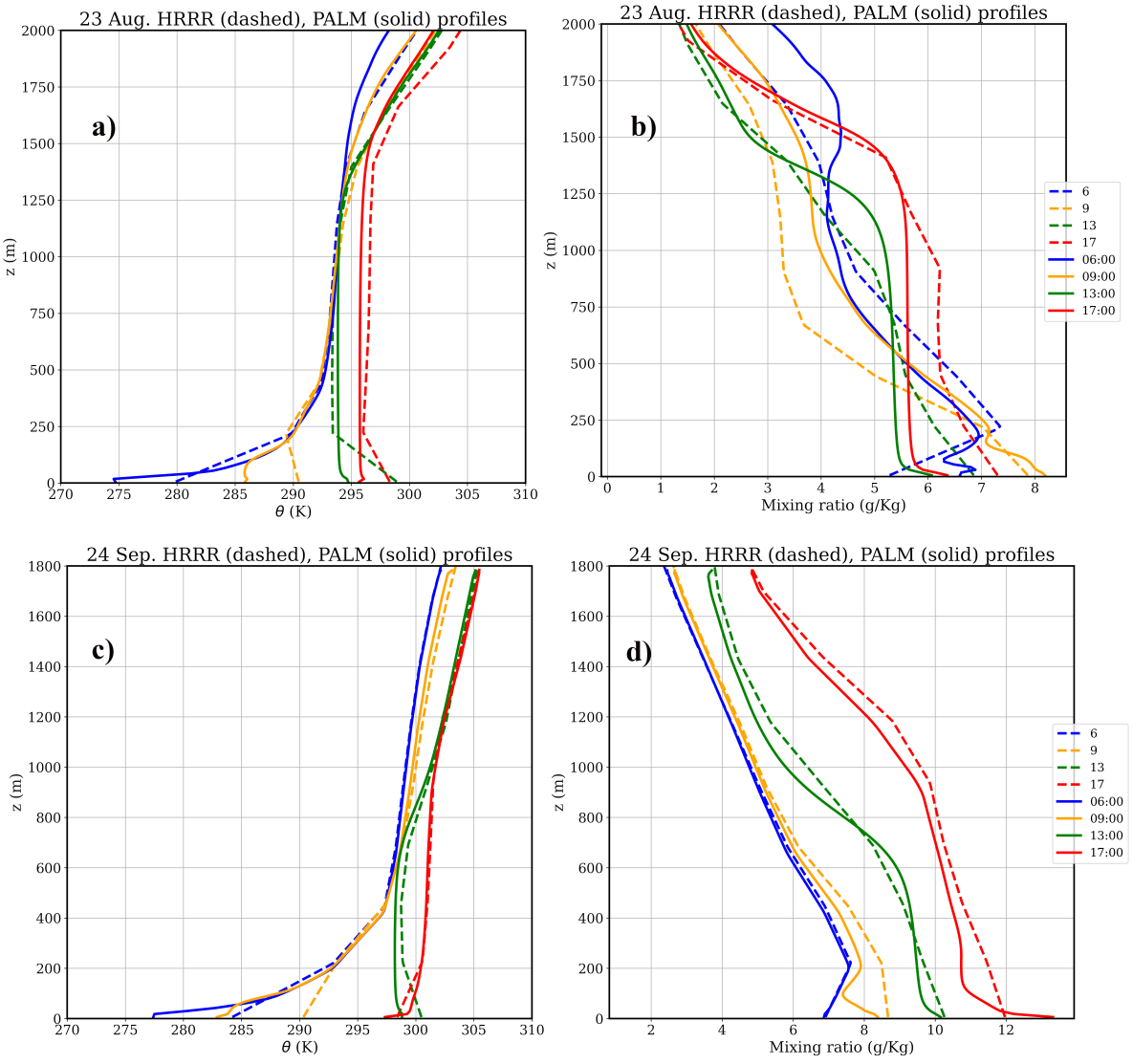

FIGURE 3.5: Comparisons between PALM simulated and input HRRR profiles of θ (a,c) and water vapour mixing ratio (b,d) for August (a,b) and September (c,d) IOPs. Different colours are used to distinguish between differing times as shown in the legend for each IOP test case. Dashed lines indicate HRRR profiles and solid lines indicate PALM simulated domain-averaged, instantaneous profiles

3.3.2 Horizontal Wind Profiles

Figures 3.6 and 3.7 present the simulated, radiosonde measured and input HRRR profiles of horizontal winds, u and v for the 23 August and 24 September simulations respectively. The simulated profiles presented alongside radiosonde profiles are ensemble averages of fixed-point, instantaneous LES data, similar to the simulated θ and q profiles presented earlier. The simulated profiles presented alongside the HRRR data are domain averaged instantaneous data. For these wind profiles, we show the standard deviation of velocity magnitudes at each heights across ensembles as an indicator for the spread of simulated values.The spatial range of velocities would be a less physically meaningful metric for model data comparisons.

In the 23 August simulations, the simulated winds are of the same order of magnitude as the measured wind profiles. The exact values of simulated and measured afternoon wind profiles at 1300 and 1700 CDT also oscillate around each other. The simulated domain mean wind profiles are closer to the input HRRR forcing profiles (Fig. 3.6 c, d). More so, for the afternoon profiles at 1300 and 1700 CDT and for heights inside the ABL, at z $\leq$ 1500 m.

Simulated and measured wind profiles for 24 September test case also show the same patterns as the summertime simulations. As expected, the boundary layer winds are also higher in the shear driven early autumn September boundary layer. The simulated and radiosonde measured profiles are close and vary around each other (Fig. 3.7 a, b). The domain mean simulated wind profiles follow the forcing HRRR profiles very closely (Fig. 3.7 c, d) for all the time steps considered.

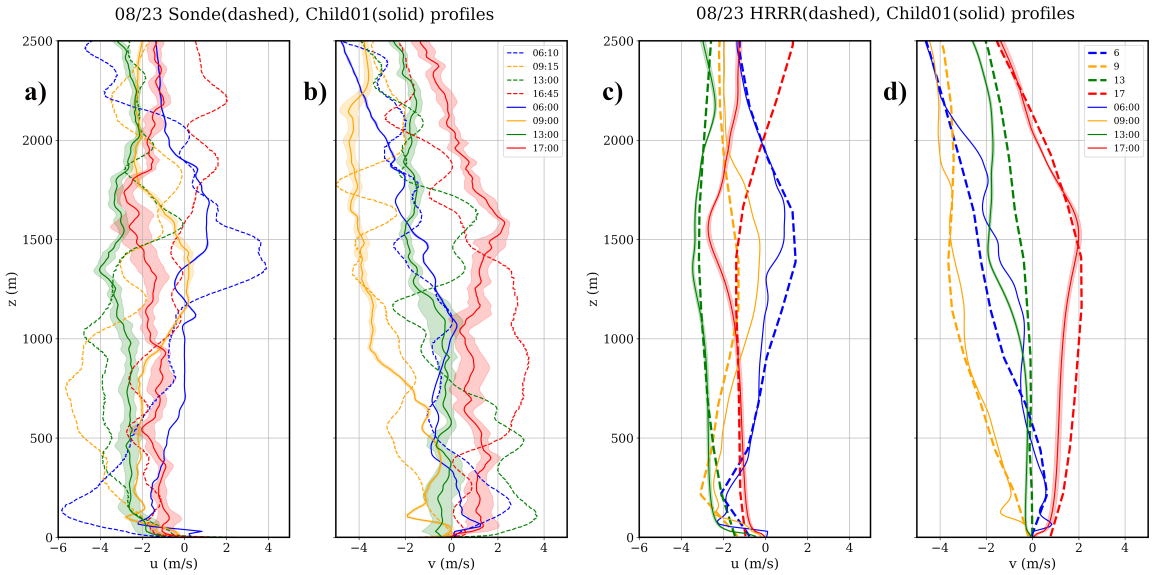

FIGURE 3.6: Panels a) and b) present comparisons between simulated (solid line) and radiosonde measured (dashed line) profiles of u and v wind respectively. Ensemble mean values of simulated profiles are presented. Shading represents the standard deviation across ensemble members. Panels c) and d) present comparisons between domain mean simulated (solid line) and the input HRRR (dashed line) profiles of u and v wind respectively. Different colours are used to distinguish between differing times as shown in the legend. Shading represents the standard deviation across ensemble members.

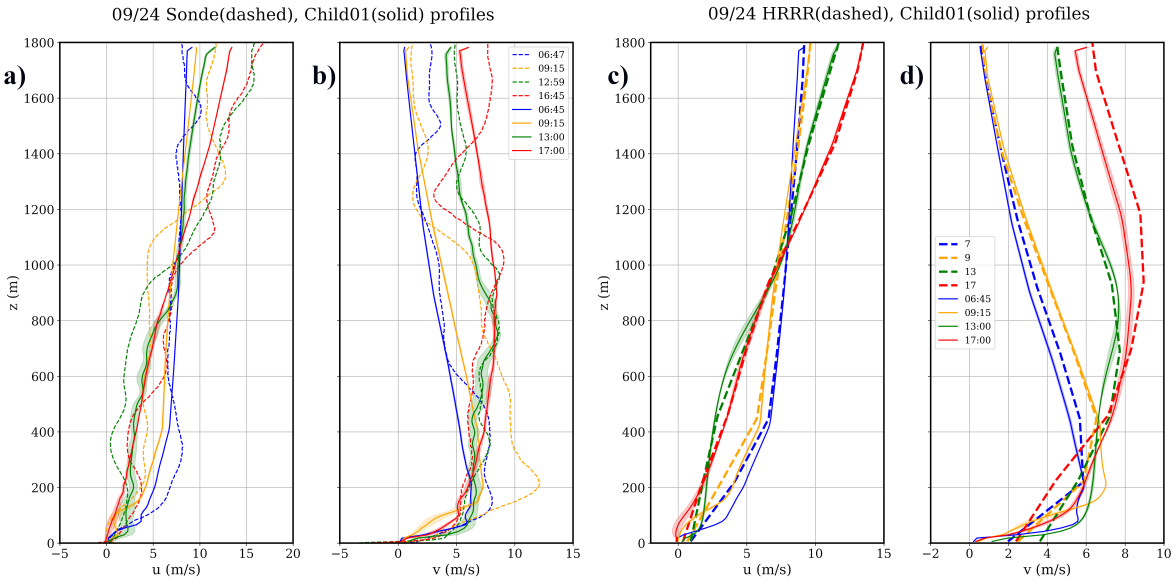

FIGURE 3.7: Same as Fig. 3.6 but for 24 September simulations

3.3.3 Near Surface Temperature and Moisture Time Series

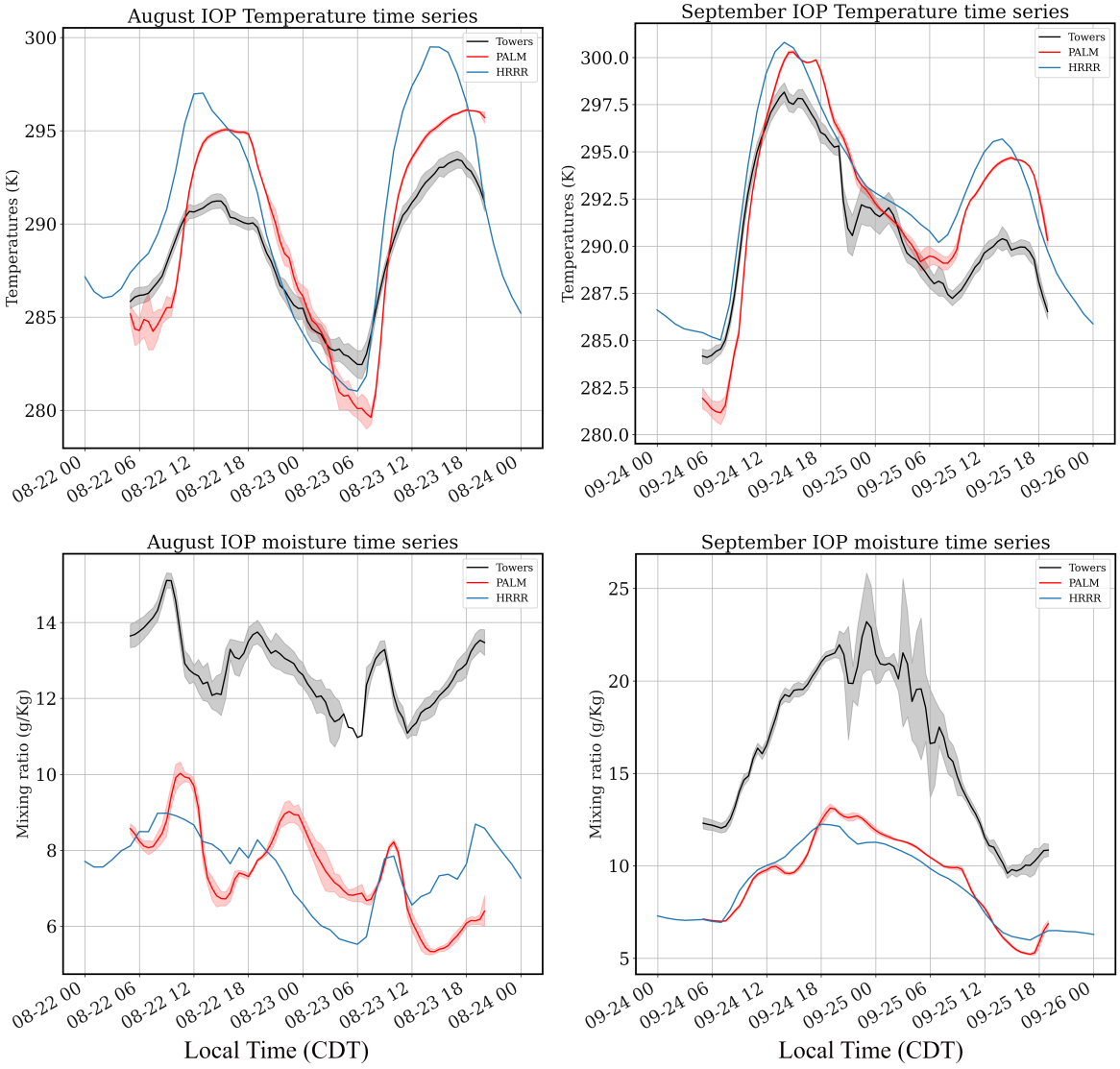

FIGURE 3.8: PALM simulated, CHEESEHEAD19 tower measured and input HRRR forcings data time series for temperature and moisture. Above-canopy time series of simulated θ and q values were extracted at $z = 32$ m from Child02 model for 12 CHEESEHEAD19 tower locations, where the field experiment measurement heights were also 32 m (Butterworth et al. 2021 supplement). The ensemble mean time series values across locations were compared between the simulations and tower data, along with the time series values from the input HRRR forcings data at the same grid level. 30-minute averaged values for August and September IOPs are presented. Shadings denote one standard deviation

The $\theta_{simulated}$ time series shows good agreement against the tower measured values for both days of the August and September IOP test cases, with a correlation coefficient of 0.94 for August and 0.88 for September days (Fig. 3.8, Table 3.3). The $\theta_{simulated}$ values in August have higher peaks and lower lows, resulting in a RMSE of 2.74 K with respect mean $\theta_{observed}$ at the towers. For 22 August the maximum $\theta_{simulated}$ was 295 K at 1530 CDT while the maximum tower measured θ value for 22 August was 291 K at 1430 CDT. Likewise, for 23 August the maximum value was 296 K at 1800 CDT and the maximum $\theta_{observed}$ was 293.5 K at 1700 CDT. The $\theta_{simulated}$ values are closer to the forcing data. The September IOP simulation is able to capture the morning warm up related to CBL initiation for the first day. The simulations miss the rainfall induced dip during 24 September night at 2130 as seen in the tower data although the cooling of the stable boundary layer is captured well, as it was reflected in the HRRR data as well. However, the $\theta_{simulated}$ peak for 25 September is higher at 294.7 K than the tower measured value of 290 K.

The simulations are dry-biased for both the August and September IOP days, with a RMSE of 5.39 g kg^{-1} in August and 7.19 g kg^{-1} in September with respect to tower measured values. Even though RMSE does not provide any directionality for the error, we use it here for the sake of consistency with the rest of the analysis. The simulated q values are of the same range of magnitudes as the forcing HRRR data, which has lower magnitudes than tower measured values. For the August IOP, the intra-day variability in $q_{simulated}$ resembles the tower measured data, where it is able to capture all three peaks as seen in the tower data at almost the same times (Fig. 3.8). However, there is a time lag between the simulated and tower measured values, of the order of a couple of hours, because of which their correlation coefficient is only 0.49. Likewise, for September IOP $q_{simulated}$ values are closer to the forcing HRRR data with the

peak around 12.5 g kg^{-1} at 24 September 1830, while the tower measured values show almost double the same values at 22.5 g kg^{-1}. The simulated values also seem to be smoother than the tower measured values here, especially for 25 September. The low frequency nature of the simulations and the observations are similar.

3.3.4 Near Surface Wind Time Series

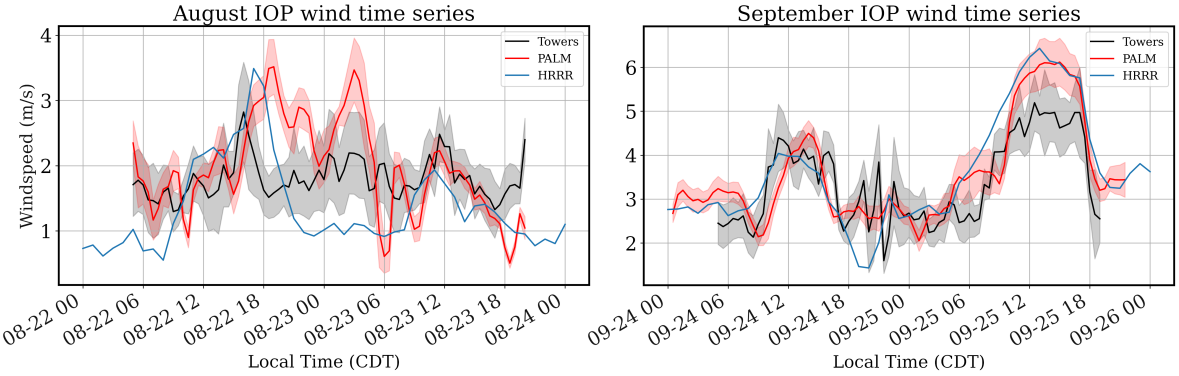

FIGURE 3.9: PALM simulated, CHEESEHEAD19 tower measured and input HRRR forcings data wind time series. Above-canopy time series of simulated wind were extracted at $z = 32$ m from Child02 model for 12 CHEESEHEAD19 tower locations, where the field experiment measurement heights were also 32 m. The simulated ensemble mean time series values across locations are compared against the mean tower measured data, along with the time series values from the input HRRR forcings data at the same grid level. Half-hourly averaged values for August and September IOPs are presented. Shadings denote one standard deviation

We present a comparison of the simulated near surface wind time series from the Child02 model domain and the CHEESEHEAD19 tower measured wind time series along with the input HRRR forcing data at the same model vertical grid level for the two IOP test cases in Fig. 3.9.

For the August simulations, the simulated and tower measured values show reasonable agreement in magnitudes. The mean simulated and tower measured daytime (0600 - 2000 CDT) winds during 22 August were 2.3 m s $^{-1}$. For 23 August, the mean tower measured winds were 1.8 m s $^{-1}$ from 0600 - 1800 CDT, while the mean simulated values were slighly lower at 1.5 m s $^{-1}$. The simulations also pick up the spike in wind speed around 22 August 1600, but it occurs

later around 1800 CDT. Simulations for 23 August are able to pick up the afternoon decrease of near surface winds from 1200 - 1800, with the same order of magnitude.

In the September IOP test case, when surface winds drive boundary layer turbulence, the simulations pick up the diurnal cycle and magnitudes of the tower measured near surface winds well. The measured winds during 24 September evening, from 1800 till midnight show much more variability than the simulations.

3.3.5 Near Surface Heat Flux Time Series

The delay in CBL initiation for 22 August simulations is also seen when comparing the near surface simulated H and LE time series with the field experiment measurements(Fig. 3.10). Since the maximum canopy height in the domain was around 32 m, only those tower sites with measurement heights $\geq$ 32 m are considered for comparisons. The simulated mean daytime H time series across CHEESEHEAD19 tower locations is greater than the tower measured values for both the August days, with a RMSE of 48 W m^{-2}. The differences are the greatest on 22 August, when the RMSE of simulated and tower measured values are 64 W m^{-2}. Despite the offset in the first day of simulations, the simulated and measured daytime H time series for both the simulation days are well correlated with a correlation coefficient of 0.87 (Fig. 3.10b, Table 3.3).

The simulated H time series on 22 August has a steep increase in the morning that peaks at 200 W m^{-2} at noon while the tower measured H peaks at 100 W m^{-2} at 1130 CDT. Similarly, the simulated LE has a higher peak of 285 W m^{-2} than tower measured value of 200 W m^{-2} and remain consistently higher through afternoon till the CBL collapse at 2000 CDT. During the

stable boundary layer of 22 August evening to 23 August morning, the mean H measurements show slightly negative heat fluxes from 1700 CDT 22 August till 0430 CDT 23 August.

The simulated H values at night-time, show a below 0 dip of -39 W m^{-2} and then goes back to near zero values, while the mean tower measured values are never as low at night in the stable boundary layer, with a mean value of -12 W m^{-2} and minimum of -25 W m^{-2}. For the 23 August simulations the CBL growth and decay occur around the same time as indicated by the heat flux measurements. The simulated daytime H magnitudes are also closer to the tower measured values with a RMSE of 23 W m^{-2}.

For 23 August (the second day) of simulations, the simulated LE magnitudes remain higher than tower measured values for most of the day. The simulated and tower measured daytime LE time series are linearly well correlated with a correlation coefficient of 0.91.

Comparisons of simulated and observed near surface fluxes during the September IOP test case reveals that the ABL growth and collapse are not as delayed for the 24 September simulations as the 22 August simulation (the first day of September simulations vs the first day of August simulations) (Fig. 3.11 a, c). The simulated and tower measured H values for both the simulation days follow a linear relationship with $r = 0.87$ and RMSE of 49 W m^{-2}.

The simulated and tower measured H magnitudes for 24 September are close to each other (Fig. 3.11 a), with RMSE = 42 W m^{-2}. The tower measured values show a spike of 85 W m^{-2} at 1530 CDT which is not reflected in the simulations. The tower measured H time series for 25 September also shows a spike of 47 W m^{-2} at 1600 CDT which the simulations do not capture. The simulated night-time H values are negative and not near zero unlike the August IOP runs.

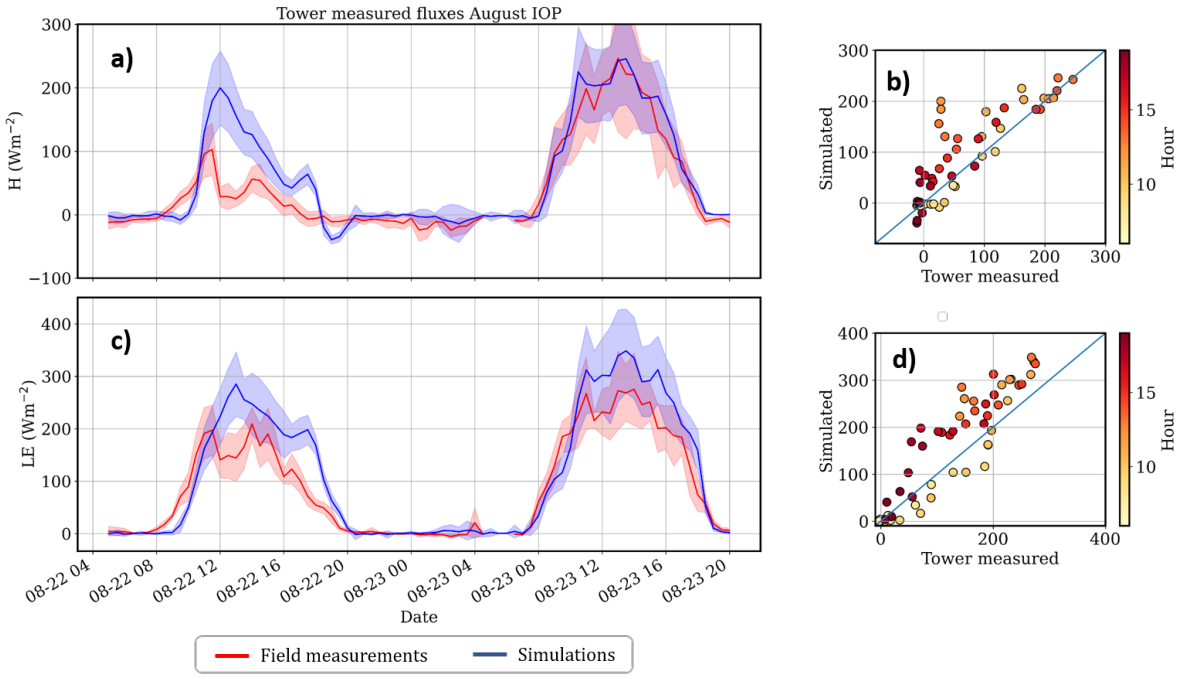

FIGURE 3.10: Simulated vs observed near surface turbulent fluxes at the CHEESEHEAD19 tower locations for the August IOP from Child02 model. Mean flux time series values across 12 tower sites with measurement heights ≥ 32 are presented. CHEESEHEAD19 flux towers in red, simulated values in blue. For LES, the mean across 8 ensembles, and all 12 towers is presented. Shading shows the standard deviation across the hole data; b, d : Scatter plots between the simulated and tower measured daytime (0600 - 2000 CDT) mean H and LE for 08/22 and 08/23

The simulated and observed daytime H start increasing from their night-time values around the same time, at 0800 CDT, for 25 September.

Simulated daytime LE values also show a linear relationship with the tower measured daytime LE time series with $r = 0.86$ and RMSE $= 59$ W m^{-2}. The simulated afternoon values are higher than tower measured values for both 24 and 25 September simulations. For the 25 September simulations, the simulated LE values in the morning are lower than the tower measured values till 1200 CDT.

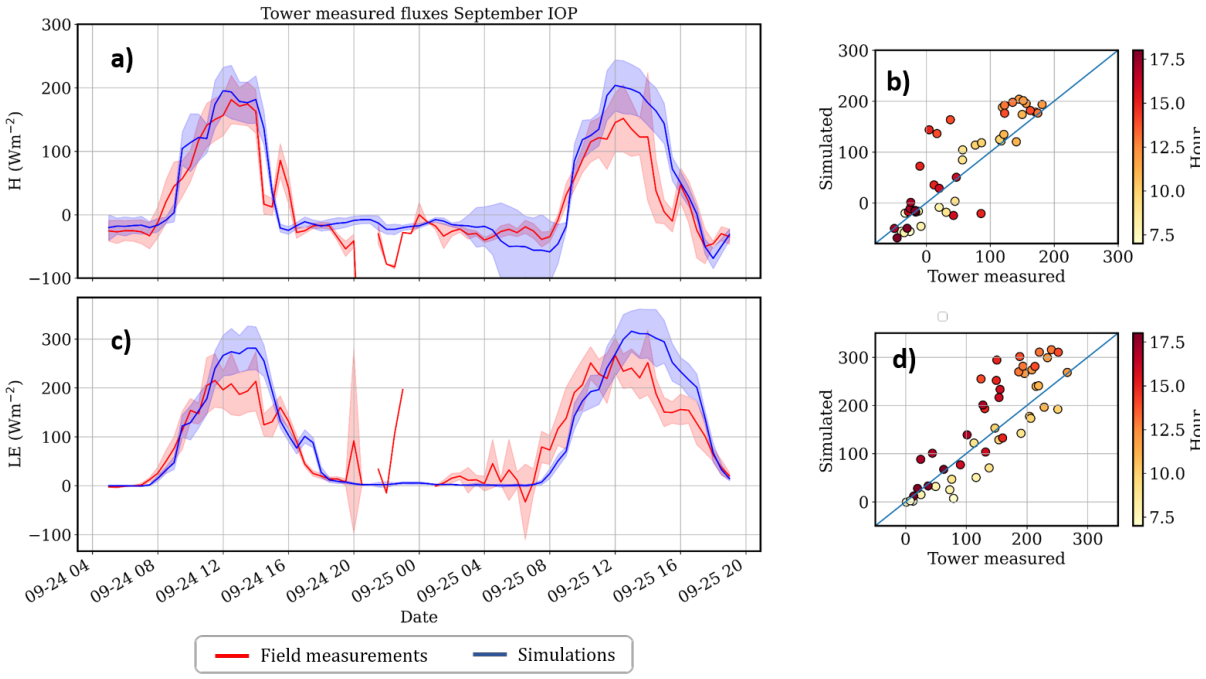

FIGURE 3.11: Same as Fig. 3.10, but for September IOP. Daytime hours 0700-1800 CDT

3.4 Discussion

Our null hypothesis was that Large Eddy Simulations, initialised with real-world surface heterogeneity, develop similar mesoscale structures and patterns as observed in reality. To include the changing synoptic scale forcings over the study domain, we used the hourly NCEP-HRRRv4 reanalysis data product as the LES boundary conditions (Sect. 3.2.2.1). This inclusion had an influence on the simulated mean quantities (Fig. 3.5 and 3.8, Table 3.3) , especially the near surface moisture values, which are lower than the measured mixing ratio values during the IOPs. However, it is as if they are offset in magnitude. For the above-canopy q time series, simulations are lower than observations for the August IOP runs with RMSE = 5.59 g kg^{-1} and the RMSE = 7.19 g kg^{-1} for the September IOP runs. When the LES runs are considered as simulations of field experiment days, we show that the mean atmospheric boundary layer state variables in the simulations are well correlated with the radiosonde and tower measurements (Sect. 3.3). The

simulated above-canopy daytime heat fluxes are also of the same order of magnitude as the tower measured values during the field experiment, with a mean RMSE between observations and simulations of 54 W m^{-2} for both the IOPs (Table 3.3). The above-canopy simulated daytime heat fluxes for 23 August and 24 September at the CHEESEHEAD19 tower locations have a Pearson correlation coefficient (r) of 0.9 with the concomitant tower measured values. They also show similar diel variations with respect to ABL growth initiation and collapse (Fig. 3.10, 3.11). This gives us confidence that our model results simulate the CHEESEHEAD19 IOP daytime boundary layers and can be used to evaluate mechanisms that generate surface-heterogeneity induced mesoscale circulations in the diel ABL.

Large Eddy Simulations have been an effective tool to simulate the observed ABL mean properties and turbulence characteristics during targeted field camapigns and experiments. Hechtel et al. (1990) simulated an afternoon CBL of the Boundary Layer Experiment 1983 (BLX83), with synthetic surface sensible and latent heat flux fields generated to match aircraft measured surface skin temperature power spectra. The heat flux amplitudes were set to vary along the diurnal cycle. They performed a control run with homogeneous surface fluxes as well and compared both with field measurements. They reported no significant differences between the two runs in mixed layer development and area averaged statistics. For the heterogeneous case, their simulations showed no clear evidence that convective thermals were preferentially localised over surface gradients. They proposed model resolution and inclusion of a imposed mean geostrophic wind ≈ 7 m s^{-1} as possible reasons for the lack of sensitivity to non-homogeneous surface boundary conditions. They used aircraft measurements to initialise the simulations and mention that related overestimations from sampling bias, such as aircraft flying over unusually high thermals, could have affected the simulated boundary layer characteristics.

Large eddy simulations of field campaign days coupled with a land surface model were later performed , to better represent the observed land-atmosphere feedbacks. Albertson et al. (2001) performed coupled LES of one day of the Monsoon '90 experiment, with periodic boundary conditions and time varying surface fluxes, computed from remotely sensed land surface properties and simulated atmospheric state variables. They used a two-source model to separately account for the contributions from bare soil and vegetation within each model grid cell for their study area, with a wide range of fractional vegetation cover. Their setup, in theory, is similar to the coupled CHEESEHEAD19 LES framework, using a LSM and PCM to resolve the surface atmospheric coupling. Spectral analysis of their simulations revealed that the surface-atmosphere feedback strength is scale-dependant, with the time-averaged air temperature containing variability in the larger scales induced preferentially from the large spatial-scale variations in surface temperature.

The spatial averages of sensible and latent heat fluxes from their simulations were within 10% of the tower measured values during the field experiment. However, the tower measured H was computed using flux variance method (Tillman, 1972)) based on empirical formulations between air temperature, standard deviation and H in MOST framework. Then LE was computed as the residual of the surface energy balance. They compared their estimates with 1D EC technique and found their estimates to be within 20% of the measured values. In a follow up study, (Kustas and Albertson, 2003) investigated the role of surface temperature variance on domain mean fluxes and spatial variance of surface heat fluxes. Their simulations indicated that higher spatial variances of surface temperatures lead to stronger surface atmospheric coupling, with reduced spatial variance in the surface heat fluxes and no significant impact on the domain mean surface fluxes.

Later investigators started exploring surface-atmospheric coupling using fully coupled land surface models and for the diurnal ABL. In their coupled LES study Huang and Margulis (2010) simulated one day (0600 - 1800 CST) of the SMACEX 2002 field experiment. Their simulated domain mean surface fluxes and profiles agreed well with tower and radiosonde measured values but they reported no significant difference in domain mean surface fluxes, between fully coupled and un-coupled simulations.They propose that this could be because the differences over the two dominant vegetation types cancel each other, and moreover the analysis was only performed for 30-minute averaged data at 1300 CST. In-line with the previous LES studies (Albertson et al., 2001; Bertoldi et al., 2007; Huang and Margulis, 2009), they suggest that surface-atmospheric coupling dampens the amplitude of the simulated heat fluxes, with simulated sensible heat fluxes reaching as low as $\approx 18\%$ lower in the fully uncoupled case. However, the land surface class distribution in their simulations is essentially very similar to an idealised 2 dimensional heterogeneity, with only soy and corn crops dominating.

Nevertheless, the RMS Deviation of their flux time series is of the same order of magnitude as ours, with 30 W m^{-2} for H and around 41 W m^{-2} for LE at the footprint scale. Their simulated and observed air temperature values agree well, with $\rho = 0.97$. The simulated moisture values are dependent on their initial values and lower than tower measured values and due to the spatial variation in measured values, the correlation coefficient is also low, and almost the same as ours at 0.47.

LeMone et al. (2010a) simulated fair weather CBL days during the 2002 International H2O Project (IHOP 2002) field campaign in Kansas, USA using the WRF-ARW version 2.1.2, coupled to the NOAH MP land surface scheme. They note that the sub-grid vegetation heterogeneity is important in modulating soil moisture, surface flux partitioning and how those would

impact CBL growth and horizontal variation of surface fluxes. In LeMone et al. (2010b) they investigate coherent mesoscale structures in the ABL and underscore the importance of non-periodic boundary conditions and a coupled land surface scheme, to simulate realistic mesoscale circulations and their diurnal evolution as observed during the field experiment days.

Shao et al. (2013) performed 12 hour daytime LES of Selhausen–Merken experimental site in Germany, with multiple land use classes. They had a multi layer canopy model, with 2 m vertical resolution and grid stretching above 80 m, coupled to a land surface and multi-layered soil model. The simulations were initialised at 0800 UTC, with radiosonde measured θ, q and wind profiles (mean boundary layer wind ≈ 3.6 m s^{-1}), with periodic boundary conditions. In their sensitivity experiments they find that with a bulk canopy scheme and the NOAH LSM, the near surface H is underestimated by as much as 100 W m $^{-2}$ in the afternoon. The near surface simulated H and LE values over short canopies (wheat and sugar beet) agreed well with tower measured fluxes in their study domain.

Heinze et al. (2017) present an evaluation of LES covering Germany, using the the ICON large eddy model at horizontal resolution of 156 m. The simulations were driven by mesoscale boundary conditions from the Consortium of Small-scale Modelling (COSMO) model at 2.8 km resolution and one-way nested from 625 m to 156 m for several days. Their LES results were able to represent the expected temporal and spatial development of turbulence by in comparison with observations from the High Definition Clouds and Precipitation for advancing Climate Prediction (HD(CP)2) project. This gives them confidence to report that the LES significantly improves the representation of small- to mesoscale variability in their model domain. They also reported lower simulated surface temperatures, along with higher near surface turbulent sensible heat fluxes.

These studies indicate that having boundary LES boundary and initial conditions reflect the large scale variability can guide the LES simulated ABL mean state and diurnal variability to be closer to the actually field measured state. This was also the basis for the implementation of the mesoscale nesting interface in PALM, detailed in Kadasch et al. (2020). Resler et al. (2020) evaluated the PALM model system, over a realistic urban canopy in Prague, Czech Republic for multiple days in Summer and Winter, including PALM's mesoscale nesting, radiative transfer, land surface modules. Their study also suggests strong sensitivity of the results to the accuracy of initialisation and boundary conditions. Moreover, they also note that the LES solution is partly reflective of the mesoscale model outputs, which our study also points towards. If a comprehensive observational dataset if available before the start of a realistic LES run, it would be beneficial to tune the mesoscale boundary conditions to be reflective of actually observed field experiment conditions.

3.5 Summary and Conclusions

We performed fully coupled large eddy simulations of the ABL over a heterogeneous, predominantly forested landscape with multiple scales of variability. The simulations were constrained and initialised by land surface properties measured and collected as part of the CHEESEHEAD19 field campaign. Three one way nested models were setup centred around the US-PFa Ameriflux regional tall tower. The simulations were driven by non periodic boundary conditions setup using the NCEP-HRRRv4 data product averaged over the 49×50 km^2 Parent domain to simulate the diurnal cycles from 0000 CDT 22 August 2019 till 2000 CDT 23 August 2019 and from 0000 CDT 24 September 2019 till 2000 CDT 25 September 2019. We present intercomparisons between simulated and observed vertical profiles and near-surface time series data. The simulated profiles and time series correlate well with observed θ and q values, with a Pearson's

correlation coefficient of 0.9 for almost all cases (Table 3.3) indicating that the simulations align well with the diurnal ABL evolution in the study domain. The mean simulated values have a dependence on the imposed HRRR boundary conditions, most strongly reflected in our study for the near surface q time series with a RMSE of 5.39 g kg^{-1} for August simulations and 7.19 g kg^{-1} for the September simulations.

Acknowledgements

This material is based in part upon work supported by the National Science Foundation through the CHEESEHEAD19 project (Grant AGS-1822420). The contribution of Luise Wanner was supported by Deutsche Forschungsgemeinschaft (DFG)Award #406980118 and the MICMoR Research School of KIT. We thank the developers of PALM at the Institute of Meteorology and Climatology of Leibniz Universität Hannover, Germany for the open source model and their technical support. We would like to acknowledge high-performance computing support from Cheyenne (doi:10.5065/D6RX99HX) provided by NCAR's Computational and Information Systems Laboratory, sponsored by the National Science Foundation.

Author contributions

SP and LW contributed equally towards modal setup with mentoring and technical support from MS. SP and MS performed initial sensitivity tests. SP, LW, and ARD acquired computational resources. SP performed the final production model runs and the formal analysis. SP, LW, and ARD were responsible for data curation. SP prepared the original draft. SP, LW, MS, ARD, and MM reviewed and edited the manuscript drafts. SP and LW created visualisations. ARD, MS and MM provided supervision. ARD and MM acquired funding.

Supplementary Information

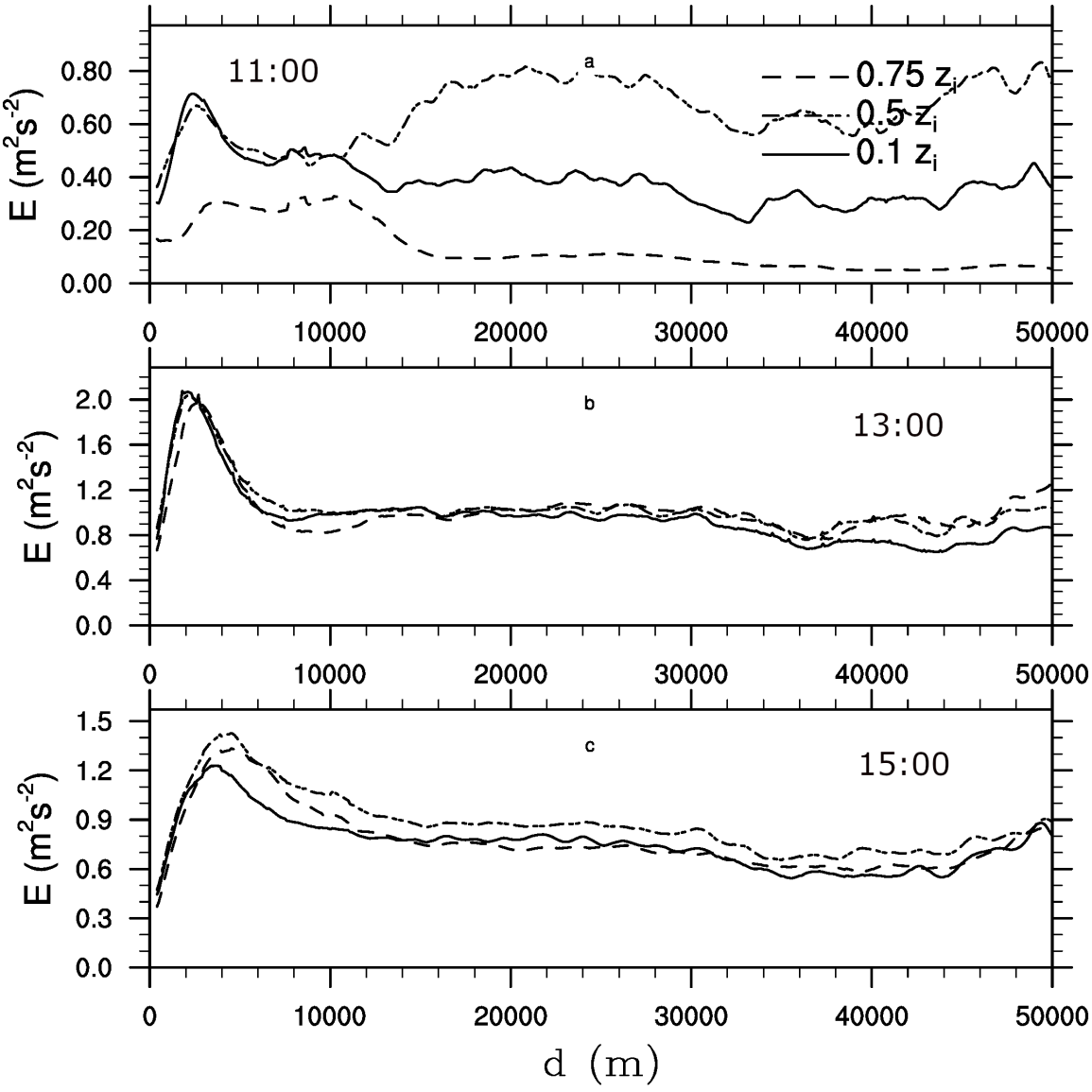

FIGURE 3.12: Horizontal profiles of 30-minute time-averaged turbulent kinetic energy at 1100 (a), 1300 (b) and 1500 CDT (c) for the 24 September simulations. Horizontal profiles are shown for $0.1z_i$ (solid line), $0.5z_i$ (dashed and dotted) and $0.75z_i$ (dashed). The x-axis shows distance to the inflow boundary. The turbulent kinetic energy was computed at each x,y grid point. Grid points with a similar distance to the inflow boundary were sorted into 1000-equally spaced bins and averaged.

Chapter 4

Impact of Surface Heterogeneity Induced Secondary Circulations on the Atmospheric Boundary Layer

S. Paleri, L. Wanner, M. Sühring, A. Desai, M. Mauder[1]

4.1 Introduction

Turbulence is the primary transport process in the ABL. Observations (Lemone, 1973, 1976; Weckwerth et al., 1997, 1999; Drobinski et al., 1998b; Eder et al., 2015; Träumner et al., 2015) and numerical simulations (Deardorff, 1972b; Moeng and Sullivan, 1994; Avissar and Schmidt, 1998; Khanna and Brasseur, 1998) have reported coherent secondary circulations in the turbulent ABL. In forced convective boundary layers, with strong winds, these structures organise as Horizontal Convective Rolls (HCR) (Lemone, 1973; Etling and Brown, 1993) and in free convective boundary layers, when the mean wind shear is weaker and surface fluxes stronger, they organise into open convective cells, akin to the cellular structures in turbulent Rayleigh-Benard

[1]This chapter is a draft of an article, Surface heterogeneity induced effects on the diurnally evolving convective boundary layer from coupled large eddy simulations of the CHEESEHEAD19 field campaign - Part II, to be submitted to *Boundary Layer Meteorology*

convection (Atkinson and Wu Zhang, 1996; Salesky et al., 2017). In the ABL over homogeneous surfaces, these secondary circulations can arise from randomly generated slow-moving turbulent organised structures (Kanda et al., 2004; Inagaki et al., 2006). With heterogeneous surface forcings, thermally induced mesoscale circulations (TMC) can be generated that become localised over gradients of land surface temperature (Blanford et al., 1991; Foken, 2008; Maronga and Raasch, 2013a; Kenny et al., 2017). With these conditions, the ABL can fail conditions for homogeneous turbulence as well, which complicates applications of Taylor's frozen turbulence and Monin-Obukhov Similarity Theory (MOST) for measurement and modelling of ABL processes.

These quasi-stationary circulations can bias fixed-point turbulent flux estimates from towers (Kanda et al., 2004; Steinfeld et al., 2007; Prabha et al., 2007; De Roo and Mauder, 2018a) if they are not carried past the towers by the mean wind and modulate surface layer turbulent transport (Salesky and Anderson, 2018; Margairaz et al., 2020; Zhou et al., 2023). Most simulation studies investigating the role of secondary circulations in the ABL have involved idealised surface heterogeneities (Inagaki et al., 2006; Huang et al., 2009; Sühring et al., 2014; Margairaz et al., 2020), with initial studies starting out using prescribed 1D, stripe like or sinusoidal heterogeneities (Hadfield et al., 1992; Avissar and Schmidt, 1998) and then exploring the effects of 2D prescribed surface fluxes (Shen and Leclerc, 1995; Raasch and Harbusch, 2001; Liu et al., 2011). Subsequently, LESs with coupled land surface model (LSM) were used to study the coupling between surface heterogeneities and vertical structure of the Convective Boundary Layer (CBL) (Albertson et al., 2001; Kustas and Albertson, 2003; Courault et al., 2007). Patton et al. (2005) studied the effects of surface heterogeneity length scales relative to the boundary layer height using idealised stripe-like heterogeneities in a coupled LES-LSM without any imposed mean wind. They found the strongest ABL response to surface heterogeneities for

heterogeneity scales ranging from 4 to 9 times z_i. Courault et al. (2007) reported that smaller scale heterogeneities (1.25 to 5 km) with horizontal wind speeds of 3-4 m s^{-1} can generate secondary circulations along surface thermal and soil moisture gradients. Prabha et al. (2007) studied the secondary circulation characteristics over irregular surface heterogeneities with prescribed surface fluxes derived from remote sensing and eddy covariance (EC) measurements, 2 m s^{-1} imposed winds with varying directions, and periodic boundary conditions. They report that the orientation of surface heterogeneities with respect to geostrophic wind, the horizontal scale and amplitude of surface heat flux gradients strongly influence the strength, location and organisation of secondary circulations.

However, as noted in Chapter 3, Sect. 3.1, modelling studies that investigated the surface-atmospheric coupling in a diurnally evolving boundary layer over realistic, irregular heterogeneities have been few. The CHEESEHEAD19 field campaign was designed to intensively sample and scale land surface and the ABL properties as the study domain transitions from late summer to early autumn. We have a comprehensive dataset at hand that allows us to investigate the intensity of large-scale coherent structures and heterogeneity induced secondary circulations. Spatially resolved airborne eddy covariance measurements revealed persistent contributions of larger scale (in the range of meso-β to meso-γ) fluxes to the daytime sensible and latent heat fluxes Paleri et al. (2022). However, due to the large range of scales, diurnal nature of surface sources and three-dimensionality of the problem, the drivers and constraints of the underlying processes can be better studied by employing LES.

Building on the CHEESEHEAD19 LES validation study in Chapter 3 we ask, whether diagnosing and quantifying surface heterogeneity induced circulations and scale-separated transport can help observe the "true" transport ? And following through, how do the effects of these

heterogeneity induced circulations vary over the diurnal cycle and across seasons, with changing atmospheric boundary layer height (z_i) and stabilities? How do their effects scale with the length scales of surface heterogeneity and the boundary layer height? In line with our research questions, we hypothesise that surface flux heterogeneity modulates the atmospheric boundary layer response to it by inducing quasi-stationary coherent structures that transition from roll vortices to cellular structures as the boundary layer becomes more convectively unstable.

To answer these questions, we parameterised, ran and evaluated our LES over CHEESEHEAD19 field experiment domain and then diagnosed it to identify secondary circulations induced by the heterogeneous land surface through time and ensemble averaging as per the formulations of Maronga and Raasch (2013a). Their diurnal evolution in free and forced convective boundary layers as the land surface undergoes seasonal transition is discussed. And in turn, how do they interact with transport and dynamics of the atmospheric boundary layer.

4.2 Methods

4.2.1 Diagnosis Of Secondary Circulations

MR13 used time and ensemble averaging to isolate the effects of surface heterogeneities and keep the signal from the primary background turbulence small to determine secondary circulation patterns over heterogeneous surface forcing. We used a similar approach with our ensemble LES runs over the CHEESEHEAD19 study domain.

4.2.1.1 Calculating Heterogeneity Induced Mesoscale Fluxes

Any 3D quantity $\Phi(x, y, z, t)$ over a heterogeneous domain, can be decomposed to a heterogeneity induced and smaller scale turbulent components as (Maronga and Raasch, 2013a; Patton et al., 2005):

$$\Phi(x, y, z, t) = \langle\Phi\rangle(z, t) + \Phi_{hi}(x, y, z, t) + \Phi_s(x, y, z, t) \tag{4.1}$$

Where $\langle . \rangle$ denote horizontal domain spatial averages, the subscript hi denotes the heterogeneity induced part and subscript s denotes the small scale turbulent part. This lets us calculate the heterogeneity induced part Φ_{hi} using time and ensemble averaging as:

$$\overline{\Phi_{hi}(x, y, z, t)} = \overline{\widetilde{\Phi(x, y, z, t)}} - \overline{\widetilde{\langle\Phi(z, t)\rangle}}, \tag{4.2}$$

where the $\widetilde{.}$ denote ensemble averages and $\overline{.}$ denote a time average. MR13 and Patton et al. (2005) used fixed 1 hour intervals and MR13 used 8 ensembles for their study. MR13 notes that, when the mean statistical properties of the flow remain the same over the ensemble runs, the second term on the right of Equation 4.2 remains the same over ensemble averages to give:

$$\overline{\Phi_{hi}(x, y, z, t)} = \overline{\widetilde{\Phi(x, y, z, t)}} - \overline{\langle\Phi(z, t)\rangle} \tag{4.3}$$

Horizontal averaging of Equation 4.3 gives $\overline{\langle\Phi_{hi}(x, y, z, t)\rangle} = 0$, so that $\overline{\Phi_{hi}(x, y, z, t)}$ gives the surface heterogeneity induced spatial variation from the domain mean state for the averaging time interval.

Equipped with such a scale separation, we can decompose the domain mean total vertical flux of $\Phi(x, y, z, t)$ as (Eq. 9 in Chen and Avissar (1994), Eq. 16 in MR13) :

$$\langle\overline{w\Phi}\rangle(z) = \overline{\langle w\rangle\langle\Phi\rangle}(z) + \langle w_{hi}\Phi_{hi}\rangle(z) + \langle\overline{w_s\Phi_s}\rangle(z) \tag{4.4}$$

The first term on the r.h.s of Equation 4.4 is the mesoscale flux associated with the imposed large scale flow, the second term is the domain mean mesoscale flux induced by land surface heterogeneities and the third term is the simulated turbulent scale fluxes. Since we are not interested in the fluxes due to the imposed large scale forcings, their contributions as per term 1 was removed while writing out half hourly averaged data outputs.

4.2.1.2 Calculating The Domain Mean Dispersive Fluxes From Secondary Circulations

Dispersive fluxes arise from the spatial correlation of temporal averages (Wilson and Shaw, 1977; Raupach and Shaw, 1982). Spatially averaging the temporally averaged equations of motion gives rise to such additional Reynolds stress terms and likewise for temperature and moisture budgets (Eq. 7, Raupach and Shaw (1982)). Hence, by definition, these fluxes would not be measured by single-point, conventional Edyy Covariance (EC) tower measurements. However, the total spatial covariance across a domain is given by the sum of the dispersive covariance and the single-point time averaged covariance (Raupach and Shaw, 1982),

$$\langle w''\Phi''\rangle(z) = \langle\overline{w}''\overline{\Phi}''\rangle(z) + \langle\overline{w'\Phi'}\rangle(z) \tag{4.5}$$

where $''$ indicate a deviation from a spatial mean.

This dispersive flux contribution to total flux transport arise from the turbulent organised structures over homogeneous surfaces as well as quasi-localised thermally induced mesoscale structures. Here the domain mean dispersive flux profiles at all vertical grid point is calculated as the spatial covariance between 30-minute averaged vertical velocity and the 30-minute averaged variable of interest $\Phi(x, y, z)$ like so:

$$\langle \overline{w}''\overline{\Phi}'' \rangle(z) = \frac{1}{nx \times ny} \sum_{1}^{nx} \sum_{1}^{ny} (\overline{w}(x, y, z) - \langle \overline{w} \rangle(z))(\overline{\Phi}(x, y, z) - \langle \overline{\Phi} \rangle(z)) \tag{4.6}$$

4.2.2 Data Analysis

In this study, we focusing on the simulated data from the Child01 model domain (3.2.2.2). The daytime data during 23 August and 24 September simulations are analysed, when all of the ABL was fully resolved within the Child01 model.

The ABL height field was calculated as the local maximum of the $d\theta(x, y)/dz$ following Sullivan et al. Sullivan et al. (1998). The domain mean boundary layer height, $\langle z_i \rangle$ was then calculated from these 2D fields. We use the z_i computed by this local-gradient method over the heterogeneous domain for scaling purposes, as suggested by MR13.

Spectrograms can be used to understand how spectral energy is partitioned between different scales of motion in the resolved flow field at different heights. They have been used to study the scale decomposition of LES simulated resolved scale flows over idealised surface heterogeneities (Brunsell et al., 2011; Margairaz et al., 2020). 2D Fourier power spectra and/or cospectra were calculated for all the fields analysed at heights starting from 60 m above the surface, till the

domain mean z_i. This ensured that the near surface fields are above the maximum canopy height and that the SGS contributions to the resolved scale flows are minimal. Since the Child01 model domain is rectangular at 30.240 km × 27 km, the southernmost 3240 m of the domain were excluded to create 27 km × 27 km square fields for input data. The 2D power spectra were azimuthally averaged over shells of radial bins of wavenumbers to compute the representative 1D power spectra at each model height analysed. The power spectra were then normalised by the total power at each vertical level, to pick out the dominant scales at each height.

4.3 Results

4.3.1 Atmospheric Boundary Layer Characteristics

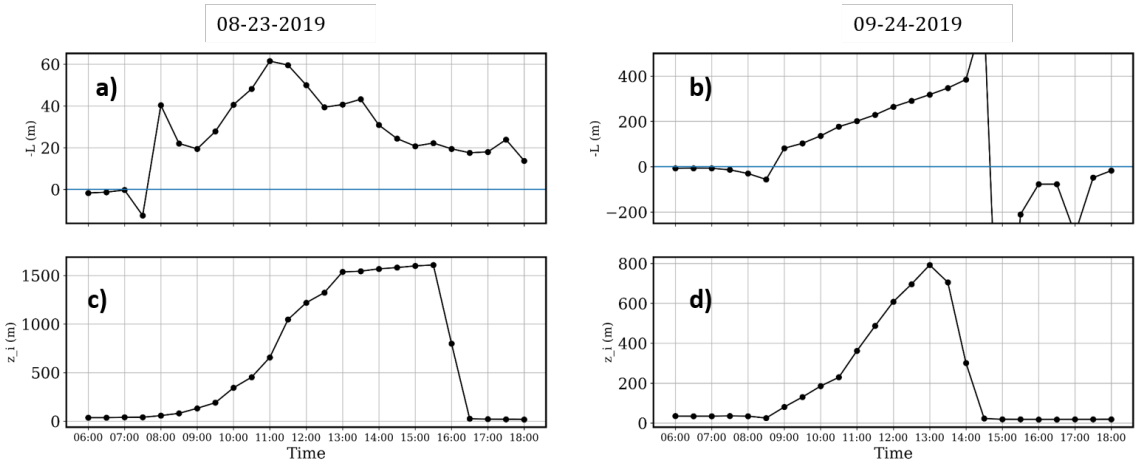

FIGURE 4.1: 30-minute, horizontal domain-mean Obukhov length (a,b, $-L$ presented) and z_i (c,d) for 08/23 (a,c) and 09/24 (b,d) runs from Child01 model

For the 23 August and 24 September day-time simulations we look at the ABL evolution and compare their wind shear vs buoyancy driven nature, using data from the Child01 model. The Obukhov length (Obukhov, 1946; Monin and Obukhov, 1954) was calculated for the Child01 model as $L = -u_*^3\overline{\theta_0}/kgQ_0$. Here, u_* is above-canopy friction velocity at 36 m ; $g/\overline{\theta_0}$, the buoyancy parameter where g is the gravitational acceleration and $\overline{\theta_0}$ the horizontal domain mean

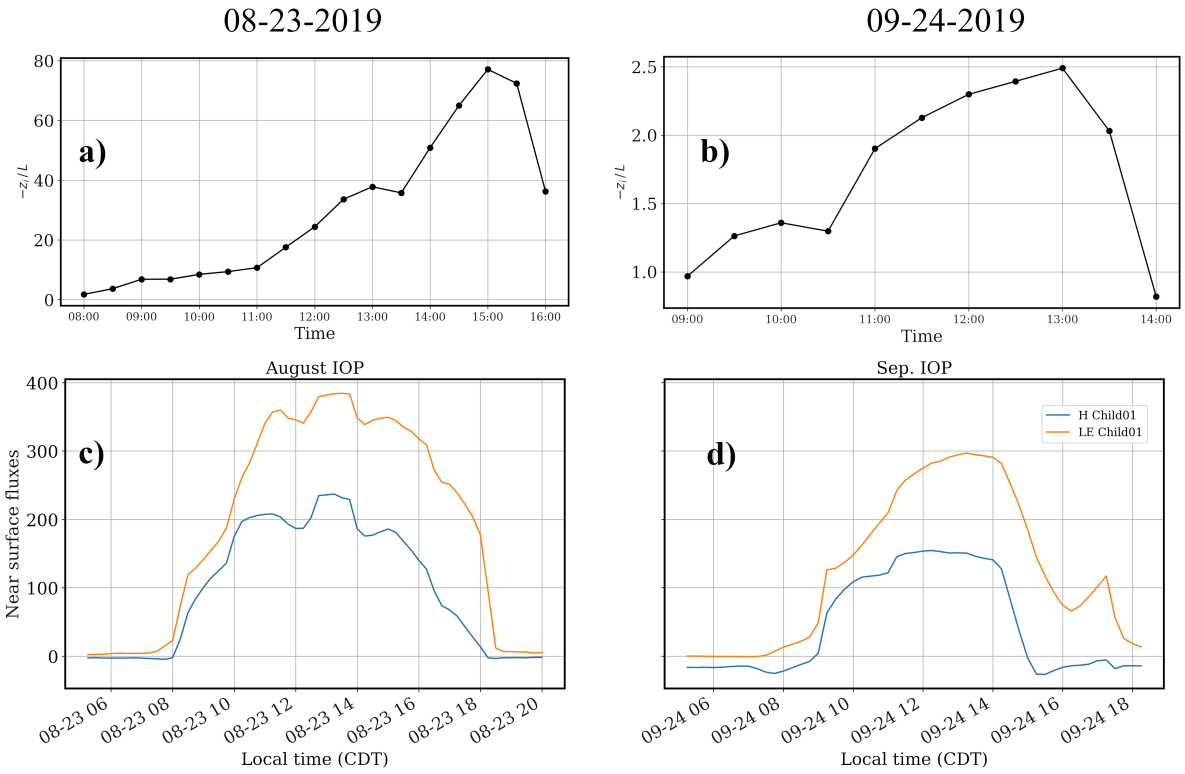

FIGURE 4.2: a,b : daytime 30-minute $-\frac{z_i}{L}$ plots for 08/23 and 09/24 Child01 simulations. Simulated, domain averaged above-canopy heat flux time series for 08/23 (c) and 09/24 (d) at 36 m above surface from Child01 model.

above-canopy potential temperature at 36 m; k the von Kármán constant = 0.4 and Q_0 the calculated above-canopy kinematic vertical heat flux ($\overline{w'\theta'}$) at 36 m. Since L has units of length, a non-dimensional stability parameter $-\frac{z_i}{L}$, can be defined with values close to 0 indicating a statically neutral, wind shear-driven, forced convective ABL and as the value increases, the ABL becomes more buoyancy-driven, free convective and statically unstable (Stull, 1988; Moeng and Sullivan, 1994).

On 23 August from 0800-1600 CDT as the simulated day-time ABL grows and decays, 30-minute $-L \in [20, 60]$ m (Fig. 4.1 a). The fully developed CBL has domain-mean, half-hourly averaged $z_i = 1500$ m, which was also the ABL height seen in the radiosonde measured θ profile at 1300 CDT on 23 August (Fig. 3.4). For the 24 September simulations, from 0900-1400 CDT as the

ABL evolves, half-hourly $-L \in [81, 385]$ m. The simulated ABL is also shallower than the 23 August simulations, with maximum z_i= 800 m at 1300 CDT (as was also seen in the profile comparisons at 1300 24 September in Fig. 3.4).

From 30-minute time series data for the 23 August simulations, $-z_i/L \in [1.8, 40]$ m for 0800-1300 CDT and later in the afternoon $-z_i/L \in [40, 80]$ from 1330-1600 CDT. The simulated domain mean total surface heat flux for 1000-1600 CDT was 535 W m^{-2} (Fig. 4.2 c) with a domain-mean above-canopy wind speed of 2.25 m s^{-1} (Fig. 4.3). The intra-day variability and range of values of $-z_i/L$ for the simulated ABL for 23 August indicate a more wind shear driven forced convective ABL in the early morning hours (0800 - 1100 CDT) as the mixing layer starts to grow and a free convective boundary layer later during the day that grows and fully develops to 1500 m by 1300 CDT.

The range of values of $-z_i/L$ for the 24 September simulations are smaller than the 23 August simulations, with $-z_i/L \in [0.4, 2.4]$. The domain and time mean daytime surface heat flux from 1000 to 1600 CDT at 36 m was 326 W m^{-2} (Fig. 4.2 d) which was 209 W m^{-2} lesser than the 23 August simulation. The domain mean boundary layer winds were also stronger, ranging from 4.5 m s^{-1} at 1100 CDT to 7 m s^{-1} at 1330 CDT (Fig. 4.3). These values indicate that the 24 September simulations have a wind-shear driven, forced convective ABL from 0900 to 1400 CDT, with a peak z_i of 800 m around 1300 CDT.

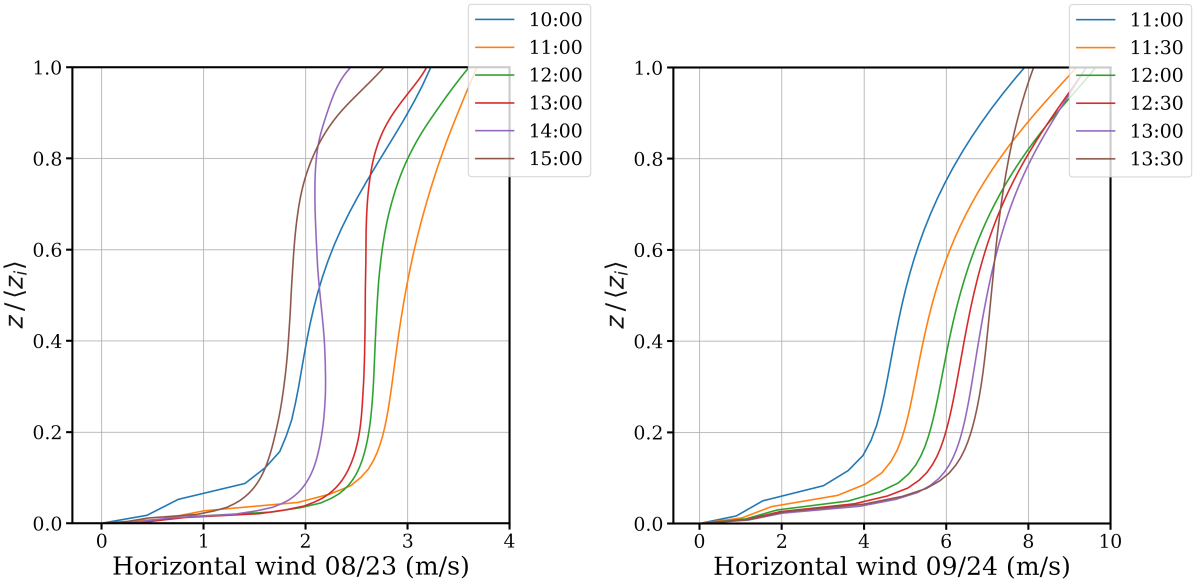

FIGURE 4.3: Simulated domain-mean horizontal-wind profiles for 23 August and 24 September. 30-minute averaged profiles for different times shown in different colours

4.3.2 Atmospheric Boundary Layer Organisation

Figure 4.4 shows the time-ensemble averaged z_i horizontal cross-sections normalised by $\langle z_i \rangle$ for the Child01 model. The cross-sections were produced using 30-minute averages and 8 ensemble runs. On 23 August morning, the boundary layer winds were easterly and the z_i cross-section plot at 1100 CDT (Fig. 4.4 a) show some signals of roll like convection that are oriented West-East of the model domain. Smaller than domain mean z_i values are seen near the lake to the north, due to colder temperature of the lake surface. ABL heights are also shallower at the southern edge of the domain as well, (around $y \in [0, 5000]$ m & $x \in [5000, 20000]$ m). In the afternoon, the fully developed CBL at 1400 CDT (Fig. 4.4 b) has lower spatial gradients, with most of the spatial variations within $0.88\langle z_i \rangle$-$1.12\langle z_i \rangle$. Within this range, the CBL was higher to the west of the model domain and lower to the east. The lower than domain mean z_i around the lake to the north can also be seen in the 1400 CDT z_i horizontal cross-section.

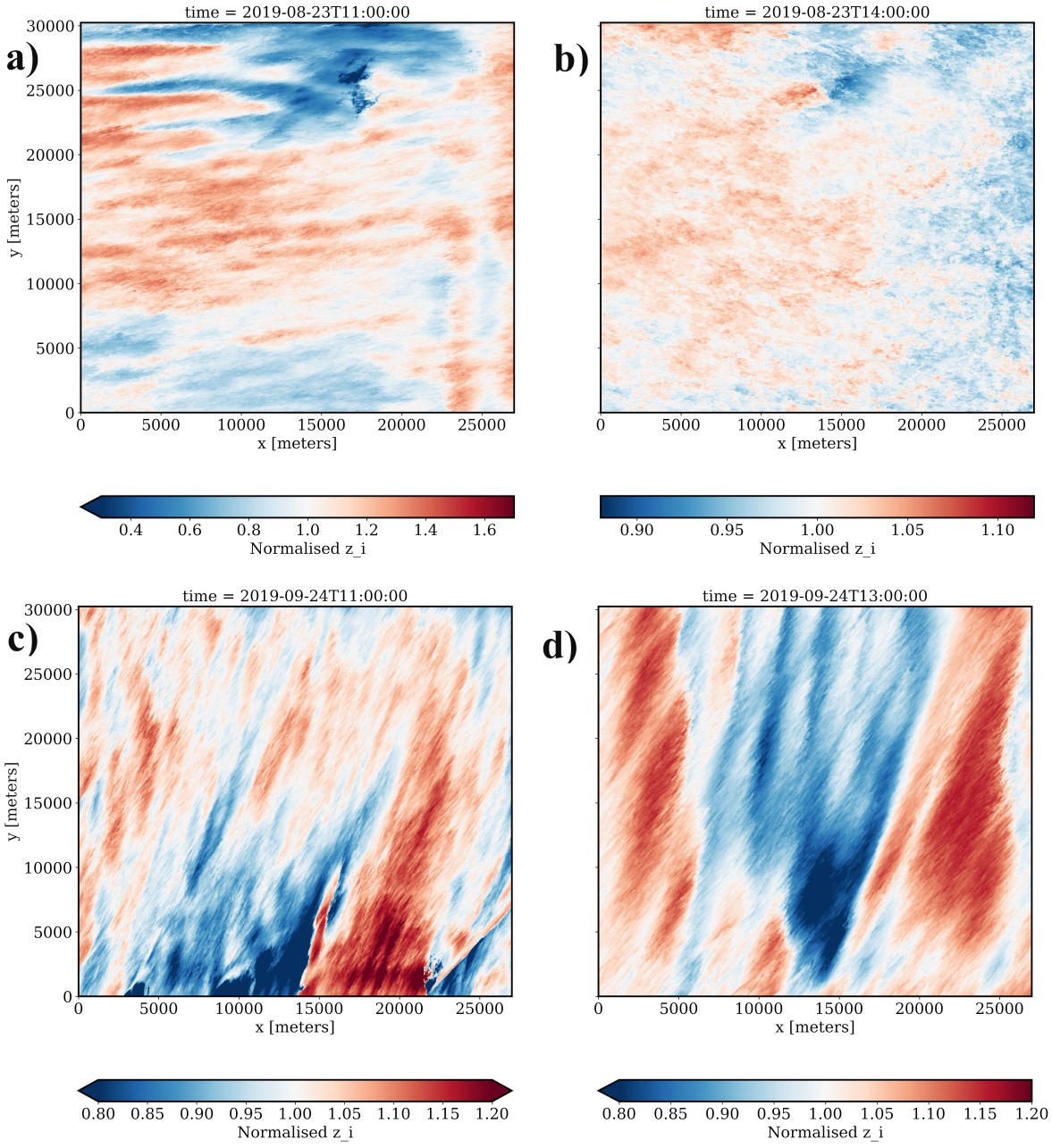

FIGURE 4.4: x-y cross sections of time-ensemble averaged z_i, normalised by $\langle z_i \rangle$ for 08/23 (a) 1100 CDT and (b) 1400 CDT; 09/24 (c) 1100 CDT and (d) 1300 CDT

Looking at the z_i horizontal cross-sections of 24 September simulations of a forced convective ABL, signals of roll-like convection aren't as distinct as in the ensemble and time averaged z_i plots of 23 August 1100 CDT simulations. At 1100 CDT 24 September, with northerly winds,

the shallower z_i at the southern edge ($x \in [5000, 14000]$ m) are elongated along-wind. In the afternoon, at 1300 CDT, the z_i variations occur at larger scales but around the same range of $0.8\langle z_i \rangle$-$1.2\langle z_i \rangle$.

4.3.2.1 Spatial Structure of Diagnosed Heterogeneity Induced Secondary Circulations

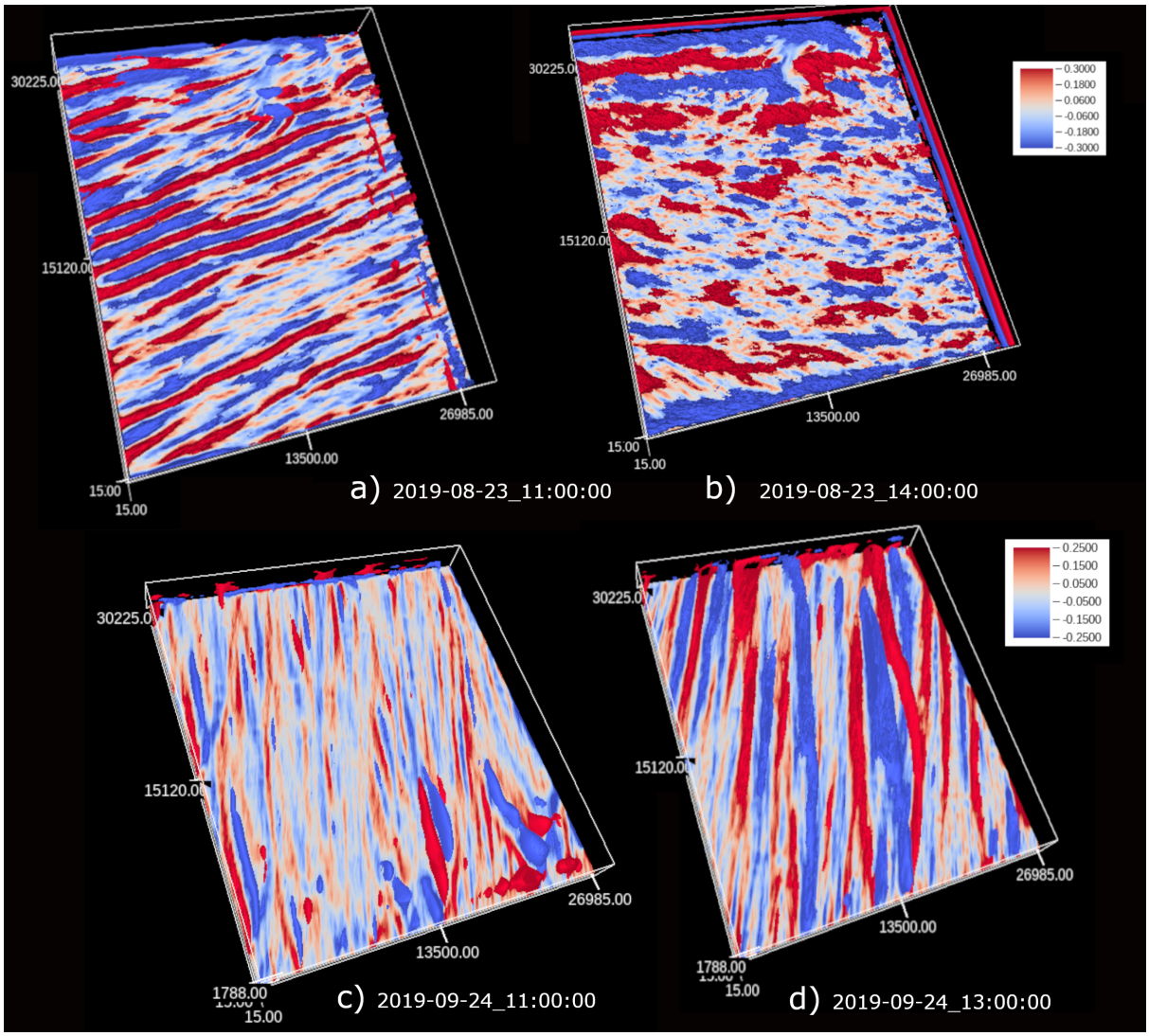

FIGURE 4.5: (a,b) show the 3D isosurfaces of heterogeneity induced 30-minute averaged vertical wind for the 08/23 magnitudes at 0.3 m s^{-1}. c,d show the same for 09/24, magnitudes of 0.25 m s^{-1}

The ensemble averaging method as detailed in Section 4.2.1 lets us filter out signals of ABL turbulence and diagnose signals of land surface heterogeneity induced coherent ABL structures. Since the structures can span all of the ABL, the heterogeneity induced vartical wind, w_{hi} can be a good measure for the strength and phenomenology of heterogeneity induced secondary circulations (Maronga and Raasch, 2013a). Isosurfaces of $w_{hi} = \pm 0.3$ m s^{-1} at 1100 CDT and 1400 CDT on 23 August and $w_{hi} = \pm 0.25$ m s^{-1} at 1100 CDT and 1300 CDT on 24 September are presented in Figure 4.5. The isosurfaces are presented for the same 30-minute intervals as the z_i plots in Figure 4.4.

23 August had north-easterly changing to easterly above-canopy winds with a mean magnitude of 2.25 m s^{-1} from 0800 to 1600 CDT. At 1100 CDT, the heterogeneity induced structures are elongated along-wind and extend almost the whole length of the domain (Fig. 4.5 a) $\approx$ 27000 m. Later in the day as the CBL grows and $-L$ decreases, the structures become more localised to land surface features (Fig. 4.5 b). At 1400 CDT on 23 August, towards the North-East of the domain a standing circulation can be seen near the lake-forest edge (Fig. 3.1). Towards the South-East of the domain, where there are more grasslands (Fig. 3.1) and the CBL is shallower (Fig. 4.4 b), the circulations become more patchy and smaller in spatial scale at 1400 CDT. The east-west oriented morning updrafts at 1100 CDT look well correlated with the higher z_i regions centred around y = 15000 m. Regions around the lake near the North East sector of the domain with lower z_i don't generate strong circulation patterns yet at 1100 CDT. The afternoon free convective ABL with lower spatial gradients of z_i has more localised structures of smaller spatial scales. The longest continuous structure at 1400 CDT is to the North West, with higher than domain mean z_i (Fig. 4.4) at y $\approx$ 25000 m, from x = 0 to x $\approx$ 15000 m.

24 September had northerly above-canopy winds of mean magnitude 3.5 m s^{-1} from 0900 to

1400 CDT. The forced convective ABL with stronger near-surface winds than 23 August show signals of persistent roll-like heterogeneity induced circulations but they are weaker than what was diagnosed from the 1100 CDT 23 August simulations (Fig. 4.5 c). The signals get stronger later in the day at 1300 CDT, along with the growth of the mixed layer. The roll-like circulations are roughly aligned along the boundary layer winds. Both at 1100 and 1300 CDT, there are no discernable signals of the heterogeneity induced circulations in the z_i cross-section plots (Fig. 4.4 c, d) as seen in the 1100 CDT 23 August simulations. However, z_i calculated as the height of minimum kinematic heat flux shows stronger signals of secondary circulations and heterogeneity induced secondary circulations (Sect. 4.4) indicating the strong role of mixed layer top entrainment.

Figure 4.6 shows the vertical profiles of spatial variances for heterogeneity induced horizontal wind, vertical velocity, potential temperature and water vapour mixing ratio ($\sigma^2_{h.\,wind_{hi}}$, $\sigma^2_{w_{hi}}$, $\sigma^2_{\theta_{hi}}$, $\sigma^2_{q_{hi}}$) for 23 August (a, c, e, g) and 24 September (b, d, f, h) simulations. The variance profiles show the same characteristics as primary circulations, as was also reported in Maronga and Raasch (2013a). During 23 August the $\sigma^2_{w_{hi}}$ peaks around the middle of the free convective ABL (Fig. 4.6 d). The peak value is lower at 1000 CDT (0.16 m^2 s^{-2}), increases at 1100 CDT and stays almost constant ($\approx$ 0.3 m^2 s^{-2}) as both the CBL height and w_* increases. The profiles of $\sigma^2_{\theta_{hi}}$ have higher near surface values from 1000-1300 CDT. Close to the surface the profiles at 1000 and 1100 CDT show a peak around the PCM top at 36 m. The profiles peak again at the CBL top, which gets more prominent and narrower from 1300 to 1500 CDT as the ABL becomes more free convective. The $\sigma^2_{q_{hi}}$ profiles behave similarly sans the near surface peaks. They peak near the CBL top and the magnitude of the peak is the highest at 1100 CDT at 0.8 g^2 Kg^{-2}, which keeps reducing then on till 1500 CDT as the CBL dries up (Fig. 3.5).

The profiles of $\sigma^2_{h.\,wind_{hi}}$ have near surface (around $0.1z_i$) and near CBL top peaks due to the horizontal outflows in the overturning heterogeneity induced circulations as one would expect in turbulent organised structures (Stull, 1988). The peaks at the CBL top indicate that the circulations extend throughout the CBL height. Furthermore, the near surface and CBL top peaks are at their maximum in the late afternoon at 1500 CDT, at 0.4 $m^2\ s^{-2}$ and 0.8 $m^2\ s^{-2}$ respectively.

During the wind shear driven ABL simulation for 24 September, the spatial variances exhibit similar variations as the 23 August profiles. Here, the $\sigma^2_{w_{hi}}$ peak magnitudes are smaller (Fig. 4.6 f) reflecting the weaker circulations. These profiles show signals of the structures as early as 0900 CDT in the morning (not shown here). For $\sigma^2_{\theta_{hi}}$ too a clear signal for a peak near ABL top isn't seen until 1200 CDT. The ABL top peaks are less narrow than the 23 August values, indicating the stronger role of entrainment in modulating ABL organisation and transport (Sect. 4.3.2.2 and 4.2). The afternoon profile at 1330 CDT shows the same order of peak magnitude $\approx 0.5\ K^2$ as the 1500 CDT profile for 23 August. The peak occurs higher in the boundary layer at $\approx 1.3\ z_i$. Likewise, the $\sigma^2_{q_{hi}}$ peak at the ABL top is wider than the same for 23 August. The afternoon peak value at 1330 is also higher than morning value at 1100 CDT, increasing from 0.2 $g^2\ Kg^{-2}$ to 0.7 $g^2\ Kg^{-2}$ as the near surface moisture values rise during the day (Fig. 3.4, 3.8). The ABL top peak in the moisture variance profiles occur around the same height as the temperature variance profiles $\approx 1.3z_i$. Profiles of $\sigma^2_{h.\,wind_{hi}}$ have a peak only near the ABL top (Fig. 4.6 h). However, for the north-south aligned roll-like heterogeneity induced circulations, variance of the u component of horizontal wind, $\sigma^2_{u_{hi}}$ is larger than that of the v component, $\sigma^2_{v_{hi}}$ and has a higher and distinct near surface peak.

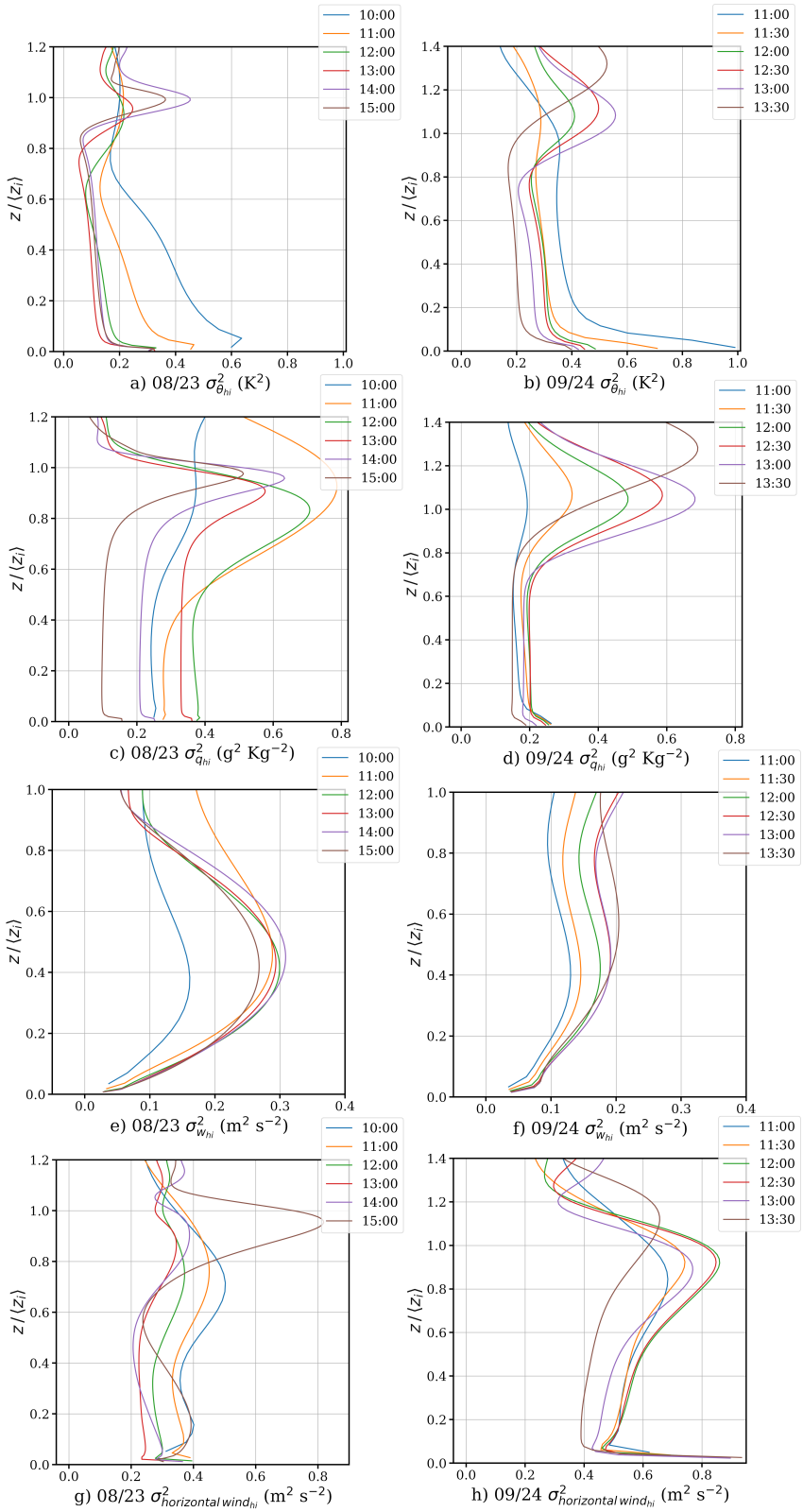

FIGURE 4.6: Vertical profiles of spatial variance of w, u,v, theta and q for Aug 23. Variances were calculated for 30-minute means. They are presented for every hour from 10:00 to 15:00

4.3.2.2 Impact of Heterogeneity Induced Secondary Circulations on Boundary Layer Transport

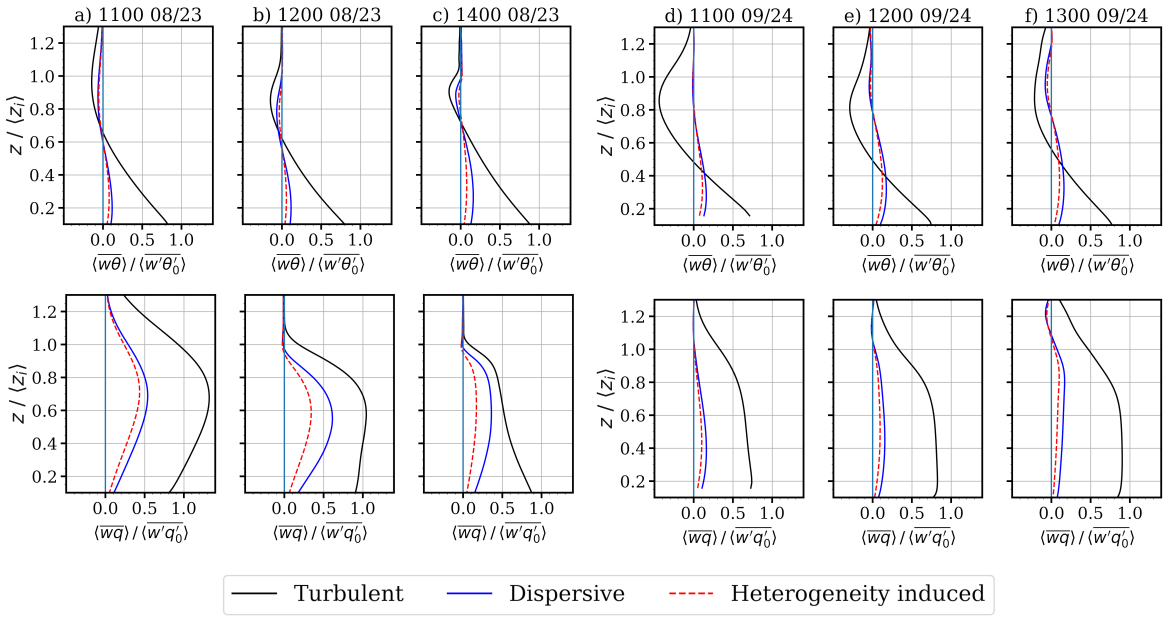

FIGURE 4.7: Domain mean, half-hourly averaged turbulent, dispersive and heterogeneity induced vertical kinematic heat and moisture flux profiles from Child01 model. Each column shows different times during 23 August (a-c) and 24 September (d-e) simulations. Profiles are normalised by the domain mean total surface fluxes at 60 m height (where the sub-grid contributions are near zero). First row shows kinematic heat flux profiles and the second row moisture fluxes

There are persistent flux contributions from heterogeneity induced circulations throughout the ABL for the 23 August and 24 September simulations (Fig. 4.7). Sühring and Raasch (2013) and MR13 also report the effects of heterogeneity induced circulations reaching till the mixed layer top in their simulations of the LITFASS field experiment. For the 23 August simulations, the percentage contribution from dispersive fluxes and their heterogeneity induced component are higher for the moisture flux than the heat flux, reflecting the surface heat flux partitioning of the smaller-scale turbulent fluxes (Fig. 3.10). Latent heat flux magnitudes are higher than the sensible heat fluxes across scales. Airborne flux measurements over the study domain during

the field campaign also reported similar latent and sensible heat flux partitioning across scales Paleri et al. (2022).

Moisture flux profiles at 1100 and 1200 CDT for 23 August indicate that the ABL humidity is controlled more by entrainment of drier air from above the mixed layer top than the surface fluxes. At 1100 CDT, the entrainment fluxes of mixing ratio are almost twice as large as the surface fluxes. The maximum contribution from dispersive moisture fluxes to the total fluxes, with respect to surface fluxes, also occurs during this entrainment driven regime at 1200 CDT and around $0.6z_i$ when they are 60% of the surface flux values (Fig. 4.7 b). Most of this dispersive flux is heterogeneity induced, which is 40% of the surface flux values. The ABL moisture changes to a surface flux driven regime later as seen in the 1400 CDT moisture flux profiles (Fig. 4.7 c). As the ABL continues to grow and becomes more free convective during the day, the peak in the dispersive moisture flux profile at $0.6z_i$ becomes less pronounced and is shifted closer to the ABL top to around $0.8z_i$. Near the CBL top most of the flux contribution to moisture transport is due to these dispersive fluxes. The near surface dispersive fluxes contribution to kinematic heat and moisture fluxes remains around 10-15% of the total surface fluxes for 1100,1200 and 1400 CDT. The heterogeneity induced heat and moisture flux profiles have their maximum values at different heights above the surface. The dispersive flux contributions from heterogeneity induced circulations decrease with increasing w_*, as turbulent convective updrafts get stronger (Fig. 4.2). For the heat fluxes, the heterogeneity induced or dispersive flux contribution for the entrainment fluxes remain low throughout the day.

The H profiles for 24 September simulations show higher mixed layer top entrainment fluxes in the wind shear-driven, forced convective ABL (Fig. 4.7 d,e). The moisture and heat flux profiles at 1100 CDT show a near surface gap because the $z_i = 260$ and with surface = 60 m a.g.l, the

lowest value for $z/z_i \approx 0.16$. For H profile at 1200 and 1300 CDT, the secondary circulations contribute 10-15% of the total surface transport. The mixed layer top entrainment has more impact over the heat flux profiles than the moisture flux profiles as compared to the 23 August simulations. At 1300 CDT when the forced convective ABL is at its maximum height, the percentage contribution from H entrainment fluxes are higher than the fully developed 23 August buoyancy driven CBL values. However, the moisture flux profiles for 1100, 1200 and 1300 CDT indicate a mixed regime, not entirely surface or entrainment driven. The dispersive (and their heterogeneity induced components) moisture flux fractional contributions remain low and are smaller than the 23 August simulations throughout the day. There exists heterogeneity induced flux contributions throughout the ABL as was the case for the free convective simulations. However, the near surface contributions are low, 0-5% for both heat and moisture fluxes throughout the day. The maximum domain mean contributions from dispersive fluxes are never more than $\approx 25\%$ of surface turbulent fluxes. Turbulent fluxes dominate the surface-atmospheric transport for these runs.

4.3.3 Scale analysis

In this section we investigate the relationships between length scales of heterogeneous surface temperature and moisture fields and the simulated atmospheric properties. For our diurnal simulations, Sect. 4.3.3.1 presents the time series of the dominant characteristic surface heterogeneity length scales. In Sect. 4.3.3.2 we present the normalised spectrograms of the instantaneous atmospheric fields, to explore the scale resolved contribution to the resolved flow field and their relationship to the dominant surface scales with respect to the boundary layer height, as the ABL evolves and becomes more free convective. We specifically look at the heterogeneity

induced circulations during the 23 August daytime simulations and also the covariance between surface fluxes and heterogeneity induced atmospheric structures in Sections 4.3.3.3 and 4.3.3.4

4.3.3.1 Effective Surface Temperature and Moisture Heterogeneity Length Scales

The near surface characteristic temperature and moisture fields, θ_* and q_* were calculated from the near surface kinematic heat and moisture flux fields like so:

$$\overline{\theta_*} = (\frac{\overline{w'\theta'_0}}{\overline{u}}),\ \overline{q_*} = (\frac{\overline{w'q'_0}}{\overline{u}}),$$

where $\overline{w'\theta'_0}$ and $\overline{w'q'_0}$ are the near surface resolved scale turbulent kinematic heat and moistue fluxes, and $\overline{u}$ is a velocity scale, chosen as w_* for the convective 23 August simulations and u_* for the wind shear driven 24 September simulations. The surface flux data was calculated as the sum of the LSM flux output and the vertically integrated canopy heat flux from the PCM.

Effective horizontal heterogeneity length scales for the study domain were calculated following Panin and Bernhofer (2008). Power spectra for the 2D θ_* and q_* fields were calculated in the x and y directions, and the length scales with maximum power were identified as l_x and l_y. This gives characteristic length scales in the x and y directions as $\overline{L_x} = 1/2(l_x)$ and $\overline{L_y} = 1/2(l_y)$. The effective heterogeneity length scale was then calculated as $L^{eff} = \frac{\overline{L_x}+\overline{L_y}}{2}$.

In the 23 August runs, the effective thermal heterogeneity length scale, L_θ^{eff} remains almost constant throughout the day from 1000 to 1600 CDT, with a maximum value of 4400 m (Fig. 4.8 a). The effective moisture heterogeneity length scale L_q^{eff} values for the same runs peak at

1030 CDT at 5500 m, decreasing to 5000 m at 1200 CDT and then stay the same throughout the day. The L_θ^{eff} and L_q^{eff} values in the fully developed CBL (from 1300 CDT) differ by $\approx$ 600 m. For the 24 September runs from 1000 to 1400 CDT, L_θ^{eff} and L_q^{eff} values are closer to each other for most of the time (Fig. 4.8 b), with no significant trends. The mean $L_\theta^{eff} = 4377$ m during this time period and the mean $L_q^{eff} = 4688$ m. The magnitudes of L_q^{eff} and L_θ^{eff} reflect the Bowen ratio patterns for the near surface fluxes during the August and September test cases (Fig. 4.2 c, d).

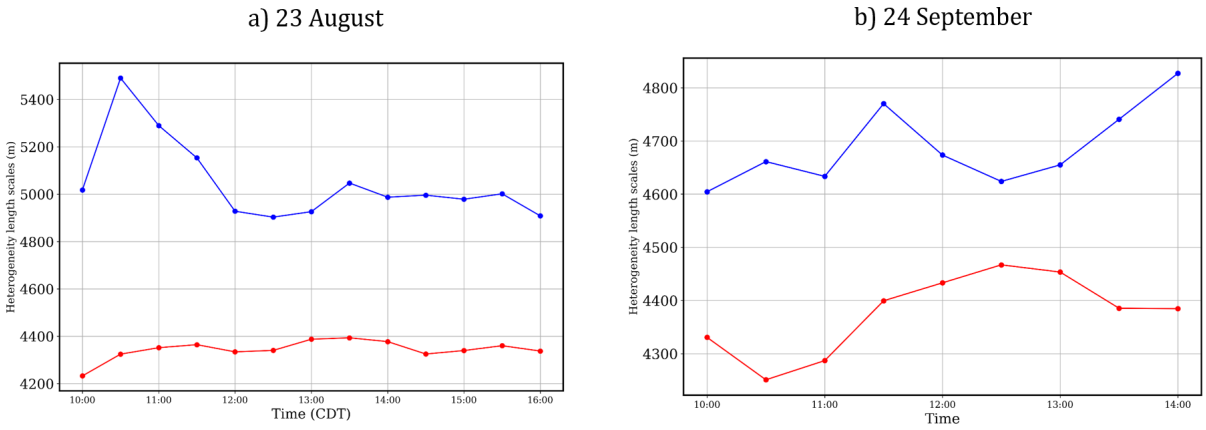

FIGURE 4.8: Effective Surface heterogeneity length scales for a) 23 August and b) 24 September simulations. Calculated from the surface sensible (in red) and latent (in blue) heat fluxes. The surface fluxes were normalised by w_* for 23 August values and u_* for the 24 September values

4.3.3.2 Length Scales of Instantaneous Atmospheric Fields

To investigate the constituent scales of motion in the resolved flow field, we investigate spectrograms (Sect. 4.2.1) of simulated atmospheric properties during the 23 August and 24 September simulations.

In Figure 4.9 we present spectrograms of azimuthally averaged and normalised 2D power spectral densities on 24 August runs for the instantaneous fields of w, theta and q in columns i, ii and

iii respectively and cospectra of w and theta in column iv and and the cospetcra of w and q in column v. The spectrograms calculated for the wind shear driven boundary layer at 1100 CDT, with $-\frac{z_i}{L} = 11$, are presented in the first row (a) and those for the convective boundary layer at 1400 CDT, with $-\frac{z_i}{L} = 51$, are presented in the second row (b). The spectrograms presented are the ensemble mean snapshots from all 8 ensemble members of both the IOP simulations.

At 1100 CDT, with $\langle z_i \rangle = 657$ m, both L_θ^{eff} and L_q^{eff} are $\sim 10\langle z_i \rangle$. Later during the day as the boundary layer grows and a well mixed CBL develops at 1400, the length scales scale as $3\langle z_i \rangle$.

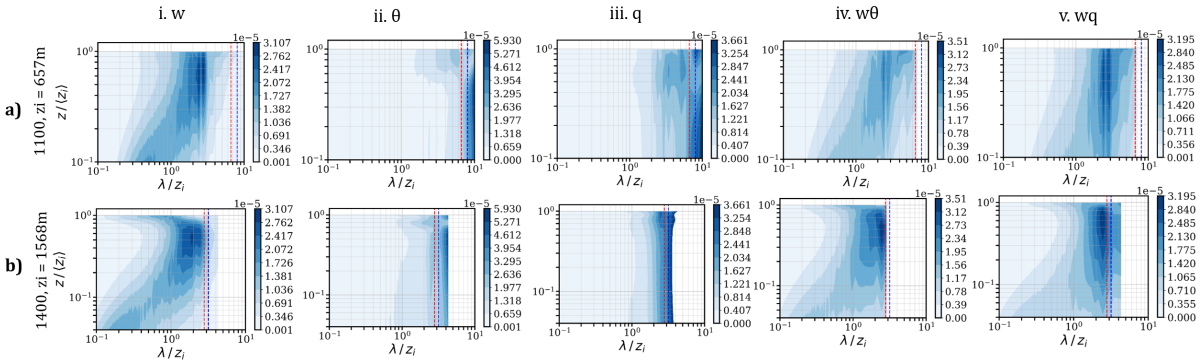

FIGURE 4.9: Spectrograms of azimuthally averaged and normalised 2D power spectral densities for the instantaneous atmospheric properties at a) 1100 CDT and b) 1400 CDT for the 23 August simulations. x-axis values are the wavelengths normalised by the domain mean z_i and y-axis is the vertical distance from the surface normalised by domain mean z_i. The dashed vertical red line represents the L_θ^{eff} and the dashed vertical blue line represents the L_q^{eff} from Fig. 4.8. Columns i, ii and iii show the spectra for w, θ q and columns iv and v show the cospectra for w and θ; w and q respectively. The spectrograms are averaged over the 8 ensemble runs

The w spectrograms at 1100 and 1400 CDT (Fig. 4.9 a.i, b.i) show two pectral peaks, the first near the surface in the surface layer of the ABL and the second higher up in the boundar layer, at heights $0.4\langle z_i \rangle$ and above at 1100 CDT and around $0.5\langle z_i \rangle$ at 1400 CDT. Near the surface, smaller scale eddies contribute the most for the vertical velocity fluctuations. At 1100 CDT, at $0.1\langle z_i \rangle$ they $\sim 0.5\langle z_i \rangle$. At 1400 in the CBL, these near surface eddies with the most spectral power become smaller with respect to $\langle z_i \rangle$ and scale as $0.2\langle z_i \rangle$ - $0.3\langle z_i \rangle$. However, considering

the ABL growth from 1100 to 1400, their absolute magnitudes remain $\approx$ 300 m. The secondary peak in the w spectra is more focused around $0.5\langle z_i \rangle$ at 1400 while at 1100 it extends from $0.4\langle z_i \rangle$ - $\langle z_i \rangle$.

The spectrograms for the scalar spectra of θ (Fig. 4.9 a.ii, b.ii) and q (Fig. 4.9 a.iii, b.iii) are qualitatively similar, with most of the power at all heights in the largest of scales, that also scale as L_θ^{eff} and L_q^{eff}. The spectrograms for the cospectra of w and θ (Fig. 4.9 a.iv, b.iv) and q (Fig. 4.9 a.v, b.v) are also qualitatively similar. At 1100 CDT both the cospectra show higher powers at wavelengths $\sim 3\langle z_i \rangle$, which extend throughout the boundary layer height. This reflects the larger scale contribution seen in the w spectra in Fig. 4.9 a.i and the dispersive flux contributions in Fig. 4.11. At 1400 CDT, eddies with higher powers are still found in scales $\sim 3\langle z_i \rangle$, moreover they are also of the same order of magnitude as L_θ^{eff} and L_q^{eff}. These larger scale eddies contribute the most to the $w\theta$ cospectra at $0.5\langle z_i \rangle$. The wq cospectra show strong contributions from the larger scale eddies from almost $0.1\langle z_i \rangle$ to $0.8\langle z_i \rangle$. In our simulations for 23 August, smaller scale boundary layer eddies contribute more for the ABL top entrainment in the well mixed CBL at 1400 CDT than the morning boundary layer at 1100 CDT.

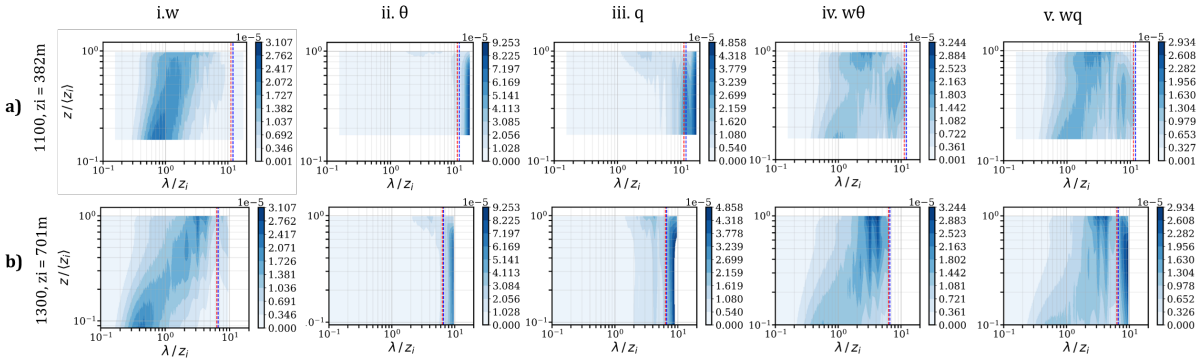

FIGURE 4.10: Same as Fig. 4.9, but for the 24 September simulations.

Figure 4.10 shows the spectrograms for the instantaneous atmospheric fields for the 24 September simulations. The spectrograms calculated at 1100 CDT, with $-\frac{z_i}{L} = 1.9$, are presented in the first row (a) and at 1300 CDT in the afternoon, with $-\frac{z_i}{L} = 2.5$, are presented in the second row (b). The spectra and cospectra show similar patterns as the 1100 CDT spectrograms for 23 August.

At 1100 CDT the w spectra show higher powers in smaller wavelengths $\sim 0.8\langle z_i \rangle$ closer to the surface (Fig. 4.10 a.i). Towards the ABL top, slightly larger scale eddies $\sim \langle z_i \rangle$ contribute more to the power spectra, indicating the role played by larger scale eddies in the entrainment fluxes in the shear driven ABL. At 1300 CDT, the eddies with most energy near the surface become smaller relative to the $\langle z_i \rangle$, at $\sim 0.4\langle z_i \rangle$. The absolute magnitudes of their length scales remain of the same order, at ≈ 300 m. Concurrently the eddies at the ABL top with the most energy become larger with respect to $\langle z_i \rangle$, scaling $\sim 3\langle z_i \rangle$ than their 1100 CDT counterparts.

The θ (Fig. 4.10 a.ii, b.ii) and q (Fig. 4.10 a.iii, b.iii) spectra are similar to the 23 August simulation results, with most of the power at all heights in the largest of scales, that also scale as L_θ^{eff} and L_q^{eff}. The cospectra for w,θ and w,q at 1100 CDT (Fig. 4.10 a.iv, a.v) show spectral

peaks that reflect contributions from the w spectra and the θ, q spectra. The cospectra show a lower wavelength peak near the surface and a higher wavelength peak near $\langle z_i \rangle$, similar to the w spectra. They also show another peak near $0.5\langle z_i \rangle$ at longer wavelengths $\sim 0.8\langle z_i \rangle$, which would be the contributions from the θ and q structures.

At 1300 CDT, the w,θ cospectra (Fig. 4.10 b.iv) show higher powers for wavelengths at $3\langle z_i \rangle$ and $4\langle z_i \rangle$, that extends from almost $0.2\langle z_i \rangle$ till the ABL top. The w,q cospectra (Fig. 4.10 b.v) show similar peaks at wavelengths $\sim 3\langle z_i \rangle$ and $4\langle z_i \rangle$. These peaks are stronger near the ABL top and decrease towards $0.2\langle z_i \rangle$. The cospectra also show another peak at larger wavelengths $\sim 10\langle z_i \rangle$, indicating the low frequency contributions from q structures.

4.3.3.3 Length Scales of Surface Heterogeneity Induced Fluxes in the Convective Boundary Layer

To examine the scale composition of the simulated heterogeneity induced fluxes, we analyse the cospectra of w_{hi}, θ_{hi} and w_{hi}, q_{hi} for the 23 August simulations, when the contributions from the heterogeneity induced fluxes were substantial. Figure 4.11 presents spectrograms for the cospectra at 1100, 1200 and 1400 CDT. Most of the cospectral powers were in wavelengths $> \langle z_i \rangle$ and so the x-axis ranges were limited to reflect the same.

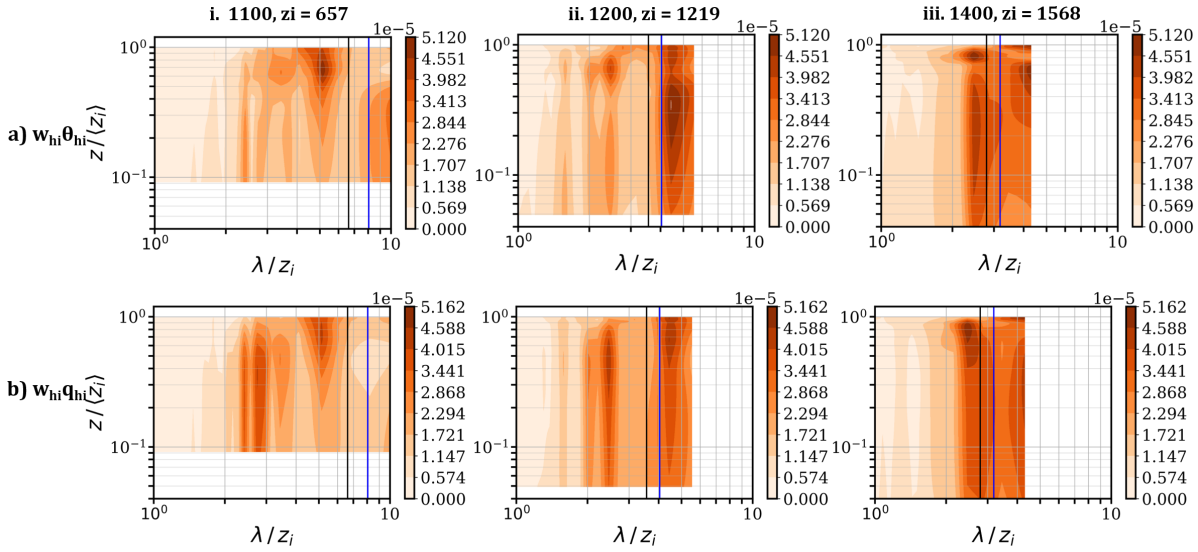

FIGURE 4.11: Spectrograms of azimuthally averaged and normalised 2D power cospectral densities of the surface heterogeneity induced a) w and θ and b) w and q for the 23 August simulations. x-axis values are the wavelengths normalised by the domain mean z_i and y-axis is the vertical distance from the surface normalised by domain mean z_i. Columns i, ii and iii show the spectrograms at 1100, 1200 and 1400 CDT respectively. The solid vertical black line represents L_θ^{eff} and the solid vertical blue line represents L_q^{eff} from Fig. 4.8

At 1100 CDT, the w_{hi}, θ_{hi} and w_{hi}, q_{hi} cospectra show higher powers at wavelengths $\sim 5\langle z_i \rangle$. This scale is slightly smaller than L_θ^{eff}, which scales as $7\langle z_i \rangle$ and L_q^{eff}, which scales as $8\langle z_i \rangle$. The w_{hi}, q_{hi} cospectra show another double peak at smaller wavelengths that $\sim$ 1.5-2$\langle z_i \rangle$ that extends from near the surface upwards till the ABL top. These would be contributions from the w_{hi} structures in the flow (Fig. 4.15 a.i). These effects of the w_{hi} structures are lower in the w_{hi}, θ_{hi} cospectra and the peak at $5\langle z_i \rangle$ stands out, extending from almost $0.2\langle z_i \rangle$ upwards from the surface till $\langle z_i \rangle$.

At 1200 CDT the cospectral structure of the fluxes are similar to the 1100 CDT patterns. The spectral peak in the longer wavelengths still scales as $5\langle z_i \rangle$ but now they also are of the same order of magnitude as L_θ^{eff} and L_q^{eff}, which are $\sim 4\langle z_i \rangle$. The peak in w_{hi}, θ_{hi} cospectra shifts lower in the boundary layer at 0.3-0.4$\langle z_i \rangle$. The spectral peaks in w_{hi}, q_{hi} cospectra have

contributions throughout all of the CBL at 1200, with the smaller scale wavelengths at $\sim$ 1-1.5$\langle z_i \rangle$ driving the surface fluxes and the larger scale eddies at $\sim 5\langle z_i \rangle$ driving the entrainment fluxes at the CBL top.

At 1400 CDT when the CBL is fully developed, the cospectral peaks and effective heterogeneity length scales scale as $3\langle z_i \rangle$. The cospectra for both w_{hi}, θ_{hi} and w_{hi}, q_{hi} show contributions in this scale throughout the CBL height. The vertical distribution of cospectral powers are in line with the scale integrated picture of the domain-mean heterogeneity induced fluxes presented in Fig. 4.7.

4.3.3.4 Surface Atmospheric Interactions

To explore the response of boundary layer structures to surface heterogeneities, we calculated spectrograms for the cospectra of surface fluxes ($w\theta_0$ and wq_0) with the heterogeneity induced atmospheric structures, w_{hi}, θ_{hi}, q_{hi} and the heterogeneity induced fluxes $w_{hi}\theta_{hi}$, $w_{hi}q_{hi}$ for the 23 August simulations.

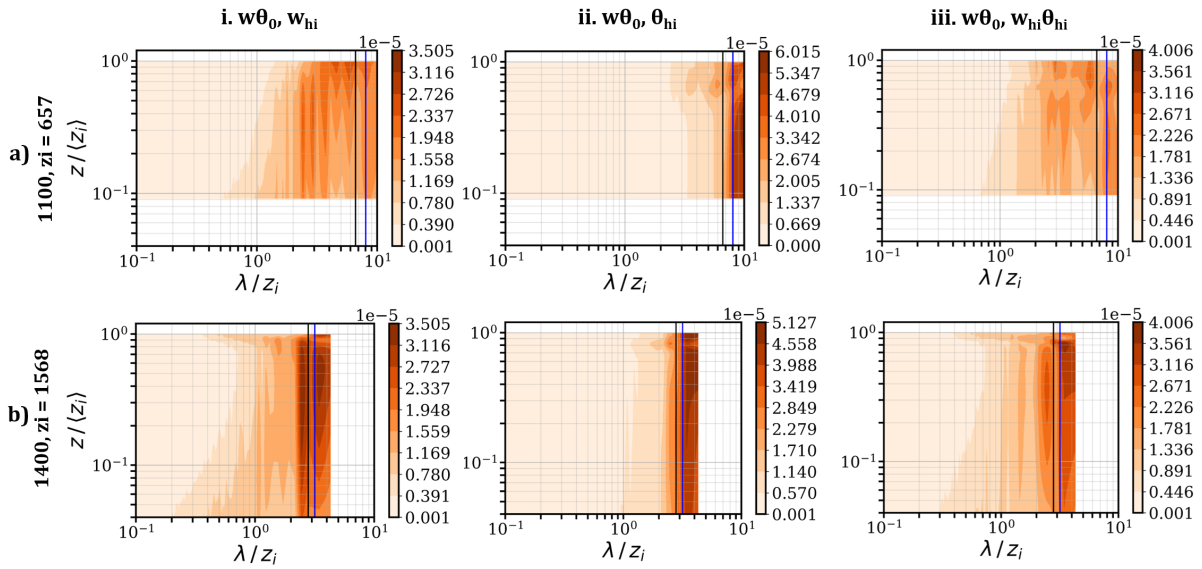

FIGURE 4.12: Spectrograms of azimuthally averaged and normalised 2D power cospectral densities of the surface heterogeneity induced a) w and θ and b) w and q for the 23 August simulations. x-axis values are the wavelengths normalised by the domain mean z_i and y-axis is the vertical distance from the surface normalised by domain mean z_i. Columns i, ii and iii show the spectrograms at 1100, 1200 and 1400 CDT respectively. The solid vertical black line represents the dominant θ_* length scale and the solid vertical blue line represents the dominant q_* length scale from Fig. 4.8

Figure 4.12 presents the cospectra of surface heat flux ($w\theta_0$) with w_{hi}, θ_{hi} and $w_{hi}\theta_{hi}$ at 1100 and 1400 CDT. At 1100 the $w\theta_0$, w_{hi} cospectra show spectral peaks at larger wavelengths from 2 to 7 times $\langle z_i \rangle$ throughout the ABL height. The peaks at 2-3$\langle z_i \rangle$ are indicative of the w_{hi} contributions seen in the Fig. 4.15 a.i. The cospectra of $w\theta_0$ with θ_{hi} and $w_{hi}\theta_{hi}$ at 1100 CDT also show stronger contributions from the larger scales throughout the ABL (Fig. 4.12 a.ii,a.iii). The $w\theta_0$, θ_{hi} cospectral peak is $\sim$ 9-10$\langle z_i \rangle$ and scales as the effective heterogeneity length scales. The $w\theta_0$, $w_{hi}\theta_{hi}$ cospectra has a broader range of energy containing wavelengths, ranging from 2 to 10 times $\langle z_i \rangle$, indicative of the cospectral power distribution for w_{hi}, θ_{hi} (Fig. 4.11 a.i)

At 1400 CDT, all of the cospectra considered show peaks at all heights at the same wavelengths as L_θ^{eff} and L_q^{eff} and they $\sim 3\ \langle z_i \rangle$. Near surface, the $w\theta_0$, $w_{hi}\theta_{hi}$ cospectra at 1400 CDT show

powers in smaller wavelengths $\sim 0.6\langle z_i \rangle$ than the 1100 CDT cospectra. This arises becasue, at 1400 CDT the w_{hi} structures tend to become smaller scale than their early morning counterparts and more localised (Figures 4.5 b, 4.15 b.i).

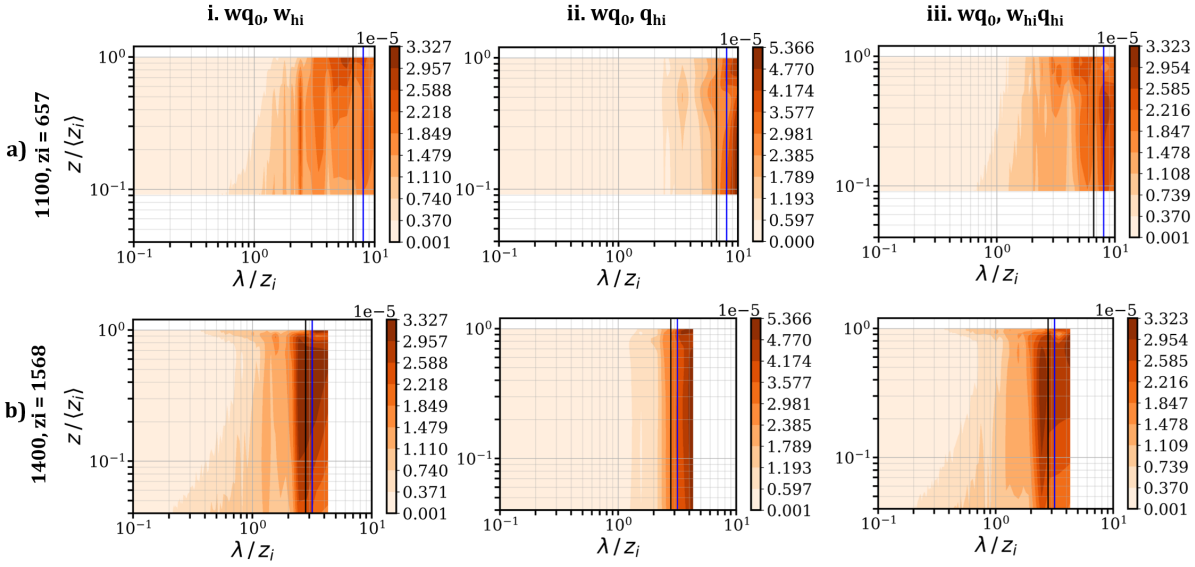

FIGURE 4.13: Spectrograms of azimuthally averaged and normalised 2D power cospectral densities of the surface heterogeneity induced a) w and θ and b) w and q for the 23 August simulations. x-axis values are the wavelengths normalised by the domain mean z_i and y-axis is the vertical distance from the surface normalised by domain mean z_i. Columns i, ii and iii show the spectrograms at 1100, 1200 and 1400 CDT respectively. The solid vertical black line represents the dominant θ_* length scale and the solid vertical blue line represents the dominant q_* length scale from Fig. 4.8

Similar to the cospectra of the surface heat flux with the heterogeneity induced fields, the cospectra of surface moisture flux (wq_0) with w_{hi}, q_{hi} and $w_{hi}q_{hi}$ show a broader range of energy containing eddy length scales at 1100 CDT and a tighter range at 1400 CDT, around the effective heterogeneity length scales (Fig. 4.13). The cospectral peaks extend throughout the ABL, indicating surface atmospheric coupling in the larger scales throughout the boundary layer height.

4.4 Discussion

Our first question was, whether diagnosing and quantifying these circulations and their associated surface flux transport can help observe the "true" transport across a heterogeneous domain? Time-ensemble averaging of the 3D LES data, following Maronga and Raasch (2013a), allowed us to separate the signals of land surface heterogeneity induced secondary circulations (Fig. 4.5) from the signals of turbulent organised structures and background ABL turbulence. Through this approach we calculated the domain mean profiles of turbulent, dispersive (Sect. 4.2.1.2) and the heterogeneity induced contribution to the dispersive fluxes (Eq. 4.4, 4.5, Fig. 4.7). The near surface dispersive fluxes' contribution to kinematic heat and moisture fluxes remain around 10-15% of the total surface fluxes for both the 23 August and 24 September simulations. This contribution increases with height in the ABL. The calculated heat and moisture flux profiles for our simulation setup indicate that there is a persistent, non-negligible surface heterogeneity induced flux transport in shear and buoyancy driven ABLs.

Secondly, we asked how do the effects of these heterogeneity induced circulations vary over the diurnal cycle and across seasons, with changing atmospheric boundary layer height (z_i) and stabilities? We found that the flux contributions from heterogeneity induced circulations are substantial in buoyancy driven CBL with weaker boundary layer winds. The heterogeneity induced flux partitioning between H and LE is reflective of the surface flux partitioning, with LE dominating over H for 23 August and of the same order of magnitudes in the 24 September simulations. This simulated dispersive flux partitioning is in line with the mesoscale fluxes measured from near surface (100 m) airborne fluxes across the domain during the August and September IOPs (Paleri et al., 2022).

Finally, we questioned how do the effects of heterogeneity induced structures scale with the length scales of surface heterogeneity and the boundary layer height? In Sect. 4.3.3 we found that in the simulated wind shear driven boundary layers, the w_{hi} structures contribute towards near surface transport of heterogeneity induced heat and moisture fluxes at wavelengths $\sim$ 2-3$\langle z_i \rangle$. At the boundary layer top longer wavelengths that $\sim 5\langle z_i \rangle$ contribute the most towards the entrainment due to heterogeneity induced fluxes. In the simulated convective boundary layers, wavelengths $\sim 3\ \langle z_i \rangle$ contribute towards most of the heterogeneity induced fluxes throughout the boundary layer height. The calculated effective surface heterogeneity length scales are also of the same order of magnitude, indicating a stronger surface-atmospheric coupling during the more convective conditions.

The evolution and transitions of organised structures in the diurnally evolving free convective turbulent boundary layer has not received much attention in literature (Salesky et al., 2017). In our simulations, we see the heterogeneity induced secondary circulations starting to transition from along-wind horizontal convective rolls to shorter length scale cellular structures around 1330 - 1400 CDT simulation time on 23 August when -$z_i/L \approx 40$ m. This value of ≈ 40 m is higher than what has been reported in some of the previous observational and numeric studies (Grossman (1982); Weckwerth et al. (1999); Salesky et al. (2017) ; -$z_i/L \approx 15 - 25$ m). The delayed break down of roll-like structures in our simulations with respect to the prior reported threshold could be due to the memory in the diel evolution of surface heat fluxes and boundary layer winds in our simulations. LeMone et al. (2010b) reported observed roll-like organisation from tower measured values of -$z_i/L = 49$ m and LES values of 41 m. The transition from horizontal rolls to cellular or disorganised local convection needs to be quantified by an objective metric for linear organisation, like the Roll factor proposed by Salesky et al. (2017) which is a

two-point correlation metric calculated in cylindrical coordinates.

During 23 August simulation, we found that the heterogeneity induced circulations become more localised and also extend throughout the CBL height as the CBL grows and becomes more free convective in the afternoon (1300-1500). LES studies with idealised 1 and 2 dimensional heterogeneities have shown that heterogeneity length scales $< z_i$ would not have appreciable effects on horizontally averaged vertical fluxes and moments of ABL turbulence statistics (Stoll et al., 2020). Using their LES over irregular and unstructured heterogeneities with multiple surface length scales, MR13 showed that smaller scales become less important with increasing z_i. AT 1500 CDT on 23 August the heterogeneity induced circulations on the western sector of the model domain have longer length scales, compared to the circulations on the east-south east sector (Fig. 4.14 b). Signals of these smaller scale circulations can be seen in the spectrogram for w_{hi} at 1400 CDT, with higher powers in smaller wavelengths (Fig. 4.15 b.i) when compared to the 1100 CDT spectra (Fig. 4.15 a.i). The rising, spatially bound secondary circulation updrafts extend the local z_i to greater than the domain mean values on the western edge of the model domain (Fig. 4.14 a, $\sim$ y = 10 km to y = 25 km). A clear signal for the same can also be seen on the eastern edge of the lake at the northern edge of the domain (Fig. 3.1). These lake-induced circulations are established perpendicular to the mean easterly wind ($\approx$ 2 m s^{-1}), consistent with previous LES studies with prescribed surface fluxes (MR13, Prabha et al. (2007)).

The z_i cross sections showed clearer signals of roll-like secondary circulations during the morning ABL at 1100 CDT on 23 August when -z_i/L = 10. However, the circulations grew taller (while the heterogeneity induced vertical velocities remain at the same strengths, Fig. 4.6 d) as the boundary layer became more free convective and well mixed later during the day. During the 24

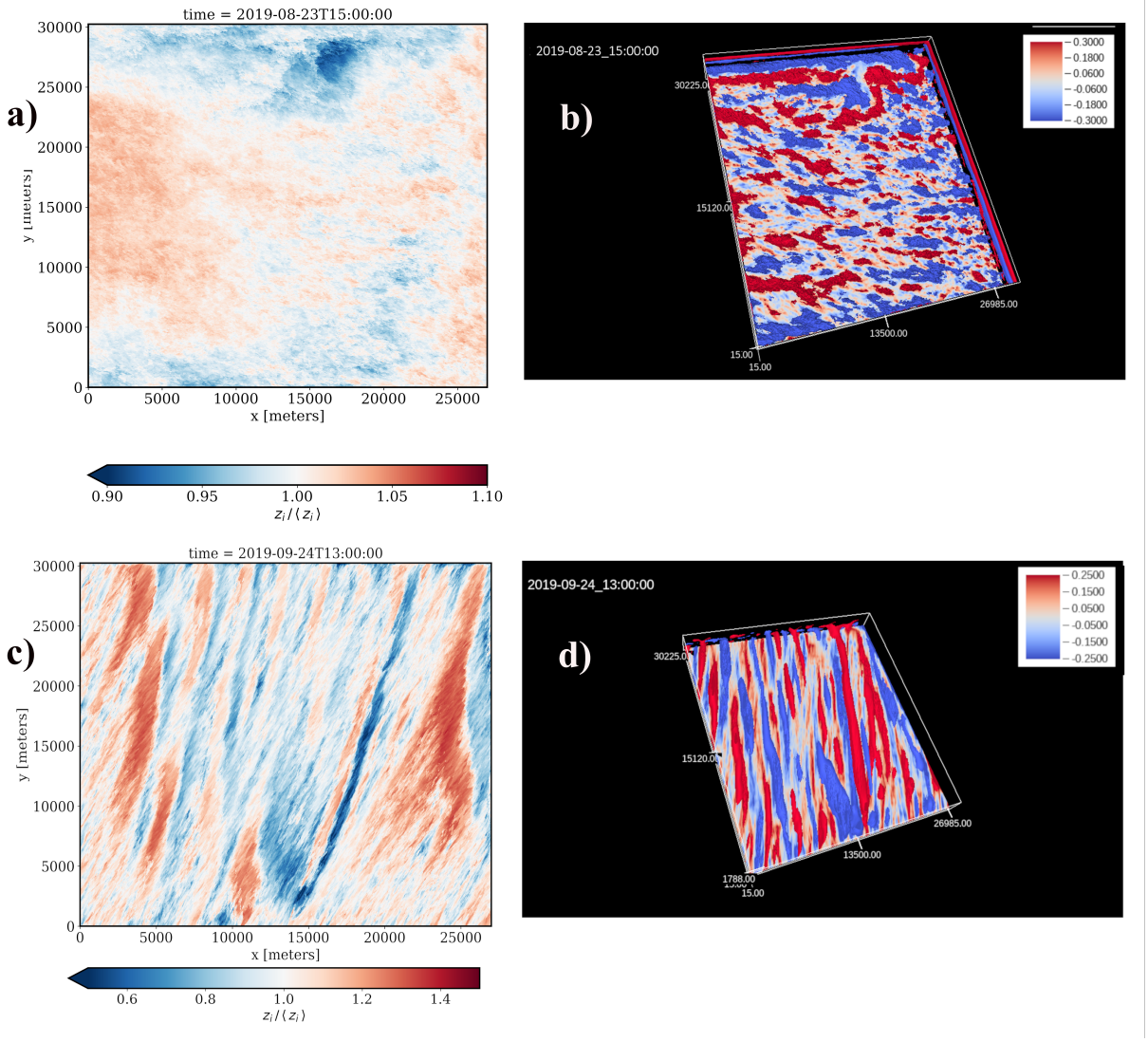

FIGURE 4.14: Time-ensemble averaged z_i (a) and w_{hi} isosurfaces (b) for 1500 08/23. Time-ensemble averaged z_i calculated as the height of minimum sensible heat flux (c) and w_{hi} isosurfaces for 1300 09/24 (d)

September simulations, the heterogeneity induced secondary circulations were much weaker (Fig. 4.6 h) due to the stronger boundary layer winds (reaching a mean value ≈ 7 m s^{-1} around 1200 CDT (Fig. 4.3) in the shear driven CBL. The circulations organised as rolls roughly along the mean wind direction and remained so throughout the ABL life cycle. However, when the mixed layer top was calculated as the height of minimum sensible heat flux, horizontal cross-sections of z_i showed clearer signals of the secondary circulations and the persistent heterogeneity induced

circulations (Fig. 4.14, c, d). This suggests a coupling between mixed layer top entrainment, ABL organisation and the land surface in forced convective ABLs as well (Sühring et al., 2014). In their LES using an idealised chessboard-type heterogeneities Raasch and Harbusch (2001) reported secondary circulations induced by surface heat flux patterns, even when the mean winds were 7.5 m s^{-1}, when the mean winds were aligned diagonally to the surface heterogeneities.

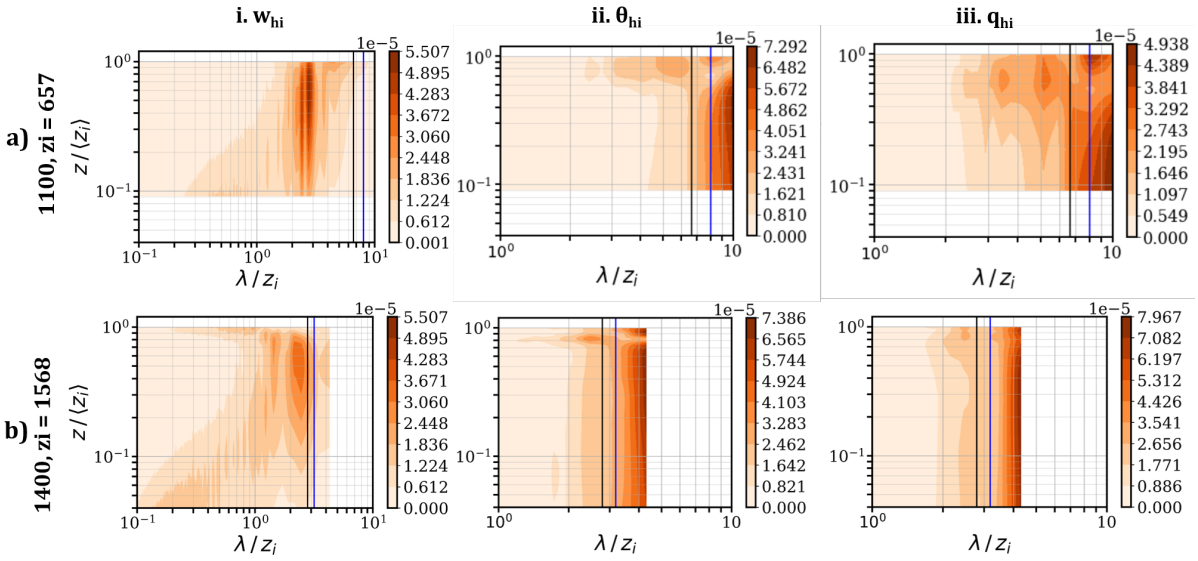

FIGURE 4.15: Spectrograms of azimuthally averaged and normalised 2D power spectral densities for the heterogeneity induced fields at a) 1100 CDT and b) 1400 CDT for the 23 August simulations. x-axis values are the wavelengths normalised by the domain mean z_i and y-axis is the vertical distance from the surface normalised by domain mean z_i. The solid vertical black line represents the L_θ^{eff} and the solid vertical blue line represents the L_q^{eff} from Fig. 4.8. Columns i, ii and iii show the spectra for w, θ q respectively. The spectrograms are averaged over the 8 ensemble runs

Blending height is a conceptual framework used to denote the vertical limit of the influence of surface heterogeneities on the atmospheric boundary layer (Mahrt 2000). The general formulation for blending height, z_{blend} can be expressed as

$$z_{blend} = C(\frac{v}{U})^p L_{hetero},$$

as per Eq. 1 in Mahrt (2000). Here C and p are numerical coefficients usually taken as 1

and 2 respectively, v a characteristic velocity such as u_* or w_*, U a velocity scale such as the mean wind and L_{hetero} a characteristic length scale of surface heterogeneities. Wood and Mason (1991) derive a thermal blending height where the velocity ratio becomes $\frac{\overline{w'\theta'_{sfc}}}{U\Theta_0}$ with $\overline{w'\theta'_{sfc}}$ the spatially averaged surface heat flux and Θ_0 the averaged potential temperature. In their LES parametric study over a range of surface roughness and characteristic length scales for neutrally stratified ABL, Bou-Zeid et al. (2004) report that internal boundary layers downstream of surface transitions reach blending height. In a follow-up study Bou-Zeid et al. (2007), they validated their analytic formulations of an effective aerodynamic roughness length over 2D squares of varying roughness for neutrally stratified ABL.

From their LES study of the LITFASS-2003 field campaign, Sühring and Raasch (2013) report correlation between surface and atmospheric heat fluxes that extend throughout the boundary layer, indicating that a blending height does not exist for their study domain. The heterogeneity induced flux profiles reported by MR13 for their simulations also showed persistent contributions throughout the boundary layer height. Our simulations of the CHEESEHEAD19 field campaign also indicate the same, especially for the free convective summer time boundary layer. We see substantial contributions from heterogeneity induced components throughout the ABL (Fig. 4.7, Fig. 4.11). Heterogeneity induced flux contributions for the moisture fluxes in the simulations for the CBL on 23 August have their maximum around $0.6z_i$ at 1100 and 1200 CDT, while the CBL humidity is dominated by mixed layer top entrainment. This peak moves further up in the ABL later in the day at 1400 CDT as the boundary layer moisture profile is dominated by surface fluxes (Fig. 4.7.

The conventional formulations for blending height is derived from linear scaling arguments based on internal boundary layer (IBL) and footprint theory Mahrt (1996). Hence, such linear

approximations would not be the best models for the atmospheric boundary layer over complex surfaces with unstructured heterogeneity at multiple scales. For example, an idealised spanwise heterogeneous (along-wind strips) surface can cause an internal boundary layer growth, resulting in a blending height which would essentially be the top of the IBL and which can be so modeled. However, with a more complex surface features and gradients, there could be internal boundary layers within internal boundary layers and the surface-atmospheric flux at a height z can have strong non-local upstream influences from multiple sources. Modeling that would not be trivial and our simulations provide a snapshot of the mean state for such a scenario.

The LES study of Omidvar et al. (2020) identifies advection-dominated (plume) and convectively-driven (bubble) regimes of surface influence on the vertical structure of ABL growth. They categorise the secondary circulations in their LES with an idealised urban canopy into the two regimes with scaling arguments based on w_* of the urban (built-up) and rural areas, and the bulk mean inflow speed (U). With sufficient heterogeneity amplitude and length scale, surface effects can scale till the ABL top to impact entrainment and boundary layer growth (Sühring et al., 2014; van Heerwaarden et al., 2014). Hence, modelling the effects of surface heterogeneities on the ABL would have to take into consideration, not only atmospheric flow fields, but also the amplitudes and scales of surface gradients (Ovchinnikov et al., 2022). This calls for scale aware parameterisation techniques for boundary layer transport in weather and climate models, which could follow on the footsteps of the mosaic-tiling approaches (Avissar and Pielke, 1989). As a first order, linear approximation, one could disentangle the dominant modes of surface heterogeneity and model their scale dependent contribution to vertical surface-atmosphere transport specific to those scales and estimate the total transport as a linear combination of all the dominant modes. The validity of such an approach needs to be investigated further with

numerical simulations over multi-scale heterogeneities that resemble realistic field conditions.

Ghannam et al. (2017) discusses the non-local character of ABL turbulence in free convective boundary layers. They give a concise review of the common modelling approaches that correct for, or modify down-gradient diffusion approximations, such as Eddy-Diffusivity Counter Gradient (EDCG) (Deardorff, 1972a; Troen and Mahrt, 1986; Holtslag and Moeng, 1991; Holtslag and Boville, 1993), Transport Asymmetry (Moeng and Wyngaard, 1984, 1989; Wyngaard and Brost, 1984; Wyngaard and Weil, 1991; Wyngaard and Moeng, 1992), Third Order Momentum Parameterization (TOMP) (Canuto et al., 1994; Abdella and McFarlane, 1997; Gryanik and Hartmann, 2002), and Eddy Diffusivity–Mass Flux (EDMF) (Siebesma and Cuijpers, 1995; Siebesma and Teixeira, 2000; Siebesma et al., 2007). Models for convective mass flux in EDMF approaches (Eq. 5 in Siebesma et al. (2007)) involve parameterisations for a mass flux along with a convective up-draft model. Using consistent assumptions for sub-grid heterogeneity in land surface schemes and convective mass fluxes (in Mass Flux based approaches such as EDMF) can help in representing the sub-grid coupling between land surface and atmospheric heterogeneities (Simon et al., 2021; Witte et al., 2022). Our findings about the surface and atmospheric heterogeneity length scales can help to inform such representations of surface-atmospheric coupling.

4.5 Summary and Conclusions

We performed coupled LES of the CHEESEHEAD19 field experiment days and then diagnosed them to identify secondary circulations induced by the heterogeneous land surface through time and ensemble averaging. We focused on the simulated daytime data during the 23 August and 24 September simulations, when all of the ABL was fully resolved in our Child01 model. Our

coupled simulations reveal quasi-stationary and persistent heterogeneity induced secondary circulations in the daytime ABL over the CHEESEHEAD19 study domain that span the entire mixed layer height. We present their variation in time and space, through diurnal simulations of two days in late summer (22, 23 August 2019) and two days in early autumn (24, 25 September 2019) CHEESEHEAD19 IOPs. The near surface dispersive flux contribution to both the kinematic heat and moisture fluxes are 10-15% of the total daytime surface fluxes for the CBL in August simulations. In the wind shear driven September simulations with a near neutral ABL, the near surface dispersive flux contribution to kinematic heat remains at 10-15% of total surface fluxes while the dispersive moisture flux contributions are lesser than 5%. Our simulations show persistent contributions from the surface heterogeneity induced fluxes throughout the atmospheric boundary layer for both the wind shear and buoyancy driven boundary layers. In the convective boundary layer, wavelengths that scale as the effective surface heterogeneity length scales at $\sim 3z_i$ contribute the most to the heterogeneity induced transport. The present study illustrates the role of ABL static stability (the relative role wind shear vs buoyancy), z_i and surface heterogeneity length scales in modulating the contributions from secondary circulations induced by unstructured land surface heterogeneity.

Acknowledgements

This material is based in part upon work supported by the National Science Foundation through the CHEESEHEAD19 project (Grant AGS-1822420). The contribution of Luise Wanner was supported by Deutsche Forschungsgemeinschaft (DFG)Award #406980118 and the MICMoR Research School of KIT. We thank the developers of PALM at the Institute of Meteorology and Climatology of Leibniz Universität Hannover, Germany for the open source model and their technical support. We would like to acknowledge high-performance computing support

from Cheyenne (doi:10.5065/D6RX99HX) provided by NCAR's Computational and Information Systems Laboratory, sponsored by the National Science Foundation.

Author contributions

SP, LW, and ARD acquired computational resources. SP performed the final production model runs and the formal analysis. SP, LW, and ARD were responsible for data curation. SP prepared the original draft. SP, LW, MS, ARD, and MM reviewed and edited the manuscript drafts. SP and LW created visualisations. ARD, MS and MM provided supervision. ARD and MM acquired funding.

Chapter 5

Conclusion

5.1 Summary and Outlook

This study aimed to address the role of land surface heterogeneities in surface atmospheric transport. Specifically, I wanted to study how unstructured land surface heterogeneities can modulate the atmospheric boundary layer response to it. To this end, I used high resolution airborne measurements and large eddy simulations of the CHEESEHEAD19 field campaign to investigate the contributions from low-frequency landscape scale eddies to surface-atmospheric fluxes. The Chequamegon Heterogeneous Ecosystem Energy-balance Study Enabled by a High-density Extensive Array of Detectors 2019 (CHEESEHEAD19) was a field campaign designed to intensively sample and scale the ABL response, surface energy balance and land surface properties within a 10 $\times$ 10 km heterogeneous forested domain (that would fit within a 'grid cell' of a weather/climate model) in northern Wisconsin, USA (Butterworth et al., 2021). The dataset provides an extensive set of scenarios to investigate my research questions and derive principles from.

Airborne turbulence data were collected over a 30 km $\times$ 30 km study domain with the University of Wyoming King Air (UWKA) research aircraft. Three seven-day Intensive Observation Periods (referred to as IOPs henceforth) were conducted during the experiment during each

month from July to September when all the available field instrumentation were deployed simultaneously, to sample the shift in surface energy budgets and the associated boundary layer response as the study domain shifts from a latent heat flux dominated late summer landscape to a sensible heat flux dominated early fall landscape. For this study, the airborne turbulence data at 100 m, above ground level was analysed.

Fully coupled large eddy simulations of two of the IOP days were performed using the PArallelized LES Model (PALM) V 6.0 (Maronga et al., 2020b). The simulations were constrained and initialised by land surface properties measured and collected as part of the field campaign. Three one way nested models were setup centred around the US-PFa Ameriflux regional tall tower. The simulations were driven by non periodic boundary conditions setup using the NOAA-HRRRv4 data product averaged over a 49×50 km^2 Parent domain to simulate the diurnal cycles from 0000 CDT 22 August 2019 till 2000 CDT 23 August 2019 and from 0000 CDT 24 September 2019 till 2000 CDT 25 September 2019.

The following three subsections give a brief overview of the research questions posed and the key findings for the same.

5.1.1 Landscape Scale Surface-Atmospheric transport in The Surface Layer

To begin with, I asked how do spatial scales of surface-atmosphere fluxes vary over heterogeneous surfaces across the day and across seasons? And what is the role of ABL stability and land surface variability in modulating these surface atmospheric exchanges? With the working hypothesis that persistent contributions of larger scale (in the range of meso-β to meso-γ) fluxes to the daytime sensible and latent heat fluxes exist with diurnal and seasonal variations.

Wavelet decomposition of airborne turbulent measurements collected during the CHEESEHEAD19 field campaign revealed low frequency surface-atmosphere fluxes with diurnal, seasonal and spatial variations. We measured substantial mesoscale flux contributions at 100 m a.g.l. During the August IOP, the mesoscale sensible heat flux contributions were 23% of the total measured sensible heat fluxes and the mesoscale latent heat fluxes were 18% of the total latent heat fluxes. In the September IOP these numbers were 14% and 28%. Examining the probability density functions of the mesoscale fractions of the fluxes revealed that there is more mesoscale transport in convectively driven boundary layers. The wavelet power spectra of the fluxes also showed higher energies in larger wavelengths during the more convective boundary layers in the August IOP.

Combining the spatially explicit airborne measurements, wavelet decomposition and the FLux topography method of Mauder et al. (2008a) we created scale-separated surface flux maps at 100 m, a.g.l. However, linking the low-frequency transport from airborne measurements at 100 m to surface gradients is not trivial. For surface heat fluxes, the non-stationarity of surface sources complicates any interpretation of causation. Nonetheless, the flux topographies revealed persistent, spatially localised mesoscale contributions to the sensible and latent heat fluxes, which would be missed by stationary, single-point tower measurements.

5.1.2 Evaluation of the CHEESEHEAD19 LES framework

Spatially resolved airborne eddy covariance measurements revealed persistent contributions of larger scale (in the range of meso-β to meso-γ) fluxes to the daytime sensible and latent heat fluxes over the CHEESEHEAD19 study domain Paleri et al. (2022). However, due to the large

range of scales, diurnal nature of surface sources and three-dimensionality of the problem, the drivers and constraints of the underlying processes can be better studied by employing LES.

Hence, I asked whether a large eddy simulation can be used to evaluate mechanisms that generate surface-heterogeneity induced mesoscale circulations in the diel ABL ? The hypothesis for this study was that large eddy simulations, initialised with real-world surface heterogeneity, develop similar mesoscale structures and patterns as observations.

The simulated profiles and time series correlate well with observed values, with a Pearson's correlation coefficient of 0.9 for θ and q for almost all cases considered (Table 3.3) indicating that the simulations align well with the diurnal ABL evolution in the study domain. The mean simulated values have a dependence on the imposed HRRR boundary conditions, most strongly reflected in our study for the near surface q time series with a RMSE of 5.39 g kg^{-1} for August simulations and 7.19 g kg^{-1} for the September simulations.

This study, gives us confidence that large eddy simulations, initialised with real-world surface heterogeneity, could develop meso scale circulations and similar patterns as observations.

5.1.3 On the nature of surface heterogeneity induced secondary circulations and their role in ABL transport

Finally, I diagnose the LES output to identify secondary circulations induced by the heterogeneous land surface through time and ensemble averaging as per the formulations of Maronga and Raasch (2013a). Their diurnal evolution in free and forced convective boundary layers as the land surface undergoes seasonal transition is discussed. And in turn, how do they interact with transport and dynamics of the atmospheric boundary layer.

The research questions posed here were, whether diagnosing and quantifying surface heterogeneity induced circulations and scale-separated transport can help observe the "true" transport ? And following through, how do the effects of these heterogeneity induced circulations vary over the diurnal cycle and across seasons, with changing atmospheric boundary layer height (z_i) and stabilities? How do their effects scale with the length scales of surface heterogeneity and the boundary layer height? In line with the research questions, I hypothesised that surface flux heterogeneity modulates the atmospheric boundary layer response to it by inducing quasi-stationary coherent structures that transition from roll vortices to cellular structures as the boundary layer becomes more convectively unstable.

The time-ensemble averaging of simulation data lets us diagnose heterogeneity induced, persistent secondary circulations in the model domain. In-line with the airborne measurements, the circulations are stronger and persist for more time in the simulated convective boundary layer on 23 August. The near surface dispersive flux contribution to both the kinematic heat and moisture fluxes are 10-15% of the total daytime surface fluxes for the CBL in August simulations. In the wind shear driven September simulations with a near neutral ABL, the near surface near surface dispersive flux contribution to kinematic heat remains at 10-15% of total surface fluxes while the dispersive moisture flux contributions are lesser than 5%. Our simulations show persistent contributions from the surface heterogeneity induced fluxes throughout the atmospheric boundary layer for both the wind shear and buoyancy driven boundary layers. In the convective boundary layer, wavelengths that scale as the effective surface heterogeneity length scales at $\sim 3z_i$ contribute the most to the heterogeneity induced transport.

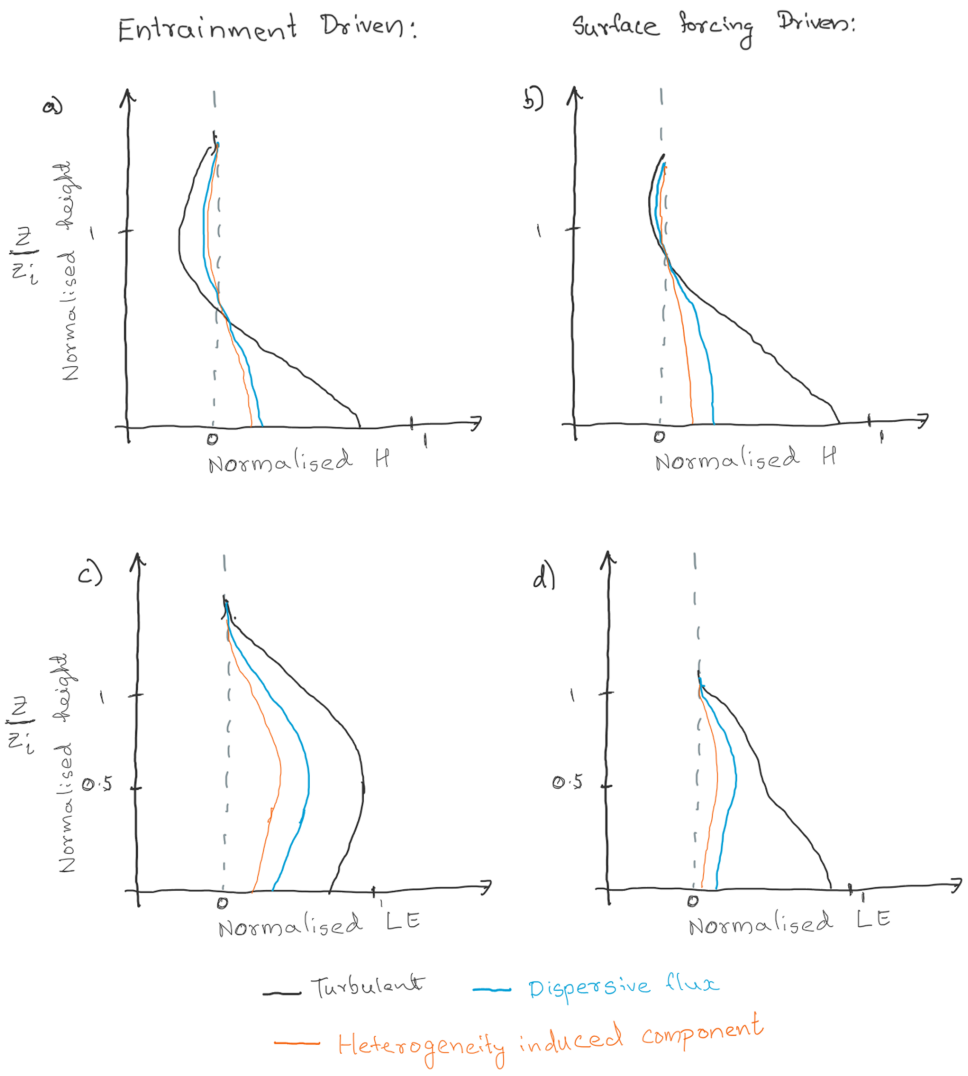

FIGURE 5.1: A schematic sketch of normalised sensible and latent heat flux profiles in the convective boundary layer, informed by our simulations. Plots on the left column: a, c, show profiles of H and LE during an ABL top entrainment dominating growth and plots on the right hand side column; b, d, show H and LE profiles during surface flux dominating CBL. Y axis is vertical height normalised by z_i and x axis is flux magnitudes normalised by total surface fluxes. Black lines denote turbulent flux profiles, blue lines the dispersive fluxes and orange lines the heterogeneity induced contribution to the same

A conceptual sketch for normalised flux profiles in the convective boundary layer in our simulations is presented in Figure 5.1. Two cases, one with ABL top entrainment dominating boundary layer (the left hand side column) and one for a surface flux dominating ABL are presented with

interesting features. For the CBL, where entrainment dominates, the turbulent flux profiles are what is expected of the total fluxes in a classical framework Deardorff (1980); Stull (1988). The dispersive flux contributions to the same are greater higher up in the boundary layer for H, at heights $0.8z_i$-$1.2z_i$. For LE the maximum dispersive flux contributions occur near $0.5z_i$, where most of the transport is done by heterogeneity induced circulations. The near surface contributions from the dispersive fluxes would be $\approx$ 10-15% of the total fluxes. For the CBL where surface heat fluxes dominate, the turbulent H profiles have a classical pattern. The dispersive and heterogeneity induced fluxes behave similarly to the entrainment driven case but with lower magnitudes near the ABL top. For LE too, the turbulent flux profiles behave similarly to a classical moisture flux profile in a convectively heated ABL, but for the dispersive fluxes, the peak of the profile moves up, closer to $0.8z_i$, where entrainment processes dominate. Likewise for the heterogeneity induced components. At $0.8z_i$ most of the dispersive flux is transported by the mesoscale heterogeneity induced structures and as we come closer to the surface the gap between the two widens.

5.2 Implications

This study underscores the role of ABL static stability (the relative role of wind shear vs buoyancy non-dimensionalised as $-z_i \,/\, L$ or $u_* \,/\, w_*$), the ABL height z_i and surface heterogeneity length scales in modulating the contributions from secondary circulations. Our study supports ongoing parameterisation efforts by our collaborators for the contributions from secondary circulations to tower measured surface energy imbalance using the non-local scaling factors (De Roo et al., 2018; Mauder et al., 2021; Wanner et al., 2022) : z_i, $u_* \,/\, w_*$ and effective surface heterogeneity length scales.

We find stronger contributions from the dispersive fluxes during the free convective summer months, when the tower measured energy balance residuals were also higher (Butterworth et al., 2021). It has to be noted that the contribution from the dispersive fluxes would only explain a part of the measured residuals, with storage terms and flux divergence terms playing some part at individual tower locations. However, we still find a substantial domain mean contribution from the dispersive fluxes and their heterogeneity induced components in our simulations for the free convective boundary layers. At the footprint scale of individual towers. contributions from mesoscale circulations through dispersive fluxes would manifest in local advective terms as the horizontal branches of the secondary circulations would cause advective flux transport near surface. There would then be a balance between the contributions from dispersive fluxes and the advective components to the measured imbalance based on the control volume one chooses (Morrison et al., 2021). This could be a future question worth investigating using this setup (Section 5.3)

Our findings about the atmospheric coupling to surface heterogeneity scales can also help to inform consistent assumptions for sub-grid heterogeneity in land surface schemes and ABL /convection schemes while representing the sub-grid coupling between land surface and atmospheric heterogeneities in weather and general circulation models. Our findings are also in agreement with parametric studies that find that heterogeneity scales greater than CBL height can lead to stronger and more entrainment driven growth of the boundary layer (Avissar and Schmidt, 1998; van Heerwaarden et al., 2014). In our study, we find that the length scales of effective surface temperature and moisture with the most amplitude dominate the heterogeneity induced flux transport. This would mean that the choice of a domain size would impact any attempts at scaling or modelling the total surface atmosphere transport. Ovchinnikov et al. (2022) did a

parametric study on the role of horizontal resolution, boundary conditions and domain size on surface atmosphere transport and report that the boundary layer structures are modulated by the location of the computation subdomain.

5.3 Limitations and future work

5.3.1 Role of land surface heterogeneity in low frequency contributions to the observed surface energy imbalance

In this study, we measured and simulated the low frequency response of the atmospheric boundary layer to its underlying land surface heterogeneity. However, a direct comparison and analysis of the tower measured energy balance residuals and budgets was outside the scope of this study. Tower measured data for the CHEESEHEAD19 campaign are being analysed as part of other studies in a spatial eddy covariance approach to include the low frequency flux contribution across the domain. Findings in the studies conducted as a part of this dissertation has helped to inform our understandings of the length scales of importance and the role of ABL stability in those. A more detailed study of connecting the two, using more data intensive approaches such as machine learning based Environment Response Functions (Metzger et al., 2013) could help to scale the airborne and tower measured fluxes throughout the heterogeneous study domain and identify the role of low frequency contributions to tower measured energy balance residuals. A similar approach was used for simulated airborne and EC tower data during the experiment design phase of CHEESEHEAD19, to choose between candidate flight patterns (Metzger et al., 2021).

5.3.2 Realistic Simulations of CHEESEHEAD19 IOP Days

5.3.2.1 Large Scale Boundary Conditions

The simulated profiles closely follow the input HRRR large scale boundary conditions, (Fig. 3.4) which guide the ABL diurnal development. For the two case study days considered, this aided in ABL growth and mean diurnal characteristics very close to the observed values. Usually, LES of field campaign days are either initialised with radisonde observations during early morning hours or nudged towards measured profiles couple of times a day. Compared to that approach, our hourly large scale boundary conditions accounts for the evolving synoptic conditions during the simulation without adding further tendency terms or nudging the LES solution. Moreover, with the initialisation of the simulations at 0000 CDT, we have enough buffer time during the night time for model spin-up by early morning.

However, this also means that the LES solution is also biased towards the HRRR forcings. This is particularly reflected in the dry bias we see in the simulated q values for both the August and September simulations. Also for the 22 August simulations, the simulated θ profile is closer to the HRRR θ profile, with a higher $z_i \approx 2500$ m. Along with a drier ABL, this could be one of the reasons we have stronger H in the simulations than tower measurements. In the next iteration of this study it would be more beneficial to tune the input forcings to be more in line with field measurements.

5.3.2.2 Cloud Formation and Feedback

Currently, the bulk cloud microphysics scheme in PALM was switched off for our ensemble simulations since we were not directly investigating questions related to cloud formation or feedback. Moreover, for the summertime CBL case study day of 23rd August, the daytime cloud cover at Park Falls was only 14%. Input data for the Radiative Transfer Model implementation in PALM was the surface incoming shortwave and longwave radiation data from the 3 km HRRR data. This would indirectly include the surface forcing effects of high clouds in the simulations.

However, in our simulations without clouds, we are missing the local scale feedback associated with the shading effects of shallow convection, that could have a strong effects on moderate to cloudy summer time ABLs. For the 22nd August IOP day simulation, the NWS projected cloud cover for Park Falls was 70% and there was a rainfall event the late night. Since we don't have the direct effects of clouds, this could also be another reason for the mismatch between simulated and tower measured surface heat fluxes. Using a semi-coupled WRF-LES, Simon et al. (2021) find that heterogeneous surface forcings over the SGP site leads to significantly more cloud production, where the land surface heterogeneities caused by prcipitation turned out to be the most influential. Our over highly vegetated and latent heat flux dominated domain, precipitation heterogeneities might not stand out as much as the SGP site, however, it would still be an important influence to consider in later studies.

5.3.2.3 Grid Dependency

There is a grid dependency for the simulated near surface fluxes, with the parent domain having the weakest signal of coherent structures. The simulated coherent structures seem weaker near the surface and above the plant canopy (maximum height at 36 m) in all 3 model domains (Fig. 5.3). The weakness of coherent structures could be one of the reasons that contribute towards higher simulated daytime turbulent heat fluxes than the tower measured fluxes (Figures 3.10 and 3.11). Such dependence was not noticed in the MR13 study. With PALM it is possible to simulate coherent secondary circulations and the dispersive flux transport due to them near the model surface, in the roughness sub-layer (De Roo and Mauder, 2018a; Wanner et al., 2022; Akinlabi et al., 2022). Our model setup uses a LSM and a vertically resolved PCM setup in the Child02 model. For the Parent and Child01 model domains with 12 m vertical grid spacing, the PCM would only act more like a distributed heat source, where all of the roughness interactions between the surface layer and plant canopy are not fully resolved. This might have an influence in the turbulent organisation (Shao et al., 2013), which could modulate the heterogeneity induced structures as well.

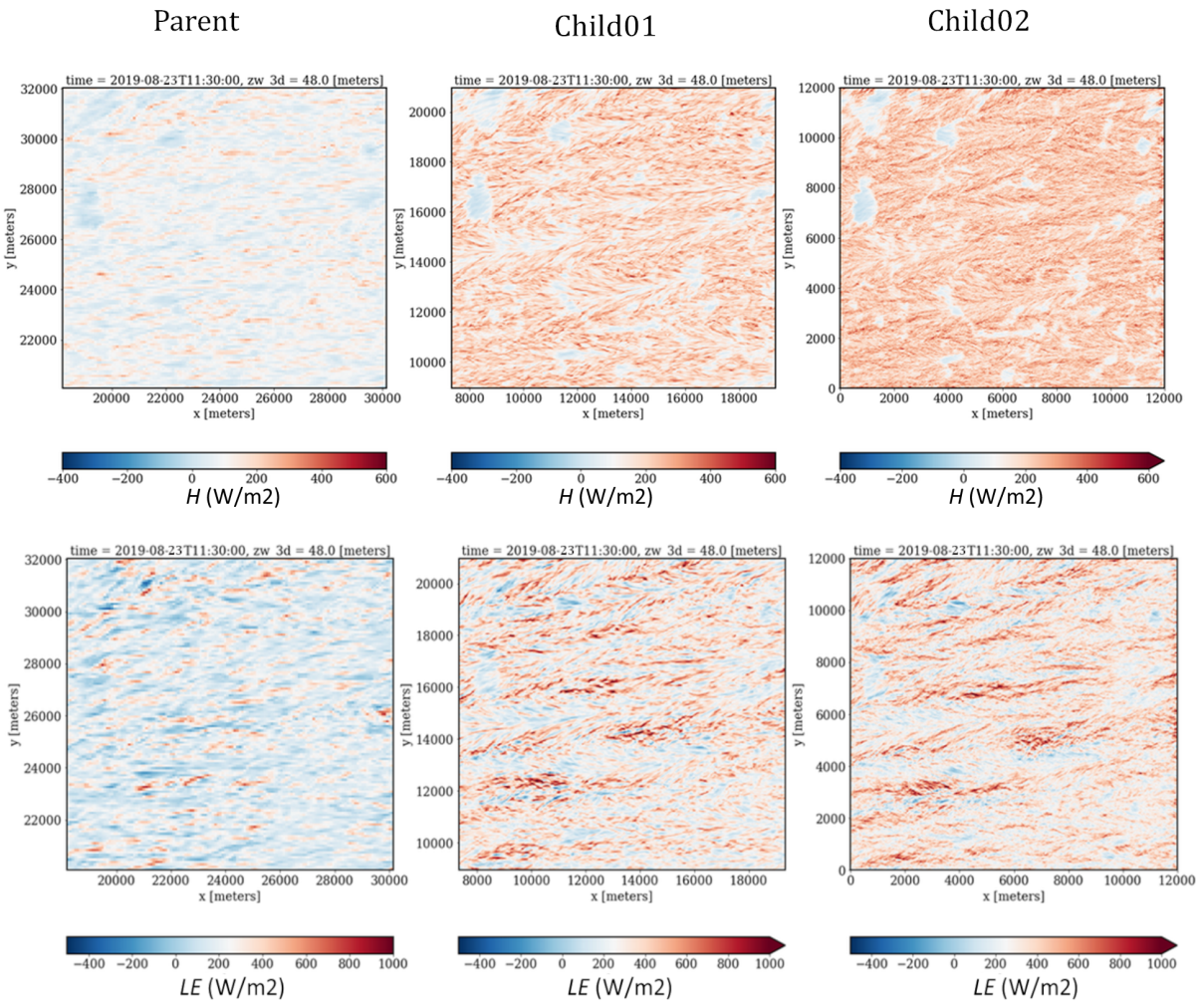

FIGURE 5.2: Simulated, resolved scale above canopy turbulent H (first row) and LE (second row) at 48 m, for Child02 model domain extent, across the 3 models. Values shown for 08/23 1130 local time. SGS contributions were added to the Parent and Child01 domains

Furthermore, the horizontal resolution of the Parent model is only 90 m. This, combined with the highly unstructured and multi-scale heterogeneity would mean that the surface-atmospheric coupling over the model domain might not be well captured in this setup with PALM's MOST based surface flux parameterisations. Because of that, the coherent structure signals could be weaker in the Parent domain and since that is fed into Child01 and Child02 models as boundary

conditions, they could be weaker therein also. We did a grid sensitivity study with the Parent model at the same horizontal resolution as the Child01 model and compared the near surface organisation between the same and the Child02 data from our production runs. There seems to be no significant difference in the strength of surface heat flux amplitudes seen in the updated grid. This is an indicator that our production Parent model grid horizontal resolution of 90 m is able to capture organisation in the CBL well and provide adequate boundary conditions for the Child01 model. However, the coarser vertical resolution of 12 m in both the models don't resolve the near surface organisation as seen in Wanner et al. (2022) or Shao et al. (2013). We find dispersive flux contributions $\approx$ 15-20% of total fluxes from 60 - 100 m in our simulations. Our suggestion here is similar to the recommendation from Mazzaro et al. (2017), who reported $\approx$ 20% weaker circulations in their nested LES vs a stand alone LES setup,to use the finest possible parent grid size in a nested LES setup.

5.3.3 Future Work

In this dissertation, I investigated the role of land surface heterogeneity and ABL stability in boundary layer organisation as roll vortices or spatially localised cellular structures. The effects of large scale turbulent coherent structures on near wall turbulence is an active area in turbulence research (Hutchins and Marusic, 2007; Mathis et al., 2009; Jacob and Anderson, 2017). Our simulation setup and the Child02 model data can be further explored to study the effects of realistic surface heterogeneities on near surface turbulence fields. This would require better representations of canopy and land surface processes at the smaller scales. Moreover, perturbations of θ and q associated with the updraft regions of horizontal convective rolls can influence convection initiation (Weckwerth, 2000; Wilson et al., 1992). Hence a better understanding of boundary layer organisation and the role of surface length scales in their modulation can help

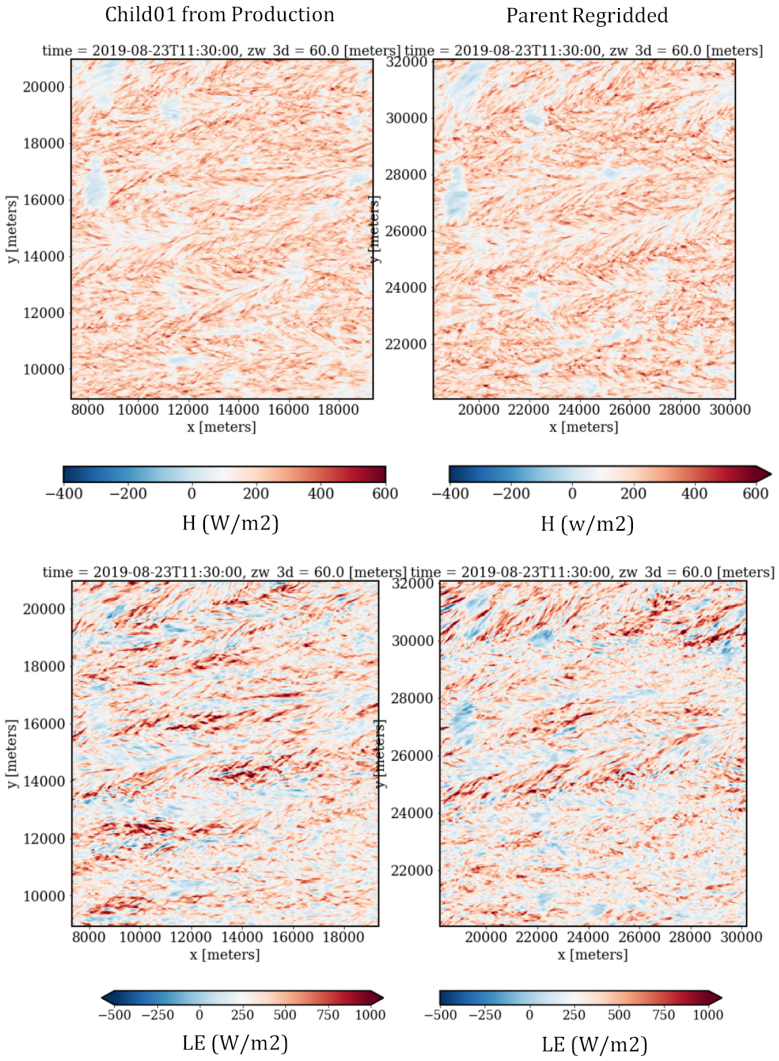

FIGURE 5.3: Simulated, resolved scale above canopy turbulent H (first row) and LE (second row) at 60 m, for Child01 model domain extent, for the current production runs (on left) and simulated values for the same from the regridded Parent model (on the right). Values shown for 08/23 1130 local time.

in bridging the scales of surface-atmospheric transport from the turbulent microscales to storm scales.

One of the proposed analysis for this dissertation was to look into Turbulent Kinetic Energy (TKE) budgets from the simulations to investigate how relationships between CBL organisation and ABL turbulence. From their analysis of the TKE budget from simulations over imposed

spanwise heterogeneous heating, Anderson et al. (2015) proposes that an imbalance between turbulent production dissipation equilibrium can cause advective velocities. They note that such a spanwise imbalance in production over dissipation induces a secondary convective velocity which ultimately sets the mean secondary motion in place (via the continuity of mass). Other investigators have also pointed out there might be a shifting balance in the TKE shear and buoyancy production terms as the coherent structures transition from horizontal convective rolls to cellular structures.

However, calculating representative statistics for TKE budget terms would need long averaging times of several hundred large eddy turnover time ($T = z_i/u_*$, during which the turbulent field should be stationary, well developed and in equilibrium with the underlying surface for robust statistics. The diurnal nature of ABL turbulence complicates stationarity requirements for long averaging times. Heinze et al. (2015) did a TKE budget study of cloud topped BL using PALM, using averaging time of 2 hours which would roughly be about 250 T for our summertime simulations. To ensure stationarity and well development of turbulence, one could do a similar analysis with high resolution time series data, grouped by ABL static stability values for the 23 August CBL, for the fully developed afternoon CBL from 1300 till 1530 CDT (Fig. 4.1.

De Roo and Mauder (2018a) did a flux budget analysis of near surface sensible heat fluxes over idealised heterogeneities using a control volume approach. They could quantify the local advective and flux divergence terms, which would cause an imbalance between the vertical turbulence flux measured on top of the control volume and the total available energy, as detailed in Section 1.1. They found that the missing fluxes are well correlated with both the advective terms and the flux divergence terms and so can be well described by either one of those. A similar control volume analysis of the flux budget terms (Equation 1.2) over the virtual CHEESEHEAD19 tower

locations can throw light on the relative contributions between advection and flux divergence, as well as how they might relate with a domain mean dispersive flux.

Dispersive fluxes are a function of the averaging area, and hence their magnitude would also depend on the chosen control volume. Nevertheless, it will be worthwhile to investigate how they correlate with tower measured advective and flux-divergence magnitudes, as well as simulated surface energy budget residuals.

PALM offers a Lagrangian Particle Model (LPM) (Steinfeld et al., 2008) that can be employed to study turbulent dispersion over the complex, vegetated CHEESEHEAD study domain. This can be set up for the convective 23 August IOP day to estimate and evaluate the flux footprints of the tower network and airborne measurements. In their idealised LES study, Steinfeld et al. (2008) demonstrated that flux footprints are severely affected by surface heterogeneities and the LPM perform better than the conventional Lagrangian dispersion models, with fully parameterised turbulence. It would also be beneficial to compare such footprint maps and climatologies with Environment Response Function footprint maps of heat fluxes across the study domain.

In our simulations, for the fully developed CBL, the effective length scales of surface heterogeneity $\approx 3z_i$. One can argue that the length scales of up and down drafts would scale with z_i for both homogeneous and heterogeneous surface forcings. Time ensemble averaged fields of w_{hi} revealed that the heterogeneity induced structures are spatially bound to land surface features or gradients, like the standing circulations at the lake edge to the north east of Child02 domain. However, the length scales of the structures need not scale with surface heterogeneity length scales throughout the domain.

In the CBL with weak mean winds, surface heterogeneity length scales of the same order of magnitude as z_i can induce local circulations and internal boundary layers that can span the entire height of the ABL and scale with z_i (Mahrt, 1996, 2000). Since the evolution of these circulations would contribute towards the entrainment driven growth of the CBL, there can be a mutual dependence between the surface heterogeneity length scales, horizontal scale of secondary circulations and z_i. Combined with a strong enough amplitude of surface flux heterogeneities in the free convective boundary layers, such a mutual dependency could result in surface heterogeneity length scales modulating the horizontal length scales of heterogeneity induced circulations as well.

To investigate this surface-atmospheric coupling and the role of realistic surface length scales therein further, we could set up idealised versions of the CHEESEHEAD19 study domain, with lower order representations of land surface classes. Brunsell et al. (2011) performed coupled LES study with realistic 2D surface forcings, where the surface forcings were band pass filtered to obtain a sequence of surface forcings with varying effective length scales for the same study domain. A similar analysis can be done for our LES setup too.

A wavelet analysis of simulated time series data at each CHEESEHEAD19 tower location can also help to study the local effect of the heterogeneity induced mesoscale circulations.Going forward from there, with time series of local profiles, wavelet spectrograms can also be calculated and averaged over all similar tower locations, to get a more local picture of length scale distribution, rather than the domain mean spectral distribution that we see currently.

Bibliography

Abdella, K. and N. McFarlane, 1997: A new second-order turbulence closure scheme for the planetary boundary layer. *Journal of the atmospheric sciences*, **54**, 1850–1867.

Addison, P. S., 2017: *The illustrated wavelet transform handbook: introductory theory and applications in science, engineering, medicine and finance*. CRC press.

Akinlabi, E., B. Maronga, M. G. Giometto, and D. Li, 2022: Dispersive fluxes within and over a real urban canopy: a large-eddy simulation study. *Boundary-Layer Meteorology*, **185**, 93–128.

Albertson, J. D., W. P. Kustas, and T. M. Scanlon, 2001: Large-eddy simulation over heterogeneous terrain with remotely sensed land surface conditions. *Water Resources Research*, **37**, 1939–1953.

Amiro, B., 1998: Footprint climatologies for evapotranspiration in a boreal catchment. *Agricultural and Forest Meteorology*, **90**, 195–201, doi:10.1016/S0168-1923(97)00096-8.
URL https://linkinghub.elsevier.com/retrieve/pii/S0168192397000968

Anderson, W., J. M. Barros, K. T. Christensen, and A. Awasthi, 2015: Numerical and experimental study of mechanisms responsible for turbulent secondary flows in boundary layer flows over spanwise heterogeneous roughness. *Journal of Fluid Mechanics*, **768**, 316–347, doi:10.1017/jfm.2015.91.
URL https://www.cambridge.org/core/product/identifier/S0022112015000919/type/journal_article

Arakawa, A. and V. R. Lamb, 1977: Computational design of the basic dynamical processes of the ucla general circulation model. *General circulation models of the atmosphere*, **17**, 173–265.

Atkinson, B. and J. Wu Zhang, 1996: Mesoscale shallow convection in the atmosphere. *Reviews of Geophysics*, **34**, 403–431.

Aubinet, M., A. Grelle, A. Ibrom, Ü. Rannik, J. Moncrieff, T. Foken, A. Kowalski, P. Martin, P. Berbigier, C. Bernhofer, R. Clement, J. Elbers, A. Granier, T. Grünwald, K. Morgenstern, K. Pilegaard, C. Rebmann, W. Snijders, R. Valentini, and T. Vesala, 1999: Estimates of the Annual Net Carbon and Water Exchange of Forests: The EUROFLUX Methodology. *Advances in Ecological Research*, Elsevier, volume 30, 113–175.
URL https://linkinghub.elsevier.com/retrieve/pii/S0065250408600185

Aubinet, M., T. Vesala, and D. Papale, eds., 2012: *Eddy Covariance: A Practical Guide to Measurement and Data Analysis*. Springer Netherlands, Dordrecht.
URL http://link.springer.com/10.1007/978-94-007-2351-1

Avissar, R. and R. A. Pielke, 1989: A parameterization of heterogeneous land surfaces for atmospheric numerical models and its impact on regional meteorology. *Monthly Weather Review*, **117**, 2113–2136.

Avissar, R. and T. Schmidt, 1998: An Evaluation of the Scale at which Ground-Surface Heat Flux Patchiness Affects the Convective Boundary Layer Using Large-Eddy Simulations. *JOURNAL OF THE ATMOSPHERIC SCIENCES*, **55**, 24.

Baldocchi, D., E. Falge, L. Gu, R. Olson, D. Hollinger, S. Running, P. Anthoni, C. Bernhofer, K. Davis, R. Evans, J. Fuentes, A. Goldstein, G. Katul, B. Law, X. Lee, Y. Malhi, T. Meyers, W. Munger, W. Oechel, K. T. P. U, K. Pilegaard, H. P. Schmid, R. Valentini,

S. Verma, T. Vesala, K. Wilson, and S. Wofsy, 2001: FLUXNET: A New Tool to Study the Temporal and Spatial Variability of Ecosystem-Scale Carbon Dioxide, Water Vapor, and Energy Flux Densities. *Bulletin of the American Meteorological Society*, **82**, 2415 – 2434, doi:10.1175/1520-0477(2001)082¡2415:FANTTS¿2.3.CO;2.

URL https://journals.ametsoc.org/view/journals/bams/82/11/1520-0477_2001_082_2415_fantts_2_3_co_2.xml

Bange, J., F. Beyrich, and D. A. M. Engelbart, 2002: Airborne measurements of turbulent fluxes during LITFASS-98: Comparison with ground measurements and remote sensing in a case study. *Theoretical and Applied Climatology*, **73**, 35–51, doi:10.1007/s00704-002-0692-6.

URL http://link.springer.com/10.1007/s00704-002-0692-6

Bange, J., T. Spieß, M. Herold, F. Beyrich, and B. Hennemuth, 2006: Turbulent fluxes from Helipod flights above quasi-homogeneous patches within the LITFASS area. *Boundary-Layer Meteorology*, **121**, 127–151, doi:10.1007/s10546-006-9106-0.

URL http://link.springer.com/10.1007/s10546-006-9106-0

Benjamin, S. G., S. S. Weygandt, J. M. Brown, M. Hu, C. R. Alexander, T. G. Smirnova, J. B. Olson, E. P. James, D. C. Dowell, G. A. Grell, et al., 2016: A north american hourly assimilation and model forecast cycle: The rapid refresh. *Monthly Weather Review*, **144**, 1669–1694.

Berger, B. W., K. J. Davis, C. Yi, P. S. Bakwin, and C. L. Zhao, 2001: Long-Term Carbon Dioxide Fluxes from a Very Tall Tower in a Northern Forest: Flux Measurement Methodology. *Journal of Atmospheric and Oceanic Technology*, **18**, 529–542, doi:10.1175/1520-0426(2001)018¡0529:LTCDFF¿2.0.CO;2.

URL http://journals.ametsoc.org/doi/10.1175/1520-0426(2001)018<0529:LTCDFF>2.0.CO;2

Bernhofer, C., 1992a: Applying a simple three-dimensional eddy correlation system for latent and sensible heat flux to contrasting forest canopies. *Theoretical and applied climatology*, **46**, 163–172.

— 1992b: Applying a simple three-dimensional eddy correlation system for latent and sensible heat flux to contrasting forest canopies. *Theoretical and Applied Climatology*, **46**, 163–172, doi:10.1007/BF00866096.

URL http://link.springer.com/10.1007/BF00866096

Bertoldi, G., J. Albertson, W. Kustas, F. Li, and M. Anderson, 2007: On the opposing roles of air temperature and wind speed variability in flux estimation from remotely sensed land surface states. *Water resources research*, **43**.

Bianco, L. and J. Duncan, 2020: NOAA Planetary Boundary Layer Heights (PBLH) derived from the NOAA/PSL 915-MHz Wind Profiler Radars. Version 1.0. Artwork Size: 221 data files, 2 ancillary/documentation files, 221 KiB Medium: ASCII: ASCII Text (text/plain) Pages: 221 data files, 2 ancillary/documentation files, 221 KiB Version Number: 1.0 Type: dataset.

URL https://data.eol.ucar.edu/dataset/592.092

Blanford, J., C. Bernhofer, and L. Gay, 1991: Energy flux mechanism over a pecan orchard oasis. *Proceedings of the 20th Agric Forest Meteorol Conf*.

Blaylock, B. K., J. D. Horel, and S. T. Liston, 2017: Cloud archiving and data mining of high-resolution rapid refresh forecast model output. *Computers & Geosciences*, **109**, 43–50.

Bou-Zeid, E., W. Anderson, G. G. Katul, and L. Mahrt, 2020: The Persistent Challenge of Surface Heterogeneity in Boundary-Layer Meteorology: A Review. *Boundary-Layer Meteorology*, doi:10.1007/s10546-020-00551-8.

URL http://link.springer.com/10.1007/s10546-020-00551-8

Bou-Zeid, E., C. Meneveau, and M. B. Parlange, 2004: Large-eddy simulation of neutral atmospheric boundary layer flow over heterogeneous surfaces: Blending height and effective surface roughness. *Water Resources Research*, **40**.

Bou-Zeid, E., M. B. Parlange, and C. Meneveau, 2007: On the parameterization of surface roughness at regional scales. *Journal of the atmospheric sciences*, **64**, 216–227.

Brunsell, N. A., D. B. Mechem, and M. C. Anderson, 2011: Surface heterogeneity impacts on boundary layer dynamics via energy balance partitioning. *Atmospheric Chemistry and Physics*, **11**, 3403–3416, doi:10.5194/acp-11-3403-2011.

URL https://acp.copernicus.org/articles/11/3403/2011/

Businger, J. A., J. C. Wyngaard, Y. Izumi, and E. F. Bradley, 1971: Flux-profile relationships in the atmospheric surface layer. *Journal of Atmospheric Sciences*, **28**, 181 – 189, doi:10.1175/1520-0469(1971)028¡0181:FPRITA¿2.0.CO;2.

URL https://journals.ametsoc.org/view/journals/atsc/28/2/1520-0469_1971_028_0181_fprita_2_0_co_2.xml

Butterworth, B. J., A. R. Desai, P. A. Townsend, G. W. Petty, C. G. Andresen, T. H. Bertram, E. L. Kruger, J. K. Mineau, E. R. Olson, S. Paleri, R. A. Pertzborn, C. Pettersen, P. C. Stoy, J. E. Thom, M. P. Vermeuel, T. J. Wagner, D. B. Wright, T. Zheng, S. Metzger, M. D. Schwartz, T. J. Iglinski, M. Mauder, J. Speidel, H. Vogelmann, L. Wanner, T. J. Augustine,

W. O. J. Brown, S. P. Oncley, M. Buban, T. R. Lee, P. Cleary, D. J. Durden, C. R. Florian, K. Lantz, L. D. Riihimaki, J. Sedlar, T. P. Meyers, D. M. Plummer, E. R. Guzman, E. N. Smith, M. Sühring, D. D. Turner, Z. Wang, L. D. White, and J. M. Wilczak, 2021: Connecting Land–Atmosphere Interactions to Surface Heterogeneity in CHEESEHEAD19. *Bulletin of the American Meteorological Society*, **102**, E421 – E445, doi:10.1175/BAMS-D-19-0346.1. URL https://journals.ametsoc.org/view/journals/bams/102/2/BAMS-D-19-0346.1.xml

Canuto, V., F. Minotti, C. Ronchi, R. Ypma, and O. Zeman, 1994: Second-order closure pbl model with new third-order moments: Comparison with les data. *Journal of the atmospheric sciences*, **51**, 1605–1618.

Cattaneo, M. D., R. K. Crump, M. H. Farrell, and Y. Feng, 2019: Binscatter regressions. *arXiv preprint arXiv:1902.09615*, [Software].

Charuchittipan, D., W. Babel, M. Mauder, J.-P. Leps, and T. Foken, 2014: Extension of the Averaging Time in Eddy-Covariance Measurements and Its Effect on the Energy Balance Closure. *Boundary-Layer Meteorology*, **152**, 303–327, doi:10.1007/s10546-014-9922-6. URL http://link.springer.com/10.1007/s10546-014-9922-6

Chen, F. and R. Avissar, 1994: The impact of land-surface wetness heterogeneity on mesoscale heat fluxes. *Journal of Applied Meteorology and Climatology*, **33**, 1323–1340.

Chetty, R., A. Looney, and K. Kroft, 2009: Salience and taxation: Theory and evidence. *American economic review*, **99**, 1145–77.

Chetty, R. and A. Szeidl, 2005: Marriage, housing, and portfolio choice: A test of grossman-laroque. *Mimeograph, UC-Berkeley*.

Computational and I. S. Laboratory, 2017: Cheyenne: Hpe/sgi ice xa system (climate simulation laboratory).

Courault, D., P. Drobinski, Y. Brunet, P. Lacarrere, and C. Talbot, 2007: Impact of surface heterogeneity on a buoyancy-driven convective boundary layer in light winds. *Boundary-layer meteorology*, **124**, 383–403.

Davis, K. J., P. S. Bakwin, C. Yi, B. W. Berger, C. Zhao, R. M. Teclaw, and J. G. Isebrands, 2003: The annual cycles of CO2 and H2O exchange over a northern mixed forest as observed from a very tall tower. *Global Change Biology*, **9**, 1278–1293, doi:10.1046/j.1365-2486.2003.00672.x.

URL http://onlinelibrary.wiley.com/doi/abs/10.1046/j.1365-2486.2003.00672.x

De Roo, F. and M. Mauder, 2018a: The influence of idealized surface heterogeneity on virtual turbulent flux measurements. *Atmospheric Chemistry and Physics*, **18**, 5059–5074, doi:10.5194/acp-18-5059-2018.

URL https://acp.copernicus.org/articles/18/5059/2018/

— 2018b: The influence of idealized surface heterogeneity on virtual¡? xmltex\break?¿ turbulent flux measurements. *Atmospheric Chemistry and Physics*, **18**, 5059–5074.

De Roo, F., S. Zhang, S. Huq, and M. Mauder, 2018: A semi-empirical model of the energy balance closure in the surface layer. *PLOS ONE*, **13**, e0209022, doi:10.1371/journal.pone.0209022.

URL http://dx.plos.org/10.1371/journal.pone.0209022

Deardorff, J., 1972a: Theoretical expression for the countergradient vertical heat flux. *Journal of Geophysical Research*, **77**, 5900–5904.

Deardorff, J. W., 1972b: Numerical investigation of neutral and unstable planetary boundary layers. *Journal of Atmospheric Sciences*, **29**, 91–115.

— 1980: Stratocumulus-capped mixed layers derived from a three-dimensional model. *Boundary-Layer Meteorology*, **18**, 495–527, doi:10.1007/BF00119502.
URL http://link.springer.com/10.1007/BF00119502

Desai, A. R., 2014: Influence and predictive capacity of climate anomalies on daily to decadal extremes in canopy photosynthesis. *Photosynthesis Research*, **119**, 31–47, doi:10.1007/s11120-013-9925-z.
URL http://link.springer.com/10.1007/s11120-013-9925-z

Desai, A. R., A. M. Khan, T. Zheng, S. Paleri, B. Butterworth, T. R. Lee, J. B. Fisher, G. Hulley, T. Kleynhans, A. Gerace, P. A. Townsend, P. Stoy, and S. Metzger, 2021: Multi-Sensor Approach for High Space and Time Resolution Land Surface Temperature. *Earth and Space Science*, **8**, doi:10.1029/2021EA001842.
URL https://onlinelibrary.wiley.com/doi/10.1029/2021EA001842

Desai, A. R., B. A. Murphy, S. Wiesner, J. Thom, B. J. Butterworth, N. Koupaei-Abyazani, A. Muttaqin, S. Paleri, A. Talib, J. Turner, et al., 2022a: Drivers of decadal carbon fluxes across temperate ecosystems. *Journal of Geophysical Research: Biogeosciences*, **127**, e2022JG007014.

Desai, A. R., S. Paleri, J. Mineau, H. Kadum, L. Wanner, M. Mauder, B. J. Butterworth, D. J. Durden, and S. Metzger, 2022b: Scaling land-atmosphere interactions: Special or fundamental?

Desai, A. R., K. Xu, H. Tian, P. Weishampel, J. Thom, D. Baumann, A. E. Andrews, B. D. Cook, J. Y. King, and R. Kolka, 2015: Landscape-level terrestrial methane flux observed from a very tall tower. *Agricultural and Forest Meteorology*, **201**, 61–75, doi:10.1016/j.agrformet.2014.10.017.

URL https://linkinghub.elsevier.com/retrieve/pii/S0168192314002688

Desjardins, R. L., J. I. MacPherson, L. Mahrt, P. Schuepp, E. Pattey, H. Neumann, D. Baldocchi, S. Wofsy, D. Fitzjarrald, H. McCaughey, and D. W. Joiner, 1997: Scaling up flux measurements for the boreal forest using aircraft-tower combinations. *Journal of Geophysical Research: Atmospheres*, **102**, 29125–29133, doi:10.1029/97JD00278.

URL http://doi.wiley.com/10.1029/97JD00278

Drobinski, P., R. a. Brown, P. H. Flamant, and J. Pelon, 1998a: Evidence of Organized Large Eddies by Ground-Based Doppler Lidar, Sonic Anemometer and Sodar. *Boundary-Layer Meteorology*, **88**, 343–361, doi:10.1023/A:1001167212584.

URL http://link.springer.com/10.1023/A:1001167212584

— 1998b: Evidence of organized large eddies by ground-based doppler lidar, sonic anemometer and sodar. *Boundary-Layer Meteorology*, **88**, 343–361.

Duncan Jr, J. B., L. Bianco, B. Adler, T. Bell, I. V. Djalalova, L. Riihimaki, J. Sedlar, E. N. Smith, D. D. Turner, T. J. Wagner, et al., 2022: Evaluating convective planetary boundary layer height estimations resolved by both active and passive remote sensing instruments during the cheesehead19 field campaign. *Atmospheric Measurement Techniques*, **15**, 2479–2502.

Eder, F., M. Schmidt, T. Damian, K. Träumner, and M. Mauder, 2015: Mesoscale Eddies Affect Near-Surface Turbulent Exchange: Evidence from Lidar and Tower Measurements. *Journal*

of Applied Meteorology and Climatology, **54**, 189–206, doi:10.1175/JAMC-D-14-0140.1.

URL http://journals.ametsoc.org/doi/10.1175/JAMC-D-14-0140.1

Engelmann, C. and C. Bernhofer, 2016: Exploring Eddy-Covariance Measurements Using a Spatial Approach: The Eddy Matrix. *Boundary-Layer Meteorology*, **161**, 1–17, doi:10.1007/s10546-016-0161-x.

URL http://link.springer.com/10.1007/s10546-016-0161-x

Etling, D. and R. A. Brown, 1993: Roll vortices in the planetary boundary layer: A review. *Boundary-Layer Meteorology*, **65**, 215–248, doi:10.1007/BF00705527.

URL http://link.springer.com/10.1007/BF00705527

Facility, N. I.-S. S. and U. O. W.-S. S. . E. C. (SSEC), 2019: NCAR/EOL ISS and UWI SPARC Radiosonde Data. Version 1.0. Artwork Size: 172 data files, 2 ancillary/documentation files, 64 MiB Medium: NetCDF: Network Common Data Form (application/x-netcdf) Pages: 172 data files, 2 ancillary/documentation files, 64 MiB Version Number: 1.0 Type: dataset.

URL https://data.eol.ucar.edu/dataset/592.001

Farge, M., 1992: Wavelet transforms and their applications to turbulence. *Annual review of fluid mechanics*, **24**, 395–458.

Finnigan, J. J., R. Clement, Y. Malhi, R. Leuning, and H. Cleugh, 2003: A Re-Evaluation of Long-Term Flux Measurement Techniques Part I: Averaging and Coordinate Rotation. *Boundary-Layer Meteorology*, **107**, 1–48, doi:10.1023/A:1021554900225.

URL http://link.springer.com/10.1023/A:1021554900225

Foken, T., 2008: THE ENERGY BALANCE CLOSURE PROBLEM: AN OVERVIEW. *Ecological Applications*, **18**, 1351–1367, doi:10.1890/06-0922.1.

URL http://doi.wiley.com/10.1890/06-0922.1

— 2017: *Micrometeorology*. Springer Berlin Heidelberg, Berlin, Heidelberg.

URL http://link.springer.com/10.1007/978-3-642-25440-6

Foken, T., M. Aubinet, J. J. Finnigan, M. Y. Leclerc, M. Mauder, and K. T. Paw U, 2011: Results Of A Panel Discussion About The Energy Balance Closure Correction For Trace Gases. *Bulletin of the American Meteorological Society*, **92**, ES13–ES18, doi:10.1175/2011BAMS3130.1.

URL https://journals.ametsoc.org/bams/article/92/4/ES13/107080/Results-Of-A-Panel-Discussion-About-The-Energy

Foken, T., M. Mauder, C. Liebethal, F. Wimmer, F. Beyrich, J.-P. Leps, S. Raasch, H. A. R. DeBruin, W. M. L. Meijninger, and J. Bange, 2010: Energy balance closure for the LITFASS-2003 experiment. *Theoretical and Applied Climatology*, **101**, 149–160, doi:10.1007/s00704-009-0216-8.

URL http://link.springer.com/10.1007/s00704-009-0216-8

Foken, T. and S. Oncley, 1995: Workshop on instrumental and methodical problems of land surface flux measurements. *Bulletin of the American Meteorological Society*, 1191–1193.

Foken, T., F. Wimmer, M. Mauder, C. Thomas, and C. Liebethal, 2006: Some aspects of the energy balance closure problem. *Atmos. Chem. Phys.*, 8.

French, J., L. Oolman, and D. Plummer, 2021: University of Wyoming King Air (UWKA) High Rate Flight Level Data. Version 1.0.

URL https://data.eol.ucar.edu/dataset/592.146

Gao, Z., H. Liu, X. Chen, M. Huang, J. E. C. Missik, J. Yao, E. Arntzen, and D. P. Mcfarland, 2020: Enlarged Nonclosure of Surface Energy Balance With Increasing Atmospheric Instabilities Linked to Changes in Coherent Structures. *Journal of Geophysical Research: Atmospheres*, **125**, doi:10.1029/2020JD032889.

URL https://onlinelibrary.wiley.com/doi/abs/10.1029/2020JD032889

Gao, Z., H. Liu, G. G. Katul, and T. Foken, 2017: Non-closure of the surface energy balance explained by phase difference between vertical velocity and scalars of large atmospheric eddies. *Environmental Research Letters*, **12**, 034025, doi:10.1088/1748-9326/aa625b.

URL http://stacks.iop.org/1748-9326/12/i=3/a=034025?key=crossref.e67b6d3d58753744f0e3e338b76995cd

Gatz, D. F. and L. Smith, 1995: The standard error of a weighted mean concentration—I. Bootstrapping vs other methods. *Atmospheric Environment*, **29**, 1185–1193, doi:10.1016/1352-2310(94)00210-C.

URL https://linkinghub.elsevier.com/retrieve/pii/135223109400210C

Gehrke, K. F., M. Sühring, and B. Maronga, 2020: Modeling of land-surface interactions in the PALM model system 6.0: Land surface model description, first evaluation, and sensitivity to model parameters. preprint, Atmospheric Sciences.

URL https://gmd.copernicus.org/preprints/gmd-2020-197/

Ghannam, K., T. Duman, S. T. Salesky, M. Chamecki, and G. Katul, 2017: The non-local character of turbulence asymmetry in the convective atmospheric boundary layer. *Quarterly Journal of the Royal Meteorological Society*, **143**, 494–507.

Gronemeier, T., F. Kanani-Sühring, and S. Raasch, 2017: Do shallow cumulus clouds have the potential to trigger secondary circulations via shading? *Boundary-Layer Meteorology*, **162**, 143–169.

Gronemeier, T., K. Surm, F. Harms, B. Leitl, B. Maronga, and S. Raasch, 2021: Evaluation of the dynamic core of the palm model system 6.0 in a neutrally stratified urban environment: comparison between les and wind-tunnel experiments. *Geoscientific Model Development*, **14**, 3317–3333.

Grossman, R. L., 1982: An analysis of vertical velocity spectra obtained in the bomex fair-weather, trade-wind boundary layer. *Boundary-Layer Meteorology*, **23**, 323–357.

Gryanik, V. M. and J. Hartmann, 2002: A turbulence closure for the convective boundary layer based on a two-scale mass-flux approach. *Journal of the atmospheric sciences*, **59**, 2729–2744.

Gryschka, M., C. Drüe, D. Etling, and S. Raasch, 2008: On the influence of sea-ice inhomogeneities onto roll convection in cold-air outbreaks. *Geophysical Research Letters*, **35**.

Hadfield, M., W. Cotton, and R. Pielke, 1992: Large-eddy simulations of thermally forced circulations in the convective boundary layer. part ii: The effect of changes in wavelength and wind speed. *Boundary-layer meteorology*, **58**, 307–327.

Haimov, S. and A. Rodi, 2013: Fixed-Antenna Pointing-Angle Calibration of Airborne Doppler Cloud Radar. *Journal of Atmospheric and Oceanic Technology*, **30**, 2320–2335,

doi:10.1175/JTECH-D-12-00262.1.

URL http://journals.ametsoc.org/doi/10.1175/JTECH-D-12-00262.1

Harlow, F. H. and J. E. Welch, 1965: Numerical calculation of time-dependent viscous incompressible flow of fluid with free surface. *The physics of fluids*, **8**, 2182–2189.

Hartmann, J., M. Gehrmann, K. Kohnert, S. Metzger, and T. Sachs, 2018: New calibration procedures for airborne turbulence measurements and accuracy of the methane fluxes during the AirMeth campaigns. **11**, 4567–4581, doi:10.5194/amt-11-4567-2018, publisher: Copernicus GmbH.

URL https://amt.copernicus.org/articles/11/4567/2018/

Hechtel, L. M., R. B. Stull, and C.-H. Moeng, 1990: The effects of nonhomogeneous surface fluxes on the convective boundary layer: A case study using large-eddy simulation. *Journal of the Atmospheric Sciences*, **47**, 1721–1741.

Heinze, R., D. Mironov, and S. Raasch, 2015: Second-moment budgets in cloud topped boundary layers: A large-eddy simulation study. *Journal of Advances in Modeling Earth Systems*, **7**, 510–536, doi:https://doi.org/10.1002/2014MS000376.

URL https://agupubs.onlinelibrary.wiley.com/doi/abs/10.1002/2014MS000376

Heinze, R., C. Moseley, L. N. Böske, S. K. Muppa, V. Maurer, S. Raasch, and B. Stevens, 2017: Evaluation of large-eddy simulations forced with mesoscale model output for a multi-week period during a measurement campaign. *Atmospheric Chemistry and Physics*, **17**, 7083–7109.

Hellsten, A., K. Ketelsen, M. Sühring, M. Auvinen, B. Maronga, C. Knigge, F. Barmpas, G. Tsegas, N. Moussiopoulos, and S. Raasch, 2020: A Nested Multi-Scale System Implemented in the Large-EddySimulation Model PALM model system 6.0. preprint, Numerical

Methods.

URL https://gmd.copernicus.org/preprints/gmd-2020-222/

Heus, T., C. C. van Heerwaarden, H. J. Jonker, A. Pier Siebesma, S. Axelsen, K. Van Den Dries, O. Geoffroy, A. Moene, D. Pino, S. De Roode, et al., 2010: Formulation of the dutch atmospheric large-eddy simulation (dales) and overview of its applications. *Geoscientific Model Development*, **3**, 415–444.

Higgins, C. W., E. Pardyjak, M. Froidevaux, V. Simeonov, and M. B. Parlange, 2013: Measured and Estimated Water Vapor Advection in the Atmospheric Surface Layer. *Journal of Hydrometeorology*, **14**, 1966–1972, doi:10.1175/JHM-D-12-0166.1.

URL http://journals.ametsoc.org/doi/10.1175/JHM-D-12-0166.1

Holtslag, A. and B. Boville, 1993: Local versus nonlocal boundary-layer diffusion in a global climate model. *Journal of climate*, **6**, 1825–1842.

Holtslag, A. and C.-H. Moeng, 1991: Eddy diffusivity and countergradient transport in the convective atmospheric boundary layer. *Journal of the Atmospheric Sciences*, **48**, 1690–1698.

Huang, H.-Y. and S. A. Margulis, 2009: On the impact of surface heterogeneity on a realistic convective boundary layer. *Water Resources Research*, **45**.

— 2010: Evaluation of a fully coupled large-eddy simulation–land surface model and its diagnosis of land-atmosphere feedbacks. *Water Resources Research*, **46**.

Huang, J., X. Lee, and E. G. Patton, 2009: Dissimilarity of scalar transport in the convective boundary layer in inhomogeneous landscapes. *Boundary-layer meteorology*, **130**, 327–345.

Hutchins, N. and I. Marusic, 2007: Evidence of very long meandering features in the logarithmic region of turbulent boundary layers. *Journal of Fluid Mechanics*, **579**, 1–28.

Högström, U., 1988: Non-dimensional wind and temperature profiles in the atmospheric surface layer: A re-evaluation. **42**, 55–78, doi:10.1007/BF00119875.
URL https://doi.org/10.1007/BF00119875

Iglewicz, B. and D. C. Hoaglin, 1993: *How to detect and handle outliers*, volume 16. Asq Press.

Inagaki, A., M. O. Letzel, S. Raasch, and M. Kanda, 2006: Impact of Surface Heterogeneity on Energy Imbalance: A Study Using LES. *Journal of the Meteorological Society of Japan*, **84**, 187–198, doi:10.2151/jmsj.84.187.
URL http://joi.jlc.jst.go.jp/JST.JSTAGE/jmsj/84.187?from=CrossRef

Jacob, C. and W. Anderson, 2017: Conditionally Averaged Large-Scale Motions in the Neutral Atmospheric Boundary Layer: Insights for Aeolian Processes. *Boundary-Layer Meteorology*, **162**, 21–41, doi:10.1007/s10546-016-0183-4.
URL http://link.springer.com/10.1007/s10546-016-0183-4

Kadasch, E., M. Sühring, T. Gronemeier, and S. Raasch, 2021: Mesoscale nesting interface of the palm model system 6.0. *Geoscientific Model Development*, **14**, 5435–5465.

Kadasch, E., M. Sühring, T. Gronemeier, and S. Raasch, 2020: Mesoscale nesting interface of the PALM model system 6.0. preprint, Atmospheric Sciences.
URL https://gmd.copernicus.org/preprints/gmd-2020-285/

Kaimal, J. C. and J. J. Finnigan, 1994a: *Atmospheric boundary layer flows: their structure and measurement*. Oxford university press.

— 1994b: *Atmospheric boundary layer flows: their structure and measurement*. Oxford University Press, New York.

Kanani-Sühring, F. and S. Raasch, 2017: Enhanced scalar concentrations and fluxes in the lee of forest patches: a large-eddy simulation study. *Boundary-Layer Meteorology*, **164**, 1–17.

Kanda, M., A. Inagaki, M. O. Letzel, S. Raasch, and T. Watanabe, 2004: LES Study of the Energy Imbalance Problem with Eddy Covariance Fluxes. *Boundary-Layer Meteorology*, **110**, 381–404, doi:10.1023/B:BOUN.0000007225.45548.7a.

URL http://link.springer.com/10.1023/B:BOUN.0000007225.45548.7a

Kenny, W. T., G. Bohrer, T. H. Morin, C. S. Vogel, A. M. Matheny, and A. R. Desai, 2017: A numerical case study of the implications of secondary circulations to the interpretation of eddy-covariance measurements over small lakes. *Boundary-Layer Meteorology*, **165**, 311–332.

Khanna, S. and J. G. Brasseur, 1998: Three-dimensional buoyancy-and shear-induced local structure of the atmospheric boundary layer. *Journal of the atmospheric sciences*, **55**, 710–743.

Kim, Y., I. P. Castro, and Z.-T. Xie, 2013: Divergence-free turbulence inflow conditions for large-eddy simulations with incompressible flow solvers. *Computers & Fluids*, **84**, 56–68.

Kljun, N., P. Calanca, M. W. Rotach, and H. P. Schmid, 2004: A Simple Parameterisation for Flux Footprint Predictions. *Boundary-Layer Meteorology*, **112**, 503–523, doi:10.1023/B:BOUN.0000030653.71031.96.

URL http://link.springer.com/10.1023/B:BOUN.0000030653.71031.96

Kljun, N., M. Rotach, and H. Schmid, 2002: A Three-Dimensional Backward Lagrangian Footprint Model For A Wide Range Of Boundary-Layer Stratifications. *Boundary-Layer Meteorology*, **103**, 205–226, doi:10.1023/A:1014556300021.

URL http://link.springer.com/10.1023/A:1014556300021

Kohnert, K., A. Serafimovich, S. Metzger, J. Hartmann, and T. Sachs, 2017: Strong geologic methane emissions from discontinuous terrestrial permafrost in the Mackenzie Delta, Canada. *Scientific Reports*, **7**, 5828, doi:10.1038/s41598-017-05783-2.

URL http://www.nature.com/articles/s41598-017-05783-2

Koitzsch, R., M. Dzingel, T. Foken, and G. Mücket, 1988: Probleme der experimentellen erfassung des energieaustausches über winterweizen. *Zeitschrift für Meteorologie*, **38**, 150–155.

Krč, P., J. Resler, M. Sühring, S. Schubert, M. H. Salim, and V. Fuka, 2021: Radiative transfer model 3.0 integrated into the palm model system 6.0. *Geoscientific Model Development*, **14**, 3095–3120.

Kröniger, K., F. De Roo, P. Brugger, S. Huq, T. Banerjee, J. Zinsser, E. Rotenberg, D. Yakir, S. Rohatyn, and M. Mauder, 2018: Effect of secondary circulations on the surface–atmosphere exchange of energy at an isolated semi-arid forest. *Boundary-Layer Meteorology*, **169**, 209–232.

Kröniger, K., F. De Roo, P. Brugger, S. Huq, T. Banerjee, J. Zinsser, E. Rotenberg, D. Yakir, S. Rohatyn, and M. Mauder, 2018: Effect of Secondary Circulations on the Surface–Atmosphere Exchange of Energy at an Isolated Semi-arid Forest. *Boundary-Layer Meteorology*, **169**, 209–232, doi:10.1007/s10546-018-0370-6.

URL http://link.springer.com/10.1007/s10546-018-0370-6

Kumar, P. and E. Foufoula-Georgiou, 1994: Wavelet analysis in geophysics: An introduction. *Wavelets in geophysics*, **4**, 1–43.

Kumar, V., J. Kleissl, C. Meneveau, and M. B. Parlange, 2006: Large-eddy simulation of a diurnal cycle of the atmospheric boundary layer: Atmospheric stability and scaling issues. *Water resources research*, **42**.

Kustas, W. P. and J. D. Albertson, 2003: Effects of surface temperature contrast on land-atmosphere exchange: A case study from monsoon 90. *Water Resources Research*, **39**.

Lemone, M. A., 1973: The structure and dynamics of horizontal roll vortices in the planetary boundary layer. *Journal of Atmospheric Sciences*, **30**, 1077–1091.

— 1976: Modulation of turbulence energy by longitudinal rolls in an unstable planetary boundary layer. *Journal of the Atmospheric Sciences*, **33**, 1308–1320.

LeMone, M. A., F. Chen, M. Tewari, J. Dudhia, B. Geerts, Q. Miao, R. L. Coulter, and R. L. Grossman, 2010a: Simulating the ihop_2002 fair-weather cbl with the wrf-arw–noah modeling system. part i: Surface fluxes and cbl structure and evolution along the eastern track. *Monthly weather review*, **138**, 722–744.

— 2010b: Simulating the ihop_2002 fair-weather cbl with the wrf-arw–noah modeling system. part ii: Structures from a few kilometers to 100 km across. *Monthly Weather Review*, **138**, 745–764.

Lenschow, D. H., J. Mann, and L. Kristensen, 1994: How Long Is Long Enough When Measuring Fluxes and Other Turbulence Statistics? *Journal of Atmospheric and Oceanic Technology*, **11**, 661 – 673, doi:10.1175/1520-0426(1994)011¡0661:HLILEW¿2.0.CO;2.

URL https://journals.ametsoc.org/view/journals/atot/11/3/1520-0426_1994_011_0661_hlilew_2_0_co_2.xml

Lenschow, D. H. and B. B. Stankov, 1986: Length Scales in the Convective Boundary Layer. *Journal of Atmospheric Sciences*, **43**, 1198 – 1209, doi:10.1175/1520-0469(1986)043¡1198:LSITCB¿2.0.CO;2.

URL https://journals.ametsoc.org/view/journals/atsc/43/12/1520-0469_1986_043_1198_lsitcb_2_0_co_2.xml

Leuning, R., O. T. Denmead, A. R. G. Lang, and E. Ohtaki, 1982: Effects of heat and water vapor transport on eddy covariance measurement of CO2 fluxes. *Boundary-Layer Meteorology*, **23**, 209–222, doi:10.1007/BF00123298.

URL http://link.springer.com/10.1007/BF00123298

Li, D. and E. Bou-Zeid, 2011: Coherent Structures and the Dissimilarity of Turbulent Transport of Momentum and Scalars in the Unstable Atmospheric Surface Layer. *Boundary-Layer Meteorology*, **140**, 243–262, doi:10.1007/s10546-011-9613-5.

URL http://link.springer.com/10.1007/s10546-011-9613-5

Lin, D., B. Khan, M. Katurji, L. Bird, R. Faria, and L. E. Revell, 2021: Wrf4palm v1. 0: a mesoscale dynamical driver for the microscale palm model system 6.0. *Geoscientific Model Development*, **14**, 2503–2524.

Liu, G., J. Sun, and L. Yin, 2011: Turbulence characteristics of the shear-free convective boundary layer driven by heterogeneous surface heating. *Boundary-layer meteorology*, **140**, 57–71.

Liu, S. and Y. Shao, 2013: Soil-layer configuration requirement for large-eddy atmosphere and land surface coupled modeling. *Atmospheric Science Letters*, **14**, 112–117.

Mahrt, L., 1996: The bulk aerodynamic formulation over heterogeneous surfaces, 33.

— 1998: Flux Sampling Errors for Aircraft and Towers. *JOURNAL OF ATMOSPHERIC AND OCEANIC TECHNOLOGY*, **15**, 14.

— 2000: Surface Heterogeneity and Vertical Structure of the Boundary Layer. *Boundary-Layer Meteorology*, **96**, 33–62, doi:10.1023/A:1002482332477.

URL http://link.springer.com/10.1023/A:1002482332477

— 2010: Computing turbulent fluxes near the surface: Needed improvements. *Agricultural and Forest Meteorology*, **150**, 501–509, doi:10.1016/j.agrformet.2010.01.015.

URL https://linkinghub.elsevier.com/retrieve/pii/S0168192310000389

Mahrt, L., J. I. Macpherson, and R. Desjardins, 1994: Observations of fluxes over heterogeneous surfaces. *Boundary-Layer Meteorology*, **67**, 345–367, doi:10.1007/BF00705438.

URL http://link.springer.com/10.1007/BF00705438

Margairaz, F., E. R. Pardyjak, and M. Calaf, 2020: Surface Thermal Heterogeneities and the Atmospheric Boundary Layer: The Relevance of Dispersive Fluxes. *Boundary-Layer Meteorology*, **175**, 369–395, doi:10.1007/s10546-020-00509-w.

URL http://link.springer.com/10.1007/s10546-020-00509-w

Maronga, B., S. Banzhaf, C. Burmeister, T. Esch, R. Forkel, D. Fröhlich, V. Fuka, K. F. Gehrke, J. Geletič, S. Giersch, et al., 2020a: Overview of the palm model system 6.0. *Geoscientific Model Development*, **13**, 1335–1372.

Maronga, B., C. Knigge, and S. Raasch, 2020b: An Improved Surface Boundary Condition for Large-Eddy Simulations Based on Monin–Obukhov Similarity Theory: Evaluation and

Consequences for Grid Convergence in Neutral and Stable Conditions. *Boundary-Layer Meteorology*, **174**, 297–325, doi:10.1007/s10546-019-00485-w.

URL http://link.springer.com/10.1007/s10546-019-00485-w

Maronga, B. and S. Raasch, 2013a: Large-Eddy Simulations of Surface Heterogeneity Effects on the Convective Boundary Layer During the LITFASS-2003 Experiment. *Boundary-Layer Meteorology*, **146**, 17–44, doi:10.1007/s10546-012-9748-z.

URL http://link.springer.com/10.1007/s10546-012-9748-z

— 2013b: Large-eddy simulations of surface heterogeneity effects on the convective boundary layer during the litfass-2003 experiment. *Boundary-Layer Meteorology*, **146**, 17–44.

Mathis, R., N. Hutchins, and I. Marusic, 2009: Large-scale amplitude modulation of the small-scale structures in turbulent boundary layers. *Journal of Fluid Mechanics*, **628**, 311–337.

Mauder, M., R. L. Desjardins, and I. MacPherson, 2007a: Scale analysis of airborne flux measurements over heterogeneous terrain in a boreal ecosystem: SCALE ANALYSIS OF FLUX MEASUREMENTS. *Journal of Geophysical Research: Atmospheres*, **112**, n/a–n/a, doi:10.1029/2006JD008133.

URL http://doi.wiley.com/10.1029/2006JD008133

— 2008a: Creating Surface Flux Maps from Airborne Measurements: Application to the Mackenzie Area GEWEX Study MAGS 1999. *Boundary-Layer Meteorology*, **129**, 431–450, doi:10.1007/s10546-008-9326-6.

URL http://link.springer.com/10.1007/s10546-008-9326-6

Mauder, M., R. L. Desjardins, E. Pattey, Z. Gao, and R. van Haarlem, 2008b: Measurement of the Sensible Eddy Heat Flux Based on Spatial Averaging of Continuous Ground-Based

Observations. *Boundary-Layer Meteorology*, **128**, 151–172, doi:10.1007/s10546-008-9279-9.

URL http://link.springer.com/10.1007/s10546-008-9279-9

Mauder, M., T. Foken, and J. Cuxart, 2020: Surface-Energy-Balance Closure over Land: A Review. *Boundary-Layer Meteorology*, doi:10.1007/s10546-020-00529-6.

URL http://link.springer.com/10.1007/s10546-020-00529-6

Mauder, M., A. Ibrom, L. Wanner, F. De Roo, P. Brugger, R. Kiese, and K. Pilegaard, 2021: Options to correct local turbulent flux measurements for large-scale fluxes using a LES-based approach. preprint, Others (Wind, Precipitation, Temperature, etc.)/In Situ Measurement/Data Processing and Information Retrieval.

URL https://amt.copernicus.org/preprints/amt-2021-126/

Mauder, M., S. P. Oncley, R. Vogt, T. Weidinger, L. Ribeiro, C. Bernhofer, T. Foken, W. Kohsiek, H. A. R. De Bruin, and H. Liu, 2007b: The energy balance experiment EBEX-2000. Part II: Intercomparison of eddy-covariance sensors and post-field data processing methods. *Boundary-Layer Meteorology*, **123**, 29–54, doi:10.1007/s10546-006-9139-4.

URL http://link.springer.com/10.1007/s10546-006-9139-4

Mazzaro, L. J., D. Muñoz-Esparza, J. K. Lundquist, and R. R. Linn, 2017: Nested mesoscale-to-les modeling of the atmospheric boundary layer in the presence of under-resolved convective structures. *Journal of Advances in Modeling Earth Systems*, **9**, 1795–1810.

Meijninger, W. M. L., F. Beyrich, A. Lüdi, W. Kohsiek, and H. A. R. D. Bruin, 2006: Scintillometer-Based Turbulent Fluxes of Sensible and Latent Heat Over a Heterogeneous Land Surface – A Contribution to Litfass-2003. *Boundary-Layer Meteorology*, **121**, 89–110,

doi:10.1007/s10546-005-9022-8.

URL https://doi.org/10.1007/s10546-005-9022-8

Metzger, S., D. Durden, S. Paleri, M. Sühring, B. J. Butterworth, C. Florian, M. Mauder, D. M. Plummer, L. Wanner, K. Xu, and A. R. Desai, 2021: Novel approach to observing system simulation experiments improves information gain of surface–atmosphere field measurements. *Atmospheric Measurement Techniques*, **14**, 6929–6954, doi:10.5194/amt-14-6929-2021.

URL https://amt.copernicus.org/articles/14/6929/2021/

Metzger, S., D. Durden, C. Sturtevant, H. Luo, N. Pingintha-Durden, T. Sachs, A. Serafimovich, J. Hartmann, J. Li, K. Xu, and A. R. Desai, 2017: eddy4R 0.2.0: a DevOps model for community-extensible processing and analysis of eddy-covariance data based on R, Git, Docker, and HDF5. *Geoscientific Model Development*, **10**, 3189–3206, doi:10.5194/gmd-10-3189-2017.

URL https://www.geosci-model-dev.net/10/3189/2017/

Metzger, S., W. Junkermann, M. Mauder, K. Butterbach-Bahl, B. Trancón y Widemann, F. Neidl, K. Schäfer, S. Wieneke, X. H. Zheng, H. P. Schmid, and T. Foken, 2013: Spatially explicit regionalization of airborne flux measurements using environmental response functions. *Biogeosciences*, **10**, 2193–2217, doi:10.5194/bg-10-2193-2013.

URL https://www.biogeosciences.net/10/2193/2013/

Moeng, C.-H. and P. P. Sullivan, 1994: A comparison of shear-and buoyancy-driven planetary boundary layer flows. *Journal of Atmospheric Sciences*, **51**, 999–1022.

Moeng, C.-H. and J. C. Wyngaard, 1984: Statistics of conservative scalars in the convective boundary layer. *Journal of Atmospheric Sciences*, **41**, 3161–3169.

— 1988: Spectral Analysis of Large-Eddy Simulations of the Convective Boundary Layer. *Journal of Atmospheric Sciences*, **45**, 3573 – 3587, doi:10.1175/1520-0469(1988)045¡3573:SAOLES¿2.0.CO;2.

URL https://journals.ametsoc.org/view/journals/atsc/45/23/1520-0469_1988_045_3573_saoles_2_0_co_2.xml

— 1989: Evaluation of turbulent transport and dissipation closures in second-order modeling. *Journal of the Atmospheric Sciences*, **46**, 2311–2330.

Monin, A. and A. Obukhov, 1954: Osnovnye zakonomernosti turbulentnogo peremeshivanija v prizemnom sloe atmosfery (basic laws of turbulent mixing in the atmosphere near the ground). *Trudy geofiz. inst. AN SSSR*, **24**, 163–187.

Morrison, T., M. Calaf, C. W. Higgins, S. A. Drake, A. Perelet, and E. Pardyjak, 2021: The Impact of Surface Temperature Heterogeneity on Near-Surface Heat Transport. *Boundary-Layer Meteorology*, **180**, 247–272, doi:10.1007/s10546-021-00624-2.

URL https://link.springer.com/10.1007/s10546-021-00624-2

Nordbo, A. and G. Katul, 2013: A Wavelet-Based Correction Method for Eddy-Covariance High-Frequency Losses in Scalar Concentration Measurements. *Boundary-Layer Meteorology*, **146**, 81–102, doi:10.1007/s10546-012-9759-9.

URL http://link.springer.com/10.1007/s10546-012-9759-9

Obukhov, A., 1946: Turbulentnost'v temperaturnoj-neodnorodnoj atmosfere. *Trudy Inst. Theor. Geofiz. AN SSSR*, **1**, 95–115.

Omidvar, H., E. Bou-Zeid, Q. Li, J.-P. Mellado, and P. Klein, 2020: Plume or bubble? Mixed-convection flow regimes and city-scale circulations. *Journal of Fluid Mechanics*, **897**,

A5, doi:10.1017/jfm.2020.360.

URL https://www.cambridge.org/core/product/identifier/S0022112020003602/type/journal_article

Oncley, S. P., T. Foken, R. Vogt, W. Kohsiek, H. A. R. DeBruin, C. Bernhofer, A. Christen, E. v. Gorsel, D. Grantz, C. Feigenwinter, I. Lehner, C. Liebethal, H. Liu, M. Mauder, A. Pitacco, L. Ribeiro, and T. Weidinger, 2007: The Energy Balance Experiment EBEX-2000. Part I: overview and energy balance. *Boundary-Layer Meteorology*, **123**, 1–28, doi:10.1007/s10546-007-9161-1.

URL http://link.springer.com/10.1007/s10546-007-9161-1

Orlanski, I., 1975: A rational subdivision of scales for atmospheric processes. *Bulletin of the American Meteorological Society*, 527–530.

Ovchinnikov, M., J. D. Fast, L. K. Berg, W. I. Gustafson Jr, J. Chen, K. Sakaguchi, and H. Xiao, 2022: Effects of horizontal resolution, domain size, boundary conditions, and surface heterogeneity on coarse les of a convective boundary layer. *Monthly Weather Review*, **150**, 1397–1415.

Paleri, S., B. Butterworth, and A. R. Desai, 2023: Here, there, and everywhere: Spatial patterns and scales. *Conceptual Boundary Layer Meteorology*, Elsevier, 37–58.

Paleri, S., A. R. Desai, S. Metzger, D. Durden, B. J. Butterworth, M. Mauder, K. Kohnert, and A. Serafimovich, 2022: Space-scale resolved surface fluxes across a heterogeneous, mid-latitude forested landscape. *Journal of Geophysical Research: Atmospheres*, e2022JD037138.

Panin, G. N. and C. Bernhofer, 2008: Parametrization of turbulent fluxes over inhomogeneous landscapes. *Izvestiya, Atmospheric and Oceanic Physics*, **44**, 701–716.

Patton, E. G., P. P. Sullivan, and C.-H. Moeng, 2005: The Influence of Idealized Heterogeneity on Wet and Dry Planetary Boundary Layers Coupled to the Land Surface. *Journal of the Atmospheric Sciences*, **62**, 2078–2097, doi:10.1175/JAS3465.1.

URL https://journals.ametsoc.org/doi/10.1175/JAS3465.1

Pielke, R. A., . Sr, R. Avissar, M. Raupach, A. J. Dolman, X. Zeng, and A. S. Denning, 1998: Interactions between the atmosphere and terrestrial ecosystems: influence on weather and climate. *Global Change Biology*, **4**, 461–475, doi:https://doi.org/10.1046/j.1365-2486.1998.t01-1-00176.x, _eprint: https://onlinelibrary.wiley.com/doi/pdf/10.1046/j.1365-2486.1998.t01-1-00176.x.

URL https://onlinelibrary.wiley.com/doi/abs/10.1046/j.1365-2486.1998.t01-1-00176.x

Prabha, T. V., A. Karipot, and M. W. Binford, 2007: Characteristics of secondary circulations over an inhomogeneous surface simulated with large-eddy simulation. *Boundary-layer meteorology*, **123**, 239–261.

Raasch, S. and G. Harbusch, 2001: An Analysis Of Secondary Circulations And Their Effects Caused By Small-Scale Surface Inhomogeneities Using Large-Eddy Simulation. *Boundary-Layer Meteorology*, **101**, 31–59, doi:10.1023/A:1019297504109.

URL http://link.springer.com/10.1023/A:1019297504109

Raupach, M. R. and R. H. Shaw, 1982: Averaging procedures for flow within vegetation canopies. *Boundary-layer meteorology*, **22**, 79–90.

Resler, J., K. Eben, J. Geletič, P. Krč, M. Rosecký, M. Sühring, M. Belda, V. Fuka, T. Halenka, P. Huszár, J. Karlický, N. Benešová, J. Ďoubalová, K. Honzáková, J. Keder, Nápravníková,

and O. Vlček, 2020: Validation of the PALM model system 6.0 in real urban environment; case study of Prague-Dejvice, Czech Republic. preprint, Atmospheric Sciences.

URL https://gmd.copernicus.org/preprints/gmd-2020-175/

Rey-Sanchez, C., A. Arias-Ortiz, K. Kasak, H. Chu, D. Szutu, J. Verfaillie, and D. Baldocchi, 2022: Detecting hot spots of methane flux using footprint-weighted flux maps. *Journal of Geophysical Research: Biogeosciences*, **127**, e2022JG006977.

Rodi, A., 2011: King of the air: The evolution and capabilities of wyoming's observation aircraft. *Meteorological Technology International*, 44–47.

Rodi, A. R. and D. C. Leon, 2012: Correction of static pressure on a research aircraft in accelerated flight using differential pressure measurements. *Atmospheric Measurement Techniques*, **5**, 2569–2579, doi:10.5194/amt-5-2569-2012.

URL https://amt.copernicus.org/articles/5/2569/2012/

Rodi, A. R. and P. A. Spyers-Duran, 1972: Analysis of Time Response of Airborne Temperature Sensors. *Journal of Applied Meteorology and Climatology*, **11**, 554 – 556, doi:10.1175/1520-0450(1972)011¡0554:AOTROA¿2.0.CO;2.

URL https://journals.ametsoc.org/view/journals/apme/11/3/1520-0450_1972_011_0554_aotroa_2_0_co_2.xml

Rotach, M. W., S.-E. Gryning, and C. Tassone, 1996: A two-dimensional lagrangian stochastic dispersion model for daytime conditions. *Quarterly Journal of the Royal Meteorological Society*, **122**, 367–389.

Saiki, E. M., C.-H. Moeng, and P. P. Sullivan, 2000: Large-Eddy Simulation Of The Stably Stratified Planetary Boundary Layer. *Boundary-Layer Meteorology*, **95**, 1–30,

doi:10.1023/A:1002428223156.

URL http://link.springer.com/10.1023/A:1002428223156

Salesky, S. and W. Anderson, 2018: Buoyancy effects on large-scale motions in convective atmospheric boundary layers: implications for modulation of near-wall processes. *Journal of Fluid Mechanics*, **856**, 135–168.

Salesky, S. T. and W. Anderson, 2020: Coherent Structures Modulate Atmospheric Surface Layer Flux-Gradient Relationships. *Physical Review Letters*, **125**, 124501, doi:10.1103/PhysRevLett.125.124501.

URL https://link.aps.org/doi/10.1103/PhysRevLett.125.124501

Salesky, S. T., M. Chamecki, and E. Bou-Zeid, 2017: On the Nature of the Transition Between Roll and Cellular Organization in the Convective Boundary Layer. *Boundary-Layer Meteorology*, **163**, 41–68, doi:10.1007/s10546-016-0220-3.

URL http://link.springer.com/10.1007/s10546-016-0220-3

Schröter, M., J. Bange, and S. Raasch, 2000: Simulated Airborne Flux Measurements in a LES generated Convective Boundary Layer. *Boundary-Layer Meteorology*, **95**, 437–456, doi:10.1023/A:1002649322001.

URL http://link.springer.com/10.1023/A:1002649322001

Scott, D. W., 1979: On optimal and data-based histograms. *Biometrika*, **66**, 605–610.

— 2015: *Multivariate density estimation: theory, practice, and visualization*. John Wiley & Sons.

Shao, Y., S. Liu, J. H. Schween, and S. Crewell, 2013: Large-Eddy Atmosphere–Land-Surface Modelling over Heterogeneous Surfaces: Model Development and Comparison with Measurements. *Boundary-Layer Meteorology*, **148**, 333–356, doi:10.1007/s10546-013-9823-0.
URL http://link.springer.com/10.1007/s10546-013-9823-0

Shaw, R. H. and U. Schumann, 1992: Large-eddy simulation of turbulent flow above and within a forest. *Boundary-Layer Meteorology*, **61**, 47–64, doi:10.1007/BF02033994.
URL http://link.springer.com/10.1007/BF02033994

Shen, S. and M. Y. Leclerc, 1995: How large must surface inhomogeneities be before they influence the convective boundary layer structure? a case study. *Quarterly Journal of the Royal Meteorological Society*, **121**, 1209–1228.

Siebesma, A. and J. Cuijpers, 1995: Evaluation of parametric assumptions for shallow cumulus convection. *Journal of Atmospheric Sciences*, **52**, 650–666.

Siebesma, A. and J. Teixeira, 2000: An advection–diffusion scheme for the convective boundary layer: Description and 1d results. *Preprints, 14th Symp. on Boundary Layers and Turbulence, Aspen, CO, Amer. Meteor. Soc*, volume 133, 136.

Siebesma, A. P., P. M. Soares, and J. Teixeira, 2007: A combined eddy-diffusivity mass-flux approach for the convective boundary layer. *Journal of the atmospheric sciences*, **64**, 1230–1248.

Simon, J. S., A. D. Bragg, P. A. Dirmeyer, and N. W. Chaney, 2021: Semi-coupling of a Field-scale Resolving Land-surface Model and WRF-LES to Investigate the Influence of Land-surface Heterogeneity on Cloud Development. *Journal of Advances in Modeling Earth Systems*, doi:10.1029/2021MS002602.

URL https://onlinelibrary.wiley.com/doi/10.1029/2021MS002602

Starr, E. and B. Goldfarb, 2020: Binned scatterplots: A simple tool to make research easier and better. *Strategic Management Journal*, **41**, 2261–2274.

Steinfeld, G., M. O. Letzel, S. Raasch, M. Kanda, and A. Inagaki, 2007: Spatial representativeness of single tower measurements and the imbalance problem with eddy-covariance fluxes: results of a large-eddy simulation study. *Boundary-Layer Meteorology*, **123**, 77–98, doi:10.1007/s10546-006-9133-x.

URL http://link.springer.com/10.1007/s10546-006-9133-x

Steinfeld, G., S. Raasch, and T. Markkanen, 2008: Footprints in homogeneously and heterogeneously driven boundary layers derived from a lagrangian stochastic particle model embedded into large-eddy simulation. *Boundary-layer meteorology*, **129**, 225–248.

Stoll, R., J. A. Gibbs, S. T. Salesky, W. Anderson, and M. Calaf, 2020: Large-Eddy Simulation of the Atmospheric Boundary Layer. *Boundary-Layer Meteorology*, doi:10.1007/s10546-020-00556-3.

URL http://link.springer.com/10.1007/s10546-020-00556-3

Stoy, P. C., M. Mauder, T. Foken, B. Marcolla, E. Boegh, A. Ibrom, M. A. Arain, A. Arneth, M. Aurela, C. Bernhofer, A. Cescatti, E. Dellwik, P. Duce, D. Gianelle, E. van Gorsel, G. Kiely, A. Knohl, H. Margolis, H. McCaughey, L. Merbold, L. Montagnani, D. Papale, M. Reichstein, M. Saunders, P. Serrano-Ortiz, M. Sottocornola, D. Spano, F. Vaccari, and A. Varlagin, 2013: A data-driven analysis of energy balance closure across FLUXNET research sites: The role of landscape scale heterogeneity. *Agricultural and Forest Meteorology*,

171-172, 137–152, doi:10.1016/j.agrformet.2012.11.004.

URL https://linkinghub.elsevier.com/retrieve/pii/S0168192312003413

Strunin, M. A. and T. Hiyama, 2004: Applying wavelet transforms to analyse aircraft-measured turbulence and turbulent fluxes in the atmospheric boundary layer over eastern Siberia. *Hydrological Processes*, **18**, 3081–3098, doi:10.1002/hyp.5750.

URL http://doi.wiley.com/10.1002/hyp.5750

— 2005: Spectral Structure of Small-Scale Turbulent and Mesoscale Fluxes in the Atmospheric Boundary Layer over a Thermally Inhomogeneous Land Surface. *Boundary-Layer Meteorology*, **117**, 479–510, doi:10.1007/s10546-005-2188-2.

URL http://link.springer.com/10.1007/s10546-005-2188-2

Strunin, M. A., T. Hiyama, J. Asanuma, and T. Ohata, 2004: Aircraft Observations of the Development of Thermal Internal Boundary Layers and Scaling of the Convective Boundary Layer Over Non-Homogeneous Land Surfaces. *Boundary-Layer Meteorology*, **111**, 491–522, doi:10.1023/B:BOUN.0000016542.72958.e9.

URL http://link.springer.com/10.1023/B:BOUN.0000016542.72958.e9

Stull, R. B., 1988: An Introduction to Boundary Layer Meteorology. *An Introduction to Boundary Layer Meteorology*, R. B. Stull, ed., Springer Netherlands, Dordrecht, 1–27.

URL http://link.springer.com/10.1007/978-94-009-3027-8_1

Sullivan, P. P., C.-H. Moeng, B. Stevens, D. H. Lenschow, and S. D. Mayor, 1998: Structure of the entrainment zone capping the convective atmospheric boundary layer. *Journal of the atmospheric sciences*, **55**, 3042–3064.

Sun, J., R. Desjardins, L. Mahrt, and I. MacPherson, 1998: Transport of carbon dioxide, water vapor, and ozone by turbulence and local circulations. *Journal of Geophysical Research: Atmospheres*, **103**, 25873–25885, doi:10.1029/98JD02439.

URL http://doi.wiley.com/10.1029/98JD02439

Sun, J., D. H. Lenschow, L. Mahrt, T. L. Crawford, K. J. Davis, S. P. Oncley, J. I. MacPherson, Q. Wang, R. J. Dobosy, and R. L. Desjardins, 1997: Lake-induced atmospheric circulations during BOREAS. *Journal of Geophysical Research: Atmospheres*, **102**, 29155–29166, doi:10.1029/97JD01114.

URL http://doi.wiley.com/10.1029/97JD01114

Sühring, M., B. Maronga, F. Herbort, and S. Raasch, 2014: On the Effect of Surface Heat-Flux Heterogeneities on the Mixed-Layer-Top Entrainment. *Boundary-Layer Meteorology*, **151**, 531–556, doi:10.1007/s10546-014-9913-7.

URL http://link.springer.com/10.1007/s10546-014-9913-7

Sühring, M. and S. Raasch, 2013: Heterogeneity-Induced Heat-Flux Patterns in the Convective Boundary Layer: Can they be Detected from Observations and is There a Blending Height?—A Large-Eddy Simulation Study for the LITFASS-2003 Experiment. *Boundary-Layer Meteorology*, **148**, 309–331, doi:10.1007/s10546-013-9822-1.

URL http://link.springer.com/10.1007/s10546-013-9822-1

Thomas, C. and T. Foken, 2005: Detection of long-term coherent exchange over spruce forest using wavelet analysis. *Theoretical and Applied Climatology*, **80**, 91–104, doi:10.1007/s00704-004-0093-0.

URL http://link.springer.com/10.1007/s00704-004-0093-0

Tillman, J., 1972: The indirect determination of stability, heat and momentum fluxes in the atmospheric boundary layer from simple scalar variables during dry unstable conditions. *Journal of Applied Meteorology and Climatology*, **11**, 783–792.

Torrence, C. and G. P. Compo, 1998: A Practical Guide to Wavelet Analysis. *Bulletin of the American Meteorological Society*, **79**, 18.

Träumner, K., T. Damian, C. Stawiarski, and A. Wieser, 2015: Turbulent structures and coherence in the atmospheric surface layer. *Boundary-Layer Meteorology*, **154**, 1–25.

Troen, I. and L. Mahrt, 1986: A simple model of the atmospheric boundary layer; sensitivity to surface evaporation. *Boundary-Layer Meteorology*, **37**, 129–148.

Twine, T., W. Kustas, J. Norman, D. Cook, P. Houser, T. Meyers, J. Prueger, P. Starks, and M. Wesely, 2000: Correcting eddy-covariance flux underestimates over a grassland. *Agricultural and Forest Meteorology*, **103**, 279–300, doi:10.1016/S0168-1923(00)00123-4.
URL https://linkinghub.elsevier.com/retrieve/pii/S0168192300001234

Van Genuchten, M. T., 1980: A closed-form equation for predicting the hydraulic conductivity of unsaturated soils. *Soil science society of America journal*, **44**, 892–898.

van Heerwaarden, C. C., J. P. Mellado, and A. De Lozar, 2014: Scaling Laws for the Heterogeneously Heated Free Convective Boundary Layer. *Journal of the Atmospheric Sciences*, **71**, 3975–4000, doi:10.1175/JAS-D-13-0383.1.
URL http://journals.ametsoc.org/doi/abs/10.1175/JAS-D-13-0383.1

Wang, Z., J. French, G. Vali, P. Wechsler, S. Haimov, A. Rodi, M. Deng, D. Leon, J. Snider, L. Peng, and A. L. Pazmany, 2012: Single Aircraft Integration of Remote Sensing and In

Situ Sampling for the Study of Cloud Microphysics and Dynamics. *Bulletin of the American Meteorological Society*, **93**, 653–668, doi:10.1175/BAMS-D-11-00044.1.

URL https://journals.ametsoc.org/doi/10.1175/BAMS-D-11-00044.1

Wanner, L., M. Calaf, and M. Mauder, 2022: Incorporating the effect of heterogeneous surface heating into a semi-empirical model of the surface energy balance closure. *PloS one*, **17**, e0268097.

Wanner, L., F. De Roo, M. Sühring, and M. Mauder, 2021: How Does the Choice of the Lower Boundary Conditions in Large-Eddy Simulations Affect the Development of Dispersive Fluxes Near the Surface? *Boundary-Layer Meteorology*, doi:10.1007/s10546-021-00649-7.

URL https://link.springer.com/10.1007/s10546-021-00649-7

Watanabe, T., 2004: Large-Eddy Simulation of Coherent Turbulence Structures Associated with Scalar Ramps Over Plant Canopies. *Boundary-Layer Meteorology*, **112**, 307–341, doi:10.1023/B:BOUN.0000027912.84492.54.

URL http://link.springer.com/10.1023/B:BOUN.0000027912.84492.54

Weckwerth, T. M., 2000: The effect of small-scale moisture variability on thunderstorm initiation. *Monthly Weather Review*, **128**, 4017–4030.

Weckwerth, T. M., T. W. Horst, and J. W. Wilson, 1999: An observational study of the evolution of horizontal convective rolls. *Monthly weather review*, **127**, 2160–2179.

Weckwerth, T. M., J. W. Wilson, R. M. Wakimoto, and N. A. Crook, 1997: Horizontal convective rolls: Determining the environmental conditions supporting their existence and characteristics. *Monthly weather review*, **125**, 505–526.

Wicker, L. J. and W. C. Skamarock, 2002: Time-splitting methods for elastic models using forward time schemes. *Monthly weather review*, **130**, 2088–2097.

Williamson, J. H., 1980: Low-storage runge-kutta schemes. *Journal of computational physics*, **35**, 48–56.

Wilson, J. W., G. B. Foote, N. A. Crook, J. C. Fankhauser, C. G. Wade, J. D. Tuttle, C. K. Mueller, and S. K. Krueger, 1992: The role of boundary-layer convergence zones and horizontal rolls in the initiation of thunderstorms: A case study. *Monthly weather review*, **120**, 1785–1815.

Wilson, N. R. and R. H. Shaw, 1977: A higher order closure model for canopy flow. *Journal of Applied Meteorology (1962-1982)*, 1197–1205.

Witte, M. K., A. Herrington, J. Teixeira, M. J. Kurowski, M. J. Chinita, R. L. Storer, K. Suselj, G. Matheou, and J. Bacmeister, 2022: Augmenting the double-gaussian representation of atmospheric turbulence and convection via a coupled stochastic multi-plume mass-flux scheme. *Monthly weather review*, **150**, 2339–2355.

Wood, N. and P. Mason, 1991: The influence of static stability on the effective roughness lengths for momentum and heat transfer. *Quarterly Journal of the Royal Meteorological Society*, **117**, 1025–1056, doi:10.1002/qj.49711750108.
URL http://doi.wiley.com/10.1002/qj.49711750108

Wulfmeyer, V., D. D. Turner, B. Baker, R. Banta, A. Behrendt, T. Bonin, W. A. Brewer, M. Buban, A. Choukulkar, E. Dumas, R. M. Hardesty, T. Heus, J. Ingwersen, D. Lange, T. R. Lee, S. Metzendorf, S. K. Muppa, T. Meyers, R. Newsom, M. Osman, S. Raasch, J. Santanello, C. Senff, F. Späth, T. Wagner, and T. Weckwerth, 2018: A New Research Approach

for Observing and Characterizing Land–Atmosphere Feedback. *Bulletin of the American Meteorological Society*, **99**, 1639–1667, doi:10.1175/BAMS-D-17-0009.1.

URL http://journals.ametsoc.org/doi/10.1175/BAMS-D-17-0009.1

Wyngaard, J. C. and R. A. Brost, 1984: Top-down and bottom-up diffusion of a scalar in the convective boundary layer. *Journal of Atmospheric Sciences*, **41**, 102–112.

Wyngaard, J. C. and C.-H. Moeng, 1992: Parameterizing turbulent diffusion through the joint probability density. *Boundary-layer meteorology*, **60**, 1–13.

Wyngaard, J. C. and J. C. Weil, 1991: Transport asymmetry in skewed turbulence. *Physics of Fluids A: Fluid Dynamics*, **3**, 155–162.

Xie, Z.-T. and I. P. Castro, 2008: Efficient generation of inflow conditions for large-eddy simulation of street-scale flows. *Flow Turbulence and Combustion*, **81**, 449–470.

Xu, F., W. Wang, J. Wang, Z. Xu, Y. Qi, and Y. Wu, 2017: Area-averaged evapotranspiration over a heterogeneous land surface: aggregation of multi-point EC flux measurements with a high-resolution land-cover map and footprint analysis. *Hydrology and Earth System Sciences*, **21**, 4037–4051, doi:10.5194/hess-21-4037-2017.

URL https://hess.copernicus.org/articles/21/4037/2017/

Xu, K., M. Sühring, S. Metzger, D. Durden, and A. R. Desai, 2020: Can Data Mining Help Eddy Covariance See the Landscape? A Large-Eddy Simulation Study. *Boundary-Layer Meteorology*, doi:10.1007/s10546-020-00513-0.

URL http://link.springer.com/10.1007/s10546-020-00513-0

Zhang, G., M. Y. Leclerc, H. F. Duarte, D. Durden, D. Werth, R. Kurzeja, and M. Parker, 2014: Multi-scale decomposition of turbulent fluxes above a forest canopy. *Agricultural and*

Forest Meteorology, **186**, 48–63, doi:10.1016/j.agrformet.2013.11.010.

URL https://linkinghub.elsevier.com/retrieve/pii/S0168192313003006

Zhang, Y., H. Liu, T. Foken, Q. L. Williams, S. Liu, M. Mauder, and C. Liebethal, 2010: Turbulence Spectra and Cospectra Under the Influence of Large Eddies in the Energy Balance EXperiment (EBEX). *Boundary-Layer Meteorology*, **136**, 235–251, doi:10.1007/s10546-010-9504-1.

URL http://link.springer.com/10.1007/s10546-010-9504-1

Zhou, Y., D. Li, and X. Li, 2019: The Effects of Surface Heterogeneity Scale on the Flux Imbalance under Free Convection. *Journal of Geophysical Research: Atmospheres*, 2018JD029550, doi:10.1029/2018JD029550.

URL https://onlinelibrary.wiley.com/doi/abs/10.1029/2018JD029550

Zhou, Y., M. Sühring, and X. Li, 2023: Evaluation of energy balance closure adjustment and imbalance prediction methods in the convective boundary layer–a large eddy simulation study. *Agricultural and Forest Meteorology*, **333**, 109382.